Geometric control of active flows

Dissertation

zur Erlangung des akademischen Grades
Doctor rerum naturalium

vorgelegt

der Fakultät Physik
Bereich Mathematik und Naturwissenschaften
der Technischen Universität Dresden

von

Jonas Neipel
geboren am 03.12.1994 in Erlangen

Max-Planck-Institut für Physik komplexer Systeme
Max-Planck-Institut für molekulare Zellbiologie und Genetik

Dresden, Mai 2024

1. Gutachter:	Prof. Dr. Frank Jülicher
2. Gutachter:	Prof. Dr. Karsten Kruse

Acknowledgements

First of all, I want to thank my supervisors Frank Jülicher and Stephan Grill. Frank, you taught me how to be a good scientist. Your scientific rigor and your high esteem for the independent mind has always inspired me. Stephan, you are an infallible source of encouragement and enthusiasm. I have always felt lucky to be part of your lab. The theoretical journeys of this thesis all started from experimental observations in your lab. Thanks to your guidance, these journeys also lead to experimentally testable predictions. One particularly fruitful journey would not have been possible without Marko Popovic to whom I owe the idea of an active crack. Marko, I thank you for all your guidance and support.

Furthermore, I wish to thank all the current and former members of Stephan's lab and the Biological Physics Division of the MPI-PKS. I am very lucky to have two such welcoming scientific families. In particular, I am grateful for my experimental collaborators Teije Middelkoop, Julia Pfanzelter, Adrian Lahola-Chomiak, Lokesh Pimpale, Arjun Narayanan and Patrick Breier. Without their work, their advice and their insights, this thesis would not have been possible. I am grateful for various other colleagues that have helped and inspired me or simply made me feel at home. Here, I want to highlight in particular the scientific discussions with: Peter Fulde, Charlie Duclut, Jonathan Bauermann, Peter Hampshire, Archit Bhatnagar, Anne Materne, Ricard Alert and Stefano Bo. Moreover, I thank the administration and the IT department of the MPI-PKS, in particular Ulrike Burkert, Elise Voigt and Hubert Scherrer-Paulus. Furthermore, I thank Anne, Archit, Boyi, Christian, Gerhild, Josef, Julia, Kartik, Kathrin, Marko, Peter and Suganthan for critical reading of this thesis.

Outside of Dresden, I wish to thank Jerome Gros and his lab for their invaluable advice and their warm welcoming in Paris. Furthermore, I thank Ella Linxia Müller and Pierre Gönczy for fruitful discussions. I thank Gonca Erdemci-Tandogan and Daniel Grimes for organizing a fascinating workshop on left-right patterning. I thank all the members of this workshop for sharing their insight and enthusiasm. This workshop has profoundly impacted my understanding and fascination for developmental biology. I thank in particular Natalia Shylo for sharing her insight and data from chameleon embryos.

Throughout this thesis, a certain fascination for mathematics and in particular differential geometry will be evident. I think I owe much of this fascination to Frederic Schuller. During my Bachelor studies in Erlangen, he showed me the mathematical magic that can be found in classical and quantum mechanics. While I am afraid that this thesis cannot live up to his level of mathematical rigor, the enthusiasm for abstract mathematical concepts has survived, which has been crucial to some of the insights of this thesis.

Finally, I want to thank my family, in particular my wife Charlotte. Without her love and support, this thesis would not have been possible. Thanks to her, I have not only studied the development of worms and birds, but we have also witnessed the development of two wonderful little humans: Leonore and Thea. I want to dedicate this thesis to them.

Abstract

The development of an organism starting from a fertilized egg involves the self-organized formation of patterns and the generation of shape. Patterns and shapes are characterized by their geometry, i.e. angles and distances between features. In this thesis, we set out to understand how the given geometry of pattern and shape of a living system feeds back into the evolution of this geometry. We focus on two fundamental developmental processes: axis specification and gastrulation. Both processes rely on the directed movements of cells and molecules driven by molecular force generation. Here, we ask how the geometry of an embryo guides such active flows.

Active flows are often confined to the surface of a cell or embryo which is usually curved. We use the hydrodynamic theory of active surfaces to investigate how this curvature impacts on flows that are driven by patterns of mechanical activity. Using a minimal model of the cell cortex, we find that active cortical stresses can drive a rotation of the cell that aligns the chemical pattern of the stress regulator with the geometry of the cell surface. In particular, we find that active tension in the cytokinetic ring ensures that a cell divides along its longest axes, a common phenomenon known as Hertwig's rule. As a consequence, the body axes of the *C. elegans* embryo are aligned with the geometry of the egg shell.

We next set out to understand the impact of surface geometry on flows and patterns in more complex geometries. We focus in particular on localized sources of mechanical activity in curved fluid films. Such active particles act as sensors of the surface geometry, as the viscosity relates the local flow field to the large-scale geometry of the fluid film. We find that the impact of an anisotropic surface geometry on the flow field can generally be understood in terms of effective gradients of friction and viscosity. With this, we show that contractile points in a fluid film are attracted by protrusions and saddle geometries where the contractile point is surrounded by a maximal amount of surface area within the hydrodynamic length. Furthermore, we find that anisotropic active particles move towards or away from a saddle of the surface depending on whether they are extensile or contractile.

To understand the process of gastrulation and left-right symmetry breaking in the avian embryo, we develop a hydrodynamic theory of the primitive streak, a line of mechanically active material. With this theory of an active viscous crack, we analyze experimental data from quail embryos. We find that the embryo-scale cell movements during gastrulation are driven by mechanical activity at the streak, while the surrounding epithelium behaves like a homogeneous fluid film. With this mechanical model, we find that streak elongation does not require extensile forces along the streak. Instead, streak elongation results from the flux of tissue into the streak, the viscosity of the surrounding tissue and the polar geometry of the streak.

During avian left-right symmetry breaking, a chiral flow of tissue emerges at the tip of the streak,

the so called Hensen's node. We find that this flow results from an active torque that drives a counter-rotation of tissue layers. Thus, avian left-right symmetry breaking is facilitated by the mechanical coupling of tissue layers that the structure of node and streak provides.

Finally, we study how the geometry of a surface impacts on such chiral flows. We find that chiral flows at the avian node as well as in the cell cortex can be recapitulated as the result of molecular torque dipoles that are aligned with the tangential plane of the cell or tissue surface. Only when the surface is curved, such in-plane torques drive in-plane flows. Thus, the geometry of the avian node and the cytokinetic furrow may facilitate the chiral flows that are driven by these structures.

Taken together, we find that the geometry of an embryo is crucial to the flows and patterns that emerge in such a mechanically active system, because the geometry defines how forces and torques are transmitted.

Kurzzusammenfassung

Die Entwicklung eines Organismus ist ein selbstorganisierter Prozess, der insbesondere die Entstehung von Mustern und Formen umfasst. Muster und Formen sind durch ihre Geometrie gekennzeichnet, d.h. durch Winkel und Abstände zwischen Bestandteilen des Organismus. In dieser Arbeit untersuchen wir, wie die Geometrie von Mustern und Formen eines Embryos die weitere Entwicklung dieser Geometrie beeinflusst. Wir befassen uns insbesondere mit zwei grundlegenden Entwicklungsprozesse: Gastrulation und die Etablierung der Körperachsen durch chemische Gradienten. Beide Prozesse beruhen auf der gerichteten Bewegung von Zellen und Molekülen, die durch Motormoleküle angetrieben wird. Hier befassen wir uns damit, wie die Geometrie eines Embryos solche aktiven Strömungen prägt.

Aktive Strömungen sind oft auf die Oberfläche einer Zelle oder eines Embryos beschränkt. Diese Oberfläche ist in der Regel gekrümmt. Wir verwenden die hydrodynamische Theorie aktiver Oberflächen, um zu untersuchen, wie sich diese Krümmung auf Stömungen eines aktiven Flüssigkeitsfilms auswirkt. Dazu untersuchen wir ein minimales Modell des Zellkortex. In diesem Modell resultieren Strömungen aus Gradienten von Myosinaktivität, die durch Gradienten einer aktiven kortikalen Spannung erfasst werden. Für anisotrope Zellformen finden wir, dass aktive kortikale Spannungen eine Rotation der Zelle antreiben können, die das chemische Muster des Spannungsregulators gemäß der Geometrie der Zelloberfläche ausrichten. Insbesondere finden wir, dass die aktive Spannung im zytokinetischen Ring sicherstellt, dass sich eine Zelle entlang ihrer längsten Achsen teilt, ein weitverbreitetes Phänomen, das als Hertwig's Regel bekannt ist. Infolgedessen werden die Körperachsen des *C. elegans* Embryos gemäß der Geometrie der Eischale ausgerichtet.

Darauf aufbauend untersuchen wir Strömungen aktiver Flüssigkeitsfilme in komplexeren Geometrien. Wir konzentrieren uns insbesondere auf lokalisierte Quellen mechanischer Aktivität. Wir demonstrieren hier, dass solche aktiven Teilchen als Sensoren der Oberflächengeometrie agieren können, da aufgrund der Viskosität des Flüssigkeitsfilms das lokale Strömungsfeld von der globalen Oberflächengeometrie abhängt. Wir zeigen, dass der Einfluss einer anisotropen Oberflächengeometrie auf das Strömungsfeld mithilfe effektiver Gradienten des Reibungskoeffizienten und der Viskosität verstanden werden kann. Damit zeigen wir, dass kontraktile Punkte in einem Flüssigkeitsfilm sich hin zu Satteln und lokalisierten Aus- oder Einstülpungen bewegen. Darüber hinaus finden wir, dass anisotrope aktive Partikel sich auf einen Sattel der Oberfläche zubewegen oder von ihm wegbewegen, je nachdem wie sie an das Strömungsfeld koppeln, d.h. ob sie extensil oder kontraktil sind.

Um den Prozess der Gastrulation und der Links-Rechts-Symmetriebrechung im Vogel-Embryo zu verstehen, entwickeln wir eine hydrodynamische Theorie des Primitivstreifens, einer Linie mechanisch aktiven Materials. Mit dieser Theorie eines aktiven viskosen Risses analysieren wir experimentelle Daten von Wachtel-Embryonen. Wir stellen fest, dass die Zellbewegungen während

der Gastrulation durch mechanische Aktivität im Primitivstreifen angetrieben werden, während sich das umliegende Gewebe wie eine homogene Flüssigkeit bewegt. Mit diesem mechanischen Modell finden wir, dass die Verlängerung des Primitivstreifens keine extensilen Kräfte entlang des Streifens erfordert. Stattdessen resultiert die Verlängerung des Primitivstreifens aus dem Fluss von Gewebe in den Streifen, der Viskosität des umliegenden Gewebes und der polaren Geometrie des Streifens.

Während der Links-Rechts-Symmetriebrechung im Vogel-Embryo entsteht eine chirale Strömung von Gewebe an der Spitze des Streifens, dem sogenannten Hensenschen Knoten. Wir finden, dass dieser Fluss aus einem aktiven Drehmoment resultiert, das eine Gegenrotation der Gewebeschichten antreibt. Somit wird die Links-Rechts-Symmetriebrechung bei Vögeln durch die mechanische Kopplung der Gewebeschichten ermöglicht und somit durch die Struktur von Hensenschem Knoten und Primitivstreifen.

Schließlich untersuchen wir, wie die Geometrie einer Oberfläche solche chiralen Strömungen beeinflusst. Wir finden, dass chirale Strömungen sowohl am Hensenschen Knoten als auch im Zellkortex als das Ergebnis molekularer Drehmoment-Dipole verstanden werden können. Die Drehmomente sind dabei parallel zur Zell- oder Gewebeoberfläche. Nur wenn die Oberfläche gekrümmt ist, treiben solche tangential Drehmomente tangentiale Strömungen an. Somit kann die Geometrie des Hensenschen Knotens und der Zytokinetischen Furche die durch diese Strukturen angetriebenen chiralen Strömungen begünstigen.

Zusammenfassend stellen wir fest, dass die Geometrie eines Embryos entscheidend für die Strömungen und Muster ist, die in einem solchen mechanisch aktiven System entstehen, da die Geometrie definiert, wie Kräfte und Drehmomente übertragen werden.

Contents

1 Introduction 1
1.1 Embryogenesis from a geometric viewpoint 2
1.2 Hydrodynamic theory of active fluid films 20
1.3 Understanding active surfaces with complex numbers 34
1.4 Overview of this thesis 41

2 Crack mechanics of avian gastrulation 43
2.1 The primitive streak as a crack in a fluid film 44
2.2 Hydrodynamic theory of active viscous cracks 51
2.3 The primitive streak as a branch cut 56
2.4 Advective crack propagation 63
2.5 Discussion 65

3 Pattern formation guided by surface geometry 69
3.1 Minimal model of guided symmetry breaking 70
3.2 Diffusion on a curved surface 74
3.3 Pattern formation in an active fluid model of the cell cortex 77
3.4 Discussion 89

4 Geometry sensing by active flows 91
4.1 Geometry sensing by an active isotropic fluid 92
4.2 Deformation response of active flow in general surface geometries 96
4.3 Geometry sensing by a contractile point 105
4.4 Pattern formation guided by the geometric potential 111
4.5 Geometry sensing by active p-atic particles 115
4.6 Discussion 119

5 Chiral flows controlled by embryo geometry 123
5.1 Mechanical model of avian left-right symmetry breaking 124
5.2 Chiral flows facilitated by curvature gradients 132
5.3 Discussion 139

6 Conclusion and Outlook 143

A A crack in a surface 147

B Analytical solutions of crack boundary conditions 151

C Analysis of experimental data from quail embryos 161

D The Newman Penrose formalism applied to an active surface 171

E Definitions and applications of spin-weighted spherical harmonics 175

F A pseudo-spectral method for the simulation of active fluid films 183

G A staggered-grid method for spin-weighted fields 189

H Deformation response of active flow 193

I On multipoles in a curved surface 203

J Supplemental figures and tables 205

Bibliography 211

Chapter 1

Introduction

The development of a complex multicellular organism such as a human or a worm from a single cell is an extremely fascinating process. Modern imaging techniques allow us to look at this process in remarkable detail. Watching such a video of the emergence of complexity, where from a diffuse mass of tissue an organism with a beating heart develops, can be a very satisfying pastime activity. Watching such a video a few more times provokes a seemingly infinite chain of hows and whys. In this thesis, we study a few such questions that arose from watching worm and quail embryos develop. We focus in particular on processes, where the embryo or some part of it moves or deforms. Such processes need to be driven by mechanical forces, which are generated and controlled by chemical processes within the organism. To understand the dynamics of such systems, we use a hydrodynamic description of living matter which we review in 1.2. With this we study two fundamental processes of embryogenesis, gastrulation and axis specification, which we introduce in 1.1. There, we observe that movements and deformations of a cell or tissue are controlled by chemical patterns, but also the three-dimensional shape of an embryo (see section 1.1.6). Patterns as well shapes are characterized by their geometry, i.e. angles and distances between features. In this thesis, we set out to understand how the given geometry of pattern and shape of a living system feeds back into the evolution of this geometry. In particular, we study the following questions

- What governs the growth and shrinkage of the primitive streak, a line of material that is crucial to the process of gastrulation in avian as well as human embryos? (chapter 2)
- How does the shape of a cell impact on pattern formation in its surface? (chapter 3)
- Can localized sources of mechanical activity in the surface of a cell or tissue act as sensors of the surface geometry? (chapter 4)
- Could differences in embryo geometry explain, why the embryos of some animals, such as quails and nematodes, make use of the chirality of the actomyosin cortex to break left-right symmetry, but many others do not? (chapter 5)

A more detailed overview of this thesis can be found in section 1.4.

1.1 Embryogenesis from a geometric viewpoint

The development of an organism involves the formation of patterns and the generation of shape. The biological process that gives rise to the shape of a cell or an organism is called *morphogenesis*. Morphogenetic processes are guided or controlled by chemical patterns, but also the topology and geometry of an embryo, as we review in section 1.1.6. Chemical patterns that define the body axes are established early in development, a process we call axis specification (see section 1.1.1, 1.1.2 and 1.1.4). The basic topology of the embryo is set up in a process called *gastrulation* (see section 1.1.5). The motor of cell movements and deformations during gastrulation and axis specification is the actomyosin cortex which we describe in section 1.1.3.

1.1.1 The three body axes

Humans are bilateral animals. This means that our body plan exhibits a clearly defined mid-line, with respect to which most morphological features are mirror-symmetric. In an adult human, this line is defined by morphological features such as the nose and the belly button on the ventral side of the body and the back-bone on the dorsal side. However, the line as such is defined already early in development by a structure called the primitive streak which we will discuss in more detail in section 1.1.5. The mid-line corresponds also to the anterior-posterior (AP) axis with the head defining the anterior pole of the body. In the plane orthogonal to the AP axis one defines two orthogonal axes: the dorso-ventral (DV) axis and the left-right (LR) axis. Since the body plan is superficially symmetric with respect to the mid-line, one often speaks of a medio-lateral (ml) instead of a left-right axis with organs close to the mid-line called medial. The form and positioning of the visceral organs such as the heart and the digestive systems, however, are clearly left-right asymmetric.

When one draws vectors from A to P, D to V and L to R as in Fig. 1.1A, the three vectors define a right-handed orthogonal basis. While in the drawing in Fig. 1.1A, this appears to define a global cartesian coordinate system, this is in general not true. The mid-line as well as any other coordinate line of a body axis is usually a curved line as can be seen from the gentleman in the right panel of Fig. 1.1B. Thus a body axis may also be understood in terms of a vector field, which defines at each point in the body a vector defining AP, DV or ml polarity. Microscopically this is often realised in terms of chemical gradients. Consider for example the zygote of the nematode *Caenorhabditis elegans* as depicted schematically in Fig. 1.2B. Here the AP axis is established (lower panel), as a domain with a high concentration of so-called posterior PAR proteins forms on the future posterior side of the embryo. Hence, the concentration of posterior PAR proteins within the surface of the cell defines a vector that is the AP axis. On a tissue scale, each cell may define such a vector in terms of an asymmetric distribution of proteins, a phenomenon called cell polarity, but also large-scale gradients of certain proteins are possible, which effectively define a global coordinate system [1, 2, 3].

Such a coordinate system may also be defined and maintained topologically. In the adult human, it does not require a chemical gradient defining the medio-lateral axis to find that the hand is located more laterally than the arm. Instead it is a consequence of topology: The hand is connected to the trunk that includes the mid-line only through the arm. The medio-lateral axis is defined by this topology and by the hand, the arm and the trunk being distinct from each other.

Also in the context of left-right asymmetry, topology is crucial. Before left-right asymmetric morphologies such as the position of the heart emerge, LR asymmetry of a vertebrate embryo is defined by chemically distinct domains that give the two sides of the body a "left" or "right" identity (depicted as a red and blue half of the somite-stage human embryo in Fig. 1.1B). Typically this is realized by the expression of certain genes (in particular *Nodal* encoding a small signalling molecule) on the left side of the embryo [4]. The mid-line separates the left and right halves of the body and thereby helps to maintain left-right asymmetry [5, 6, 7]. As such, left-right asymmetry is topologically protected and not sensitive to transient asymmetries of the embryo geometry. For the process of left-right symmetry breaking, however, the geometry of the embryo is crucial as we will discuss in this thesis in section 1.1.4.

1.1.2 Embryonic axis specification in the nematode embryo

All three body axes are defined early in development, i.e. before the development of any organs or limbs [3]. We distinguish here the establishment of an axis that may be understood as a rod or two-headed arrow from the establishment of a polarity along a given body axis (Fig. 1.2). The establishment of e.g. AP polarity may also be called AP symmetry breaking. We use the term (body) axis specification for the combined process of axis and polarity establishment.

Axis specifcation typically involves the formation of a chemical gradient that guides later steps of morphogenesis [2, 11]. Here, we briefly discuss AP and DV axis specification in *C. elegans* as an instructive example. In section 1.1.4, we will discuss left-right symmetry breaking. The AP axis of the *C. elegans* embryo is already defined in the zygote, i.e. the cell that emerges from the fertilization of the egg-cell by a sperm (see Fig. 1.2B). The key player of axis specification in *C. elegans* is the cell cortex, also called actomyosin cortex [12, 13]. It is a thin mechanically active layer of proteins just underneath the cell membrane, which we will discuss in more detail in 1.1.3. AP axis is defined by a gradient of PAR polarity proteins, of which there are of two types: anterior PAR proteins, marking the anterior side, and posterior PAR marking the posterior. Until about 30 min after fertilization, no gradient is found. Anterior PAR proteins are distributed homogeneously in the cell cortex. Posterior PAR proteins are found almost exclusively in the cytoplasm, the fluid that fills the cell. AP symmetry breaking is triggered by the male pronucleus brought by the sperm. Chemical interactions between the pronucleus and the cell cortex, mediated in particular by microtubules, yield the recruitment of posterior PAR proteins to the cell cortex [14]. Chemical interactions between these proteins and the cell cortex, in particular myosin motor molecules, yields a reduced surface tension of the

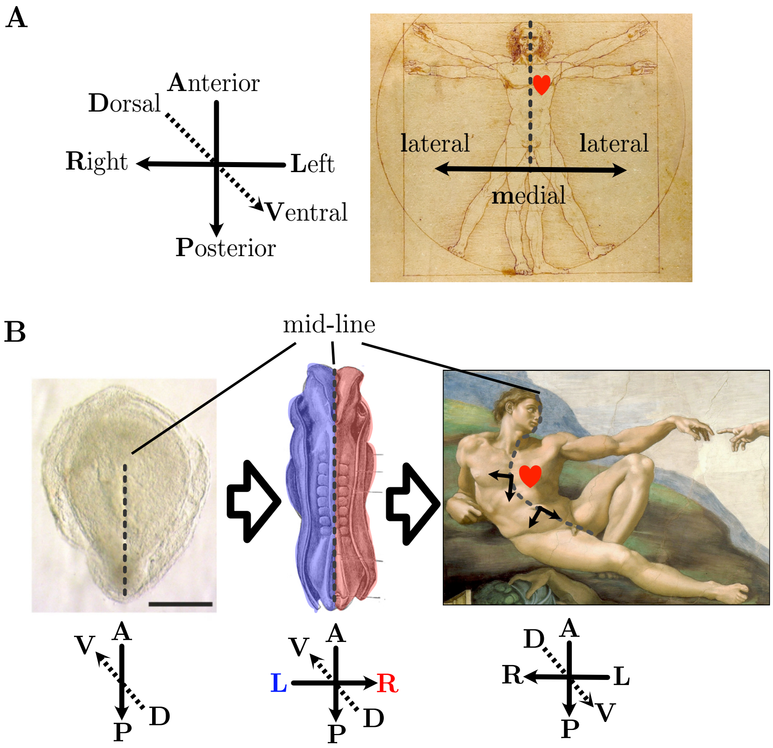

Figure 1.1: **A**: The three main body axes, anterior-posterior (AP), dorso-ventral (DV) and left-right (LR). They may be understood as a right-handed orthogonal set of vectors (left panel). As evident from the *Vitruvian Man* by L. da Vinci, most of the human body exhibits a mirror symmetry with respect to the mid-line (dashed line). With respect to this mid-line a medio-lateral axis parallel to the left-right axis is defined. However, the visceral organs such as the heart depicted in red exhibit a clear left-right asymmetry. **B:** The body axis during human development. The mid-line is established by the primitive streak during the process of gastrulation (left panel, image of human embryo taken from [8], see section 1.1.5 for more details). Subsequently, the left-right axis is specified by the production of distinct proteins on the left and right side of the mid-line as illustrated by the blue and red-shaded areas (middle panel, drawing of human embryo taken from [9]). Right panel: Adult human as painted by Michelangelo, where the body axes are defined by morphological features such as the position of the heart. We observe that the mid-line (dashed line) is curved such that the body axis can only locally be understood as a set of orthogonal vectors.

posterior cell cortex. As a result, large-scale flows in the cell cortex emerge that give rise to an expansion of the domain of posterior PAR proteins [12, 15, 13]. Due to chemical interactions between anterior and posterior PAR proteins, the domain of posterior PAR proteins is devoid of anterior PAR proteins [16, 17]. As a result two chemically distinct domains emerge in the cell cortex that define the AP axis of the embryo. This axis is maintained after the first cell division such that the posterior daughter cell, the P_1 cell, also contains a posterior PAR domain[18]

The DV axis needs to be set up orthogonal to the AP axis. In the *C. elegans* 2-cell embryo, the plane separating the AB and the P_1 cell is orthogonal to the AP axis. Importantly, the AB cell divides in a plane that is parallel to this plane of cell-cell contacts [19, 20]. This division axis in turn establishes the DV axis [21]. Similarly to AP symmetry breaking, DV symmetry breaking relies on the cell cortex. As the AB cell divides, motor proteins in the cell cortex drive counter-rotating flows in the surface of the AB cell. These surface flows result in rotation of the

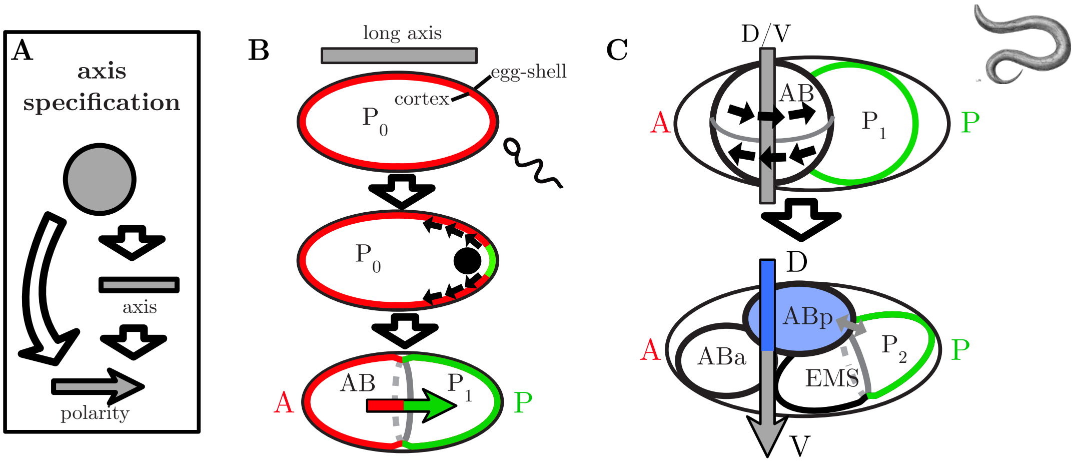

Figure 1.2: **A**: Schematic of the process of body axis specification starting from an isotropic cell (gray circle). The establishment of an axis (gray rectangle) may precede the establishment of a polarity (gray vector) as observed in the *C. elegans embryo*. **B**: AP axis specification in the *C. elegans* embryo. Upper panel: Distribution of anterior PAR proteins (red) in the cortex of zygote consisting of the P_0 cell is initially homogeneous. However, the geometry of the rigid egg shell already defines a long axis (gray rectangle). Middle panel: Interaction of the male pronucleus (carried by the sperm in the upper panel) with the cell cortex induces the formation of a domain of posterior PAR proteins (green). Cortical flows (black arrows) resulting from myosin depletion act to enlarge the posterior domain. Lower panel: Domains of anterior and posterior PAR proteins define AP axis (red-green arrow). This axis is maintained chemically as the cell divides into AB and P_1 cell. In particular, the posterior PAR domain (green) persists throughout the P cell lineage. **C**: DV axis specification in the *C. elegans* embryo. Upper panel: Division of the AB cell establishes the DV axis (gray rectangle) corresponding to the division axis in a plane orthogonal to the AP axis. As the cytokinetic ring ingresses, counter-rotating flows (black arrows) emerge in the cortex of the AB cell. Lower panel: Schematic of the 4-cell stage, after the AB and the P_1 cell have divided giving rise to ABa and ABp cell, and EMS and P_2 cell, respectively. Contact between the P_2 and the ABp cell triggers the expression of several genes (indicated by the blue shading) in the ABp and not in the ABa cell [10]. Thereby, DV polarity (blue-gray arrow) is established.

AB division axis [22]. This rotation results in an embryo geometry, where the dorsal and ventral halves are distinct from each other. Hence, it establishes DV polarity. As the P_1 cell divides along the AP axis, the asymetric embryo geometry results in an asymmetric pattern of cell-cell contacts. Only one daughter cell of the AB cell, the ABp cell is in contact with the posterior daughter cell (P_2) of the P_1 cell. Chemical interactions across this cell-cell contact trigger a signalling pathway in the ABp cell, such that it becomes chemically distinct from the ABa cell [10]. Thereby DV polarity is also chemically established.

In summary, the cell cortex powers AP as well as DV axis specification. During AP symmetry breaking, the cell cortex drives flows that help to establish a chemical gradient. During DV symmetry breaking, it drives cell rearrangements that are later read out chemically. As we will discuss in section 1.1.6 and study in chapter 3 of this thesis, the cell cortex also powers the alignment of these axis with the geometry of the rigid egg shell that confines the embryo. In particular it ensures that the AP axis coincides with the long axis of the egg shell.

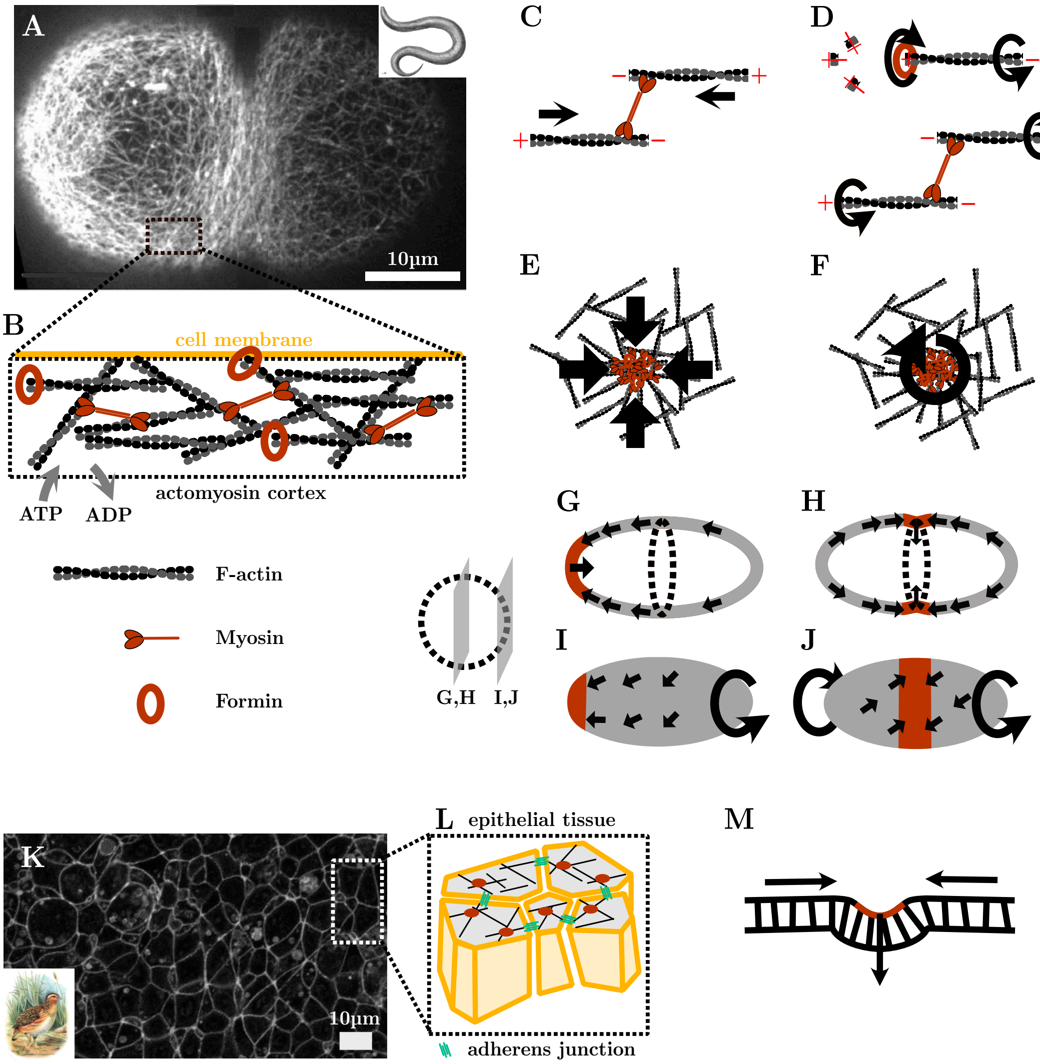

Figure 1.3: **A**: Flourescently labeled actin filaments in the cell cortex, also called actomyosin cortex, of the *C. elegans* embryo during the first cell division, image taken from [23]. **B**: Sketch of the actomyosin cortex, a gel-like material underneath the cell membrane, consisting of helical actin filaments (F-actin, gray), crosslinkers (not shown), myosin motor molecules and various other proteins such as formin that facilitate polymerization of F-actin. **C**: Myosin mini-filament exerts a pair of forces on actin filaments as its heads move towards the + end of the filaments. **D**: formin (upper panel) and myosin (lower panel) exert torques on actin filaments during polymerisation (upper panel) and sliding (lower panel) of helical actin filaments. **E**,**F**: Foci of RhoA signalling drive contractions (**E**) and chiral rotations (**F**) of the surrounding cortex due to the activity of myosin and formin (red). **G**-**J**: cortical flows (black) resulting from polar (**G**,**I**) and ring (**H**,**J**) patterns of RhoA activity. **G**,**H** show the mid-plane cross section of an ellipsoidal cell such as the *C. elegans* zygote, whereas **I**,**J** show the cortical surface as shown e.g. in **A**. **K**: Epithelial tissue in a quail embryo during gastrulation (see section 1.1.5) with the cell membrane flourescently labelled. Image was obtained by Adrian Lahola-Chomiak at the MPI-CBG Dresden. **L**: Schematic of epithelial tissue illustrating the function of adherens junctions (green) as mechanical links between the actomyosin cortices of neighboring cells. **M**: Schematic of apical constriction, where an epithelial tissue deforms (black arrows) in response to actomyosin activity (red) in the apical surface of a group of cells.

1.1.3 The actomyosin cortex: the motor of morphogenesis

The main ingredients of the cell cortex are actin and myosin [24, 25]. While actin is the building block of a meshwork that gives the cortex its rigidity, myosin is a motor molecule that makes the cortex flow and deform. Together they give the cell cortex its alternative name actomyosin cortex. Monomeric actin is a protein that polymerizes to form filaments called F-actin. These filaments are polar, i.e. they have two distinct ends (as indicated by the + and − signs in Fig. 1.3). Efficient nucleation of new filaments requires the interaction with certain proteins called actin nucleators including formins that bind to the + end of a nascent filament [26] (depicted as red circles in Fig. 1.3). Actin filaments are connected by cross-linking proteins to form a dense meshwork underneath the cell membrane. Cross-linkers and filaments undergo constant turnover on the second to minute time-scale [25]. This allows motor molecules, in particular myosin (specifically non-muscle myosin II), to set the gel-like material that is the cell cortex into motion [27, 28]. Several myosin molecules assemble into so-called myosin mini filaments. These myosin filaments binds to actin due to electrostatic interactions [29]. Upon hydrolysis of an ATP bound to myosin, myosin undergoes conformational changes. Thereby, myosin walks on actin from the − to the + end [28, 25]. When a myosin filament is bound to two oppositely oriented actin filaments, it displaces the actin filaments relative to each other. As these filaments are mechanically constrained by the surrounding network, myosin exert forces onto actin filaments (Fig. 1.3C). Thus, myosin translates the chemical energy provided by ATP hydrolysis into mechanical work. On the scale of the cortex, the mechanical action of myosin motors can be understood as a density of force dipoles exerted on the two-dimensional material that is the cortex [30]. The force dipole resulting from a single myosin mini-filament may drive a contraction or an expansion of the surrounding network depending on the arrangements of actin filaments that the myosin filament interacts with [31]. However, clustering of many myosin molecules is generally found to result in contractile flows towards the cluster. This can be understood as a consequence of the non-linear mechanical properties of actin filaments, which are easier to buckle than to stretch [32]. As a consequence, a network of actin filaments contracts even if the force dipoles acting on it are randomly oriented [32, 33]. Furthermore, the polarized movement of myosin on actin filaments can result in asters of actin filaments, where the + ends are pointing towards the middle of a myosin cluster [34]. Also in such a setting a cluster of myosin motors drives contractile flows towards it [31].

Importantly, actin filaments are chiral. This means that their structure, a right-handed double-helix, is different from its mirror-image [35, 36]. Due to this structure, a displacement of an actin filament usually implies a rotation of the filament [37]. In particular, formin molecules has been found to rotate while elongating an actin filament [38]. A rotation of the polar actin filament defines a handedness that corresponds to the handedness of the molecular structure. The rotation of a mechanically constrained filament requires a torque. Hence myosin, but also actin nucleators such as formin exert molecular torques on the actin network [39]. Strikingly, the activity of formin has been linked to rotational flows on the cell scale in various settings

[40, 41, 42, 43, 44]. In particular, Middelkoop et al. observed that a cluster of myosin and formin in the cortex of the *C. elegans* embryo drives a rotation of the cluster [44]. This rotation has a handedness, i.e. it is a clockwise rotation in all embryos of the same strain when viewed from the outside. Hence, molecular motors in the actomyosin cortex translate the chirality of the actin molecule into chiral flows on the cell scale.

As we discussed in the previous section, the actomyosin cortex is crucial to the processes of AP and DV axis specification of the *C. elegans* embryo. During these processes, cell-scale patterns of myosin activity result in cell-scale flows of cortical material. The concentration and activity of actin, formin and myosin is controlled in particular by a master-regulator, a protein called RhoA [45, 46, 47, 48]. The contracting and rotating clusters of myosin and formin, we mentioned in the previous paragraphs, correspond to so called foci of high RhoA siginalling activitiy [44]. During the processes of AP symmetry breaking in the *C. elegans* zygote (see section 1.1.2) myosin activity is polarized with high activity on the anterior side of the zygote (corresponding to the left side in the schematics in Fig. 1.3G,I). As consequence a contractile flow towards the anterior side emerges, which is crucial to the process of AP symmetry breaking [13]. During cell division such as the one that defines the DV axis (see previous section), RhoA and thus myosin activity is high at a band around the equator of the cell, called the cytokinetic ring (indicated in red in the schematics in Fig. 1.3H,J) [46]. As a consequence this ring contracts, both in terms of contractile flows towards the ring and in terms of a deformation of the cell surface such that the ring ingresses to form the cytokinetic furrow [23].

During symmetric cell divisions in the *C. elegans* embryo, also counter-rotating flows have been observed that have been linked to molecular torque generation by the actomyosin cortex [39, 22]. These flows of the cell surface are crucial to the process of left-right symmetry breaking as we will discuss in the next section. Notably, these chiral flows only emerge after the cytokinetic furrow has started to ingress [22], suggesting that these flows are highly sensitive to changes in cell shape. In addition, the net rotation that arises during asymmetric cell divisions, where the pattern of RhoA activity is polarized, has been found to be sensitive to deformations of the embryo [49]. In this thesis, we will study in chapter 5 what such a geometry-dependence of chiral flows may tell us about the nature of the torques that drive them.

At later stages of development, cells often assemble into sheets that consist of hundreds or thousands of cells with a thickness of only one or a few cells. These sheets are called epithelia. Epithelia are polarized with two sides called apical and basal that are chemically distinct [3]. The apical side faces the outside of the embryo whereas the basal side rests on a sheet of extracellular matrix that faces the inside of the embryo. Epithelial cells are connected to each other by protein complexes called junctions. Adherens junctions are junctions that are connected with the actomyosin cortex. They allow for the transmission of forces generated in the actomyosin cortex on the scale of the epithelial tissue [50]. Thereby, forces generated by the actomyosin cortex can drive movements and deformations on the scale of the tissue. One prototypical example is apical constriction: When the tension resulting from actomyosin activity is higher on the apical side than on the basal side of a cell, the apical side contracts [51, 52, 53]. When apical tension is high in a group of cells, this results in a deformation of the tissue where this group of cells ingresses [53]. When the neighboring cells are free to move within a plane but not out of the plane, this ingression results in a movement of cells towards the region of ingression [54, 55]. Both the movement and the ingression are crucial to the process of gastrulation we discuss in section 1.1.5 and which we study in this thesis in chapter 2.

1.1.4 Left-right symmetry breaking

The body of bilateral animals such as humans is superficially symmetric with respect to the mid-line. The form and position of the visceral organs such as the heart and the digestive system, however, are not left-right symmetric. Since the body is also asymmetric with respect to anterior-posterior and dorso-ventral axis, the left-right asymmetry of the body plan corresponds to a handedness or chirality of the body plan, i.e. it is different from its mirror image. Strikingly, the bodies of animals of the same species have the same handedness most of the time. In 99.99% of adult humans, the heart is positioned on the left [57]. The origin of this consistent chirality is most likely the chirality of the molecules, in particular the proteins these animals consist of [58]. In 100% of humans, actin is a right-handed double helix and DNA is a left-handed one. The process of translating this molecular chirality into a consistent left-right asymmetry on the scale of the embryo is called left-right symmetry breaking. In vertebrate embryos, it happens after the AP and DV axis as well as the mid-line have been established [59]. Like the other body axes, left right asymmetry is usually chemically defined before the development of the visceral organs [60, 61]. This chemical asymmetry, typically due to a gene that is expressed on the left but not the right side of the embryo, feeds into the left-right asymmetric morphogenesis of the visceral organs [4, 62]. As a consequence, humans with a heart on the right often exhibit also a handedness of the lungs and the digestive system that is reversed relative to the majority of humans [57]. While the genetic signalling pathways of left-right patterning are highly conserved in vertebrates and beyond, the mechanisms that translate molecular chirality into left-right patterning differ substantially, possibly even among mammals [4, 59]. The mechanism of left-right symmetry breaking in the human embryo is still unclear. In the following, we will briefly sketch how left-right symmetry is broken in three model organisms: the nematode *C. elegans*, the quail and the mouse. In this thesis, we investigate the chiral flows that underlie left-right symmetry breaking in nematodes and quails in chapter 5.

In the nematode *C. elegans* left-right symmetry is broken already at the 4 to 6 cell stage, i.e. during the divisions of the ABa and ABp cells [63, 64]. We have already encountered these cells in section 1.1.2 in the context of DV symmetry breaking. They are the daughter cells of the AB cell. As members of the so called AB cell lineage they divide symmetrically, i.e. into equally sized daughter cells. Such symmetric cell divisions are accompanied by a counter-rotating flow

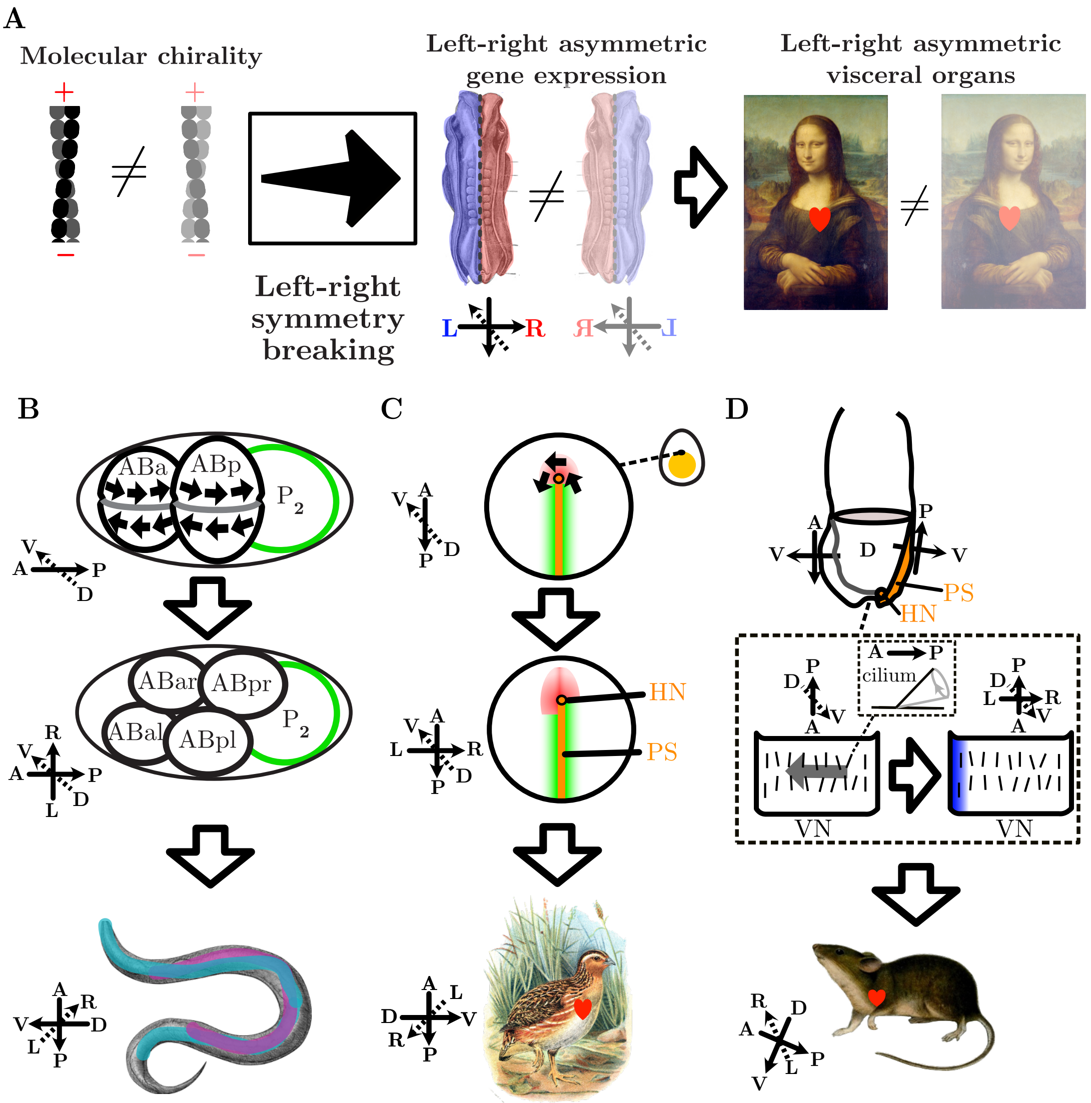
A
Molecular chirality
+
−
≠
+
−
Left-right symmetry breaking
Left-right asymmetric gene expression
≠
L
R
R
L
Left-right asymmetric visceral organs
≠
B
ABa
ABp
P2
V
A
P
D
ABar
ABpr
ABal
ABpl
P2
R
V
A
P
D
L
A
R
V
D
L
P
C
V
A
P
D
V
A
L
R
P
D
HN
PS
A
L
D
V
R
P
D
A
P
V
D
V
PS
HN
A
P
cilium
P
D
V
A
P
D
L
R
V
A
VN
VN
R
D
A
P
L
V

Caenorhabditis elegans
(nematode)

Coturnix japonica
(quail)

Mus musculus
(mouse)

Figure 1.4: **A**: Conceptual schematic of left-right symmetry breaking. Pairs of images represent the commonly found version (left) and its mirror image (right, grayish) of molecules and organisms. For details, see main text. Adult human (right panel) painted by L. da Vinci. **B**: Left-right symmetry of the *C. elegans* embryo is broken at the 4 cell (upper panel, same as Fig. 1.2C, but viewed from the dorsal side) to 6 cell stage (lower panel) due to counter-rotating flows in the cell cortex (black arrows). This controls the left-right asymmetry of the visceral organs (lower panel with the gut in cyan and the gonad in magenta). **C**: Left-right symmetry breaking in birds such as the quail. Black circle encompasses the epiblast an epithelial tissue (see also Fig. 1.5). Left-ward movement of cells (black arrows) at the Hensen's node (HN), the tip of the primitive streak (PS) results in a left-right asymmetric pattern of gene expression (green=Fgf8, red=Shh). This triggers a signalling cascade and ultimately the rightward positioning of the heart in the adult bird. **D**: Left-right symmetry in mouse embryos is broken by cilia-driven leftward movement of extracellular fluid in the ventral node (VN, middle panel), triggering calcium signal (blue) on the left side of the VN. Upper panel: cross-section of the cup shaped mouse embryo during gastrulation and left-right symmetry breaking, drawn after [56].

of the actomyosin cortex [22]. The chirality of the flow is understood as a consequence of the chirality of the actin helix [39, 22, 44]. The flow requires the activity of myosin as well as formin [39, 22]. Friction of the rotating cell surfaces with the underlying EMS and P2 cell yields a torque that drives clockwise rotation of the division axes of the ABa/p cells [22]. As a consequence, the daughter cells on the right side (AB(a/p)r) of the embryo are located more to the posterior side than the daughter cells on the left side (AB(a/p)l). Similarly to DV symmetry breaking, these cell rearrangements result in a left-right asymmetric pattern of cell-cell contacts at the 12 cell stage, which is read out chemically by signalling pathways [65].

In vertebrate embryos the left-right symmetry is broken at much later stages of development, when the embryo consists hundreds to thousands of cells. At this stage, the embryo undergoes a process called gastrulation which we will discuss in the next section. During this process also the mid-line of the embryo is defined. In amniotes such as birds and mammals, the mid-line is defined by a structure called the primitive streak (PS) [3, 66]. It is a complex structure that is embedded in an epithelium that is called epiblast. The most anterior part of the streak is called the Hensen's node (HN). In birds such as the quail, left-right symmetry is broken by a rotational movement of cells in the HN and the epiblast around it [67]. Cells anterior to the PS move leftward. Before the rotation of the HN, two distinct genes are expressed at the HN and at PS immediately posterior to the HN (depicted as red and green shaded areas in Fig. 1.4C). The rotation of the HN yields a shift of these domains of gene expression. A gene called sonic hedgehog (Shh) is expressed symmetrically at the HN before the rotation, whereas after the rotation it is mostly expressed by cells on the left side of the HN [67, 68, 60]. Thereby, a signalling cascade is triggered [60]. In particular, it initiates the production of a signalling protein called Nodal on the left side of the embryo. Importantly, this left-right patterning is perturbed, when the leftward movement of cells is perturbed by introducing an obstacle. Also a drug that inhibits myosin diminishes the leftward movement [67]. This implies that avian left-right symmetry breaking relies on chiral cell rearrangements driven by mechanical forces generated within the actomyosin cortex.

The Nodal signalling cascade on the left side is a conserved component of left-right patterning in all vertebrates [4, 69, 70]. In embryos from fish, frog but also in rabbits and mice, Nodal is also found on the left side of the embryo [4]. However, the trigger of the Nodal cascade is not a movement of cells in these embryos but an extracellular fluid flow [6, 56, 71]. This fluid flow is driven by cilia, i.e. threadlike cell appendages with a set of microtubules at their core [24, 72]. Microtubules like F-actin are cytoskeletal filaments. Like F-actin they have a chiral helix-like structure [24]. Similarly to myosin, a motor molecule called dynein can displace microtubules relative to each other. Thereby, dynein can drive rotations of the cilium [72, 73]. In the gastrulating mouse embryo, such motile cilia are found in a pit-like structure called the ventral node that is located ventral and slightly anterior to the Hensen's node. The cilia are tilted posteriorly and rotate clockwise such that they move leftward, when the tip of the cilium is farthest away from the tissue surface. Thereby, the cilia drive a leftward flow of extracellular fluid [56]. The lateral flow on the left side of the embryo is detected by immotile cilia triggering a calcium signal and ultimately the Nodal cascade [74, 75].

Also in humans, cilia appear to be necessary for left-right symmetry breaking, since genetic defects in cilia-related genes correlate with laterality defects [57, 76]. Whether they do indeed drive a leftward flow like in mouse and rabbit embryos, however, is unclear, since human embryos from the corresponding stage have not been studied. Notably, embryos from cattle and pig appear to be more similar to chick than mouse embryos both in terms of tissue architecture and in terms of the dynamics of nodal expression [67, 77]. Furthermore, a recent study from chameleon shows that also there left-right symmetry breaking is independent of cilia and is accompanied by left-right asymmetric tissue deformations [69]. Thus, the ancestral mode of left-right symmetry breaking in mammalian embryos might be cilia-independent.

In summary, molecular chirality is translated into embryo-scale chirality by motor molecules in vertebrates as well as nematode embryos. These motor molecules drive a chiral movement of cells or extracellular fluid by interacting with cytoskeletal filaments that have a helical structure. This movement triggers a signalling cascade that gives the left or right side a chemical identity that is distinct from the other side. Hence, left-right symmetry is always broken mechanically with the movement defining a rotation or a leftward vector and hence the geometric handedness of the embryo. Afterwards, however, left-right asymmetry is maintained and transmitted chemically with left and right domains topologically isolated from each other by a mid-line barrier in vertebrate embryos or cell boundaries in the nematode embryo. In all cases a mid-line structure can be identified before left-right symmetry breaking. Importantly, this structure does not span the entire embryo before left-right symmetry is broken. In the nematode the cytokinetic furrows of the ABa/p cells correspond to the mid-line of the embryo [64]. In mouse and quails, the primitive streak acts as a mid-line barrier across which cells cannot move and chemical signals may not be transmitted [7, 78]. At the node, this mechanical barrier is not yet established allowing for a leftward flow of cells at the avian HN and a leftward flow of extracellular fluid at the ventral node of the mouse. In both mouse and quail, left-right symmetry breaking is followed by the formation of a mid-line barrier anterior to the primitive streak. In quail, the time-point of left-right symmetry breaking coincides with the onset of notochord and neural groove formation [67, 79]. In mouse, much of the notochord has already formed, when left-right symmetry is broken, but a mid-line barrier at the ventral node is established only shortly after left-right symmetry breaking [7]. While the neural tube that is induced by the notochord contributes to the mid-line of the adult animal, the primitive streak shrinks away [3]. Thus in both mouse and quail, left-right symmetry breaking happens at the connection point of two lines that define the mid-lines of the embryo during early gastrulation and after gastrulation, respectively. This connection point encompasses only a small fraction of the embryo. Hence, left-right symmetry breaking depends on the leftward flow of only a small volume of material. It seems likely that this contributes to the robustness as well as the energy efficiency of left-right symmetry breaking. In the mouse embryo, the ventral node is a channel that confines the flow of the extracellular fluid. In the quail embryo, in contrast, it is unknown what restricts the leftward movement of cells to the HN. In chapter 5 of this thesis, we investigate the physical forces and torques that drive and restrict the rotation of the HN.

For completeness, we want to mention here that there have been experimental reports in the past that the distribution of ion pumps as well as the membrane potential are left-right asymmetric in chick and frog embryos much earlier in development [80]. However, there appear to be issues in terms of reproducibility with these reports [81]. More importantly, they do not falsify that the crucial trigger of the left-sided expression of nodal is the leftward movement of extracellular fluid or cells [81, 67, 82]. Instead, they may reflect a not necessarily functional chiral bias of the embryonic tissue.

1.1.5 Gastrulation

In all vertebrates, left-right symmetry breaking happens during the process of gastrulation. Before gastrulation, the embryo has the topology of a hollow sphere called blastula. The blastula consists of a single layer of tissue. Gastrulation is the morphogenetic process that transforms the blastula into a gastrula, i.e. it transforms the single-layered embryo into a multilayered embryo (see Fig. 1.5A,B). The tissue layers of an embryo at the gastrula stage are the so called germ layers [3]. Embryos of bilateral animals have three germ layers: ectoderm, mesoderm and endoderm. Cells from different germ layers are chemically distinct and contribute to different types of tissues in the adult animal. For example, only ectodermal cells, the outermost layer of the gastrula, will contribute to the epidermis of the adult animal. Gastrulation generally involves large-scale movements and deformations of tissue. In this thesis, we study the tissue movements during avian gastrulation in chapter 2.

In amniote animals, i.e. reptiles, birds and mammals, gastrulation involves a complex structure called the primitive streak (PS), which is embedded in an epithelium called the epiblast [85, 86]. Within the epiblast, cells move towards the streak, where they detach from the epithelium and fill the underlying cavity. Thereby, they form meso- and endoderm, whereas the remaining epiblast contributes to the ectoderm [3, 79, 66]. In birds, the epiblast starts out as a flat circular disk of cells. This disk lies on top of another disk of cells, the hypoblast that later contributes to extra-embryonic tissue. On the edges, the disks are glued together by extraembryonic tissue, the so called area opaca. There, embryonic and extraembryonic tissues form a continuous tissue, whereas underneath the epiblast a layer of extracellular matrix separates the epiblast from the underlying hypoblast (yellow line in Fig. 1.5D). Hence, the tissue consisting of epi- and hypoblast connected by the area opaca has the topology of a hollow sphere, even though its geometry is mostly flat [3, 79]. This flattened sphere is immersed in the yolk (Fig. 1.5C). The yolk is enveloped by a protein membrane called vitelline membrane. Cells at the outer edge of the area opaca adhere to the vitteline membrane, which is crucial to the expansion of the

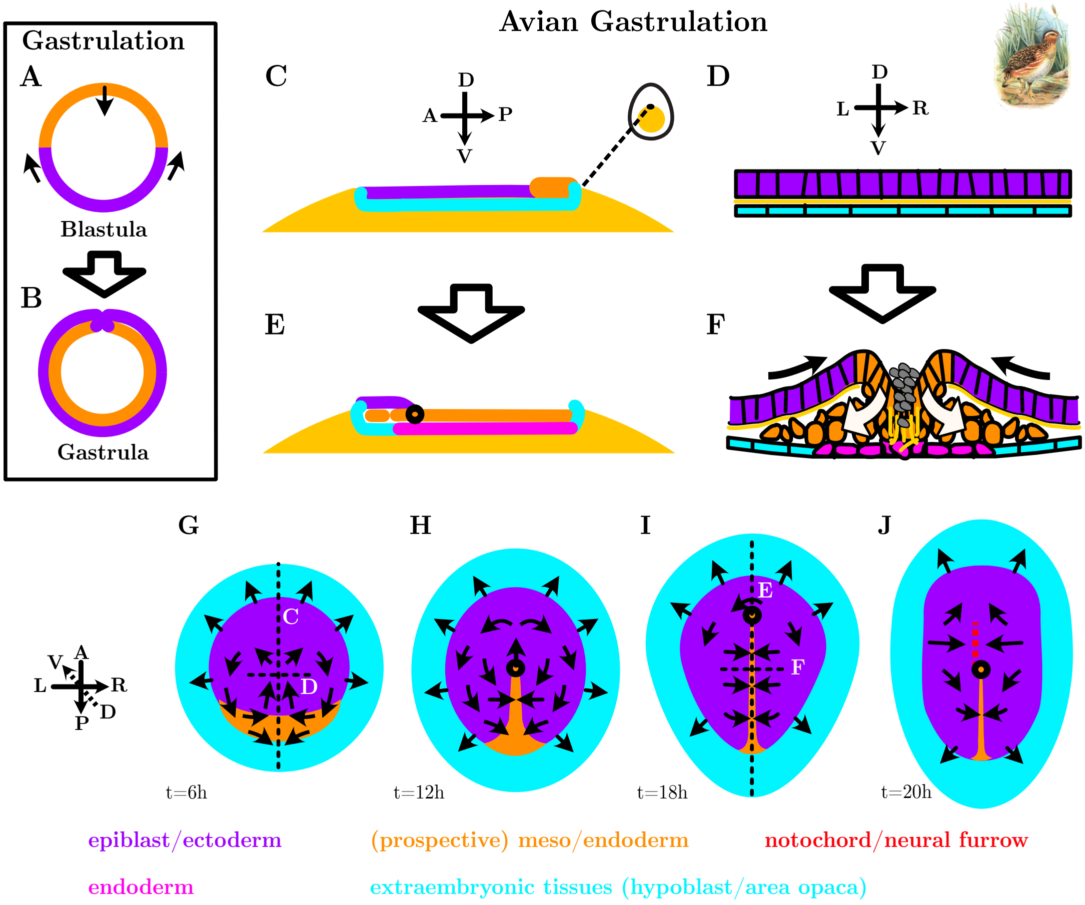
Gastrulation
A
Blastula
B
Gastrula
Avian Gastrulation
C
D
A
P
V
D
L
R
V
E
F
G
H
I
J
V
A
L
R
P
D
C
D
E
F
t=6h
t=12h
t=18h
t=20h
epiblast/ectoderm
(prospective) meso/endoderm
notochord/neural furrow
endoderm
extraembryonic tissues (hypoblast/area opaca)

Figure 1.5: **A**,**B**: Schematic of the process of gastrulation, a morphogenetic process involving large-scale tissue movements and deformations (black arrows). At the blastula stage (**A**), the embryo has the topology of an unilayered hollow sphere, whereas at the gastrula satge, the meso/endoderm layers (orange) have been folded inward. **C-J** sketches of embryo geometry and tissue movements during avian gastrulation. **C-F** cross sections of the embryo at the onset of streak formation (**C**,**D**, corresponding to the dorsal view in **G**) and at maximal streak extension (**E**,**F**, corresponding to dorsal view in **I**). **C**,**E**: Cross sections of the embryo along the primitive streak in the AP-DV plane with the definitive endoderm drawn in pink. **D**,**F**: Cross sections in the DV-LR plane (see lines in **G**,**I**) with cell boundaries drawn in black, extracellular matrix in yellow and debris from apoptotic cell deaths in gray. White arrows denote the migration of individual mesynchymal mesoderm cells (orange), whereas black arrows indicate the movement of the continuous epiblast tissue towards the primitive streak. **G-J** Dorsal view of the avian embryo during gastrulation at different times (t) after the beginning of incubation as found in embryos from chicken and quails[83, 84]. Large-scale fluid like motions of the epiblast tissue are illustrated by black arrows.

embryonic tissue [79, 87].

At the onset of gastrulation (about 6h after the egg was laid in chicken and quails), the epiblast is homogenous up to crescent-shaped region of thickened tissue at the future posterior end of the embryo. The crescent, called Koller's sickle, will contribute to meso- and endoderm (orange region in Fig. 1.5C,G) [84, 83]. Gastrulation is initialized by large-scale movements of cells akin to flows of a fluid (black arrows in Fig. 1.5G). These tissue flows are driven by myosin cables at the apical (=dorsal) side of the posterior epiblast [88, 89]. Myosin cables are actin bundles that are connected across several cells through adherens junction and which contract due to the activity of myosin motor molecules [90]. They drive so called convergent extension flows that move cells towards the midline in the posterior half of the embryo and yield an extension of the posterior epiblast along the midline. In the anterior half of the epiblast, cells close to the midline move away from the mid-line, whereas lateral cells move posteriorly. Taken together, we observe two vortices: a clockwise rotation of the epiblast in the right half of the embryo and an anti-clockwise rotation in the left half. These large scale flows have been called polonaise flows in the literature after a Polish dance [79]. Note that at the same time the epiblast is growing as cells are constantly dividing such that the epiblast-hypoblast boundary in the AP-LR plane is moving outward [87] (see black arrows at the boundary of the violet/orange epiblast in Fig. 1.5G-J)

At the posterior mid-line of the epiblast, cells start to undergo an epithelilial-mesenchymal transition (EMT), meaning they detach from the epithelium and move between epiblast and hypoblast as single cells or small groups of cells. This transition requires the breakdown of the extracellular matrix that seperates the epiblast and hypolast layers [79]. The breakdown of the epithelium also involves programmed apoptotic cell death. The debris from cell deaths as well as poorly understood structure of extracellular matrix forms a barrier at the mid-line of the embryo. Cells on the left and right side of the mid-line do not cross this barrier. Cells from the right half of meso- and endoderm can be traced back to epiblast cells from the right half of the embryo [78]. The streak of disordered tissue that encompasses the barrier as well as surrounding epithelium constantly undergoing turnover by EMT is called the primitive streak (Fig. 1.5F). While the surrounding epiblast is a flat epithelium, the primitive streak has characteristic 3D morphology: A ventral valley along the midline is surrounded laterally as well as anteriorly by a dorsal elevation [3, 68]. This shape may be understood as a result of apical constriction of the primitive streak (see schematic in Fig. 1.3M). The anterior elevation at the tip of the streak is called the Hensen's node (HN, black dot in Fig. 1.5E,H-J).

The primitive streak forms as a result of convergent extension movements and then elongates anteriorly until it reaches about 3/4 of the AP diameter of the epiblast. At this time-point left-right symmetry is broken by a rotation of the HN as we outlined in the previous section [67]. Subsequently the PS retracts and two structures called notochord and neural furrow form along a line anterior to the HN [79, 3]. Neural furrow formation involves convergent extension movements as well as a 3D deformation of the ectoderm where the tissue along the mid-line is deformed ventrally, similarly to the PS [3]. Note that the line of convergent extension tends to be displaced to the left with respect to the PS, which might be a result of the anti-clockwise rotation of the HN [91, 68, 67].

In this thesis, we develop a mechanical model of the primitive streak during the transition between streak elongation and retraction. With this, we obtain a mechanical understanding of the transition in chapter 2. In chapter 5, we investigate the rotation of the HN. There, we focus

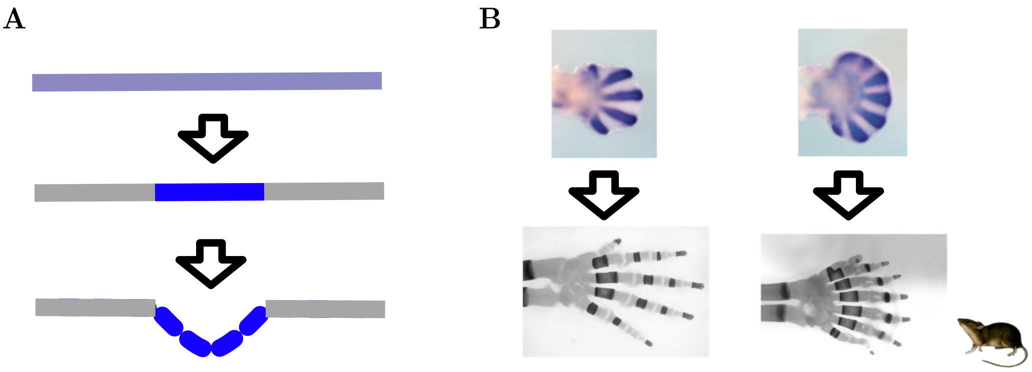

Figure 1.6: **A**: Schematic of morphogen-controlled morphogenesis of an epithelial tissue (gray). Distribution of morphogen (blue) becomes spatially inhomogeneous in an initially homogeneous tissue. This chemical pattern controls latter changes in tissue morphology including its shape. **B**: Digit formation in mouse embryos, images taken from [92]. Left panels show development in a wild-type mouse whereas the embryos on the right have been mutated such that a gene called *Gli3* has been removed. Upper panels: expression of the morphogen gene *Sox-9* in the embryonic limb bud. Lower panel: Ossified (dark gray) and cartilaginous (light gray) tissue in the digits of newborn mice.

in particular on how the rotation of the HN is facilitated by the geometry and topology of the avian embryo, i.e. that all tissue layers are in close contact and thus likely mechanically coupled at the HN and that the epiblast is curved only along the PS.

1.1.6 Interplay between chemical pattern and shape in morphogenesis

Recently, it has been argued, that the overall flatness of most amniotic embryos is the mechanical reason for the evolutionary innovation of the primitive streak [85, 55]. In frog embryos, for example, the tissue folds inwards along a ring. At the same time the ectoderm that is bounded by this ring expands. As the ectoderm has a curved sphere-like geometry, the expansion of the ectoderm corresponds to a contraction of the ring [85]. In [55], such a contracting ring has been induced in the flat epiblast of a chick embryo by chemical perturbations. The ring contracts within the plane, thereby preventing the expansion of the epiblast (=ectoderm). When only a segment of the ring contracts and expands perpendicularly, it undergoes convergent extension to form a streak, while the epiblast is free to expand [55, 54]. This way, the primitive streak may have evolved from the contracting ring as the embryos have become more flat due to a larger yolk volume [85]. Hence, mechanics appear to be the clue to the coevolution of a pattern (from a closed ring to a streak) and the geometry of the embryo. Strikingly, this causal relation between geometry and a resulting chemical pattern is opposite to how most morphogenetic processes are understood, as we will discuss in the following.

Many if not most morphogenetic processes are understood in terms of morphogens [2, 3]. For example, the protein Nodal which determines the identity of the left body half in much of vertebrate development is such a morphogen. Also the PAR molecules we encountered in section

1.1.2 are prototypical examples of morphogens. In general, a morphogen is a signalling molecule that impacts on the state of a cell in a concentration-dependent manner. While many molecules are involved in the process of morphogenesis, a morphogen is a molecule that appears to control the production and degradation of many other molecules and thereby a morphogenetic process [3]. Before or at the onset of a morphogenetic process, the spatial distribution of the morphogen becomes non-homogeneous and this chemical pattern defines the spatial profile of the morphogenetic process including tissue deformations (see schematic in Fig. 1.6A).

The formation of digits in the mouse embryo is a particular beautiful example of this phenomenon. Here a transcription factor called SOX-9 becomes non-homogeneously distributed in the so called limb bud as studied in [92, 93] (see upper panel in Fig. 1.6B). Subsequently, this chemical pattern controls which parts of the limb bud develop into the bones and cartilage of the fingers. The formation of this chemical pattern results from the interaction between several proteins. When one of these proteins is removed from the system by genetic modifications, the pattern changes. Notably, it has been found that the removal of certain proteins reduces the characteristic length scale of the SOX-9 pattern. As a result, more stripes fit into the limb bud, which develop into more than five digits (Fig. 1.6C). Thus, protein-protein interactions control the formation of a chemical pattern. This pattern in turn controls the shape change that is the formation of distinct digits from the limb bud. Importantly, the shape change does not appear to impact on the formation of the chemical pattern, as the two processes are well seperated in time. This is typical for our understanding of various morphogenetic processes [3, 94].

In the gut, in contrast, finger-like projections, called villi, form simultaneously with a morphogen pattern [100, 95]. The surface of the intestinal tissue starts out homogenous, both in terms of its shape and chemical patterns within this surface. As this epithelium grows it buckles, because the growth of the epithelium is restricted by an underlying muscle layer [100]. At the same time the epithelial cells produce a morphogen that diffuses into the underlying tissue (blue shaded area in Fig. 1.7A). Production of this morphogen is found to be initially homogeneous, even when the concentration of the morphogen in the bulk of the tissue becomes non-homogeneous. It is found that the morphogen concentrates beneath outward deformations of the surface of the tissue, which can be understood from a simple diffusion model [95]. Subsequently, the morphogen triggers a transition in the state of the cell at the tip such that the protrusion of the initially homgeneous epithelium develops into a proper villus. While this later stage of development is reminiscent of the process of digit formation in mouse, the formation of the initial pattern is not. During villi formation, chemical pattern of the morphogen results from change in tissue geometry and not the other way around. The coupling between surface geometry and chemical pattern results here from the diffusion of the morphogen in the bulk of the tissue. We may thus say that diffusion of the morphogen gives the gut tissue a sense of its geometry, specifically the geometry of its surface.

Also on smaller scales, biological surfaces have been found to have a sense of their geometry.

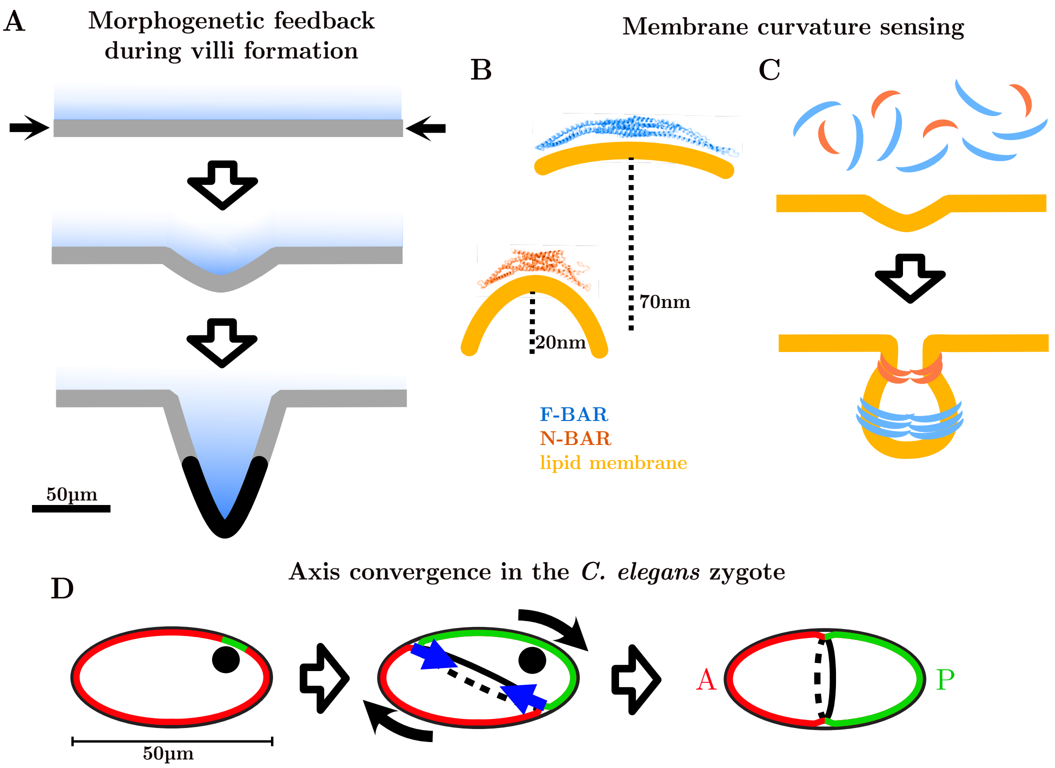
A
Morphogenetic feedback during villi formation
50μm
Membrane curvature sensing
B
C
70nm
20nm
F-BAR
N-BAR
lipid membrane
D
Axis convergence in the *C. elegans* zygote
50μm
A
P

Figure 1.7: **A**: Schematic of the formation of villi in the chick gut, where a tissue deformation results in the localization of a diffusing morphogen (middle panel) observed in [95]. Concentration of morphogen is illustrated by blue shading. Black arrows in upper panel denote forces from surrounding tissue that constraints the growth of the gray epithelium and drive its buckling (middle panel). Lower panel: Due to morphogen localization, cells at the tip of the villus (black area) become distinct from the neighboring epithelium. **B**: Different types of BAR-domains (blue, red) preferentially bind to lipid membranes (yellow) with distinct radii of curvature (denoted by black dahsed line). Crystal structures taken from [96]. **C**: Schematic of endocytic vesicle formation, where curvature-dependent binding of proteins containing BAR domains facilitates the formation of a vesicle from an initial pit in the cell membrane. Drawn schematics in [97, 98]. **D**: Alignment of the AP axis with the long axis of the egg shell in the *C. elegans* zygote as studied in [99]. Schematics correspond to Fig. 1.2B, but with an initially off-center positioning of the male pronucleus. Blue arrows denote the tension in the pseudo-cleavage furrow (black solid/dashed line) that drives a cortical and cytoplasmic rotation to align the AP axis with the geometric long axis.

In particular in the context of lipid membranes, curvature sensing has been extensively studied [101]. Such curvature sensing is typically understood in terms of specific curvature-sensing proteins, in particular proteins with a so-called BAR domain [102, 101, 96]. These proteins have a peculiar structure that makes them bind preferentially to lipid membranes with a certain radius of curvature. This radius is specific to a protein and ranges roughly between 10nm and 100nm [96]. Such proteins play a crucial role in certain types of endocytosis [97, 103]. When a pit in the membrane of a cell forms, certain curvature sensing proteins localize to this pit due to its inward curvature. Interaction between the lipid membrane and the curvature-sensing proteins makes the membrane curve further inward [102, 97]. Hence, curvature-sensing proteins act to enhance and stabilize an initially transient deformation of the membrane, similarly to the morphogen that controls villi formation. Subsequently, other proteins act to close the neck forming an endocytic vesicle [96]. Thereby, the deformation of the surface is translated into a topological transition.

Both during villi formation and endocytosis, the coupling between surface geometry and chemical pattern relies on a chemical flux between the surface and the bulk material underneath the surface. During villi formation, a morphogen is secreted into the bulk of a tissue. As the morphogen diffuses in the bulk of the tissue, patterns arise that depend on the geometry of the surface where it is secreted. Membrane curvature sensing, in contrast, relies on curvature-dependent association rates of certain cytoplasmic proteins to the membrane. Recently, however, it has been found that such a sense of geometry may also result from movements within a biological surface [99]. This surface is the cell cortex of the *C. elegans* zygote we have already encountered in section 1.1.2. As we have discussed there, a chemical pattern forms within the cell cortex, which defines the AP axis of the embryo. Strikingly, this axis is always aligned with the long axis of the rigid egg shell [104, 105]. Importantly, the chemical pattern impacts on the density of myosin motor molecules within the cortex, which results in large-scale flows of cortical material. Bhatnagar et al., have shown that this cortical flow not only contributes to the formation of the pattern but also to the alignment of the axis of the pattern with the egg-shell geometry [99]. They find that the alignment relies primarily on the pseudo-cleavage furrow, a contractile ring-like structure akin to the cytokinetic ring. This ring forms perpendicular to the AP axis. When the AP axis is not aligned with the long axis of the egg shell, the ring drives a rotational flow in the cortex that rotates the AP axis towards the long axis of the egg shell. This flow can be understood from an effective line tension that yields a flow that minimizes the circumference of the pseudo-cleavage furrow.

In this thesis, we set out to get a more fundamental understanding of how flows driven by motor molecules give a biological surface such as the cell cortex or an epithelial tissue a sense of its geometry. To this end, we define geometry sensing of a biological surface as the localization of certain chemical species to certain points in the surface that are defined purely be the geometry of the surface. In chapter 3, we focus on how chemical patterns in the cell cortex align with the long axis of the cell. In chapter 4, we generalize this phenomenon to general surface geometries. There, we study small patches in a biological surface that exert forces on the surrounding surface due to the activity of motor molecules. As we lay out in that chapter, such patches move to certain points in a surface which are defined by the geometry of the surface.

1.1.7 Hertwig's rule

Strikingly, also biology knows a rule that relates the geometry of a system to the localization and orientation of active processes that happen within this geometry: Cells divide along their longest axis. This rule is termed Hertwig's rule after embryologist Oscar Hertwig who discovered this phenomenon in the late 19th century [106]. It applies to various eukaryotic cells and is crucial to many developmental processes and tissue epistasis [107, 108, 109, 110, 111]. The cell division is defined by the spindle, a complex protein structure that acts to segregate the chromosome copies and orchestrates the formation of the cytokinetic ring by interacting with the cell cortex. The cytokinetic ring then ingresses to seperate the cell into two daughter cells

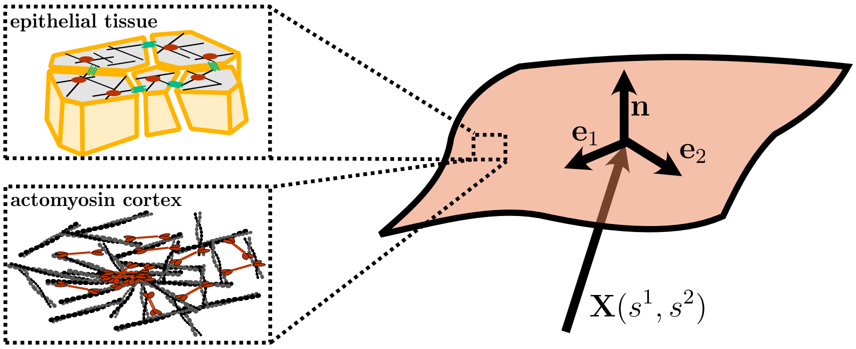

Figure 1.8: Active surfaces: Thin sheets of living matter (e.g. epithelial tissues or the actomyosin cortex, see section 1.1.3) are modelled as two-dimensional materials. The three-dimensional shape of such a surface is given by $\mathbf{X}(s^1, s^2)$ denoting a position in three-dimensional space as function of the coordinates s^1, s^2. This defines the covariant tangent vectors $\mathbf{e}_i$ (Eq. 1.1) and the normal vector $\mathbf{n}$ (Eq. 1.2).

[24, 112]. The spindle apparatus consists in particular of microtubule filaments. In the original article, Hertwig suggested that the cytoplasmic mass pulling at the microtubules is responsible for centering the spindle and aligning it with the geometric long axis [106]. Consider an object that pulls at the cytoplasm and is located to the right of the cell center. As more mass is pulling to the left of the embryo, it moves towards the center. Recently, this hypothesis has been formalized in terms of length-dependent microtubule pulling forces and experimentally validated [107, 113, 114, 115]. Interestingly, Oscar Hertwig also noted that his rule implies that the circumference of the cytokinetic ring is minimized. He suggested that this minimizes the work that is required to constrict the ring. Such a minimization principle is not unlike the effective line tension with which Bhatnagar et al. have understood the alignment of the AP axis of the *C. elegans* zygote with the long axis of the egg shell [99]. Notably, the AP axis is also the axis of the first cell division of the *C. elegans* embryo. Hence the rotation driven by the pseudo-cleavage furrow ensures Hertwig's rule in the *C. elegans* P_0 cell. While the pseudocleavage furrow is a structure that is specific to this cell, it is akin to the cytokinetic ring that forms during the division of any animal cell. In section 3.3.3 of this thesis, we study whether this contractile ring contributes to the robustness of Hertwig's rule. There, we link Hertwig's rule to a mechanical principle: torque balance.

1.2 Hydrodynamic theory of active fluid films

In the following, we introduce a physical description of living matter. In order to gain conceptual understanding of morphogenetic processes, we adopt a hydrodynamic description, where densities and orientations of molecules or cells are coarse-grained in terms of continuous fields. We focus on thin sheets of living matter such as epithelial tissues and the cell cortex. These nearly two-dimensional surfaces are usually curved. In this thesis, we study how this curvature impacts the dynamics of these living systems. This requires some notions from differential geometry which we introduce in 1.2.1. We write down continuity equations within the surface in section

1.2.2, corresponding to conservation laws of matter and momentum, as derived in [116]. In 1.2.3, we briefly review the framework of non-equilibrium thermodynamics which allows us to obtain constitutive equations in a systematic manner. In 1.2.5, we give constitutive equations for an active fluid, which capture the dynamics of tissues and cell cortex on time scales longer than the life time of the constituent cells or molecules. Such active fluids exhibit self-organized pattern formation. In section 1.2.6, we review examples of this phenomenon.

1.2.1 Differential geometry of surfaces

Let us a consider a surface $\mathcal{S}$ embedded in three-dimensional space. A parametrisation of this surface can be written as a function $\mathbf{X}(s^1, s^2)$ that assigns a position $\mathbf{X} \in \mathbb{R}^3$ to a pair of coordinates $(s^1, s^2) \in \mathbb{R}^2$ (see Fig. 1.8). By evaluating the derivative of $\mathbf{X}$ with respect to the coordinates at some point $p \in \mathcal{S}$, we obtain a pair of tangential vectors:

$$\mathbf{e}_i := \partial_i \mathbf{X}, \tag{1.1}$$

where here and in the following $i \in \{1, 2\}$ and $\partial_i := \partial_{s^i}$. These two vectors form the so-called covariant basis which are a basis of vectors that are tangential to the surface $\mathcal{S}$ at p. We also define a normalized vector $\mathbf{n}$ that is orthogonal to $\mathcal{S}$:

$$\mathbf{n} := \frac{\mathbf{e}_1 \times \mathbf{e}_2}{|\mathbf{e}_1 \times \mathbf{e}_2|} \tag{1.2}$$

$\mathbf{e}_i$ are in general neither orthogonal with respect to each other nor normalized. The scalar products of $\mathbf{e}_i$ define the metric tensor

$$g_{ij} = \mathbf{e}_i \cdot \mathbf{e}_j. \tag{1.3}$$

We write the inverse of this matrix as

$$g^{ij} = (g_{ij})^{-1}. \tag{1.4}$$

With this, we define the contravariant basis

$$\mathbf{e}^i := \sum_{j \in 1,2} g^{ij} \mathbf{e}_j. \tag{1.5}$$

implying that $\mathbf{e}^i \cdot \mathbf{e}_j = \delta^i_j$. In the following, we will use Einstein sum convention, i.e. we omit the sum sign and understand that we some over pairs of up/down indices. With the thus defined basis vectors, we can write any vector field on the surface as

$$\mathbf{f} = f^i \mathbf{e}_i + f_{\mathrm{n}} \mathbf{n}, \tag{1.6}$$

where $f^i = \mathbf{e}^i \cdot \mathbf{f}$ and $f_\mathrm{n} = \mathbf{n} \cdot \mathbf{f}$. The scalar product of two vector fields **ab** can then be written as

$$\mathbf{a} \cdot \mathbf{b} = g_{ij} a^i b^j + a_\mathrm{n} b_\mathrm{n}. \tag{1.7}$$

The cross-product

$$\mathbf{a} \times \mathbf{b} = \epsilon_{ij} a^i b^j \mathbf{n} + a_\mathrm{n} b^i \epsilon_i{}^j \mathbf{e}_j - b_\mathrm{n} a^i \epsilon_i{}^j \mathbf{e}_j \tag{1.8}$$

requires the notion of the Levi-Cevita tensor ϵ_{ij} which we define as

$$\epsilon_{ij} = \mathbf{n} \cdot (\mathbf{e}_i \times \mathbf{e}_j). \tag{1.9}$$

When the surface is curved, the surface normal **n** rotates as one moves across the surface. This rotation corresponds to derivative of **n** with respect to the coordinates, which defines the curvature tensor $C_i{}^j$:

$$\partial_i \mathbf{n} = C_i{}^j \mathbf{e}_j. \tag{1.10}$$

The tensor field $C_i{}^j$ corresponds to the so-called second fundamental form (with the first fundamental form being the metric). It is distinct from the Riemann and Ricci curvature tensors which contain only the Gaussian curvature. Gaussian curvature can be defined in terms of the $C_i{}^j$ as the determinant

$$\kappa = \mathrm{det} C_i{}^j = \frac{1}{R_1 R_2}, \tag{1.11}$$

where $R_{1/2}$ are the two prinicipal radii of curvature, i.e. the inverse of the eigenvalues of $C_i{}^j$. Gaussian curvature is an intrinsic property of the surface, i.e. it can be calculated from the metric g_{ij} and its derivatives [117]. Intuitively, this means that the Gaussian curvature of a surface can be determined from length and angle measurements within this surface (see Fig. 1.5 for some illustrative examples). For a surface that has only one radius of curvature at each point in the surface, such as a cylinder, $\kappa = 0$. As such it can be deformed into a flat surface without stretching or contracting the surface. In this sense, we say it is extrinsically but not intrinsically curved. The extrinsic curvature quantified $C_i{}^j$ is non-vanishing, but the intrinsic curvature quantified by κ or equivalently the Ricci and Riemann curvature tensors vanishes. The relation between length scales and Gaussian curvature will become more explicit in section 1.3.2, where we consider a so-called isothermal parametrisation of the surface.

In order to write conservation laws within a surface, we need to define derivatives of (tangential) vector fields within the surface. Even if a surface is flat, the covariant vectors $\mathbf{e}_i$ are in general not constant. Their derivatives can be written as

$$\partial_i \mathbf{e}_j = \Gamma^k_{ij} \mathbf{e}_k - C_{ij} \mathbf{n}, \tag{1.12}$$

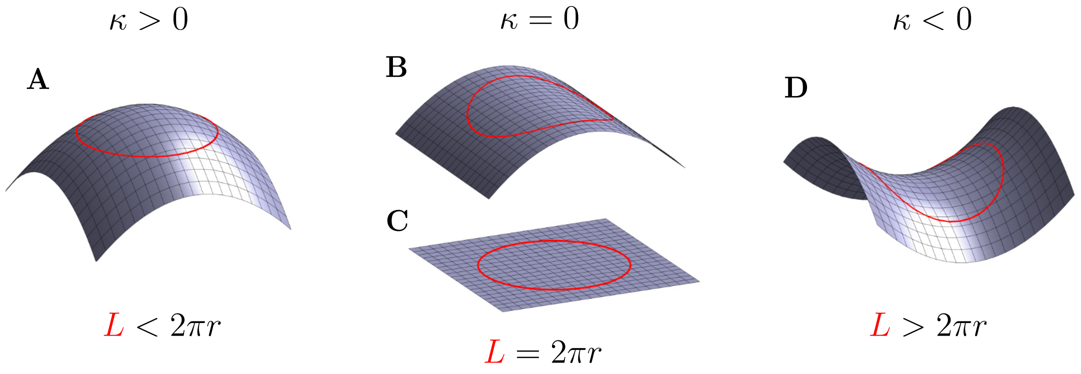

Figure 1.9: Circles with equal radii have distinct perimeters L in different surface geometries. For a spherical surface geometry, i.e. positive Gaussian curvature κ (**A**), the perimeter is smaller than for a flat surface (**C**). The perimeter is $2\pi r$ for a flat surface as well as all other surfaces with vanishing Gaussian curvature such as a cylinder (**B**). For a saddle geometry, i.e. $\kappa < 0$ (**D**), the perimeter is larger than for a flat surface. On all surfaces, we define the outline of a circle as a set of points that all have the same minimal distance with respect to a reference point. Hence, the Gaussian curvature of a surface can be determined from length measurements in the plane, demonstrating that Gaussian curvature is an intrinsic property of the surface [117].

where Γ^k_{ij} are the Cristoffel symbols which are defined in terms of the metric as

$$\Gamma^k_{ij} = \frac{1}{2} g^{km} \left(\partial_i g_{jm} + \partial_j g_{im} - \partial_m g_{ij} \right). \tag{1.13}$$

With this, we define the covariant derivative of a tangential vector field $\mathbf{v} = v^i \mathbf{e}_i$ as

$$\nabla_i v^j = \mathbf{e}^j \partial_i \mathbf{v} = \partial_i v^j + \Gamma^j_{ik} v^k, \tag{1.14}$$

i.e. the projection of the derivative of $\mathbf{v}$ into the tangential plane. If $\mathbf{v}$ is constant, $\partial_i v^j$ can be non-zero depending on the parametrisation of the surface, but the covariant derivative is not, as it defines a covariant quantity, i.e. $(\mathbf{e}^i \otimes \mathbf{e}_j) \nabla_i v^j$ is parametrisation-independent. For a general vector field $\mathbf{f}$ on the surface, we can write its derivative as

$$\partial_i \mathbf{f} = (\nabla_i f^j + C_i^{\ j} f_\mathrm{n}) \mathbf{e}_j + (\partial_i f_n - C_{ij} f^j) \mathbf{n}. \tag{1.15}$$

For understanding conservation laws within the surface, the following divergence theorem is crucial [118]:

$$\int_{\mathcal{S}'} \mathrm{d}S \nabla_i v^i = \int_{\mathcal{C}} \mathrm{d}l \nu_i v^i, \tag{1.16}$$

where $\mathcal{S}' \subset \mathcal{S}$ and $\mathcal{C} = \partial \mathcal{S}'$ is the bounding contour of $\mathcal{S}'$. Furthermore $\mathrm{d}S$ is the differential area element defined as

$$\mathrm{d}S = \sqrt{\det(g_{ij})} s^1 s^2. \tag{1.17}$$

$\mathrm{d}l$ is the length element $|\partial_s \mathbf{X}| \mathrm{d}s$ and $\boldsymbol{\nu}$ is the outward pointing normal to the contour $\mathcal{C}$ tangential to $\mathcal{S}$:

$$\boldsymbol{\nu} := \frac{\mathbf{e}_s \times \mathbf{n}}{|\mathbf{e}_s \times \mathbf{n}|} \tag{1.18}$$

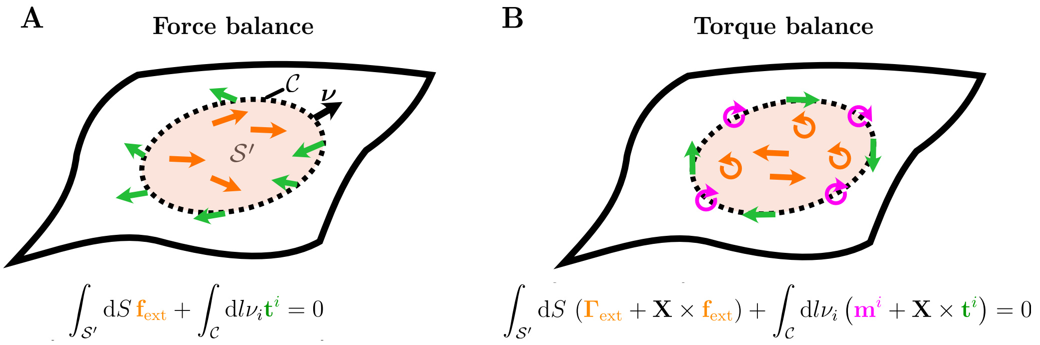
A
Force balance
$\mathcal{C}$
$\boldsymbol{\nu}$
$\mathcal{S}'$
$\int_{\mathcal{S}'} \mathrm{d}S\, \mathbf{f}_{\mathrm{ext}} + \int_{\mathcal{C}} \mathrm{d}l \nu_i \mathbf{t}^i = 0$
B
Torque balance
$\int_{\mathcal{S}'} \mathrm{d}S\, (\boldsymbol{\Gamma}_{\mathrm{ext}} + \mathbf{X} \times \mathbf{f}_{\mathrm{ext}}) + \int_{\mathcal{C}} \mathrm{d}l \nu_i \left(\mathbf{m}^i + \mathbf{X} \times \mathbf{t}^i\right) = 0$

Figure 1.10: Force and torque balance on a surface. Due to momentum and angular momentum conservation, the sum of all forces (**A**) and torques (**B**) acting on patch $\mathcal{S}'$ of a surface has to vanish. The differential form of these equations is given in Eq. 1.24,1.27. $\mathcal{C}$ denotes the contour enclosing $\mathcal{S}'$ and $\boldsymbol{\nu}$ is the outward-pointing normal vector of this contour that is tangent to the surface. Contraction of the stress (moment) tensor $\mathbf{t}^i$ ($\mathbf{m}^i$) with ν_i yields the forces (torques) the surrounding surface is exerting on the patch $\mathcal{S}'$. $\mathbf{f}_{\mathrm{ext}}$ (orange vectors) and $\boldsymbol{\Gamma}_{\mathrm{ext}}$ (orange curved vectors) denote forces and torques that the surrounding bulk material is exerting on the surface, respectively.

1.2.2 Conservation laws

Interpreting the vector field v^i as a tangential flux density, Eq. 1.16 says that the divergence $\nabla_i v^i$, corresponding to a source density, equals the tangential outward flux through the bounding contour. Thereby, Eq. 1.16 allows to understand physical conservation laws in the surface in terms of the covariant derivative. In the following, we will use it to give continuity equations corresponding to the conservation laws of mass, momentum and angular momentum. These conservation laws are generally valid. On length scales that are large compared to the constitutive particles, we can write them in terms of continous fields.

We write the area density of mass of the surface as $\rho(s^1, s^2)$. The mass M of a patch $\mathcal{S}' \subset \mathcal{S}$ is given by

$$M = \int_{\mathcal{S}'} \mathrm{d}S \rho. \tag{1.19}$$

As mass is a conserved quantity, changes in M over time have to be balanced by fluxes of mass to the surrounding:

$$\partial_t M = \int_{\mathcal{S}'} \mathrm{d}S J_{\mathrm{n}} - \int_{\mathcal{C}} \mathrm{d}l \nu_i j^i, \tag{1.20}$$

where J_{n} is the mass flux density from the surrounding bulk material to the surface and the tangential flux density j^i describes mass transport within the surface. Using the divergence theorem (Eq. 1.16), we can write the change in mass of a differential area element as

$$\partial_t(\rho \mathrm{d}S) = (J_{\mathrm{n}} - \nabla_i j^i)\mathrm{d}S, \tag{1.21}$$

corresponding to a continuity equation. In this thesis, we consider surfaces with a static shape, i.e. $\partial_t \mathbf{X} = 0$. With this, the above equation becomes

$$\partial_t \rho = J_\mathrm{n} - \nabla_i j^i. \tag{1.22}$$

Furthermore, we define the center of mass velocity $\mathbf{v} = v^i \mathbf{e}_i$ of the surface such that $j^i = \rho v^i$. Then, the momentum density of the surface is $\rho \mathbf{v}$. The flux of momentum within the surface is given by vector-valued flux density $-\mathbf{t}^i$, where

$$\mathbf{t}^i = t^{ij} \mathbf{e}_j + t_\mathrm{n} \mathbf{n} \tag{1.23}$$

is the stress tensor of the surface. Conservation of momentum yields the force balance equation:

$$\nabla_i \mathbf{t}^i = -\mathbf{f}_\mathrm{ext} - \rho \mathbf{a}, \tag{1.24}$$

where $\mathbf{f}_\mathrm{ext}$ is density of forces that the surrounding material exerts on the surface. $\rho \mathbf{a}$ is an inertial force density resulting from the acceleration $\mathbf{a}$ of the surface. In the following, we neglect such inertial effects, as we consider fluid films at low Reynolds number, where inertia forces are negligible compared the forces resulting from friction and viscosity.

Eq. 1.15 allows us to write the force balance equation in terms of its tangential and normal components:

$$\nabla_j t^{ji} + C^i{}_j t^j_\mathrm{n} = -f^i_\mathrm{ext} \tag{1.25}$$

$$\nabla_i t^i_\mathrm{n} - C_{ij} t^{ij} = -\, f_\mathrm{ext,n}. \tag{1.26}$$

We observe that in plane stresses yield a normal force density $C_{ij} t^{ij}$ when the surface is curved. In this thesis, we consider fluid films whose shape is fixed by external forces such that $f_\mathrm{ext,n}$ acts as a Lagrange multiplier with a value given by 1.26. For a fluid film, the in plane stress tensor t^{ij} is a function of the covariant derivatives of the tangential flow field v^i (See section 1.2.5). When the surface is flat, Eq. 1.25 then yields a differential equation for v^i that is the governing equation of the flow field. For ($C_{ij} \neq 0$), also normal stresses contribute to the tangential force balance equation.

The normal stress tensor is further constrained by angular momentum conservation. Neglecting inertial terms, conservation of angular momentum yields the torque balance equation [116]:

$$\nabla_i \mathbf{m}^i = -\mathbf{\Gamma}_\mathbf{ext} - \mathbf{e}_i \times \mathbf{t}^i, \tag{1.27}$$

where $\mathbf{m}^i = m^{ji} \mathbf{e}_j + m^i_\mathrm{n} \mathbf{n}$ is the moment tensor, which may be understood as a surface density of torque dipoles, which result from the passive bending rigidity of a surface but also active processes. In plane torque dipoles (m^{ji}) result in particular from a non-homeogeneous distribution of stresses across the thickness of the surface, such as during apical constriction (see Fig. 1.3M)

The tangential and normal components of the torque balance equation reads

$$\nabla_j m^{ji} + C^i{}_j m^j_\mathrm{n} = -\,\Gamma^i_\mathrm{ext} - \epsilon^j{}_i t^i_\mathrm{n} \tag{1.28}$$

$$\nabla_i m^i_\mathrm{n} - C_{ij} m^{ij} = -\,\Gamma_\mathrm{ext,n} - \epsilon_{ij} t^{ij}. \tag{1.29}$$

We observe that the normal stress t^i_n and the antisymmetric stress $\epsilon_{ij}t^{ij}$ yield a torque which cannot be set independently from the moment tensor and external torques.

1.2.3 Irreversible thermodynamics and virtual work

In this thesis, we consider living systems, which are generally out of thermodynamic equilibrium due to a continuous influx of chemical energy. However, we consider a regime, where small volume elements of the living material equilibrate quickly compared to the system-scale dynamics. This *local equilibrium* is the basis of the framework of non-equilibrium thermodynamics [119, 120], which has been found to quantitatively describe living as well as non-living systems out of equilibrium [121, 122].

Applying this framework to a thin sheet of living matter, we define the free energy of a small area element dS as the free energy density f. Summing the free energy density of all the area elements that make up the surface defines a free energy

$$\mathcal{F} = \int \mathrm{d}V f. \tag{1.30}$$

As the system is locally at equilibrium, f and hence $\mathcal{F}$ are well defined, even though the system is globally out of equilibrium. Similarly, one obtains an entropy density s. s and f are understood as functions of the local densities of mass, momentum and angular momentum, as well as the number densities c_I of chemical species $I \in \{1, ..., N\}$.

When a system is at thermodynamic equilibrium, its free energy is minimal. Hence any variation $\delta\mathcal{F}$ with respect to a variation δx of a hydrodynamic field x that obeys the conservation laws has to vanish at equilibrium. This yields equilibrium conditions for the derivatives of f [120, 123]. During a quasistatic process that leaves the system at equilibrium, the associated change in free energy is given by the work that the surrounding performs at the boundary of the system (we neglect here interactions at a distance, such as electromagnetic fields). Mathematically, this work is given by the change in free energy that results from a change in boundary conditions that define the system at equilibrium. When the change in in the hydrodynamic fields is equivalent to a deformation $\delta\mathbf{X}$ of the surface, the change in free energy can be understood as purely mechanical work:

$$\delta\mathcal{F} = \delta W = \int_{\mathcal{S}'} \left(\mathbf{f}_\mathrm{ext}\cdot\delta\mathbf{X} + \boldsymbol{\Gamma}_\mathrm{ext}\cdot\delta\boldsymbol{\theta}\right) + \int_{\mathcal{C}} \mathrm{d}l\nu_i \left(\mathbf{t}^i\cdot\delta\mathbf{X} + \mathbf{m}^i\cdot\delta\boldsymbol{\theta}\right), \tag{1.31}$$

where $\delta\boldsymbol{\theta} = \frac{1}{2}(\epsilon^{ij}\nabla_i\delta X_j)\mathbf{n} - \mathbf{n}\times\delta\mathbf{n}$ is the rotation of surface elements associated with the deformation. By calculating the differential of $\delta\mathcal{F}$ with respect to $\delta\mathbf{X}$, the above equation allows to infer expressions for stress and moment tensors at thermodynamic equilibrium.

δW can be calculated in and out of equilibrium and is called the *virtual work* [116]. Using the divergence theorem (Eq. 1.16, one obtains

$$\delta W = \int_{\mathcal{S}'} \mathrm{d}S \left[\tilde{t}^{ij} \frac{\delta g_{ij}}{2} + \tilde{m}^i{}_j \delta C_i{}^j + m_\mathrm{n}^i \frac{\epsilon^j{}_k \delta\Gamma^k_{ij}}{2} \right], \tag{1.32}$$

where the in-plane tension tensor $\tilde{t}^{ij}$ and the bending moment tensor $\tilde{m}^i{}_j$ are defined as

$$\tilde{t}^{ij} = \frac{1}{2} \left(t^{ij} + t^{ji} + \tilde{m}^{ki} C_k{}^j + \tilde{m}^{kj} C_k{}^i \right) \tag{1.33}$$

$$\tilde{m}^{ij} = -\, m^{ik} \epsilon_k{}^j . \tag{1.34}$$

We observe that $\tilde{t}^{ij}$ is conjugate to the variation of the metric and hence the intrinsic geometry of the surface. In particular the trace $\tilde{t}^i{}_i$ is conjugate to changes in area. We note that $\tilde{t}^{ij}$ depends also on the moment tensor, whenever the surface is curved, as an area expansion in a curved surface implies out-of plane deformations of area elements. The bending moment $\tilde{m}^i{}_j$ is conjugate to $\delta C_i{}^j$, i.e. changes in the extrinsic geometry of the surface. In other words, the work one needs to perform to deform a flat surface into a cylinder depends solely on the bending moment. For a surface with non-vanishing Gaussian curvature, however, changes in intrinsic and extrinsic geometry are strictly coupled. Furthermore, local changes in area (δg_{ij}) in general also imply in-plane rotations of area elements ($\sim \epsilon^j{}_k \delta\Gamma^k_{ij}$), which are conjugate to the normal moment m_n^i.

By calculating the change in free energy for a deformation of an isotropic fluid surface, one obtains the following equilibrium values for tension and moment tensors [116]:

$$\tilde{t}^{ij}_\mathrm{eq} = (f_0 - \sum_I c_I \mu_I) g^{ij}, \quad \tilde{m}^{ij}_\mathrm{eq} = K^{ij}, \quad m^i_\mathrm{n,eq} = 0, \tag{1.35}$$

where $f_0 = f - \rho|\mathrm{v}|^2/2$ is the Galilei-invariant component of the free energy density, whose differential is given by

$$\mathrm{d}f_0 = \sum_I \mu_I \mathrm{d}c_I + K^i{}_j \mathrm{d}C_i{}^j - s\mathrm{d}T. \tag{1.36}$$

Angular momentum conservation then yields the equilibrium normal and antisymmstric stress tensor. The thus obtained equilibrium stress obeys the following Gibbs-Duhem relation:

$$\nabla_j t_{\mathrm{eq}}{}^j{}_i + C_{ij} t^j_\mathrm{n,eq} = -\sum_I c_I \partial_i \mu_I, \tag{1.37}$$

i.e. it yields a force proportional to the gradient of the chemical potential.

For non-equilibrium dynamics of a surface, Eq. 1.31 is no longer valid, as energy is dissipated. Instead, the dynamics of s and f can be written as continuity equations [116]

$$\partial_t f + \nabla_i j^i_f = J^f_{\mathrm{n}} - T\pi_s \tag{1.38}$$

$$\partial_t f + \nabla_i j^i_s = J^s_{\mathrm{n}} + \pi_s, \tag{1.39}$$

where $j^i_{f/s}$ and $J^{f/s}_{\mathrm{n}}$ describe transport within the surface and exchange with the surrounding bulk material, respectively. The transport of free energy includes in particular the work that the surrounding surface and bulk material perform on an area element. T is the temperature, which we consider to be constant in space and time. π_s denotes the entropy production that results from the non-equilibrium dynamics of the system. When a system is at globally equilibrium, the entropy is maximal and $\pi_s = 0$. When the system is out of equilibrium, dissipation results in an entropy production $\pi_s > 0$.

The entropy production can generally be written in terms of so called generalized fluxes J_k and forces X_k:

$$\pi_s = \sum_k X_k J_k \tag{1.40}$$

By calculating the time-derivative of the free energy, π_s and, hence, X_k and J_k can be expressed in terms of derivatives of f and the flux densities of conserved quantities. For an isotropic fluid film, one obtains [116]

$$T\pi_s = \tilde{t}^{ij}_{\mathrm{d}} v_{ij} + \tilde{m}^{ij}_d \frac{DC_{ij}}{Dt} + m^i_{\mathrm{n}} \mathbf{n} \cdot \partial_i \boldsymbol{\omega} - \sum_I (\partial_i \mu_I) j^i_I + \sum_\alpha \Delta\mu_\alpha r_\alpha, \tag{1.41}$$

where we have the following generalized forces: the dissipative tension $\tilde{t}^{ij}_d = \tilde{t}^{ij} - \tilde{t}^{ij}_{\mathrm{eq}}$, the dissipative bending moment $\tilde{m}^{ij}_d = \tilde{m}^{ij} - \tilde{m}^{ij}_{\mathrm{eq}}$, the normal moment m^i_{n}, the gradient of chemical potential $-\partial_i \mu_I$ and the chemical potential difference $\Delta\mu_\alpha$ of chemical reaction α. Conjugate to the these forces, we have there are the following generalized fluxes: the in-plane shear v_{ij}, the bending rate DC_{ij}/Dt, the vorticity gradient $\mathbf{n} \cdot \partial_i \boldsymbol{\omega}$, the diffusion fluxes j_I and chemical reaction rates r_α [116, 120]. Here, vorticity, bending and shear rate of a non-deforming fluid film ($v_{\mathrm{n}} = 0$) are defined as

$$v_{ij} = \frac{1}{2}(\nabla_i v_j + \nabla_j v_i), \quad \boldsymbol{\omega} = \mathbf{e}^i \times (\partial_i \mathbf{v}), \quad \frac{DC_{ij}}{Dt} = v^k \nabla_k C_{ij} + \omega_n ({\epsilon_i}^k C_{kj} + {\epsilon_j}^k C_{ki}) \tag{1.42}$$

At equilibrium, the generalized fluxes and forces vanish. Close to equilibrium, the generalized forces may be written in terms of linear constitutive equations

$$X_k = \sum_l L_{kl} J_l \tag{1.43}$$

The coupling matrix L_{kl} contains phenomological coefficients, e.g. viscosity and diffusion constant. When, the time reversal signatures of X_k and J_l are equal (different), the coupling L_{kl} is reactive (dissipative). As the entropy production has time reversal signature -1, only dissipative couplings contribute to the entropy production. This antisymmetry with respect to time-reversal also yields the *Onsager reciprocal relations* [124, 125], which for reactive/dissipative couplings $L_{kl}^{\mathrm{r/d}}$ can be written as

$$L^{\mathrm{r}}_{kl} = -L^{\mathrm{r}}_{lk}, \quad L^{\mathrm{d}}_{kl} = L^{\mathrm{d}}_{lk}. \tag{1.44}$$

Furthermore, the second law of thermodynamics implies that the quadratic form $\sum_{kl} J_k L_{kl} X_l$ must be positive definite. This yields the following constraints on dissipative couplings:

$$L^{\mathrm{d}}_{kk} \geq 0, \quad L^{\mathrm{d}}_{kl} \leq \sqrt{L^{d}_{kk} L^{\mathrm{d}}_{ll}}, \tag{1.45}$$

where we do not sum over indices.

1.2.4 Curie principle

The constitutive equations Eq. 1.43 can be further constrained by the spatial symmetries of the material [119, 120]. If the physical state of a system is invariant under a transformation such as a rotation of the observable fields, this symmetry has to be reflected by the physical model given by the matrix L_{kl}. This is known as the Curie principle [126]. The physical state of an active surface is always invariant under a reparametrization of the surface. While the components of a tensor field t_{ij} depend on the choice of coordinates, a contraction of tensors $t_{ij}h^{ij}$ is invariant under a change of coordinates, when the t_{ij}, h_{ij} are components of a coordinate invariant tensor field. This includes physical observables like the stress tensor, but also the following fields that reflect the intrinsic and extrinsic geometry of the surface:

$$g_{ij}, \quad C_{ij}, \quad \epsilon_{ij} \tag{1.46}$$

The matrix L_{kl} has to be constructed from such tensors and contractions of them. Thereby, the model is also invariant under rotations. Furthermore, we consider the symmetry of the system with respect to inversion of the orientation $\mathbf{n}$ of the surface (O) and mirror transformations ($\mathcal{M}$). We define them in terms of the basis vectors as

$$\mathcal{O}: \ \{\mathbf{e}_1, \mathbf{e}_2, \mathbf{n}\} \to \{\mathbf{e}_2, \mathbf{e}_1, -\mathbf{n}\}, \quad \mathcal{M}: \{\mathbf{e}_1, \mathbf{e}_2, \mathbf{n}\} \to \{\mathbf{e}_2, \mathbf{e}_1, \mathbf{n}\} \tag{1.47}$$

$\mathcal{O}$ maps the right-handed basis to a right-handed basis with inverted orientation. It can also be understood as a rotation of the basis around a tangent vector. $\mathcal{M}$ transforms a right-handed basis to a left-handed basis while preserving the orientation of the surface. A physical system that is not invariant under this inversion of handedness is called chiral. When applying these transformations to tensors on the sphere, some change sign whereas others do not as given in Table 1.1.

	$\bar{t}_{ij}$	t_{n}^{i}	$\bar{m}_{ij}$	m_{n}^{i}	C_{ij}	g_{ij}	ϵ_{ij}
$\mathcal{O}$	1	-1	1	-1	-1	1	1
$\mathcal{M}$	1	1	1	-1	1	1	-1

Table 1.1: Signature of up-down ($\mathcal{O}$) and mirror ($\mathcal{M}$) symmetry on tensor fields of the surface.

The physical state of thin film of an isotropic material is invariant under $\mathcal{O}$ and $\mathcal{M}$. A physical model of such a surface has to reflect this up-down and mirror symmetry. Writing the matrix with components L_{kl} as $\mathcal{L}$, this condition can be written in abstract terms as

$$\mathcal{O}^{-1}\mathcal{L}\mathcal{O} = \mathcal{L}, \quad \mathcal{M}^{-1}\mathcal{L}\mathcal{M} = \mathcal{L}, \tag{1.48}$$

where a transformation on the right side of $\mathcal{L}$ act on the fluxes J_l whereas a transformation on the left side of $\mathcal{L}$ acts on the generalized forces X_k.

Living surfaces are often not isotropic. Epithelial tissues, for examples, are always up-down asymmetric due to apico-basal polarity. Furthermore, most molecules living systems are built from are chiral, i.e. their stucture is distinct from its mirror image. In general, this gives rise to a chirality of the material. In fact, various types of cells exhibit chiral behaviour in vitro, in particular due to activity of the actomyosin cortex that consists of helical actin filaments (see section 1.1.3). So far, however, a sense of handedness has only been demonstrated for a few cell types [127]. Moreover, there are strikingly many morphogenetic processes, where a sense of handedness on the cell or tissue scale appears not evident (see e.g. [128] and references therein, or the tissue movements during early avian gastrulation [88]). After all, most bilateral animals seem mirror symmetric from the outside. Given the chirality of the constituent molecules, such a lack of chirality on the macroscopic scale amounts to a fine-tuning of the physical interactions. While such a fine-tuning might be surprising for a passive material, it is not necessarily so for a living system that is the result of evolution. It appears that a pronounced mesoscopic chirality of the actomyosin cortex is not beneficial to an organism in most biological contexts. Furthermore, not any chiral coupling in a physical model may manifest in a pronounced chirality of patterns or flows. As we demonstrate in this thesis, flows and patterns in a living surface crucially depend on its geometry. Motivated by this, we investigate in chapter 5 of this thesis, whether differences in embryo geometry could explain why the chirality of the actomyosin cortex manifests only in some embryos as a chiral rearrangements of cells that is crucial to the process of left-right symmetry breaking (see section 1.1.4).

1.2.5 Active fluid films

In most of this thesis, we consider an isotropic fluid film. For an isotropic material, all couplings between quantities that have the same signature with respect to $\mathcal{O}, \mathcal{M}$ can be written in terms of Kronecker deltas or the metric tensor [119, 129]. For example,there are the following couplings between shear rate and stress tensor:

$$t^{ij}_{\text{visc}} = \eta_s(v^{ij} + v^{ji} - g_{ij}v^{ij}) + \eta_b g_{ij} v^{ij}, \tag{1.49}$$

where η_s is the shear viscosity and η_b is the bulk viscosity. Mathematically, η_b couples the trace of the shear tensor, i.e. the divergence of the flow, to the trace of the stress tensor, i.e. the surface tension. η_s, in contrast couples the trace-less symmetric components of shear rate and stress tensor. Physically, η_b describes the dissipation associated with in-plane compression or expansion of the fluid film, whereas η_s describes dissipation associated with shearing the fluid film in the plane.

In this thesis, we study growing epithelia and the cell cortex. Both represent thin sheets of comdensed matter, which we represent here as two-dimensional surfaces. On short time scales (< 1min. for the cortex, $< 1h$ for the epiblast of the quail embryo), these surfaces resist elastically to in-plane as well as out-of plane deformations due to the molecular crosslinks between filaments and cells. However, the morphogenetic processes we study here in quail and nematode embryos take place on longer time scales. On these time scales, crosslinks as well as the filaments and cells themselves undergo continuous turnover. This turnover enables the relaxation of elastic stresses by irreversible rearrangements of filaments and cells. In a fluid film model of these living sheets, the dissipation associated with rearrangements that do not involve a net exchange of material with the surrounding bulk is quantified by the shear viscosity. When exchange of material with the bulk allows for expansions and contractions of the sheet in the plane, also a bulk viscosity needs to be considered. Flows in the cell cortex have been well described with bulk and shear viscosities being on the same order of magnitude, i.e. $\eta_b/\eta_s \sim 1$ [39, 130]. Epithelial tissues have been modelled as incompressible fluid films [131, 132], as elastically compressible fluid films [87] and as compressible fluid films with compressible flows limited by a bulk viscosity that is much larger than the shear viscosity, i.e. $\eta_b/\eta_s \gg 1$ [54, 88, 133]. In this thesis, we use $\eta_b = \eta_s =: \eta$ for the cell cortex (see chapter 3). For the epiblast of the quail embryo, a quickly growing epithelium, we will compare the experimental flow field to model predictions across a range of bulk viscosities (see chapter 2 and section 5.1).

In contrast to a cup of tea, where fluid flows are driven externally by the person handling the spoon, flows in living matter such as tissues and the cell cortex are driven internally, in particular due to the activity of the motor molecule myosin (see section 1.1.3). Myosin performs mechanical work on the actin meshwork. This energy is provided by the hydrolysis of ATP to ADP. In a hydrodynamic model, this mechanical activity can be captured by a contribution to the stress tensor that results from a coupling to the chemical potential difference $\Delta\mu$ that is associated with the chemical reaction of ATP to ADP. At thermodynamic equilibrium, the thermodynamic force $\Delta\mu$ vanishes. However a cell is maintained out of equilibrium, as the energy lost due to dissipation and mechanical work is balanced by a continuous influx of chemical energy, i.e. food. ADP is phosphorylated to ATP in the mitochondria as part of the metabolism of a cell. As ATP is small molecule that diffuses quickly ($D = 700\mu m^2/s$ in aqueous solution [134]), we consider the ATP concentration and hence $\Delta\mu$ to be spatiotemporally homogeneous in the cell including the cell cortex.

In an isotropic fluid film, the active stress is proportional to the metric tensor:

$$t_{\text{act}}^{ij} = \tilde{\chi}_{\text{act}} \Delta\mu g^{ij} \tag{1.50}$$

In the cell cortex, myosin activity drives in-plane contractions of the cortex, implying $\chi = \chi_{\text{act}}\Delta\mu > 0$. We note that the coupling constant χ_{act} is generally non-constant in space and time as the activity of myosin is regulated in spatially and temporally heterogeneous manner (see section 1.1.3). A gradient of χ_{act} and hence the active stress yields a force $\nabla_j t_{\text{act}}^{ji} = \partial^i \chi$ that drives flows (see Eq. 1.52). When the active stress is regulated by a molecule that is advected by the flow, patterns arise as we will discuss in section 1.2.6. In systems, where the rotational symmetry is broken locally, also active contributions to the trace-less symmetric component of the stress tensor arise. For example, actin filaments in the cytokinetic ring align along the ring [23]. This alignment locally defines an axis. On top of the isotropic contraction captured by Eq. 1.50, the cortex contracts along the axis of the filaments and expands perpendicular to it. Active fluid films with such a trace-less symmetric contribution to the active stress are called active nematics, analogous to nematic liquid crystals. They exhibit complex dynamics that result from a coupling of the local axis that governs the active stress to the resulting flow [131].

Active and viscous stress are components of the dissipative stress $\tilde{t}_{\text{d}}^{ij}$. In general, one needs to consider also equilibrium contributions to the stress tensor. For an isotropic fluid film, this yields a force that is proportional to the gradients of the chemical potentials (Eq. 1.37). However, we consider here a scenario, where differences in chemical potential within the fluid film are limited by exchange with a homogeneous bulk material such that force given by Eq. 1.37 is small compared to the gradients of the active and viscous stress. Therefore, we will neglect the equilibrium stress in the following. We also do not consider couplings of the stress tensor to the bending rate, as we consider gradients in curvature to be shallow compare to the gradients in velocity. For simplicity, we also do not dissipative contributions to the bending moment or normal moment for most of this thesis. Only in section 5.2, we consider active contributions to the moment tensor. Otherwise, we have

$$\tilde{m}^{ij} = 0, \quad m_{\text{n}}^{i} = 0, \quad \tilde{t}^{ij} = \tilde{t}_{\text{d}}^{ij} = t_{\text{visc}}^{ij} + t_{\text{act}}^{ij}. \tag{1.51}$$

We consider the fluid film to be coupled to a substrate such as the egg shell of the nematode embryo that fixes the shape of the fluid film at all times by exerting forces $f_{\text{n,ext}}$ normal to the surface given by Eq. 1.26. Additionally, the substrate exerts tangential forces f_{ext}^{i} on the fluid film, which we consider to be proportional to the velocity of the fluid film with a friction

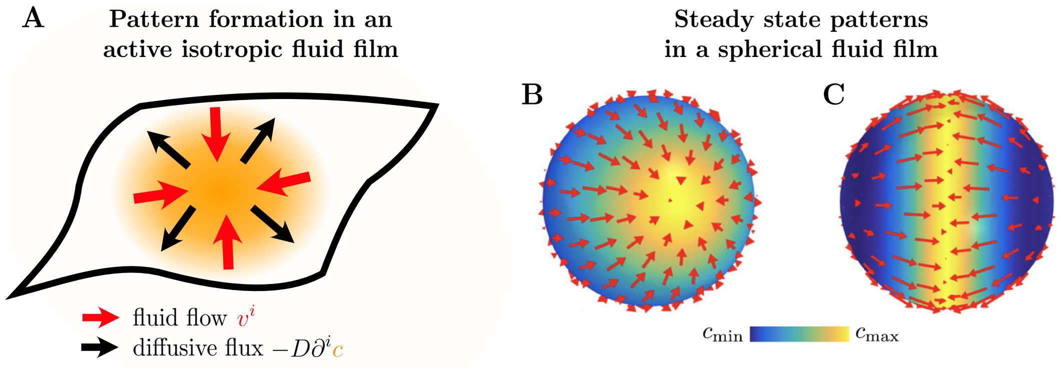
A
Pattern formation in an active isotropic fluid film
fluid flow v^i
diffusive flux $-D\partial^i c$
Steady state patterns in a spherical fluid film
B
C
$c_{\min}$
$c_{\max}$

Figure 1.11: A: Schematic of pattern formation in an isotropic active fluid model (see constitutive equations Eq. 1.49-1.51 and 1.53). A small accumulation of the stress regulator (orange shade) drives contracting flows. When the flux due to advection by the fluid flow overcomes the flux due to diffusion, the homogeneous state is unstable and a pattern emerges. **B,C** Numerically calculated steady state patterns in terms of the stress regulator pattern (color) and the resulting flow field (red arrows) for a spherical geometry (images taken from [135]). In contrast to 1.52, the surface is surrounded by a incompressible bulk fluid instead of a rigid substrate. **B**: Solution for large hydrodynamic length resulting in a pattern with polar symmetry. **C**: Solution for small hydrodynamic length resulting in pattern with nematic symmetry.

coefficient γ. With this the tangential force balance equation, Eq. 1.25, reads

$$\eta_s \nabla_j (\nabla^j v^i + \nabla^i v^j) + (\eta_b - \eta_s)\partial^i \nabla_j v^j - \gamma v^i = -\nabla_j t^{ji}_{\mathrm{act}}. \tag{1.52}$$

This is the differential equations that governs the flow field v^i for a given pattern of active stresses t^{ij}_{act}. It depends on the intrinsic geometry of the surface through the covariant derivative. Understanding how this geometry dependence impacts on the dynamics of an active fluid film will be at the heart of chapters 3 and 4.

1.2.6 Pattern formation in active fluids

In the cortex of the *C. elegans* zygote before polarization no large-scale cortical flows are observed, even though myosin is already present in the cortex. This is because myosin and all other constituent molecules of the cortex are distributed homogeneously in the surface of the cell. At the onset of polarization, myosin molecules are displaced from a small patch of the posterior cell cortex (see section 1.1.2 and Fig. 1.2B). In a hydrodynamic model the localized removal of myosin from the cortex is captured by a localized reduction in χ and hence the active stress. The resulting gradient in active stress drives a flow that transports myosin (and the anterior PAR proteins) from the posterior to the anterior half of the cortex. Ultimately a steady state emerges, where myosin and anterior PAR proteins are localized to the anterior half of the cortex. At this time-point the cortex still flows from the posterior to the anterior side of the embryo, but the resulting transport of myosin and PAR proteins is balanced by exchange with the cytoplasm as well as diffusional fluxes within the cortex.

To capture the emergence of a chemical pattern driven by active stresses, we consider the following dynamics of the chemical concentration c of a stress regulator

$$\partial_t c = -\nabla_i (cv^i - D\partial^i c) - k(c - c_0), \tag{1.53}$$

where D is a diffusion constant capturing diffusion within the cortex and k is rate of exchange with the cytoplasm with c_0 being a reference concentration to which c relaxes. This dynamical equation is complemented by the governing equation of the flow field (Eq. 1.52) and a expression $\chi_0 f(c/c_0)$ for χ, i.e. the dependence of the active stress on the regulator concentration c with f being a dimensionless function with $f'(1) > 0$. Gradients in c result in a flow v^i that feeds back into the dynamics of c as the advective flux cv^i.

This model has been analyzed for a spherical geometry and in a one-dimensional domain, both in terms of the linear stability of the homogeneous state and in terms of non-linear steady states [136, 135]. The linear stability can be understood in terms of the ratio between advective fluxes that transport the stress regulator towards maxima in c (with $\chi_0 > 0$) and diffusive fluxes that counter-act this accumulation of the stress regulator. This ratio is the dimensionless Peclet number Pe, which may be written as

$$\mathrm{Pe} = \frac{\chi_0}{D\gamma_{\mathrm{eff}}}, \tag{1.54}$$

where $\gamma_{\mathrm{eff}} = \gamma$ for friction limited flow and $\gamma_{\mathrm{eff}} = \eta_b/R^2$ for viscosity limited flow in a finite domain with characteristic length scale R. When the Peclet number is greater than a critical value Pe^*, the homogeneous state ($c = c_0$) becomes unstable with respect to pertubations, as advective fluxes dominate over diffusive fluxes yielding the self-organized formation of chemical patterns. In a one-dimensional term, the pattern collapses into a single peak in c in the non-linear regime [136]. Mietke et al. have studied this model in a spherical geometry incorporating the coupling to an enclosed and a surrounding bulk fluid instead of a rigid substrate [135]. They found that two kind of steady state patterns emerges: a polar pattern with a single peak in c (Fig. 1.11B) and patterns with nematic symmetry (Fig. 1.11C), where the stress regulator accumulates either at a ring around the equator of the sphere or in two patches at opposing poles of the sphere. While the polar pattern is reminiscent of the cortex of *C. elegans* zygote during polarization, the contractile ring may be understood as a minimal model of the cytokinetic ring.

Pe^* as well as shape and symmetry of the steady state patterns depend on the ratio of the viscosities η_b/η_s, the rate of exchange with the cytoplasm, the hydrodynamic length $\sqrt{\eta_s/\gamma}$ and the geometry of the fluid film. In chapter 3, we will study this geometry dependence of this minimal model of pattern formation in the cell cortex.

1.3 Understanding active surfaces with complex numbers

In this thesis, we study fluid films. When studying such two-dimensional manifolds, may they be curved or flat, we have found that notation and analytical calculations become more elegant and

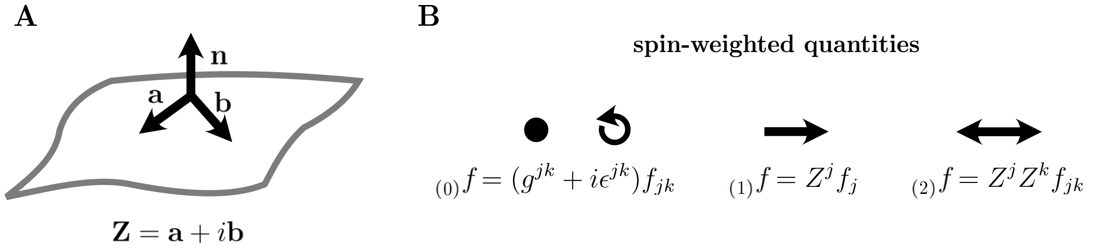
A
n
a
b
$\mathbf{Z} = \mathbf{a} + i\mathbf{b}$
B
spin-weighted quantities
${}_{(0)}f = (g^{jk} + i\epsilon^{jk})f_{jk}$
${}_{(1)}f = Z^j f_j$
${}_{(2)}f = Z^j Z^k f_{jk}$

Figure 1.12: **A**: A right-handed orthonormal basis $\{\mathbf{a}, \mathbf{b}, \mathbf{n}\}$, with $\mathbf{n}$ being the normal vector of the surface, allows to define complex basis $\mathbf{Z}$. **B**: Projections of vector and tensor fields onto $\mathbf{Z}$ define complex valued fields, so called spin-weighted fields or quantities. The spin weight, indicated by the prescript, denotes the local rotational symmetry of the field. See main text for details.

efficient by mapping two-dimensional vectors to complex numbers. Specifically, we will adopt the Newman-Penrose formalism for much of this thesis, where vector and tensor fields on a surface are understood as complex-valued so called spin-weighted fields [137]. In the following, we will introduce this formalism which was originally developed in the context of general relativity. Here, we adopt it to the study of active surfaces. Furthermore, we introduce a certain kind of parametrisation, called isothermal coordinates, that can be found for any surface in section 1.3.2. For such a parametrisation, the intrinsic geometry of a surface is uniquely defined by a scalar field which we term the geometric potential. This enables us to study general surface geometries in chapter 4. Finally, we introduce some basic notions of complex analysis, in particular holomorphic functions, in section 1.3.3, which will enable us to analytically understand flow fields in the quail embryo in chapter 2.

1.3.1 Newman Penrose formalism

The Newman Penrose formalism can best be understood by introducing a complex basis vector field

$$\mathbf{Z} = \mathbf{a} + i\mathbf{b} \tag{1.55}$$

where at each point on the manifold $\mathbf{a}, \mathbf{b}$ are a real orthonormal basis of the tangent vector space at this point and the (outward) pointing normal vector is $\mathbf{n} = \mathbf{a} \times \mathbf{b}$ [137, 138] (see Fig. 1.12A). For a given normal vector field $\mathbf{n}$, defining an orientation of $\mathbf{X}$, $\mathbf{Z}$ is defined up to a rotation around $\mathbf{n}$ corresponding to a gauge transformation. With this, we understand scalar, vector and tensor fields as so called spin-weighted fields. A spin-weighted field is a complex valued function denoted as

$${}_{(s)}f(s^1, s^2, \mathbf{Z}) = f(s^1, s^2)e^{is\theta(s^1, s^2, \mathbf{Z})} \tag{1.56}$$

whose phase θ depends on the local choice of $\mathbf{Z}$. s is the so-called spin-weight of ${}_{(s)}f$ and denotes the rotational symmetry of ${}_{(s)}f$, i.e. ${}_{(s)}f$ transforms under rotations of the local basis ($\mathbf{Z}' = e^{-i\psi}\mathbf{Z}$) as

$${}_{(s)}f'(z) := {}_{(s)}f(z, \mathbf{Z}') = e^{-is\psi}\, {}_{(s)}f(s^1, s^2, \mathbf{Z}) \tag{1.57}$$

For example, for a real vector field $\mathbf{v}$, we denote the tangential components as the spin fields ${}_{(1)}v = \mathbf{Z}\cdot\mathbf{v}$ and ${}_{(-1)}v = \bar{\mathbf{Z}}\cdot\mathbf{v}$, where $\bar{..}$ is the complex conjugate. As we consider only real vector and tensor fields here, we have ${}_{(s)}f = {}_{(-s)}\bar{f}$ for $|s| > 0$. The normal component $v_n = \mathbf{n}\cdot\mathbf{v}$ is a scalar quantity on the surface and hence defines a real valued spin 0 field. Pseudoscalars like the vorticity correspond to imaginary spin 0 fields. Fields with spin-weight $s > 1$ correspond to trace-less symmetric rank s tensors such as the order parameter of an s-atic [139, 140]. A rank 2 tensor t_{ij} defines a spin 2 field ${}_{(2)}t$, corresponding to its trace-less symmetric component, as well as a spin 0 field ${}_{(0)}t$ corresponding to its trace and antisymmetric component:

$$
{}_{(2)}t = Z^i Z^j t_{ij} = \frac{1}{2} Z^i Z^j (t_{ij} + t_{ji} - g_{ij} t_k{}^k), \quad {}_{(0)}t = \bar{Z}^i Z^j t_{ij} = (g^{ij} + i\epsilon^{ij}) t_{ij}, \tag{1.58}
$$

where we used Eq. D.2. Contractions of multiple tensors correspond to products of spin-weighted fields. Consider for example a vector field f_i given by the contraction of a rank 2 tensor t_{ij} and a vector p_j by $f_i = t_{ij} g^{jk} p_k$. Then, the corresponding spin-field can be written as

$$
{}_{(1)}f = Z^i f_i = \frac{1}{2}\left({}_{(2)}t \,{}_{(-1)}p + {}_{(0)}t \,{}_{(1)}p\right) \tag{1.59}
$$

where spin-weights add up, i.e. the spin-weight of the product is the sum of the spin-weights of the factors. Covariant derivatives of vector or tensor fields can be understood using the derivative operators ð ("edth" or spin-raising operator) and $\bar{\text{ð}}$ ("edth bar" or spin-lowering operator):

$$
\eth \,{}_{(s)}f = Z^i \partial_i \,{}_{(s)}f + s\Gamma \,{}_{(s)}f \tag{1.60}
$$

$$
\bar{\eth} \,{}_{(s)}f = \bar{Z}^i \partial_i \,{}_{(s)}f - s\bar{\Gamma} \,{}_{(s)}f, \tag{1.61}
$$

where Γ is the spin-connection which we define as

$$
\Gamma = \frac{1}{2}\mathbf{Z}\cdot Z^i \partial_i \bar{\mathbf{Z}} = \frac{1}{2}\mathbf{Z}\cdot \eth\bar{\mathbf{Z}} \tag{1.62}
$$

corresponding to the rotation of the basis $\mathbf{Z}$ relative to parallel transport [141, 137]. Γ is the complex analog to the Cristoffel symbols Γ^k_{ij}. The spin-raising operator ð yields a field with spin-weight $s + 1$. For $s > 0$, it corresponds to the symmetrised gradient of ${}_{(s)}f$ for $s > 0$. The spin-lowering operator $\bar{\eth}$ is the complex conjugate of ð and yields a field with spin-weight $s - 1$. For $s > 0$, $\bar{\eth}\,{}_{(s)}f$ yields the divergence (or curl) of the tensor field associated with ${}_{(s)}f$. Applying the complex derivatives to the three-dimensional representation of the surface $\mathbf{X}$ understood as a spin-0 field, one recovers the complex basis $\mathbf{Z}$:

$$
\eth\mathbf{X} = Z^i \partial_i \mathbf{X} = \mathbf{Z}, \quad \bar{\eth}\mathbf{X} = \bar{\mathbf{Z}} \tag{1.63}
$$

The curvature tensor C_{ij} can be understood in terms of the mean curvature $2\,{}_0C$ and the anisotropic curvature ${}_2C$ defined as

$$ {}_0C = C_i{}^i, \quad {}_2C = Z^i Z^j C_{ij}. \tag{1.64} $$

There are related to the Gaussian curvature κ via

$$ \kappa = \frac{1}{4}({}_0C\,{}_0C - {}_2C\,{}_{-2}C). \tag{1.65} $$

Importantly, κ can also be expressed in terms of the commutator of the covariant derivative [141]

$$ (\bar{\eth}\eth - \eth\bar{\eth})\,{}_sf = 2s\kappa\,{}_sf \quad \Rightarrow \quad \kappa = \frac{1}{2}(\eth\bar{\Gamma} + \bar{\eth}\Gamma), \tag{1.66} $$

which demonstrates that Gaussian curvature is an intrinsic property of a surface geometry.

To calculate the flow field of a fluid film, it is often useful to write the flow field as a Hodge decomposition [142, 143, 144], which is the generalization of the more well known Helmholtz decomposition in three-dimensional cartesian space to general manifolds. Using the Newman Penrose formalism, the Hodge decomposition of the flow field ${}_{(1)}v$ can be written as:

$$ {}_{(1)}v = \eth\,{}_{(0)}F + {}_{(1)}v_h, \tag{1.67} $$

where ${}_{(0)}F = F = A + iB$ is a spin 0 field composed of a scalar field A and a pseudoscalar field iB with $A(s^1, s^2), B(s^1, s^2) \in \mathbb{R}$. ${}_{(1)}v_h$ is the harmonic component of the flow field with $\bar{\eth}\,{}_{(1)}v_h = 0$, i.e. a flow field with vanishing divergence and vorticity. It is only non-vanishing for a surface with non-spherical topology. For a cylinder, it corresponds to rigid body rotation and translation of the cylinder. The imaginary part of ${}_{(0)}F$ corresponds to the stream function and hence the rotational component of the flow field with vanishing divergence. The real part of ${}_{(0)}F$ corresponds to the velocity potential and hence the irrotational component of the flow field with vanishing vorticity but non-vanishing divergence.

Using the spin raising and lowering operators, the tangential force balance equation of an isotropic active fluid film (Eq. 1.52) reads

$$ \eta_s\bar{\eth}\eth\,{}_{(1)}v + \eta_b\eth\,\mathrm{Re}[\bar{\eth}\,{}_{(1)}v] - \gamma\,{}_{(1)}v = -\eth\,{}_{(0)}\chi, \tag{1.68} $$

where ${}_{(0)}\chi = \chi\Delta\mu$. This equation can be rewritten by making use of the Hodge decomposition (Eq. 1.67) and the commutator of the covariant derivative (Eq. 1.66), yielding

$$ \eta\eth\Delta_{LB}(F + \alpha\,\mathrm{Re}\,F) - (\gamma - 2\eta\kappa)\,(\eth F + {}_{(1)}v_h) = -\eth\,{}_{(0)}\chi \tag{1.69} $$

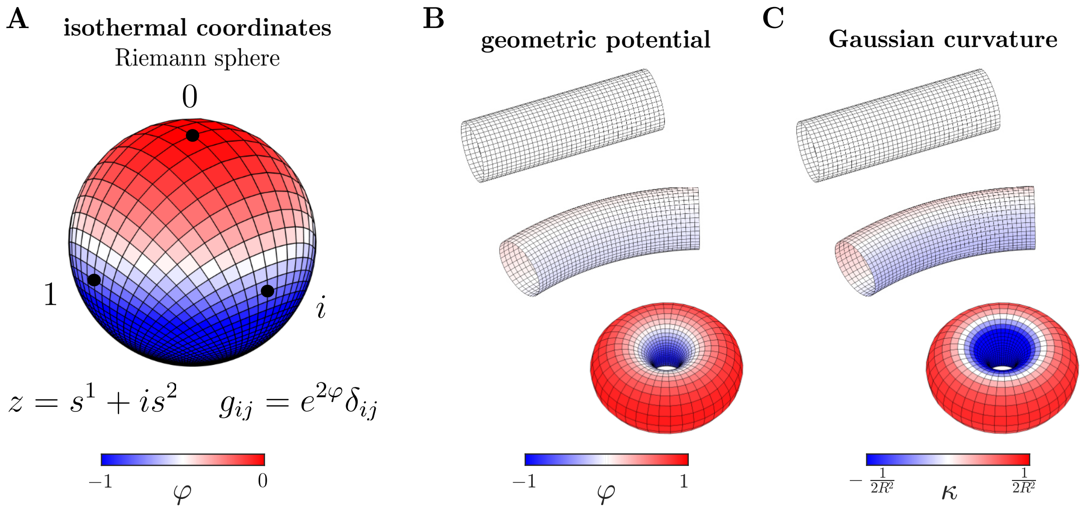

Figure 1.13: A: Plot of the Riemann sphere understood as the complex plane mapped to a sphere such that squares are mapped to squares, i.e. $g_{ij} \sim \delta_{ij}$. Coordinates of a general surface that obey this condition (Eq. 1.70) are called isothermal (see main text for details). **B**,**C**: Plots of a cylinder that is deformed to a torus while keeping isothermal coordinates such that the deformation is understood in terms of a change in φ, i.e. as locally isotropic expansions or contractions. **B**: Plots with $\varphi = \log l$, also called the geometric potential, indicated by the colormap. **C**: Plots with the Gaussian curvature κ indicated by the colormap. Note that κ and φ are closely related as stated by Liouville's equation, Eq. 1.71.

1.3.2 Isothermal coordinates

As shown by Gauss [145], there exist coordinates for any point on any surface such that in an open set around this point, the metric tensor becomes

$$g_{ij} = l(s^1, s^2)^2 \delta_{ij}, \tag{1.70}$$

where $l(s^1, s^2)$ is a length scale. This may be understood as a (conformal) mapping that maps squares in the coordinate space to squares on the surface, where the size of the square, however, varies across the surface according to the length scale l (see Fig. 1.13 for examples. As l is strictly positive, we can write it as $l = e^{\varphi}$. φ is often called a geometric potential as it obeys a Poisson-like equation [146, 139]. This equation, called Liouville's equation, relates the length scale with the Gaussian curvature:

$$\Delta_{LB}\varphi = -\kappa, \tag{1.71}$$

where $\Delta_{LB} = g^{ij}\nabla_i\partial_j = \bar{\partial}\partial$ is the Laplace-Beltrami operator. Importantly, this operator simplifies to the ordinary Laplace operator $\Delta_0 = \partial_{s^1}^2 + \partial_{s^2}^2$, when using isothermal coordinates:

$$\Delta_{LB} = \frac{1}{l^2}\Delta_0 = e^{-2\varphi}\Delta_0 \tag{1.72}$$

Thereby, Liouvilles equation (Eq. 1.71) becomes a self-consistency equation for φ.

In isothermal coordinates we can identify the real and imaginary parts of **Z** with the normalized

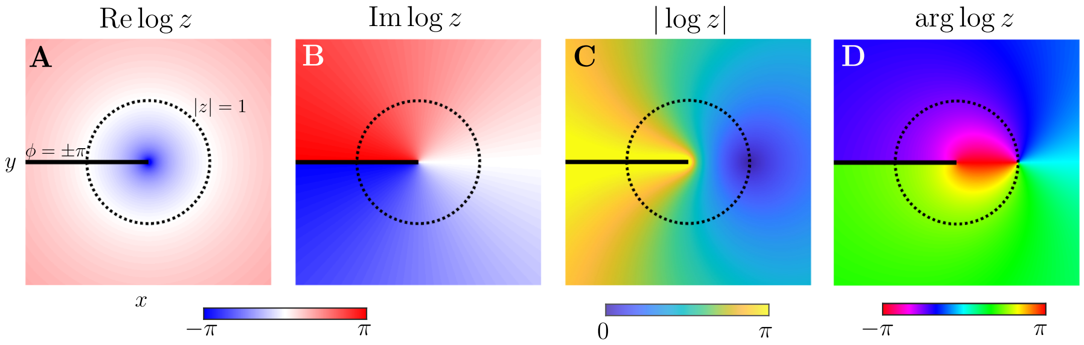

Figure 1.14: Plots of the complex logarithm $\log z$ with the branch cut (black solid line) along the negative real line.

covariant basis, i.e. $Z^i = (1/l, i/l)$. Then, the spin-raising and lowering operators read

$$\eth_{(s)} f = \frac{2}{l^{1-s}}\partial_{\bar{z}}(l^{-s}\,{}_{(s)}f), \quad \bar{\eth}_{(s)} f = \frac{2}{l^{1+s}}\partial_{z}(l^{s}\,{}_{(s)}f), \tag{1.73}$$

where we make use of the so called Wirtinger derivatives defined as

$$\partial_z = \frac{1}{2}\left(\partial_1 - i\partial_2\right), \quad \partial_{\bar{z}} = \frac{1}{2}\left(\partial_1 + i\partial_2\right) \tag{1.74}$$

For functions that can be written as differentiable functions in z and $\bar{z}$, these operators behave as ordinary derivatives [147, 148]. On a complex manifold, the Wirtinger derivatives yield the Dolbeault operators $\partial, \bar{\partial}$, i.e. covariant derivative operators acting on differential forms, to which the spin-raising and lowering operators $\eth, \bar{\eth}$ can be mapped [149]. Thereby, the two-dimensional surface is mapped to a Riemann surface, i.e. a complex one-dimensional manifold with complex coordinate

$$z = s^1 + is^2. \tag{1.75}$$

Isothermal coordinates have recently also been used by Vafa and co-authors to understand nematic surfaces [139, 150]. There, they also make use of a complex formalism that appears equivalent to the Newman-Penrose formalism we have introduced above when using isothermal coordinates.

1.3.3 Holomorphic functions

For a fluid film with vanishing Gaussian curvature, we can parametrize the surface such that $l = 1$. In chapter 2, we study such a flat fluid film with vanishing friction and in the absence of gradients of active stresses. In this case,the governing equation of the flow field (Eq. 1.69) yields

$$\partial_{\bar{z}}\partial_z\partial_{\bar{z}}(F + \alpha\,\mathrm{Re}\,F) = 0. \tag{1.76}$$

Solution to this equation can be written in terms of holomorphic functions (see sections 2.3,B.2), which we introduce in the following.

A function f is called holomorphic, when it obeys the Cauchy-Riemann equations, which can be written using the Wirtinger derivatives as

$$\partial_{\bar{z}} f = 0. \tag{1.77}$$

A holomorphic function is n times complex differentiable with $n \in \mathbb{N}$, i.e. the derivatives

$$f^{(n)}(z) = (\partial_z)^n f(z, \bar{z}) \tag{1.78}$$

are well defined. Furthermore, every holomorphic function is analytic, meaning that it is identical to its Taylor series

$$f_a(z) = \sum_{n=0}^{\infty} f^{(n)}(a) \frac{(z-a)^n}{n!} \tag{1.79}$$

in an open disk around the point $a \in \mathbb{Z}$. The coefficients $f^{(n)}(a)$ can also be calculated from the values at the boundary of this disk. By virtue of Cauchy's integral formula [147], we have

$$f^{(n)}(a) = \frac{n!}{2\pi i} \oint_{\mathcal{C}} \mathrm{d}z \, \frac{f(z)}{(z-a)^{n+1}}, \tag{1.80}$$

where $\mathcal{C}$ is a curve in the complex plane that winds once around a and encloses an open region in which f is holomorphic. Hence, f and all its derivatives are defined by the boundary values of f. Choosing $a = 0$ and $\mathcal{C}$ as a circle with radius r around the origin, we have

$$f^{(n)}(0) = \frac{n!}{2\pi r^n} \int_0^{2\pi} \mathrm{d}\theta \, f\left(re^{i\theta}\right) e^{-in\theta}, \tag{1.81}$$

i.e. the coefficients of the Taylor expansion correspond to the Fourier coefficients of f on the boundary.

When f is holomorphic in an annulus with $r < |z| < R$, it can be written as a Laurent series:

$$f(z) = \sum_{n=-\infty}^{\infty} f_n z^n, \tag{1.82}$$

with $f_n \in \mathbb{C}$. In the limit $R/r \to \infty$, the coefficients f_n with $n < 0$ ($n > 0$) correspond to the Fourier coefficients of f evaluated at the inner (outer) circle with $|z| = r$ ($|z| = R$).

Any function that can be written as a Laurent or Taylor series in terms of $(z - a)$ is holomorphic. This includes in particular the complex exponential and logarithm, and functions that derive from it such as trigonometric functions and non-integer power-laws like the square root $\sqrt{z}$. The complex logarithm $\log(z)$ is holomorphic in the complex plane except along a curve $z(\lambda)$ with $\lambda \in [0, \infty)$, $z(0) = 0$ and $\partial_\lambda |z(\lambda)| > 0$. This curve is the so called branch cut across which $\log(z)$

is discontinuous. It results from the multivaluedness of $\log(z)$, which in turn is a consequence of $\exp(z)$ not being injective, i.e.

$$\exp(z + 2\pi n i) = \exp(z) \tag{1.83}$$

for $n \in \mathbb{Z}$. A branch of $\log z$ is a single-valued function corresponding to a convention for the angle $\phi = \operatorname{Im} \log z$ with $z = r\exp(i\phi)$. The standard branch is $\phi \in (-\pi, \pi)$ with the branch cut along the negative real axis (see Fig. 1.14).

1.4 Overview of this thesis

In the following chapters we present the results of theoretical calculations and the analysis of experimental data from quail and nematode embryos. Thereby we use the physical theories and mathematical methods we discussed in the previous sections to understand the biological processes we discussed in section 1.1.

We start by considering the process of gastrulation in the avian embryo in chapter 2. Adopting some notions from fracture mechanics, we develop a mechanical model of the primitives streak as an active viscous crack. This model allows us to understand experimental flow fields in terms of forces generated within the primitive streak. To this end, we make use of the mathematical methods introduced in the previous section, in particular in section 1.3.3. Using the thus inferred mechanical model of the primitive streak we elucidate the process of streak elongation.

In chapter 3, we turn to the process of axis specification in the nematode embryo. As we discuss there, the geometry of the egg shell determines the axes along which the body axes are established in terms of chemical gradients with the help of flows generated within the actomyosin cortex. To elucidate this phenomenon we consider a minimal model of guided symmetry breaking. To understand how such guiding arises from the mechanics of the actomyosin cortex, we use a minimal model of the cortex introduced by Mietke et al. [135]. We investigate how anisotropies in the cell shape impact flows and pattern formation in this active fluid model. We obtain exact results for a slightly deformed sphere. To this end, we make extensive use of the Newman Penrose formalism we introduced in section 1.3.1 and in particular spin-weighted spherical harmonics which were originally defined within this formalism (see appendix E). We then compare these results to experimental observations in the nematode embryo and generalize these findings to a principle called Hertwig's rule, i.e. the phenomenon that cells tend to divide along their longest geometric axis. Finally, we develop a numerical method to understand how surface geometry guides pattern formation in the non-linear regime of the active fluid model (see appendix F).

In chapter 4, we investigate how surface geometry guides flows in an active fluid film for more general surface geometries. To this end we make extensive use of the Newman Penrose formalism and the notion of isothermal coordinates which we introduced in section 1.3.2. With this, we map the governing equations of a curved fluid film to flat geometry by rescaling viscosities and friction coefficient. Furthermore, we obtain exact bounds for how the flow field around a force monopole changes upon a deformation of the surface. These results allow us to understand the movement of a tension monopole in general anisotropies of the surface geometry. We then compare these results to numerical solutions of an active fluid model in complex geometries. Finally, we investigate how anisotropies in the surface geometry guides translations and rotations of a localized source of anisotropic active stresses.

In chapter 5, we make use of the methods developed in the preceding chapters to understand how torque dipoles generated by the actomyosin cortex give rise to chiral flows during left-right symmetry breaking in quail and nematode embryos. In particular, we analyze experimental flow fields from quail embryos during the process of left-right symmetry breaking.

Chapter 2

Crack mechanics of avian gastrulation

The primitive streak is complex structure (see cross section in Fig. 2.1C) in the embryos of amniote animals such as birds and mammals. It forms during the process of gastrulation and enables the rearrangements of cells across tissue layers (see section 1.1.5). In Fig. 2.1B, an image of a quail embryo with flourescent membrane marker is shown. On this scale, the primitive streak looks like bright line drawn by a pencil on rather homogeneous sheet of tissue. During the development of avian or mammalian embryos, the line first elongates and then regresses, i.e. it shrinks away as the process of gastrulation comes to a close. In this chapter, we model this living line that is the primitive streak as a one-dimensional active material. With this hydrodynamic model, we study the transition between streak elongation and regression in terms of the forces that drive these movements and deformations of tissue. To do so, we analyze experimental data obtained from quail embryos by Julia Pfanzelter and Adrian Lahola-Chomiak from the lab of Stephan Grill at the MPI-CBG, Dresden.

The primitive streak is embedded in the epiblast, an unicellular quickly proliferating epithelium. Motivated by previous studies [88, 54, 87], we model the epiblast as a flat fluid film to understand the large-scale movements and deformations of the epiblast tissue. In such a hydrodynamic theory, the line that is the primitive streak introduces discontinuities in the stress and flow field, not unlike a crack in a passive elastic material. These discontinuities in the model correspond to sharp gradients within the streak or crack that are facilitated by distinct material properties. In a fracturing elastic material, breaking down of covalent bonds facilitate large relative displacements of the two crack faces. In the quail embryo, an epithelial to mesynchymal transition allows cells to detach from the epiblast within the $100\mu m$ wide primitive streak [79, 3]. Also, out-of plane deformations of the avian epiblast are restricted to the primitive streak and its immediate surrounding [68]. Thus, the streak is also a line of material that is mechanically distinct from the sheet of matter, the epiblast, it is embedded in. Such lines can be found in various biological settings (see Fig. 2.7B-D for some examples). They shape the material properties and dynamics of the organ or organism they are embedded in. Unlike passive cracks, living cracks like the primitive streak or the cytokinetic ring undergo continuous turnover and perform mechanical work due to the activity of molecular motors, in particular Myosin. Next to understanding avian gastrulation, the purpose of this chapter is to present a general hydrodynamic theory of such active viscous cracks.

We will start by introducing a crack in a fluid film as a boundary with a peculiar geometry (section 2.1). We define this geometry (section 2.1.1) and discuss the flow field for prototypical crack boundary conditions (section 2.1.2). To test whether the epiblast does indeed behave as a fluid film, we analyze experimental flow fields from quail embryos, using microscopy images obtained by Julia Pfanzelter and Adrian Lahola-Chomiak (section 2.1.3). In section 2.2, we develop a mechanical theory of an active crack to understand how mechanical activity and material properties of the crack material define crack boundary conditions. In section 2.3, we use this theory and analytical solutions of crack boundary conditions to infer an effective mechanical model of the primitive streak as an active crack. Finally, we investigate in 2.4 the propagation of such an active viscous crack resulting from the advection of the crack tip. This will allow us to understand how mechanical activity in the streak controls the elongation of the streak.

2.1 The primitive streak as a crack in a fluid film

2.1.1 Geometry of a crack in a surface

In a thin sheet of material, a crack may be represented as a curve

$$\mathcal{C} = \{\mathbf{Y}(\lambda) \in \mathcal{S} | \lambda \in [0, L]\} \tag{2.1}$$

embedded in the surface $\mathcal{S}$ that is the sheet, with λ being a coordinate along the crack. $\mathbf{Y}(0)$ and $\mathbf{Y}(L)$ correspond to crack tips. With this, we define the covariant tangent vector of the crack

$$\mathbf{e}_\lambda := \partial \mathbf{Y} / \partial \lambda \tag{2.2}$$

which yields the length element $\mathrm{d}l := |\mathbf{e}_\lambda| \mathrm{d}\lambda$. Furthermore, we define the crack normal vector

$$\boldsymbol{\nu}_C := \mathbf{n} \times \mathbf{e}_\lambda / |\mathbf{e}_\lambda| \tag{2.3}$$

which is normal to the crack contour but tangent to the surface (see Fig. 2.1E). Close to the crack and away from the cracktips, we may parametrize the surface as

$$\mathbf{X}(\lambda, x) = \mathbf{Y}(\lambda) + x\boldsymbol{\nu}. \tag{2.4}$$

Identifying $\mathbf{Y}(0)$ as the Hensen's node, the anterior tip of the primitive streak, $x > 0$ and $x < 0$ correspond to the epiblast on the right and left side of the primitive streak. With this parametrisation, we evaluate a vector or tensor field $\mathbf{h}$ on the surface $\mathcal{S}$ on the two sides of the

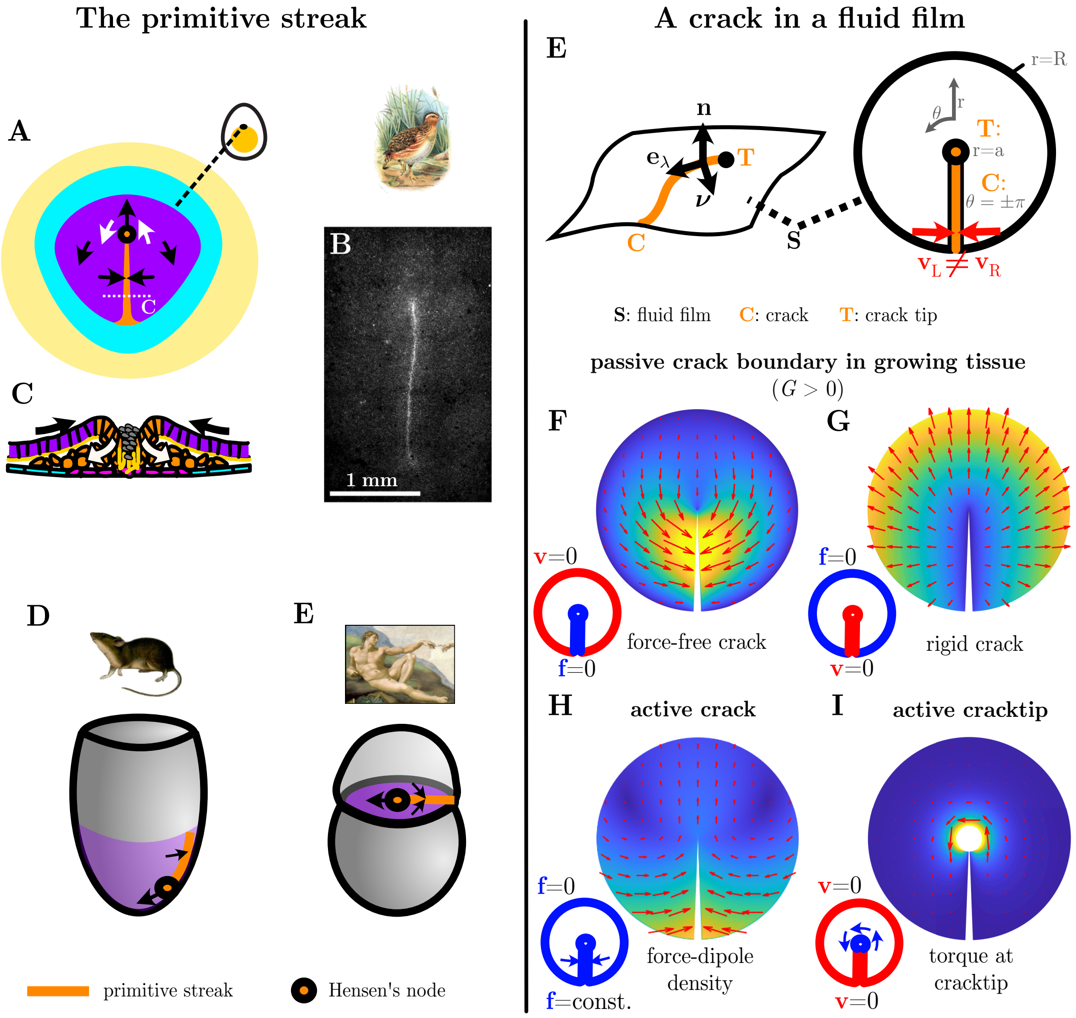
The primitive streak
A crack in a fluid film
A
C
B
1 mm
C
D
E
E
n
e$_\lambda$
T
ν
C
S
r=R
θ
r
T:
r=a
C:
$\theta = \pm\pi$
v$_L \neq$ v$_R$
S: fluid film
C: crack
T: crack tip
passive crack boundary in growing tissue
$(G > 0)$
F
G
v=0
f=0
force-free crack
f=0
v=0
rigid crack
H
active crack
I
active cracktip
f=0
f=const.
force-dipole density
v=0
v=0
torque at cracktip
primitive streak
Hensen's node

Figure 2.1: Modelling the primitive streak as a crack in a fluid film. **A**-**C**: the primitive streak in the avian embryo during the process of gastrulation, shortly before maximum streak elongation. **A**,**C** Schematics of dorsal view (**A**) and cross section of the primitive streak **C** as in Fig. 1.5. **B**: Microscopy image of the dorsal side of the avian embryo using a fluorescent membrane marker, obtained by Julia Pfanzelter at the MPI-CBG, Dresden. **D**,**E**: Schematics of mouse (**D**) and human embryo (**E**) at a corresponding stage, drawn after [66, 3]. Black arrows denote anterior movement of the Hensen's node (black/orange circle) and tissue movements towards the primitive streak (orange line). **E**: Geometry of a crack in a curved surface (left panel) and of a straight crack in a flat surface using polar coordinates (right panel), see main text for details. In **F**-**I**, we use the latter geometry for numerical solutions of the flow field (**v**, red arrows) of a fluid film around a crack as a model for the epithelial tissue around the primitive streak. The color denotes $|\mathbf{v}|$ with yellow corresponding to the maximum and blue to $|\mathbf{v}| = 0$. Blue/red schematics illustrate the stress (blue) and velocity (red) boundary conditions. In all four examples, we allow only for a rigid body translation and rotation of the crack tip boundary. In **F**-**H**, we use $l_{\mathrm{h}} \to \infty$. As this makes the flow field in **H** degenerate with respect to a translation of the entire system, we further impose a vanishing net velocity of the outer boundary. For further details on material parameters and boundary conditions see Table J.1 in the appendix.

crack as

$$\mathbf{h}_R(\lambda) = \lim_{x \to 0^+} \mathbf{h}(\lambda, x), \quad \mathbf{h}_L(\lambda) = \lim_{x \to 0^-} \mathbf{h}(\lambda, x). \tag{2.5}$$

As the crack represents a material that is distinct from the sheet represented by $\mathcal{S}$,

$$\mathbf{h}_R(\lambda) \neq \mathbf{h}_L(\lambda). \tag{2.6}$$

In general, this is true for all hydrodynamic fields on $\mathcal{S}$, including the flow field $\mathbf{v}$ and the stress tensor $\mathbf{t}^i$. In other words, these fields are discontinuous at the crack. Of course, this discontinuity in a mathematical sense is a property of the model. In reality, a crack in a fracturing material as well as the primitive streak have a finite extension in all three spatial directions. The discontinuity of the model represents a sharp gradient within the crack material that is facilitated by the distinct material properties of the crack. In section In section 2.2, we link the discontinuities in of flow and stress field, i.e. $\mathbf{v}_R - \mathbf{v}_L$ and $\mathbf{t}^i_R - \mathbf{t}^i_L$, to a mechanical model of the crack.

Importantly, this requires also a model of the crack tip, as it is finite-sized object, denoted in the following by $\mathcal{T}$, that is mechanically distinct from the crack as well as the sheet the crack is embedded in. In a fracturing elastic material, the immediate surrounding of the crack tip is plastically deforming, which is crucial to calculating the critical load at which the crack propagates (REF). The Hensen's node is a peculiar structure with an extension of about 200 μm within the plane of the epiblast to which specific morphogens are localized (REF).

2.1.1.1 A crack in the flat plane

The epiblast is a mostly flat epithelium as it is localized to the surface of the much larger spherical egg-yolk. Therefore, we will represent the epiblast as a flat surface in the following. We parametrize this surface using polar coordinates r, θ (see right panel in Fig. 2.1E). As the primitive streak is a mostly straight line (see Fig. 2.1B for a typical example), we identify it with the line $\theta = \pm\pi$ with the crack tip or Hensen's node $\mathcal{T}$ at the origin of the coordinate system. To account for the finite size of the crack tip, we identify $\mathcal{T}$ with the circle $r \leq a$. In this parametrisation ($\lambda = r$), we have

$$\mathbf{e}_\lambda = \mathbf{r}, \quad \boldsymbol{\nu} = \boldsymbol{\theta}, \quad \mathbf{h}_R = \mathbf{h}(\theta = -\pi), \quad \mathbf{h}_L = \mathbf{h}(\theta = \pi). \tag{2.7}$$

In principle, the primitive streak has a posterior tip or node. While in mouse this is called the allantoic core domain [151], a similar structure has not or only poorly been characterized in birds. In the experiments we analyze here, that were originally designed to image cell movements around the Hensen's node, the posterior half of the primitive streak is often outside the field of view. Therefore, we consider here only a circular domain around the Hensen's node, i.e. $r < R$ with $R = 600\mu\text{m}$.

2.1.2 Crack boundary conditions in a fluid film

While Hensen's node and primitive streak are highly complex structures, the surrounding epiblast appears flat and homogeneous around the time point of maximum streak extension which we study here. Furthermore, it is a quickly proliferating tissue with cells constantly dividing. Such cell division fluidise an epithelium by facilitating the relaxation of elastic stresses [152]. Therefore, we model the epiblast in the following as a flat fluid film. Using cartesian coordinates, the in-plane stress tensor is given by

$$t_{ij} = \eta \left(\tilde{v}_{ij} + \alpha(\operatorname{div} \mathbf{v} - G)\delta_{ij} \right), \tag{2.8}$$

where η is the shear viscosity α is the ratio of bulk over shear viscosity and $\tilde{v}_{ij}$ is the trace-less symmetric component of the shear tensor v^{ij} as defined in Eq. 1.42. $G > 0$ is a growth rate of the tissue that is independent from the stresses that act on patch of tissue, in contrast to the bulk viscosity $\eta_b = \alpha\eta$ which captures a coupling of cell division and death rates to the tissue stress [152]. In the following, we consider G as well as the viscosities to be spatially homogeneous.

The epiblast is attached to the vitelline membrane, a protein membrane that encompasses the egg-yolk. We take into account friction between the vitelline membrane and the epiblast by a tangential force density

$$\mathbf{f}^i_{\text{ext}} = -\gamma v^i \tag{2.9}$$

that is acting on the epiblast. γ is a friction coefficient that defines a hydrodynamic length $l_{\text{h}} = \sqrt{\eta/\gamma}$. With this, the force balance equation, Eq. 1.25, yields the governing equation of the flow field $\mathbf{v}$ of the fluid film, given by Eq. 1.52 with $t^{ij}_{\text{act}} = -\eta\alpha G$.

The flow field is defined by the differential equation Eq. 1.52 as well as boundary conditions at the crack ($\theta = \pm\pi$), the crack tip ($r = a$) and the enclosing circle ($r = R$). We consider two types of boundary conditions: velocity and force boundary conditions. A velocity boundary condition, i.e. prescribing the velocity $\mathbf{v}$ at the boundary, amounts to a Dirichlet type of boundary condition. We understand force boundary conditions as prescribing the forces $\mathbf{f}$ the boundary exerts onto the fluid film. The boundary forces are given by the fluid stress projected onto the outward pointing normal vector of the boundary contour. Thus, prescribing the boundary forces amounts to a Neumann type of boundary condition. In section 2.2, we consider a mechanical model of an active viscous crack, where such boundary conditions result from force and torque balance and constitutive equations for fluxes at the crack. This mechanical model yields also boundary conditions in terms of linear combinations of boundary forces and velocities, akin to Robin boundary conditions.

To illustrate how crack boundary conditions shape the flow field, we plot numerical solutions for combinations of Dirichlet and Neumann boundary conditions in Fig. 2.1F-I. To this end, we make use of a staggered grid in terms of $\log r$ and θ (see appendix G for more details). In 2.1F,G, we consider a tissue that is incompressible, but homogenously growing, i.e. $G > 0$, $\eta_b \to \infty$. This implies a flux of tissue through the boundaries. In 2.1F and G, we limit this flux to the crack and the outer boundary, respectively, by imposing $\mathbf{v} = 0$ at the corresponding boundary. These boundary conditions break the symmetry of the otherwise homogeneous system, such that the tissue moves anteriorly (up in Fig. 2.1F) or posteriorly (down in Fig. 2.1G). The crack boundary condition in Fig. 2.1F corresponds to a prototypical text book example from the field of fracture mechanics. As a crack in such a setting is understood as a domain of broken molecular bonds, one considers a model where left and right boundaries of the crack cannot sustain any forces, i.e. $\mathbf{f}_{L/R} := \pm t^{ij}_{L/R}\nu_i = 0$ yielding a Neumann condition for the flow or displacement field. Applied to the epiblast, it corresponds to a scenario, where the breakdown of extracellular matrix and cell-cell adhesions allows for an unconstrained flux of the epiblast tissue into the primitive streak, whereas the boundary to the extra-embryonic tissue acts a rigid constraint. This is similar to previous ideas suggesting that ingression at the primitive streak results from fracture of the underlying extracellular matrix [153]. In Fig. 2.1G, the situation is reversed with the crack acting as a rigid constraint, while the outer-boundary is force-free.

It is instructive to calculate the mechanical work performed at the crack boundaries per time, i.e.

$$j^f_L = +\mathbf{t}^\nu_L \cdot \mathbf{v}_L, \quad j^f_R = -\mathbf{t}^\nu_R \cdot \mathbf{v}_R \tag{2.10}$$

which quantify the flux of free energy from the crack to the fluid film (see also section 1.2.3). In the examples discussed above (Fig. 2.1F,G), the flux of free energy j^f vanishes at the crack as well as all other boundaries. We call such crack boundary conditions, where $j^f_{L/R} \leq 0$, passive, as the crack does not drive the flow, i.e. it does not contribute to the mechanical work that is required to balance dissipation due to viscosity and friction. The flow field in Fig. 2.1F,G is entirely driven by the growth G of the tissue. For $G = 0$, the passive boundary conditions considered there yield a vanishing flow field.

Importantly, the primitive streak is an active material. In particular, the activity of myosin motor molecules has been found to be crucial for the cell movements during primitive streak formation [88, 89]. Hence, the primitive streak may very well perform mechanical work on the epiblast, also at the time point we are considering here. In Fig. 2.1H,I we consider such active crack boundary conditions, where $j^f \geq 0$ at the crack boundaries or the crack tip. Furthermore, we use $G = 0$ and use boundary conditions at the outer boundary such that we have $j^f = 0$ there. Hence, the fluid flow is driven entirely by the crack and the crack tip. In Fig. 2.1H, we consider a constant force-dipole density along the crack ($\mathbf{f}_{L/R} \sim \pm\boldsymbol{\nu}$) that pulls the fluid into the crack, whereas the outer boundary and the crack tip are force-free. The flow field exhibits two counter-rotating vortices on the left and the right side of the crack tip, reminiscent of the so-called polonaise movements in the avian epiblast (see section 1.1.5). At the crack tip, these flows yield an anterior movement of fluid surrounding cracktip relative to the outer boundary. When the cracktip is advected by the fluid flow, this translates into a growth of the crack. In

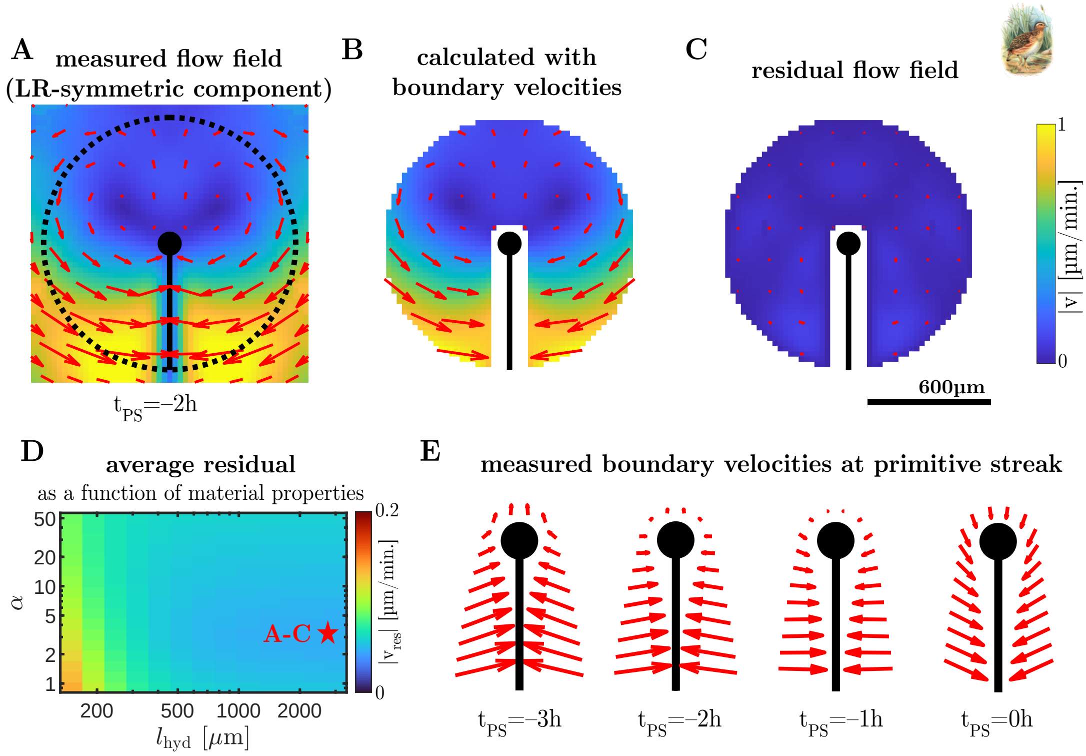

Figure 2.2: Tissue flows during avian gastrulation are captured by a fluid model A: LR-symmetric component of the average flow field of the epiblast of 15 quail embryos 2h before the onset of streak regression (see appendix C and Fig. C.2 therein). **B**: Flow field of a homogeneous fluid film with $l_h \to \infty$ and $\alpha = 3$ calculated with measured boundary velocities, i.e. the velocities at the boundaries of streak and node and at a circle with $R = 600\mu$m (dashed line in **A**). See Fig. C.4 for a plot of the boundary velocities and for other time points. **C**: residual of measured flow field (**A**) after subtracting the flow field in **B**. **D**: Residual as in **C** averaged over the entire colored area in **C** and over time points $-4h < t_{PS} < -1h$ for a range of the material parameters α, l_h. Red star corresponds to the values used in **B**. **E**: Velocities measured at the boundary of the primitive streak measured for different time points up to the onset of streak regression ($t_{PS} = 0$). Experimental data was obtained by Julia Pfanzelter and Adrian Lahola-Chomiak from the lab of Stephan Grill, and then analyzed by me.

section 2.4, we investigate this advective crack growth to understand why the primitive streak elongates. In contrast to crack propagation in a fracturing material, such crack growth is driven by mechanical activity of the crack.

In Fig. 2.1I, we consider an active torque at the crack tip, driving a rotational flow around the crack tip. In contrast to the other examples, this boundary condition and the resulting flow field breaks the left-right symmetry of the fluid film. Importantly, a similar movements of cells around the Hensen's node has been found to underlie left-right symmetry breaking in the avian embryo. In section 5.1, we will investigate this chiral flow further, using a model of an active chiral crack (tip).

2.1.3 Tissue flows during avian gastrulation are driven by the primitive streak

In this chapter, we want to understand the large-scale movements of the avian epiblast prior to left-right symmetry breaking. To this end, we model the primitive streak as a crack in a fluid film. In the following, we validate this model using experimental data from quail embryos. The raw data was obtained by Julia Pfanzelter and Adrian Lahola-Chomiak from the lab of Stephan Grill at the MPI-CBG Dresden, and then analyzed by me (see appendix C for details). Briefly, time-lapse microscopy data from quail embryos developing on a nutritive medium outside the egg were analyzed using particle image velocimetry (PIV, [154]) to infer tissue movements. Data from 15 embryos was aligned in space and time using the Hensen's node as a spatial reference point and the onset of primitive streak regression as a reference time point ($t_{\mathrm{PS}} = 0$). From this data set an average flow field was obtained for different time-points $-5h \leq t_{\mathrm{PS}} \leq 5h$, averaging the flow field around a given time point in a 1h window. Finally, this flow field was decomposed in a left-right symmetric and left-right antisymmetric component (see Fig. C.2). In Fig. 2.2A, the left-right symmetric component two hours before streak regression is shown in a 600 μm window around the Hensen's node.

We use this flow field to validate that the epiblast behaves as a homogeneous fluid film set into motion by the primitive streak and possibly the outer boundary. To this end, we use the measured boundary velocities, i.e. the velocities at a circular boundary with a radius $R = 600\mu$m centered at the Hensens' node and the velocities at the boundary of streak and node. The latter boundary is defined as points with a minimal distance between 100μm and $125\mu m$ to the centers of streak or node (corresponding to black line and circle in Fig. 2.2A. With this velocity boundary condition, we calculate the flow field of an enclosed fluid film for a range of material parameters, i.e. α and l_h, as the velocity field is independent of a constant pressure that results from a constant G for such boundary conditions. To this end, we make use of analytical solutions of the governing equation Eq, see appendix B.1 C.5 for details. With this, we find that the calculated flow field ($\mathbf{v}_{\mathrm{calc}}$) is in very good agreement with the measured flow field ($\mathbf{v}_{\mathrm{meas}}$) at time points $t_{PS} < 0$ for a hydrodynamic length that is larger than the system size (Fig. 2.2B-D), i.e. the modulus of the residual, $|\mathbf{v}_{\mathrm{meas}} - \mathbf{v}_{\mathrm{calc}}| < 0.1\mu$m/min. is smaller than the experimental standard deviation of the set of embryos (Fig. 2.4C,C.4). This validates our model. The epiblast around the Hensen's node indeed behaves as a homogeneous fluid film before left-right symmetry breaking and streak regression.

The large value of l_{h} we infer from the experimental flow field implies that friction forces resulting from mechanical interaction with the vitelline membrane are negligible compared to the viscous forces that result from mechanical interactions within the epiblast (see section 5.1.4 for a discussion of mechanical interactions between the tissue layers). Therefore, we will neglect those friction forces in the remainder this chapter, yielding $l_{\mathrm{h}} \to \infty$. In this regime, the calculated flow field is in good agreement with the measured flow field for any $\alpha > 1$ (Fig. 2.2D), suggesting that tissue growth is largely independent from tissue-internal stresses. In fact div **v** is relatively homogeneous and positive away from the primitive streak before streak regression (Fig. C.3). We find that the residual is minimal for $\alpha \sim 3$ which we use in the following. Notably, this corresponds to the value one obtains for a thin film of an incompressible fluid [155, 156]. Taken together, the epiblast around the Hensen's node behaves as a thin film of an incompressible fluid with negligible substrate friction.

The flow field changes over time, as do the boundary velocities (Fig. 2.2E). For early time points, the node moves anteriorly as the streak elongates. At latter time points this movement comes to halt $t_{PS} = -1h$, followed by streak regression $t_{PS} = 0h$. In this chapter, we want to obtain a mechanical understanding of this transition. This requires a mechanical model of streak and node, which we introduce in the following section.

Importantly, we find that such a model cannot capture streak regression. For $t_{\mathrm{PS}} > 0$, we find that the calculated flow field is no longer in qualitative agreement with the experimentally measured flow field (Fig. C.4. We find that the epiblast anterior to the Hensen's node undergoes a striking shear flow, corresponding to convergent-extension rearrangements of the tissue, that a model of a homogeneous fluid film cannot capture (Fig. C.3). This suggests that streak-regression is at least partially driven by active convergent extension movements at the mid-line anterior to the node. Notably, this line is known to become chemically distinct in terms of the morphogen *Shh* at about this time point, i.e. immediately after left-right symmetry breaking around $t_{\mathrm{PS}} = 0$ [67]. Furthermore, it is the line where a structure called the notochord forms underneath the epiblast at around this time-point, which then induces a folding of the epiblast to form the neural furrow [3]. It is beyond the scope of this thesis to understand the mechanics of notochord and neural furrow formation. Therefore, we will focus on the time points $t_{\mathrm{PS}} < 0$. However, it is worth noting that our approach can detect this mechanical heterogeneity of the epiblast at later time points.

2.2 Hydrodynamic theory of active viscous cracks

2.2.1 Conservation laws

In the following, we set out to write down a physical model of an active viscous crack as a model for the primitive streak, by considering the fluxes of momentum and angular momentum into the crack and within the crack, similarly to section 1.2.2. For an extended version, including the conservation of mass and considering a general parametrisation of a crack in a curved surface, see section A.2 in the appendix.

Due to momentum conservation the net force acting on a line segment of the crack has to vanish, when inertia forces are negligible. We consider mechanical interactions of the crack with the surrounding fluid film and an underlying substrate. Mechanical interactions within the crack are captured by the crack tension $\mathbf{t}_C$. It has units of force and yields the force a line segment is exerting on its anterior neighbor (i.e. the line segmented located in negative $\mathbf{e}_\lambda$ direction with respect to segment of interest). When the tension of two line segments differs, they exert a net force on the line segment in between, which has to be balanced by other forces acting on the this line segment. This balance of forces can be written in terms of a differential equation for $\mathbf{t}_C$

$$\partial_\lambda \mathbf{t}_C = -\mathbf{f}_{\text{sub}} + \mathbf{f}_C, \tag{2.11}$$

where ∂_λ is the derivative with respect to the crack coordinate using an arc-length parametrisation of the crack. $\mathbf{f}_{\text{sub}}$ denotes the force line density the substrate is exerting on the crack, whereas $\mathbf{f}_C$ is the force density the crack exerts onto the surrounding fluid film. $\mathbf{f}_C$ is balanced by the boundary forces resulting from the stress $\mathbf{t}^i$ of the fluid surface, i.e.

$$\mathbf{f}_C = -\left(\mathbf{t}^\theta_R - \mathbf{t}^\theta_L\right), \tag{2.12}$$

where $\mathbf{t}^\theta_{L/R} = \mathbf{t}^i_{L/R}\theta_i$ is the projection of the stress tensor $\mathbf{t}^i$ onto the normalized vector $\boldsymbol{\nu} = \boldsymbol{\theta}$, evaluated at the left and right sides of the crack as defined in Eq. 2.7. This implies that a boundary condition in terms of $\left(\mathbf{t}^\theta_R - \mathbf{t}^\theta_L\right)$, corresponds in fact to the force balance equation Eq. 2.11. At the crack tip, the crack tension $\mathbf{t}_C$ yields a force the crack is exerting on the crack tip. Again, the net force acting on the crack tip has to vanish, yielding

$$\mathbf{F}_{\text{sub}} + \mathbf{t}_C\big|_{\lambda=0} = \mathbf{F}_T, \tag{2.13}$$

where $\mathbf{F}_{\text{sub}}$ denotes the force the substrate is exerting on the crack tip, whereas $\mathbf{F}_T$ is the force the crack tip exerts on the fluid film, defined by contour integral of the fluid stress along the boundary of the crack tip $\mathcal{T}$ In the geometry and parametrisation we consider here (right panel in Fig. 2.1E), with $\mathcal{T}$ corresponding to a circle with radius a centered at the origin, we have

$$\mathbf{F}_T = -a \int_{-\pi}^{\pi} \mathrm{d}\theta \, \mathbf{t}^r(a, \theta), \tag{2.14}$$

where $\mathbf{t}^r$ denotes the contraction of the stress tensor $\mathbf{t}^i$ with the unit vector $\mathbf{r}$.

In particular for understanding left-right symmetry breaking in chapter 5, we need to consider also angular momentum conservation. We capture torque dipoles within the crack with the crack moment $\mathbf{m}_C$ which has units of a torque. In general $\mathbf{m}_C$ is a three-dimensional vector. However, we consider here a crack in a flat surface to understand forces and movements within this plane. To this end, it is sufficient to consider the normal component of $\mathbf{m}_C$ which we denote as m_C to simplify the notation (see Eq. A.16 for torque balance in a curved crack in a curved surface). The balance of torques acting on a line segment of the crack then yields:

$$\partial_\lambda m_C = -\tau_{\text{sub}} + \tau_C - \mathbf{t}_{\mathcal{C}} \cdot \boldsymbol{\theta}, \tag{2.15}$$

where τ_{sub} denotes the torque line density the substrate is exerting on the crack, whereas τ_C is the torque density the crack is exerting on the fluid film. Similarly to Eq. 1.27, we find that crack stresses normal to the crack correspond to a torque density that is constrained by torque balance. When omitting, normal surface moments, the τ_C balances a torque resulting from the fluid stress, i.e.

$$\tau_C = d\left(\mathbf{t}_R^\theta + \mathbf{t}_L^\theta\right) \cdot \mathbf{r}, \tag{2.16}$$

where d is the width of the crack in the plane. For any real crack $d > 0$ such that a dipole of forces that are parallel to the crack yields a torque. Finally, torque balance at the crack tip reads

$$T_{\text{sub}} + m_C\big|_{\lambda=0} = T_T, \tag{2.17}$$

where T_{sub} is the torque the substrate exerts on the crack tip and the torque T_T the crack tip exerts on the surface. For the crack tip geometry we are using here, the torque is given by

$$T_T = -a^2 \int_{-\pi}^{\pi} \mathrm{d}\theta\, \mathbf{t}^r(a,\theta) \cdot \boldsymbol{\theta}. \tag{2.18}$$

In chapter 5, these expressions will be crucial. In this chapter, however, we consider a left-right symmetric crack and fluid film, implying $t^{r\theta}(\theta) = -t^{r\theta}(-\theta)$ and hence $\tau_C = 0 = T_T$.

2.2.2 Constitutive equations for a left-right symmetric crack

In the field of fracture mechanics, a crack model is usually defined by a crack boundary condition. Here, we consider a physical model of the crack, i.e. constitutive equations for the fluxes within the crack, which then yield boundary conditions by making use of force and torque balance equation. Since we consider here a straight left-right symmetric achiral crack, the flux of angular momentum m_C and the normal crack stress $\mathbf{t_C} \cdot \boldsymbol{\theta}$ vanish. For the crack tension along the crack $t_C^r = \mathbf{t}_C \cdot \mathbf{r}$, we consider the following form

$$t_C^r = \eta_C \partial_r v_C + t_C^{\text{act}}, \tag{2.19}$$

where $\eta_C > 0$ denotes a one-dimensional viscosity of the crack material, with v_C being the (radial) velocity of the crack material (see illustration in Fig. 2.3A). For simplicity, we use $v_C = (v_L^r + v_R^r)/2$ in the following. Due to left-right symmetry, this is equivalent to $v_C = v_L^r = v_R^r$. t_C^{act} is an active line tension, which may be related to the concentration of a stress regulator in the spirit of section 1.2.6.

Since friction with a substrate appears negligible in the epiblast, we omit here such substrate interactions also at the crack and crack tip, i.e. $\mathbf{f}_{\text{sub}} = 0 = \mathbf{F}_{\text{sub}}$. Force balance then yields the following equation

$$\eta_C \partial_r^2 v_C + \partial_r t_C^{\text{act}} = -t_R^{\theta r} + t_L^{\theta r} \tag{2.20}$$

Together with $v_C = v_{L/R}^r$, this represents a non-standard boundary condition involving a deriva-

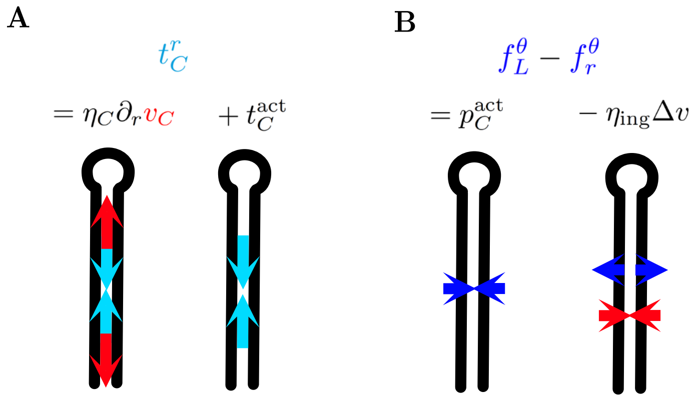
A
t_C^r
$= \eta_C \partial_r v_C$
$+ t_C^{\mathrm{act}}$
B
$f_L^\theta - f_r^\theta$
$= p_C^{\mathrm{act}}$
$- \eta_{\mathrm{ing}} \Delta v$

Figure 2.3: Mechanical model of active viscous crack. Illustration of the active viscous crack model discussed in the main text. $f^\theta_{L/R}$ denote the forces the left (L) and right (R) sides of the crack exert on the surrounding fluid film.

tive of $\mathbf{v}$ along the contour of the boundary when $\eta_C \neq 0$. However, this boundary condition is not sufficient to uniquely define a left-right symmetric flow field, since it does not yield conditions for $v^\theta_{L/R}$ or $t^{\theta\theta}_{L/R}$. We understand this necessary condition as a constitutive equation for the force dipole $d(t_R^{\theta\theta} + t_L^{\theta\theta})$ with which the crack is pulling at the fluid film:

$$d(t_R^{\theta\theta} + t_L^{\theta\theta}) = p_C^{\mathrm{act}} - \eta_{\mathrm{ing}} \Delta v, \tag{2.21}$$

where p_C^{act} is an active force dipole that may result from myosin cables in the primitive streak, and $\Delta v := v_L^\theta - v_R^\theta$ is the flux into the crack (see illustration in Fig. 2.3). η_{ing} has units of a two-dimensional viscosity. Where understand it as an effective viscosity of a cross-section of the primitive streak that quantifies dissipation associated with the process of ingression.

At the crack tip, force balance yields

$$\mathbf{F}_T = (t_C^r \mathbf{e}_\lambda)\big|_{\lambda=0}, \tag{2.22}$$

where $\mathbf{e}_\lambda = \mathbf{r}(\theta = \pm\pi)$. Furthermore, we have T_T due to left-right symmetry. For a finite sized crack tip, one needs to consider also higher order force multipoles. In general, such force multipoles imply a divergence of the flow field at the crack tip, implying strong deformations of the crack tip. We do not find such a divergence at the Hensen's node, when considering the left-right symmetric component of the flow field. Therefore, we consider an effectively rigid crack tip, that can move and rotate but not deform, implying

$$\mathbf{v}(r = a, \theta) = \mathbf{V}_T + a\Omega_T \boldsymbol{\theta}, \tag{2.23}$$

where we define the velocity $\mathbf{V}_T$ and the angular velocity Ω_T of the crack tip as

$$\mathbf{V}_T = \frac{1}{2\pi} \int_{-\pi}^{\pi} \mathrm{d}\theta \, \mathbf{v}(r = a, \theta), \quad \Omega_T = \frac{1}{2\pi a} \int_{-\pi}^{\pi} \mathrm{d}\theta \, \mathbf{v}(r = a, \theta) \cdot \boldsymbol{\theta}, \tag{2.24}$$

where $\Omega_T = 0$ in this chapter due to left-right symmetry.

Together with a Dirichlet or Neumann boundary condition at $r = R$, Eq. 2.20-2.23 are sufficient to define a unique flow field of the fluid film (up to a rigid body translation in the case of Neumann boundary conditions due to the Galilei invariance of the model). They allow us to map the boundary conditions used in in Fig. 2.1F-H to material properties of the primitive streak. A force-free crack, as in Fig. 2.1F, corresponds to the limit

$$\frac{\eta_C}{\eta R} \to 0, \quad \frac{t_C^{\mathrm{act}}}{\eta G R} \to 0, \quad \frac{\eta_{\mathrm{ing}}}{\eta}\frac{R}{d} \to 0, \quad \frac{p_C^{\mathrm{act}}}{\eta G d} \to 0, \tag{2.25}$$

where viscous and active stresses of the crack are negligible compared to the viscous stresses of the fluid film. A rigid crack, as in Fig. 2.1G, corresponds to the limit of infinite crack viscosities, i.e.

$$\frac{\eta_C}{\eta R} \to \infty, \quad \frac{t_C^{\mathrm{act}}}{\eta_C G} \to 0, \quad \frac{\eta_{\mathrm{ing}}}{\eta}\frac{R}{d} \to \infty, \quad \frac{p_C^{\mathrm{act}}}{\eta_{\mathrm{ing}} G R} \to 0. \tag{2.26}$$

In contrast, a crack that is no longer a crack, i.e. it yields a fluid film as if there was no crack, would be given by

$$\frac{\eta_C}{\eta R} \to 0, \quad \frac{t_C^{\mathrm{act}}}{\eta G R} \to 0, \quad \frac{\eta_{\mathrm{ing}}}{\eta}\frac{R}{d} \to \infty, \quad \frac{p_C^{\mathrm{act}}}{\eta_{\mathrm{ing}} G R} \to 0, \tag{2.27}$$

where η_C vanishes but η_{ing} not.

Finally, the active crack considered in Fig. 2.1H is given by

$$\frac{\eta_C}{\eta R} \to 0, \quad \frac{t_C^{\mathrm{act}}}{\eta G R} \to 0, \quad \frac{\eta_{\mathrm{ing}}}{\eta}\frac{R}{d} \to 0, \quad \frac{p_C^{\mathrm{act}}}{\eta G d} \to \infty. \tag{2.28}$$

In general, we consider a crack to be mechanically active, when the active line tension t_C^{act} or the active force dipole p_C^{act} are not negligible.

While the constitutive equations considered so far are sufficient to define the flow field, they do not contain any information about growth and deformations of the crack in time. Due to left-right symmetry, we consider here only the growth of the crack along its axis, and not deformations of the crack away from the mid line. When keeping the outer boundary fixed, crack growth (and shrinkage) corresponds to a motion of the crack tip $\mathbf{e}_\lambda \cdot \partial_t \mathbf{Y}(0) < 0$ ($\mathbf{e}_\lambda \cdot \partial_t \mathbf{Y}(0) < 0$). We consider advection of the crack tip as well as flow-field independent crack growth, quantified by the velocity G_{act}:

$$\partial_t \mathbf{Y}(0) = \mathbf{V}_T - G_{\mathrm{act}} \mathbf{e}_\lambda \tag{2.29}$$

$G_{\mathrm{act}} d$ corresponds to a rate with which material of the fluid film becomes crack material in terms of a chemical transition that is independent of the flow field. As such, it may represent chemical but not mechanical activity of the crack. Crack growth in a fracturing elastic material may be understood as a stress-dependent G_{act} that quantifies the rate of plastic deformations and breakdown of molecular bonds in response to the stresses that act on the crack tip.

2.3 The primitive streak as a branch cut

In the previous section, we have introduced a theoretical framework for a mechanical understanding of the primitive streak as an active crack, i.e. a one-dimensional active material embedded in an otherwise continous surface material. This framework allows to understand boundary velocities and forces at the crack in terms of mechanical interactions within the crack material. Such boundary conditions, however, are already a property of a model. The true physical observable is the flow field away from the boundary condition in the model. In section 2.1.3, we have established that experimental flow field of quail embryos is consistent with a model of a crack embedded in a homogeneous fluid film with infinite hydrodynamic length. While the method we used allows to test, if there are some crack boundary conditions that yield the observed flow field, it does not yield a robust estimate of these boundary conditions, as the fitting functions are ill-behaved close to the crack. In the following, we will make use of holomorphic functions to understand in analytical terms how the flow field around a crack is controlled by crack boundary conditions. In particular, we write the flow field as an analytical expansion, with the first terms dominating away from the boundaries. Truncating this expansion allows to infer an effective crack model of the primitive streak from the measured flow field.

2.3.1 Solving crack boundary conditions with holomorphic functions

The equation (Eq.B.13) that governs the flow field of a flat homogeneous fluid film in the absence of friction is mathematically equivalent to the equation that governs displacement fields of an elastic sheet with the function F known as the Airy stress function. In the field of elasticity, it has long been known that this equation can be solved using harmonic or equivalently holomorphic functions [157], which we introduced in section 1.3.3. This can be seen for example by making use of the Newman Penrose formalism (see section 1.3.1) and Wirtinger calculus (see section 1.3.2). As we show in the appendix in section B.2, the flow field and the resulting stress field can be written in terms of two holomorphic functions $f$and g (see Eq. B.15-B.17). Solving boundary conditions amounts to finding appropriate functions that are holomorphic in the enclosed domain. When the domain is a circle (without a crack), f and g are given by Taylor expansions (Eq. 1.79). The power m in this expansion translates into a power-law exponent of the r dependence and an frequency of the θ dependence of flow and stress fields (see Eq. B.18,B.26,B.27). Thus, the Taylor coefficients of $f$and g correspond to Fourier components of the boundary condition (see also Eq. 1.81). As higher modes decay with faster (i.e. with a greater power-law exponent) inside the circle, this allows for a robust calculation of the flow field from measured boundary velocities. In Fig. 2.4, we use this to determine $f$and g from the measured flow field interpolated along a circle with radius 600μm. We find that the calculated flow field does not agree even qualitatively with the measured flow field (Fig. 2.2A). Thus, as expected, the primitive streak does not behave like a homogeneous fluid film.

In order to incorporate a crack, one can augment the Taylor (or Laurent) expansion with non-integer power laws, i.e. $f, g \sim z^m$ with $m \in M \not\subset \mathbb{Z}$ [158, 159, 160]. For a passive crack ($t_C^{\mathrm{act}} = 0 = p_C^{\mathrm{act}}$), the crack viscosities $\eta_{\mathrm{ing}}, \eta_C$ together with the viscosities $\eta, \alpha\eta$ of the fluid film define a set of power-laws M that solves the crack boundary conditions, as we discuss in appendix B.2.2. This allows to capture the flow and stress field on length scales r with $a \ll r \ll R$ in terms of a few analytic functions. The amplitudes of these modes result from the boundary conditions at $r = R$. In the field of fracture mechanics, one usually finds a divergence of the stress at the crack tip scaling as $1/\sqrt{r}$. The amplitude of this divergence is known as the stress intensity factor and corresponds to the external load that drives the fracture of the material. The function that translates the external load, i.e. the boudary forces at $r = R$ into the stress intensity factor depends on the geometry of the system, the material properties of the sheet, as well as the specific crack boundary conditions. In order to understand crack propogation, the stress intensity factor is the key aspect of the stress field one needs to consider [161, 158, 162, 163]. While the powerlaw exponent of 1/2 may be modified by certain crack condition, the principle of a divergence of stresses quantified by a well defined stress intensity factor appears robust [159, 162, 164]

In the quail embryo, no such divergence of stresses at the node is evident, when considering the symmetric component of the flow field (Fig. B.2). That the usual ansatz from fracture mechanics does not apply to the primitive streak is not surprising for two reasons: Firstly, the system does not exhibit such a clear separation of length scales. The size of the node ($a \sim 100\mu$m) is only one order of magnitude smaller than the size of the system which is on the order of millimeters. Thus there is no regime where $a \ll r \ll R$ with $R \sim 1$mm. Secondly, the primitive streak is mechanically active and potentially patterned. The pattern of mechanical activity determines the flow field. However, we do not know this pattern, neither the mechano-chemical processes that define it.

Therefore, we will use an agnostic approach (see appendix B.2), using an expansion of the flow field that is valid away from the boundaries for any power-law or any other form of flow field around a crack. Specifically, we consider an expansion of f, g in terms of the complex logarithm $\log z = \log r/R_0 + i\theta$, i.e.

$$f = \sum_{n=0}^{\infty} \tilde{f}_n (\log z)^n \quad g = \sum_{n=0}^{\infty} \tilde{g}_n (\log z)^n, \tag{2.30}$$

where $\tilde{f}_n, \tilde{g}_n$ are complex numbers that are given by the boundary conditions and define the flow field. The crack is identified as the branch cut of the complex logarithm. In the usual convention, the branch cut is the negative real axis. We use this convention also here, as we consider a straight crack. We note, however, that this expansion can also be used for curved cracks as long as $\mathbf{r} \cdot \partial_\lambda \mathbf{Y} > 0$ (see section 1.3.3).

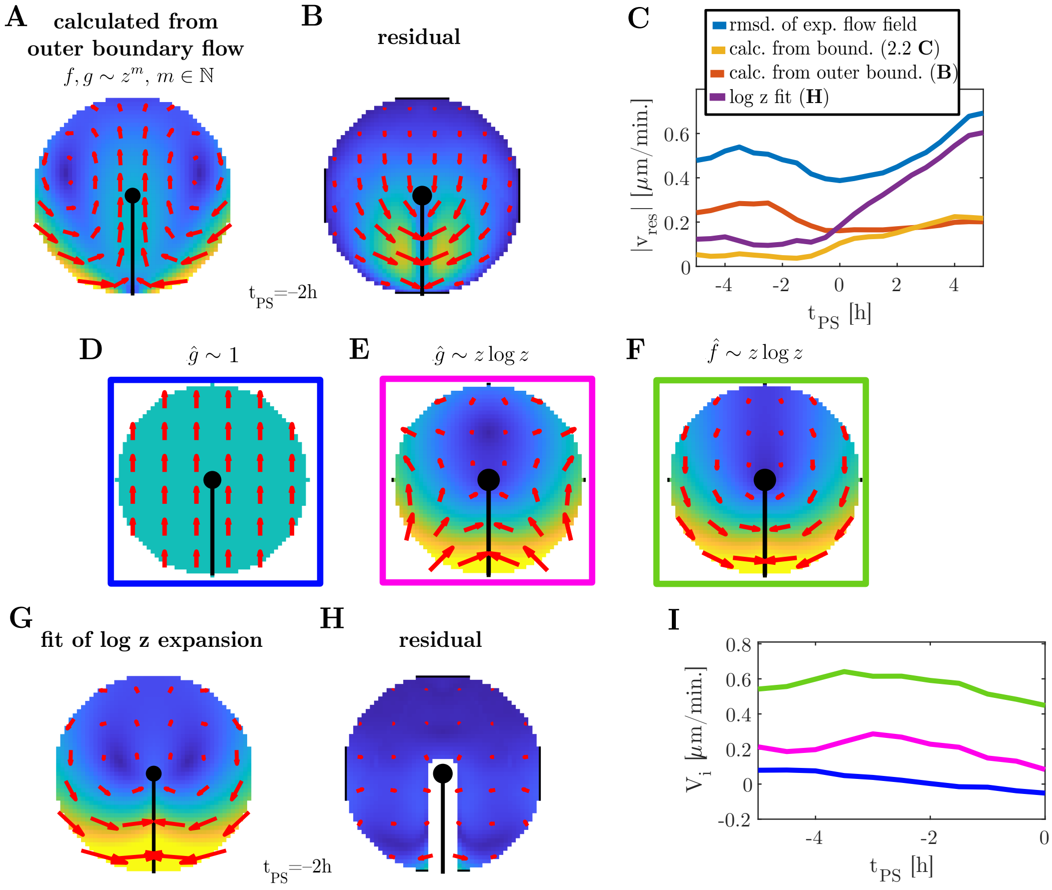

Figure 2.4: Capturing experimental flow fields with holomorphic functions. **A**: Flow field calculated from measured boundary velocities at $r = R$, corresponding to a scenario where epiblast as well as the streak behave as a homogeneous fluid film. We used $l_h \to \infty$, where the flow field can be understood in terms of the holomorphic functions f, g for which we use here Taylor expansions up to order 50. **B**: Residual of measured flow field after subtracting the flow field in **A**. **C**: Spatial average of residuals over the circle with $R = 600\mu$m excluding streak and node. Blue: Residual of measured flow field after subtracting the average velocity. Yellow correspond to the residual in Fig. 2.2C, whereas red and violet correspond to **B** and **G** of this figure. **D**-**F** flow fields corresponding to the coefficients V, A, and B, in that order, in Eq. 2.31. Flow fields were normalized such that they all have the same average modulus. **G**: Fit to measured flow field (excluding streak and node) at $t_{PS} = -2h$ using Eq. 2.31. **H**: Residual of the measured flow field after subtracting the flow field in **G**. **I**: coefficients of fits as in **G** over time. Blue, pink and green correspond to the normalized flow components in **D**, **E** and **F**, respectively.

2.3.2 Deciphering the forces driving primitive streak elongation and ingression with the complex logarithm

In the following, we make use of expansion of the flow field in terms of the complex logarithm to infer an effective mechanical model of the primitive streak. Using Eq. 2.30, we find that the flow field of a fluid film around a left-right symmetric crack away from the boundaries (i.e. $|\log r/R_0| < 1$ using $a < R_0 < R$) can be written as

$${}_{(1)}v = V_0 - A\bar{z}(\log \bar{z}) + Bz\left[(2+\alpha)(\log z) - \alpha\left(\log \bar{z} + 1\right)\right] + {}_{(1)}v_{\mathrm{cont}} + \mathcal{O}(r|\log r/R_0 + i\theta|^2), \quad (2.31)$$

where ${}_{(1)}v = v_y - iv_x$ is the flow field with y corresponding to the axis of the primitive streak (see appendix B.2.3 and C.6). We use here the notation of spin-weighted fields we introduced in section 1.3.1. ${}_{(1)}v_{\mathrm{cont}}$ is a continuous component of the flow field scaling linearly with r representing a global shear and expansion of the epiblast. For simplicity, we omit ${}_{(1)}v_{\mathrm{cont}}$ in the following. V_0, A, B are real coefficients corresponding to different components of the flow field. V_0 corresponds to a rigid body translation (Fig. 2.4D). A corresponds to a harmonic flow field with vanishing divergence and vorticity that is discontinous at the crack (Fig. 2.4E). B corresponds to a non-harmonic flow field that is dominated by a term of the form $v_\theta \sim r\theta$ (Fig. 2.4F). We want to capture the experimental flow field in terms of these three coefficients to obtain an analytical representation of the flow field.

To this end, we determine the coefficients as a fit to the flow field away from the streak and the node. We find that the fit captures the flow field well for $t_{PS} < 0$, meaning that we can capture the experimental flow field with only three fitting parameters (Fig. 2.4C,G,H). Notably, the fit is dominated by the non-harmonic component, i.e. the term proportional to B plotted in Fig. 2.4F, at all times $t_{PS} < 0$. Strikingly, we find that the fit fails for $t_{PS} > 0$, i.e. the mean residual is considerably greater than the experimental uncertainty of about 0.1μm/min. and even approaches the average modulus of the flow field when subtracting the rigid body component (Fig. 2.4C). This provides further evidence, that the epiblast does not behave as a homogeneous fluid film during streak regression (i.e. $t_{PS} > 0$).

The fit provides an analytical representation of the tissue during avian gastrulation (Eq. 2.31) that coincides with the experimental flow field away from streak and node up to experimental uncertainty. Importantly, this expression fulfills Eq. B.13 up to $\theta = \pm\pi$ and is well behaved there, meaning that it does neither diverge nor contain oscillatory patterns that are absent in the experimental data (Fig. 2.4G). Thus, evaluating Eq. 2.31 at $\theta = \pm\pi$ allows to understand the experimental flow field in terms of effective crack boundary conditions. Evaluating Eq. 2.31 at $r = a$ with $a = 100\mu$m, yields boundary conditions at the cracktip corresponding to the Hensen's node. In particular, it yields the crack tip velocity V_T (Eq. 2.24) and the crack tip force F_T (Eq. 2.14) the node is exerting on the epiblast. The hydrodynamic theory we presented in the previous section then allows to map such boundary conditions to an effective mechanical model of the primitive streak as an active viscous crack. With this, we want to understand what drives and stops the elongation of the streak. Note that in the following, we focus on time points before the onset of streak regression ($t_{PS} \leq 0$), since the model of a crack in a homogeneous fluid film does not apply to later time points ($t_{PS} > 0$).

In Fig 2.5A, we plot the boundary velocities on the left (L) side of the crack parallel to the crack ($v^{\theta}_{L} = -v^{\theta}_{R}$). v^{θ}_{L} is positive along the crack at all times reflecting the flux of the epiblast into the primitive streak. Over time v^{θ}_{L} and thus the flux of material into the crack decreases. We define the total flux J as the integrated flux through the boundaries of the crack and the crack tip (Eq. C.9). From the experimental data, a corresponding value can be calculated from the integrated divergence of the flow field (Fig. C.3) inside the area of streak and node. We find that the experimental value agrees well with the flux J calculated from the crack model, which validates the crack model (Fig. 2.5C). We understand this inward flux of material in the plane of the epiblast to be balanced by an outward flux out of the plane, in particular due to cells detaching from the epiblast to form the lower germ layers, a process called ingression. We find that this flux decreases over time, also at latter time points $t_{PS} > 0$. In other words, ingression slows down and eventually comes to a halt, as the streak stops to elongate and regresses.

Importantly, the crack model allows to understand this process in terms of the forces the streak is exerting on the epiblast. We find that the streak pulls the material inside, i.e. $f^{\theta}_{L} = -f^{\theta}_{R} < 0$ at all times $t_{PS} < 0$ (Fig. 2.5B). In our crack model (section 2.2.2), this implies a non-negligible mechanical activity, in terms of $p_C > 0$. Thus, the primitive streak is not just a special type of tissue that locally allows the growing tissue to leave the plane in response to in plane stresses, like the force-free crack we considered in Fig. 2.1F. Instead the primitive streak is a mechanically active crack that pulls the surrounding tissue towards it. This is consistent with previous studies that understood the primitive streak to form from a patch of active stresses resulting from actomyosin cables [88, 89, 55, 54, 165]. Over time, the pulling force decreases as the flux does, suggesting that ingression slows down because the streak pulls less strongly on the epiblast.

At the same time, the streak in our field of view is moving upwards ($-v_r > 0$, Fig. 2.5D), as the streak as a whole is elongating. We note that the epiblast at the streak close to the node ($r = 100\mu$m) is moving slower than at posterior segments of the streak. This corresponds to a contractile flow along the streak. We determine also the boundary forces parallel to the streak and use force balance (Eq. 2.11, 2.13) to obtain the line tension t^{r}_{C} of the streak in a regime of negligible substrate interactions (Fig. 2.5E). We find that for early time points ($t_{PS} \leq -2h$), the line tension is positive $t^{r}_{C} < 0$, i.e. the streak as a line is contracting. Together with the contractile flow ($\partial_r v_r < 0$), this implies $t^{\mathrm{act}}_{C} > 0$ in our crack model, i.e. mechanical activity in the streak drives the contraction. At latter time points t^{r}_{C} vanishes and even becomes negative at $t_{PS} = -1h$, while the gradient $-\partial_r v_r$ corresponding to the contraction decreases but never vanishes such that we may attribute the negative line tension to the line viscosity η_C. Taken

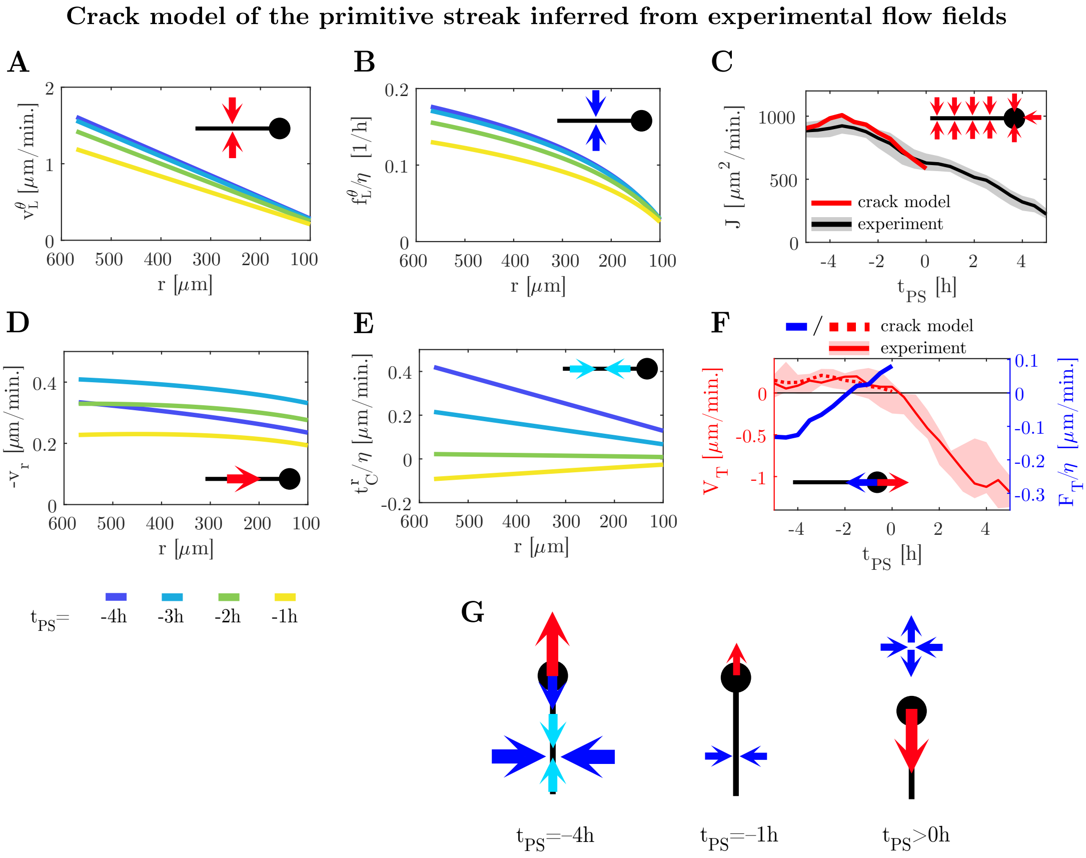

Figure 2.5: **A**,**B**,**D**,**E**: Crack boundary conditions obtained from fit in Fig. 2.4G to left-right symmetric component measured flow fields, modelling the streak in the epiblast as a crack in a fluid film. Colors correspond to different time points (t_{PS}) with respect to streak regression. r corresponds to the distance from the node along the streak. **A**,**D**: boundary velocities on the left side of the crack $v_L^\theta = -v_R^\theta$, $v_L^r = v_R^r = v_r$. **B** boundary force density $f_L^\theta = -f_R^\theta$ with which the crack pulls the fluid film inside, relative to viscosity η of the fluid film. **E** Line tension t_C^r of the crack obtained from boundary force density f^r and the crack tip force F_T in **F** using Eq. 2.11,2.13. **C**: Total flux into streak and node. Red line corresponds to J as defined in Eq. C.9 using the crack boundary velocities inferred from the measured data. Black line corresponds to integrated divergence of measured flow field (Fig. C.3) over area of streak and node with shaded area representing the $[5\%, 95\%]$ confidence interval from bootstrapping (see section C.3). **F**: Velocity (red, left y-axis) of the crack tip, i.e. the node, and force (blue, right y axis) the crack tip exerts on the fluid film, in the direction parallel to the streak axis pointing away from the streak. Thus, blue vector in schematic represents the negative value of F_T for early time points. Solid blue line and dashed red line represent crack model using Eq. 2.24,2.14. Solid red is the median time derivative of manually determined node positions, and shaded area is the corresponding confidence interval from bootstrapping. **G**: Schematic of node velocity (red arrows), (boundary) forces (blue arrows) and line tension (light blue arrows), that drive flows during streak elongation ($t_{PS} = -4h$), when elongation comes to a halt ($t_{PS} = -1h$), and during streak regression ($t_{PS} > 0$) where the measured flow field suggests the presence of active stresses above (i.e. anterior to) the node. For detailed interpretation, see main text.

together, we infer that mechanical activity of the streak gives rise to an active line tension t_C^{act} that decreases over time as does the active horizontal pulling force p_C^{act}.

For time points $t_{PS} < 0$ the streak elongates as the Hensen's node moves upwards. As we discussed in section 2.2.2, such a growth of an active viscous crack can have two contributions (Eq. 2.29): First, a movement of the crack tip material as it is advected by the surrounding fluid. Second, a flow-independent type of growth where fluid film material becomes crack tip material in terms of a chemical transition. As we track the position of the node manually, we can compare the time derivative of this position, with the crack tip velocity V_T (Eq. 2.24) that we calculate from the fitted flow field (solid and dashed lines in Fig. 2.5F, respectively). We find that these two velocities agree well, implying that the streak grows because the node moves upwards (i.e. anteriorly) with the epiblast.

We also calculate the force $\mathbf{F}_T$ (Eq. 2.14) that the node exerts on the epiblast, which we used also to calculate the line tension t_C^r. Strikingly, $\mathbf{F}_T$ points towards the streak ($F_T < 0$ in Fig. 2.5F), i.e. the node is pulling the epiblast downward while the node and the epiblast in its immediate surrounding is moving upward. This force is balanced by a force from the epiblast resulting from viscous stresses, meaning the epiblast pulls the node upward. As the node comes to a halt, this force decreases and ultimately switches sign such that node pushes the epiblast upwards. The change in the force F_T directly corresponds to change in line tension t_C^r of the streak directly posterior to node. Notably, the change in t_C^r is consistent across the streak. At early time points ($t_{PS} < -2h$), t_C^r is maximal at $r = R = 600\mu$m and decreases monotonously from there up to a positive value at the node, such that the streak is pulling the epiblast downward along the entire streak and at the node. Just before streak regression ($t_{PS} = -1h$), t_C^r is minimal at $r = R$ and increases monotonously from there up to a negative value at the node, such that the streak is pushing the epiblast upward along the entire streak. We note, though, that the pushing forces at late times are almost an order of magnitude smaller than the pulling forces at early times. Taken together, the streak elongates against an active line tension of the streak as viscous forces from the epiblast pull the node and the anterior part of the streak anteriorly.

Using our crack model, we inferred that the viscous pulling force vanishes as the mechanical activity of the streak decreases, both in terms of t_C^{act} and p_C^{act}. This suggests that elongation of the streak as well as ingression slows down, because the overall mechanical activity of the streak decreases, possibly due to a reduction in myosin activity (Fig. 2.5G). Subsequently active convergent extension movements in the epiblast anterior to the streak result in streak regression, as we inferred from the flow field of the epiblast in section 2.1.3.

As the active line tension t_C^{act} drives a contraction of the streak, we hypothesise that the active force dipole p_C^{act} with which the streak pulls the epiblast inside is responsible for the elongation of the streak. In the next section, we study how viscosity links the actively driven flux into such an active viscous crack with the (advective) growth of the crack.

2.4 Advective crack propagation

In a fracturing elastic material, crack propagation is typically driven by an external load that yields diverging stresses at the crack tip resulting in plastic deformations and rupture of the material. Here, we consider instead an active crack in a fluid film that drives flows which advect the crack including the crack tips. In general, we define the growth of such a crack as a change in length of the crack. The rate of growth $\partial_t L$ is given by an integral of the deformation rates $\partial_t \mathbf{Y}(\lambda)$ along the entire length of crack, which depend on the flow field at the crack boundaries. As such, crack growth is a global phenomenon that depends on the flow field along the entire crack, not just the flow and stress fields at the crack tips. However, we consider here a straight crack (i.e. $\boldsymbol{\nu} \cdot \partial_\lambda \mathbf{Y} = \mathbf{0}$). In this case, the growth rate is given by a change of the crack tip positions relative to each other, i.e.

$$\partial_t L = \hat{\mathbf{e}}_\lambda \cdot \partial_t (\mathbf{Y}(L) - \mathbf{Y}(0)). \tag{2.32}$$

We note a deformation $\partial_t \mathbf{Y}$ may result not just from advection, but also processes that transform fluid film material into crack material independently from the flow field (see Eq. 2.29). However, we will not consider such flow-field independent contributions to crack growth in the following. Instead we focus on crack growth resulting from the movement of crack tips advected by fluid film, a phenomenon we call advective crack propagation.

As a generic example, let us consider a straight active crack that is mechanically homogeneous (i.e. $t_C^r = t_C^{\text{act}} = \text{const.}$ with $\mathbf{r} = \mathbf{e}_\lambda$) and that drives a constant flux $\Delta v = j_{\text{act}} = \text{const.}$ into the crack, corresponding to parameter regime with $\eta_{\text{ing}}/\eta \to \infty$ with $p_C^{\text{act}}/\eta_{\text{ing}} = j_{\text{act}} > 0$. Solving such crack boundary conditions in appendix B.3, we find that the flow field diverges logarithmically at the crack tip yielding a crack tip velocity $V_T = -\mathbf{e}_\lambda \cdot \mathbf{V}_T$ given by

$$V_T = V_{\text{act}} \log \frac{R}{a} + \mathcal{O}(1) \tag{2.33}$$

with

$$V_{\text{act}} = \frac{1}{2\pi(\alpha + 1)} \left(j_{\text{act}} - \frac{2 + \alpha}{2\eta} t_C^{\text{act}} \right). \tag{2.34}$$

Importantly, V_{act} is independent from boundary conditions at a circle with radius R that encloses the crack tip we consider here. For $R/a \gg 1$, V_{act} dominates over any other contributions to the crack tip velocity V_T that result from the boundary conditions at $r = R$, as well as crack boundary conditions at $r/a \gg 1$. In this regime, we can understand crack propagation purely in terms of the active flux j_{act} and the active line tension t_C^{act} at the crack tips. As expected a line tension $t_C^{\text{act}} > 0$ drives a contraction of the crack (i.e. $V_T < 0$). Importantly, we observe that shear viscosity yields also a growth of the crack (i.e. $V_T > 0$) that results from the flux j_{act}

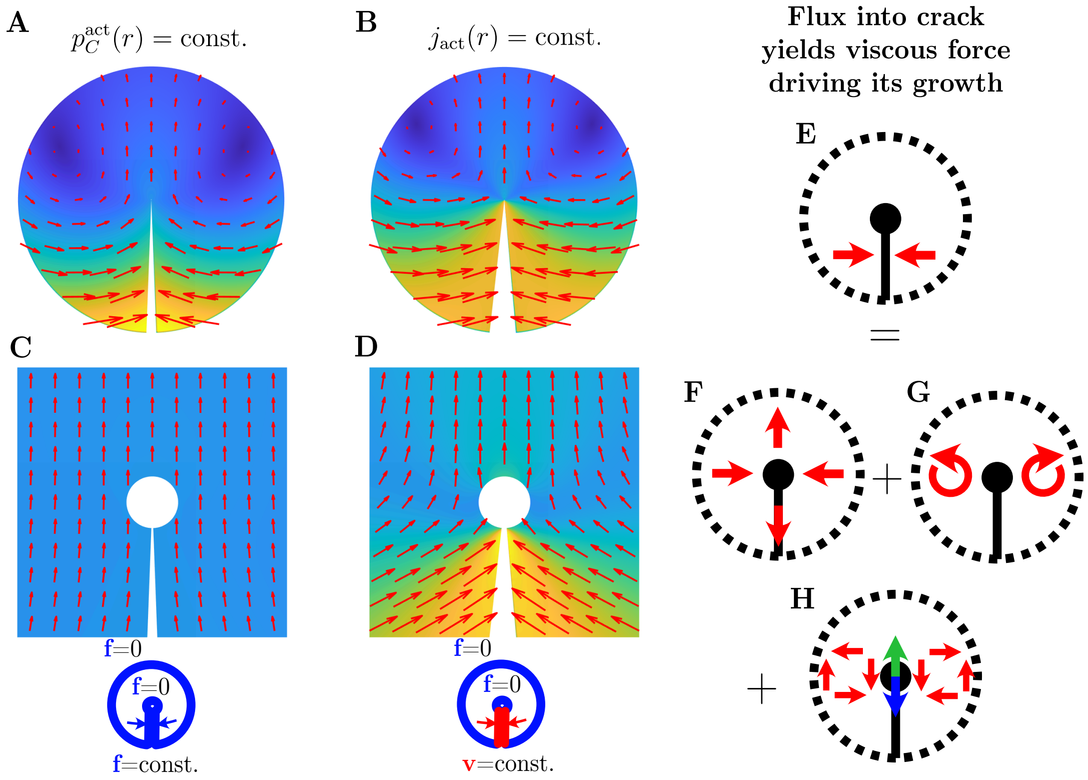

Figure 2.6: Flux into active viscous crack yields crack propagation by advection of the cracktip. **A,B** numerical solutions of the flow field of a fluid film with $l_h \to \infty$, $\alpha = 3$ to boundary conditions given in table J.2, using a staggered grid. In **A**, the crack exerts a constant force dipole p_C^{act} on the fluid film, whereas in **B** it drives a constant flux j_{act} into the crack. **C,D**: Close-ups of the flow field around the crack tip (white circular area) for the numerical solutions in **A,B** respectively. **E-H**: Schematics for understanding the upward movement of the crack tip resulting from a flux into the crack (**E**) in terms of a net movement (**F**), a rotation (**G**) and a shear (**H**) of patches next to the crack tip, as explained in the main text. Red arrows illustrate the flow field, whereas the green arrow denotes force the fluid film exerts on the crack tip due to shear viscosity which is balanced by a force (blue arrow) that the crack tip exerts on the fluid film.

into the crack. Thus, an actively driven flux into a crack can drive growth of the crack against a non-vanishing line tension, as we observed for the primitive streak in the previous section.

In Fig. 2.6A,B, we plot numerical solutions of the full velocity field for a constant flux j_{act} (B) and for a constant force dipole p_C^{act} (A) and a vanishing line tension t_C^r, using force-free boundary conditions at $r = R$. In both cases, we observe counter-rotating vortices on the two sides of the crack tip akin to the so called polonaise movements in the avian epiblast. These flows involve an upward movement of the fluid film around the crack tip and the crack relative to the boundary at $r = R$. Close to the crack tip, the flow fields differ qualitatively (Fig. 2.6C,D). For a constant force dipole, the flow field around the crack tip is given by a rigid body translation, as all other flow components vanish close to the crack tip. A constant flux, in contrast, implies a non-vanishing flux into the crack next to the crack tip and, thereby, a non-constant velocity. We note that the upward component of the flow increases towards the crack tip consistent with analytical calculations. Thus, a constant flux j_{act} yields an upward movement of the crack tip relative to the crack, whereas for a constant force dipole p_C^{act}, crack tip and crack move upwards as a whole.

For the streak, we expect the flux into the streak to saturate away from the node, such that we may understand the flow into the epiblast in terms of a constant flux into the streak on the scale of the embryo. As we have shown here, this implies a movement of the epiblast around the node relative to the remainder of the epiblast, when the line tension of the streak is not sufficient to result in a contraction. Based on these calculations, we predict that the elongation of the streak is directly related to the flux into the streak and is fairly independent of the geometry of the epiblast boundary, which may be tested in future experiments.

So far, we have understood the movement of crack and crack tip that results from a flux into the crack in terms of numerical and analytically calculations. However, we find that it can also be understood in more intuitive terms: Consider two small patches of the fluid film on the left and the right side of the crack tip. The flow in such a small patch may be understood in terms of a translation, a rotation and a shear of the patch, as illustrated in Fig. 2.6F,G,H respectively. A net movement of the patches towards the mid line may correspond to a global shear flow resulting in an elongation of the midline, as observed during streak elongation. As we consider patches next to the crack tip, the flux into the crack implies a movement of the lower half of the patch towards the crack relative to the upper half. Such a movement may result from a rotation (Fig. 2.6G) or a shear (Fig. 2.6H) of the patch. A rotation as observed in Fig. 2.6A,B and the quail embryo implies an upward movement of the crack tip, whereas a shear implies a downward movement. Such a shear movements results in a viscous shear stress such that the fluid pulls the crack tip upwards. Taken together, the crack tip moves upwards due to the flux into the crack, when the crack tip is force free.

2.5 Discussion

In this chapter we have presented a mechanical theory of active cracks in fluid films to understand the tissue movements during avian gastrulation. Using experimental data from quail embryos, we have shown that large-scale movements and rearrangements of cells in an epithilial tissue called epiblast are consistent with a model of a homogeneous fluid film with a hydrodynamic length that is larger than the system size. To understand how this fluid film is set into motion by mechanical activity in a structure called the primitive streak, we introduced a mechanical theory of active viscous cracks, i.e. lines of active material embedded in a fluid film. We gave force and torque balance equations for such a system, as well as constitutive equations for an active viscous non-chiral crack. With this, we inferred an effective model of the primitive streak as an active crack. To this end, we made use of analytical solutions in terms of holomorphic functions that allowed us to capture the experimental flow field with just three fitting parameters corresponding to boundary conditions. Thereby, we found that the primitive streak pulls the epiblast towards

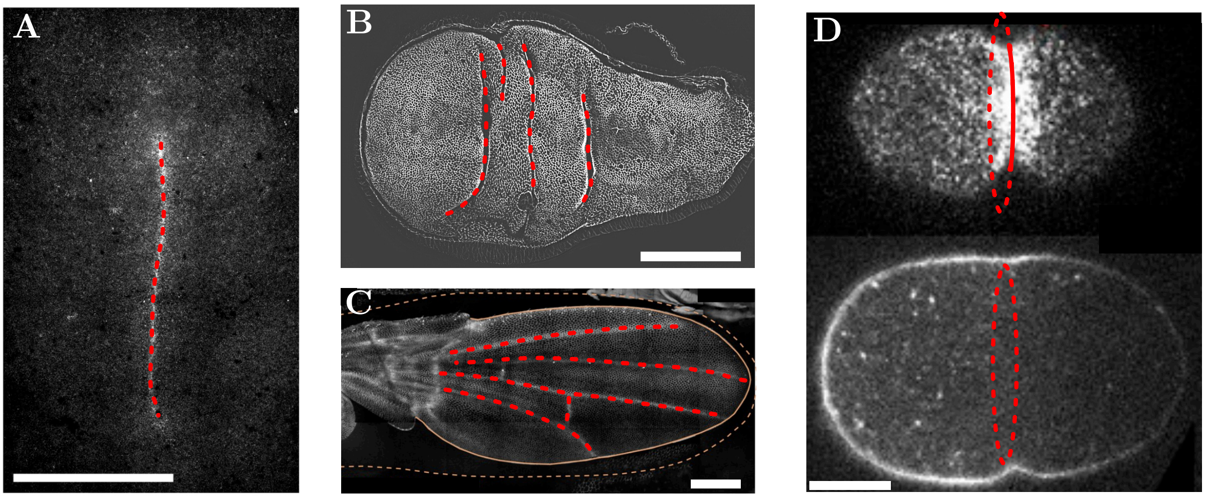

Figure 2.7: Active cracks in developing epithelia and the cell cortex. Mechanically distinct lines of material (red dashed lines) embedded in living sheets of matter, i.e. epithelial tissues (**A**-**C**) and the cell cortex (**D**), as seen in fluorescent microscopy images. **A**: Primitive streak in the epiblast of a quail embyo. **B**: Folds in the larval wing disc of the fruit fly *Drosophila melanogaster*. **C**: Veins of the pupal wing disc of *D. melanogaster*. **D**: Cytokinetic ring in the cell cortex of the *C. elegans* zygote. Upper image corresponds to cortical plane and lower image to mid-plane of the ellipsoidal cell. Scale bars: 1mm (**A**), 100μm (**B**, **C**), 10μm (**D**). Microscopy images in **A**,**B** were obtained by Julia Pfanzelter from the lab of Stephan Grill at the MPI-CBG Dresden (**A**) and Jana Fuhrmann from the lab of Natalie Dye at the TU Dresden (**B**). **C** was taken from [166] and **D** was taken from [23], both with permission.

it. Strikingly, our model suggests that the elongation of the primitive streak does not result from extensile mechanical activity of the streak. As such, the primitive streak does not push the node through the epiblast, but the epiblast pulls at the node due to the viscosity of the epiblast, thereby elongating the streak against an active line tension of the streak. Using analytical and numerical calculations we show that such a viscous force generally arises from an actively driven flux into an active crack such as the primitive streak.

Lines of material that are mechanically distinct from the rather homogeneous sheet of living matter they are embedded in can be found in various biological settings (see 2.7 for some examples from animal development). During development, these effectively one-dimensional structures have a crucial impact on the movement of cells and the propagation of signals in the surrounding two-dimensional tissue. We propose that many such systems may be understood with the mechanical theory of active cracks we presented here. We suggest the term crack for such lines for two reasons: First, the mechanical properties of these lines often allow large deformations, in-plane as well as out of plane, or gradients thereof that are absent from the surrounding tissue, just like a classical crack allows for large deformations that are absent from the surrounding elastic material. Typical examples are tissue folds as well as the cytokinetic ring that drives a very very localized ingression, when the cell is constrained [23, 167]. Second, an important aspect of such lines is what defines their length, not unlike cracks in the field of fracture mechanics, where the primary concern is under which conditions a crack propagates. For example, the cytokinetic ring of the *C. elegans* zygote as well as the AB cell starts to ingress from one side [168, 169]. For a cell to divide successfully, this ingressing line needs to span the equator of the cell.

Here, we have found that the growth of such a line that pulls material towards it is governed by the resulting flux of material. We have found that due to shear viscosity of the surrounding fluid film, an active flux into a crack results in a movement of the crack tip, when the line tension of the crack vanishes such that the crack tip is force free. Such a movement of a force free object in response to a force dipole is reminiscent of an active swimmer such as a bacterium. A bacterium exerts a dipole of forces on the surrounding fluid that results in a net movement due the polarized shape of the bacterium [170]. In the case of the active viscous crack, force dipoles along the crack drive a movement of the crack tip due to the polar geometry of the boundary, i.e. the crack with the crack tip on top. The rationale of movements resulting from an anisotropic geometry due to shear viscosity will be at the heart of the next two chapters. There, we study how an anisotropic surface geometry of a fluid film shapes active flows and patterns that emerge in it.

Chapter 3

Pattern formation guided by surface geometry

The body plan of bilateral animals contains three body axes (see section 1.1.1). These body axes are defined early in development, typically by the formation of persistent chemical gradients, a process we call axis specification (see section 1.1.2). The specification of a body axis is a typical example of symmetry breaking. As such it can be understood in terms of an order parameter that quantifies the order or anisotropy that is established as the symmetry of the initial state is broken. As we discuss in the following, body axis specification, as observed in the *C. elegans* embryo, can be understood in terms of a polar and a nematic order parameter. These order parameters quantify anisotropies in the distribution of certain proteins (see Fig. 3.1A,B).

Notably, the *C. elegans* zygote (i.e. the fertilized egg cell) already exhibits a consistent anisotropy before the first body axis, the AP axis, is specified: It has a prolate shape with a well defined long axis, which corresponds to the shape of the rigid egg shell that encompasses the embryo. Strikingly, the AP axis is always specified along this geometric axis [104, 99]. When the protein composition of the zygote is experimentally perturbed, a nematic pattern with two posterior domains forms. Also this pattern is found to align with the long axis of the egg shell [105]. Thus, the geometry of the surface of the embryo guides the formation of chemical patterns in this surface in a profound way.

In this chapter we will elucidate the physical basis of this phenomenon. We will start by considering a minimal model of guided symmetry breaking (section 3.1). This model forms the basis of the subsequent sections, where we study how the geometry of a surface impacts the formation of chemical patterns within this surface. As a minimal example of chemical dynamics in a curved surface, we investigate diffusion in section 3.2. In section 3.3, in contrast, we study how surface geometry impacts patterns that form due to flows in the actomyosin cortex. This thin film of actin filaments and motor molecules plays a key role in the specification of all three body axes of the *C. elegans* embryo (see section 1.3). Here, we will understand this sheet of active matter using a minimal hydrodynamic model, where cortical flows are driven by an active cortical tension which is controlled by the concentration of a single stress regulator. With this model of the cortex, we study pattern formation on a cell with static anisotropic shape. In particular, we study how small anisotropies of the surface geometry impact the concentration dynamics in the linear regime (section 3.3.1). To this end, we make use of the Newman Penrose formalism, in particular spin-weighted spherical harmonics, to obtain analytical results in the linear regime of the shape anisotropy (see appendix E). In section 3.3.2, we investigate how active tension drives global rotations of the cell surface that align the pattern of the cortical stress regulator with the surface geometry of the cell. There, we compare our analytical results also to experimental data from *C. elegans* embryos during the process of DV axis establishment obtained by Teije Middelkoop. In section 3.3.3, we generalize the phenomenon of rotational alignment due to active force generation by including also mechanical interactions between the cortex and the mitotic spindle. In particular, we investigate what forces ensure that a cell divides along its longest axis. To this end, we compare also our theoretical predictions to the results of perturbation experiments obtained by Teije Middelkoop. Finally, in section 3.3.4, we investigate the non-linear dynamics of the minimal cortex model for a prolate spherical geometry of the cell surface. To this end, we make use of a numerical method we developed (see appendix F).

3.1 Minimal model of guided symmetry breaking

In this chapter, we study symmetry breaking in a non-equilibrium system guided by an externally defined static cue. In order to gain a conceptual understanding of the process of guided symmetry breaking we begin with a minimal coarse-grained model of the process. This model yields generic phenomena, which we will also find in a model of the cell cortex in the remainder of this chapter.

We consider a static nematic order parameter corresponding to the long axis of the egg-shell geometry in the case of the *C. elegans* zygote. This static axis guides the self-organized formation of a body axis, which we understand in terms of an uniaxial nematic order parameter, corresponding to the axis as such, and a polar order parameter. Such order parameters can be mapped to the distribution of proteins on the spherical surface of a cell [171, 172] (see Fig. 3.1A and B for polar and nematic chemical patterns, respectively, in the surface of the *C. elegans* zygote). However, the model we consider here is more general. The nematic order parameter may for example also correspond to the cell division axis as defined by the mitotic spindle, a protein complex (Fig. 3.1C).

For simplicity, we consider here a two-dimensional setting where both axes and the polarity lie in one statically defined plane. In two dimensions nematic and polar order parameters can be understood in terms of a magnitude $W > 0$ and an angle or phase $\varphi \in [-\pi, \pi]$. Using the formalism of spin-weighted quantities we introduced in section 1.3.1, we write the order parameters as

$$ {}_{(2)}X = Xe^{2i\varphi_X}, \quad {}_{(2)}Q = Q(t)e^{2i\varphi_Q(t)}, \quad {}_{(1)}p = p(t)e^{i\varphi_p(t)}, \tag{3.1}$$

where ${}_{(2)}X$, ${}_{(2)}Q$, ${}_{(1)}p$ correspond to static nematic, dynamic nematic and dynamic polar order parameters, respectively. The prescripts denote the spin-weight, corresponding to the rotational symmetry of the quantity (Eq. 1.57). In the following, we consider a frame such that $\varphi_X = 0$. Then φ_Q and φ_p correspond to the angles of axis and polarity with respect to the axis defined by ${}_{(2)}X$. ${}_{(2)}Q$ and ${}_{(1)}p$ may then be defined in terms of Fourier components of the line density of a chemical on a circular outline, such as the mid-plane of a cell. Then, ${}_{(2)}Q$ and ${}_{(1)}p$ correspond to distinct components of the concentration field c, i.e. the projection of $c(\varphi)$ onto the orthogonal functions $e^{-2i\varphi}$ and $e^{-i\varphi}$, respectively. In this sense, polar and nematic order parameter are independent from each other. However, a polarity ${}_{(1)}p$ also defines an axis ${}_{(2)}p = {}_{(1)}p\,{}_{(1)}p$, to which ${}_{(2)}Q$ may dynamically couple.

In the following, we study dynamical couplings between ${}_{(2)}Q$ and ${}_{(1)}p$ as well as ${}_{(2)}X$, which can result in alignment of the corresponding three axes. We consider all terms that are allowed by symmetry up to quadratic order in the dynamic anisotropy $W \sim Q, p$, and up to linear order in X, except a dampening non-linearity of cubic order in Q, p. This corresponds to a scenario where a slight anisotropy guides the process of self-organized symmetry breaking. With this, we have the following equations

$$\begin{aligned}\partial_t\,{}_{(1)}p =& (\gamma_1^p + \gamma_2^p p^2)\,{}_{(1)}p + \chi_1\,{}_{(2)}Q\,{}_{(-1)}p \\ &+ \zeta^p\,{}_{(2)}X\,{}_{(-1)}p + \zeta_1^{pQ}\,\mathrm{Re}[{}_{(-2)}Q\,{}_{(2)}X]\,{}_{(1)}p + i\zeta_2^{pQ}\,\mathrm{Im}[{}_{(-2)}Q\,{}_{(2)}X]\,{}_{(1)}p \end{aligned}\tag{3.2}$$

$$\begin{aligned}\partial_t\,{}_{(2)}Q =& (\gamma_1^Q + \gamma_2^Q Q^2)\,{}_{(2)}Q + \chi_2\,{}_{(1)}p\,{}_{(1)}p \\ &+ (\zeta_1^Q + \zeta_3^{pQ} p^2)\,{}_{(2)}X + \zeta_2^Q\,\mathrm{Re}[{}_{(-2)}Q\,{}_{(2)}X]\,{}_{(2)}Q + i\zeta_3^Q\,\mathrm{Im}[{}_{(-2)}Q\,{}_{(2)}X]\,{}_{(2)}Q, \end{aligned}\tag{3.3}$$

where negative spin-weights denote the complex conjugate and i is the imaginary unit. We consider a non-chiral system in this chapter, corresponding to model that is invariant under the mirror transformation $\varphi_{p/Q} \to -\varphi_{p/Q}$. This implies that all coefficients (γ_n^x, χ_n,ζ_n^x) are real numbers. The dynamical equations of a spin quantity ${}_{(s)}f = We^{is\varphi}$ can be mapped to dynamical equations of the magnitude W and phase φ using

$$\partial_t W = \frac{1}{W}\,\mathrm{Re}[{}_{(-s)}f\,\partial_t\,{}_{(s)}f], \quad \partial_t\varphi = \frac{1}{sW^2}\,\mathrm{Im}[{}_{(-s)}f\,\partial_t\,{}_{(s)}f]. \tag{3.4}$$

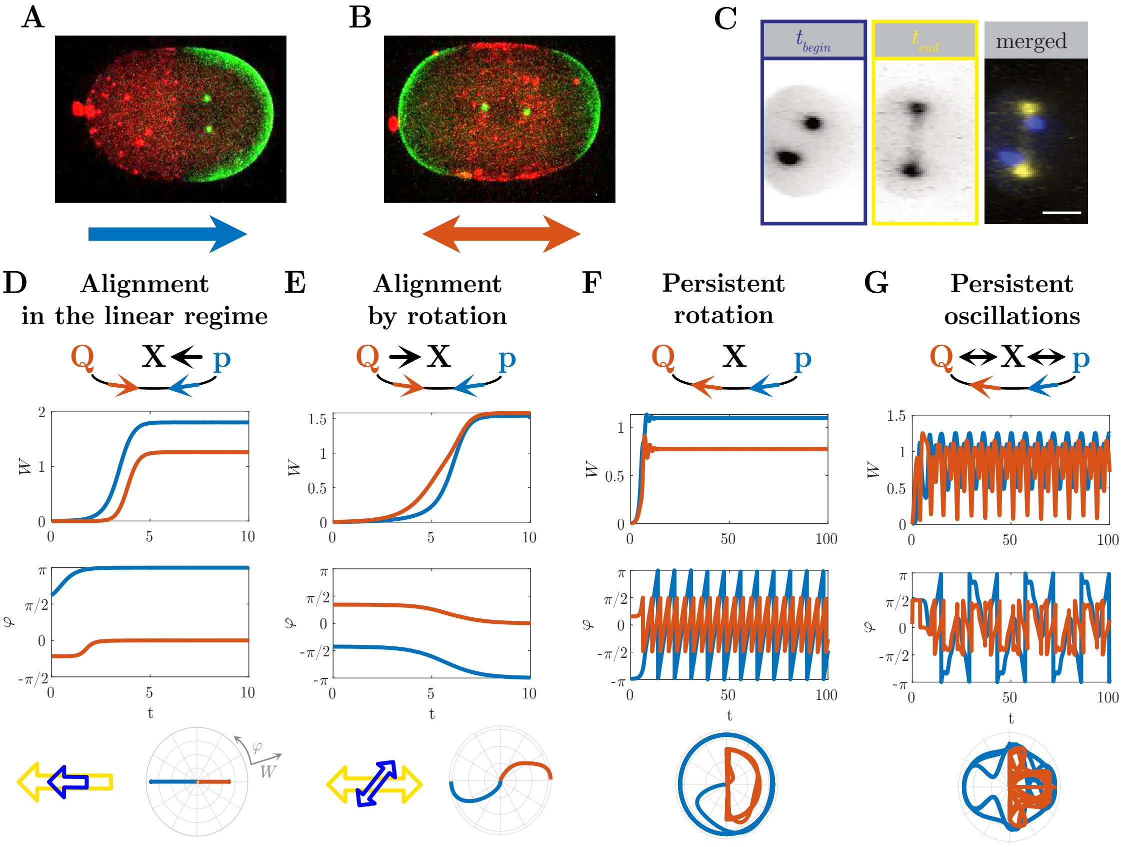

Figure 3.1: Minimal model of guided symmetry breaking. A,B: Chemical patterns with polar (A) and nematic (B) symmetry form along the long axis of the surface shape, as observed in the surface of the *C. elegans* zygote. Red and green color correspond to the intensity of labelled proteins defining the future anterior and posterior side, respectively. The zyogte in B has been perturbed giving rise to the bipolar pattern. Images were taken from [105]. **C**: Mitotic spindle defining the cell divison axis of the *C. elegans* AB cell rotates towards the long axis. Microscopy images were obtained by Teije Middelkoop as published in [167]. **D-F**: numerical solutions of equations 3.5-3.8 defining a minimal model of guided symmetry breaking motivated by the patterns observed in A,B. The plots show the time evolution of polar (${}_{(1)}p$, blue lines) and nematic (${}_{(2)}Q$, red lines) order parameter for four different sets of parameters as given in Table J.3. In the upper row, the magnitudes are plotted as a function of time. In the middle row, the corresponding angles are plotted. The bottom row shows trajectories as polar plots, where the magnitude corresponds to the distance from the origin and the angle corresponds to the angles φ_p, φ_Q of the order parameters. **D**: alignment in the linear regime due to coupling of ${}_{(1)}p$ to the external axis ${}_{(2)}X$. **E**: alignment in the non-linear regime due to coupling of ${}_{(2)}Q$ to ${}_{(2)}X$. Blue and yellow represent nematic order parameter at early and late times, akin to the spindle configurations in **C**. **F**: Rotation arising from non-potential couplings between ${}_{(1)}p$ and ${}_{(2)}Q$. **G**: Complex oscillatory dynamics arising from non-potential couplings between ${}_{(1)}p$ and ${}_{(2)}Q$ in the presence of couplings to ${}_{(2)}X$.

With this we obtain

$$\partial_t p =(\gamma_1^p + \gamma_2^p p^2)p + \chi_1 Q p \cos[2(\varphi_Q - \varphi_p)] + \zeta^p X p \cos(2\varphi_p) + \zeta_1^{pQ} X Q p \cos 2\varphi_Q, \tag{3.5}$$

$$\partial_t Q =(\gamma_1^Q + \gamma_2^Q Q^2)Q + \chi_2 p^2 \cos[2(\varphi_Q - \varphi_p)] + (\zeta_1^Q + \zeta_2^Q Q^2 + \zeta_3^{pQ} p^2) X \cos 2\varphi_Q, \tag{3.6}$$

$$\partial_t \varphi_p =- \chi_1 Q \sin[2(\varphi_p - \varphi_Q)] - \left(\zeta^p + \zeta_2^{pQ} Q\right) X \sin 2\varphi_p, \tag{3.7}$$

$$\partial_t \varphi_Q =- \chi_2 \frac{p^2}{2Q} \sin[2(\varphi_Q - \varphi_p)] - \left(\zeta_1^Q \frac{1}{Q} + \zeta_3^Q Q + \zeta_3^{Qp} p^2\right) X \sin 2\varphi_Q. \tag{3.8}$$

We observe that coupling to ${}_{(2)}X$ can come in two ways: First we find terms of the form $\partial_t \varphi \sim -X \sin 2\varphi$, yielding an aligning rotation. For φ dynamics of this form, we have fixed points at $\varphi = 0, \pm\pi$ and $\varphi = \pm\pi/2$ corresponding to parallel and perpendicular alignment, respectively. The sign of the coupling coefficient defines whether the dynamic axis rotates towards parallel or perpendicular alignment. Second, we obtain terms of the form $\partial_t W \sim X \cos 2\varphi$, corresponding to a magnitude that grows faster in the aligned configuration. This yields a stabilization of the aligned state. Again, the sign of the coupling coefficient defines whether alignment means parallel or perpendicular alignment.

Notably, the couplings of ${}_{(2)}Q$ and ${}_{(1)}p$ to ${}_{(2)}X$ involve distinct orders of p, Q. In particular, ζ_1^Q yields a coupling of ${}_{(2)}Q$ to ${}_{(2)}X$ even in the isotropic state $Q = 0 = p$. For the *C. elegans* embryo, this corresponds to a scenario where the anisotropic shape directly induces the formation of a pattern, e.g. due to curvature-dependent binding of cytoplasmic proteins. However, such a geometry-dependent pattern is not observed in the isotropic state before AP symmetry breaking. Hence, we consider $\zeta_1^Q = 0$ in the following. In this regime ${}_{(2)}Q$ couples to ${}_{(2)}X$ only in quadratic order of Q and p. In contrast, ${}_{(1)}p$ contrast couples to ${}_{(2)}X$ already in linear order of p.

This has a profound impact on the dynamics of alignment. To illustrate this, let us consider two scenarios: First, a scenario where only the polarity ${}_{(1)}p$ couples to the static axis ${}_{(2)}X$ (i.e. $\zeta^p = 1$, all other ζ_n^x=0). Second, a scenario where only the dynamic axis ${}_{(2)}Q$ couples to the static axis ${}_{(2)}X$ by means of an aligning rotation (i.e. $\zeta_3^Q = 1$, all other $\zeta_n^x = 0$). In both scenarios, we consider the dynamic axis ${}_{(2)}Q$ to be closely aligned with the polarity ${}_{(1)}p$ (i.e. $\chi_1 = \chi_2 = 1$). In Fig. 3.1D,E, we plot numerical solutions for these scenarios of a symmetry breaking process, starting from a small perturbation of the isotropic state $p = 0 = Q$ that is linearly unstable due to $\gamma_1^p > 0$ or $\gamma_1^Q > 0$. With this, we find that the second scenario (B) involves a rotation of ${}_{(1)}p$ and ${}_{(2)}Q$ while p and Q approach their steady state values. In the first scenario (A), in contrast, ${}_{(1)}p$ and ${}_{(2)}Q$ are already aligned with ${}_{(2)}X$ when the magnitudes p, Q are still exponentially growing. This is a consequence of the linear order in p of the coupling of ${}_{(1)}p$ to ${}_{(2)}X$. For ${}_{(2)}Q$ such a linear order coupling is not allowed by symmetry. Instead, ${}_{(2)}Q$ aligns with ${}_{(2)}X$ by a rotation in the non-linear regime. Also a coupling given by ζ_2^Q is possible, which only affects the magnitude Q. However such a coupling does not yield true alignment, as it does not affect the fixed points of the angle φ_Q, but only yields a φ_Q dependence of the steady state magnitude.

In summary, an (unpolar) axis that does not couple to the static axis in the isotropic state can only align with an external axis by a visible rotation. Strikingly, such rotations have indeed been observed during the establishment of the AP and DV axes of the *C. elegans* embryo [99, 167]. We will study these rotations in section 3.3.2 using a minimal model of the cell cortex.

So far, we considered only scenarios where the couplings between ${}_{(2)}Q$ and ${}_{(1)}p$ amount to an alignment of the two dynamic axes they define, i.e. $\chi_1\chi_2 > 0$. Such a coupling can be understood in terms of a minimization of an effective potential $F(p, Q)$. When $\chi_{1,2} > 0$, the couplings favor parallel alignment, for $\chi_{1,2} < 0$ one obtains perpendicular alignment of ${}_{(1)}p$ and ${}_{(2)}Q$. However, in an non-equilibrium system, also non-potential couplings with $\chi_1\chi_2 < 0$ are possible. This corresponds to a scenario where e.g. ${}_{(1)}p$ rotates towards ${}_{(2)}Q$ but ${}_{(2)}Q$ rotates away from ${}_{(1)}p$, or viceversa. This gives rise to persistent rotations of ${}_{(1)}p$ and ${}_{(2)}Q$ (Fig. 3.1F). Couplings to the static axis ${}_{(2)}X$ in this regime give rise to persistent oscillatory dynamics when the coupling to the static axis is not sufficient to yield stable steady state (Fig. 3.1G). We note that we have not found a parameter regime where the dynamical system governed by Eq. 3.5-3.8 exhibits chaotic behaviour. In section 3.3.4, we will observe similar complex oscillatory patterns in numerical solutions of a minimal model of the cell cortex.

3.2 Diffusion on a curved surface

We want to understand how the shape of a cell impacts a chemical pattern forming on its surface. As a start, let us consider the simplest non-trivial example of chemical dynamics on a curved surface: diffusion of a single chemical species with concentration c, i.e.

$$\partial_t c = D\Delta_{LB} c. \tag{3.9}$$

Here, D is the diffusion constant and Δ_{LB} is the Laplace-Beltrami operator which is the generalization of the Laplace operator to curved surfaces defined as $\Delta_{LB} = g^{ij}\nabla_i\partial_j$. On a closed surface Δ_{LB} is a self-adjoint operator with eigenvalues λ_i obeying

$$0 = \lambda_0 > \lambda_1 \geq \lambda_2 \geq ... \tag{3.10}$$

Hence, we can write the dynamics of the concentration field as

$$c(s^1, s^2, t) = c_0 + \sum_{i=1}^{\infty} c_i f_i(s^1, s^2) e^{D\lambda_i t}, \tag{3.11}$$

where f_i is the eigenfunction with eigenvalue λ_i and the initial condition is given by

$$c(s^1, s^2, 0) = c_0 + \sum_{i=1}^{\infty} c_i f_i(s^1, s^2). \tag{3.12}$$

Here, the geometry of the surface manifests in the eigenvalues and eigenfunctions of the Laplace-Beltrami operator. The relation between surface geometry and the spectrum of the Laplace Beltrami operator has been the subject of a considerable amount of research in the past [173]. We may mention in particular the influential lecture "Can one hear the shape of a drum?" [174]. Here we want to ask whether a patterning surface feels its shape. As an illustrative but also biologically relevant example we consider a slightly deformed sphere parametrized as

$$\mathbf{X}'(\theta,\varphi) = (R_0 + \delta R(\theta,\varphi))\mathbf{r}(\theta,\varphi), \tag{3.13}$$

where δR corresponds to a deformation normal to the spherical reference surface $\mathbf{X}_0 = R_0\mathbf{r}$. The eigenfunctions of Δ_{LB} on $\mathbf{X}_0$ are the spherical harmonic functions Y_{lm} (Eq. E.2) with eigenvalues

$$\lambda_{lm} = -\frac{1}{R_0^2} l(l+1). \tag{3.14}$$

Upon deformation the Laplace Beltrami operator changes as

$$\Delta'_{LB} = \Delta^0_{LB} + \delta\Delta_{LB}, \quad \delta_{LB} = -2\frac{\delta R}{R_0}\Delta^0_{LB} \tag{3.15}$$

in linear order of $\delta R/R_0$, where Δ^0_{LB} is the Laplace-Beltrami operator on the sphere (see appendix E.4.1 for more details of the calculation). From this, we calculate the spectrum of Δ'_{LB} up to linear in δR. For simplicity, we consider an axisymmetric deformation δR and identify the **z**-axis as the axis of symmetry, such that an axisymmetric deformation can be written as

$$\delta R = \sum_l \delta R_l Y_{l,0}. \tag{3.16}$$

A calculation of the change in the spectrum in linear order of a perturbation is analogous to perturbation theory in quantum mechanics. Using analogous notation, the spectrum changes as

$$\lambda'_{lm} = -\, l(l+1) + \langle l,m|\, \delta\Delta_{LB}\, |l,m\rangle\,, \tag{3.17}$$

$$Y'_{lm} = Y_{lm} + \sum_{l'\neq l} \frac{\langle l',m|\, \delta\Delta_{LB}\, |l,m\rangle}{l'(l'+1)+l(l+1)} Y_{l'm}, \tag{3.18}$$

where λ'_{lm} and Y'_{lm} denote eigenvalues and eigenfunctions of Δ'_{LB}. We define $\langle l',m|\, \delta\Delta_{LB}\, |l,m\rangle$ analogously to a bra-ket from quantum mechanics as the projection onto $Y_{l'm}$ of $\delta\Delta_{LB}$ acting on Y_{lm}. It can be calculated using Wigner 3j matrices (appendix E.4.3.1). They are closely related to the better known Clebsch-Gordan coefficients and obey several symmetry relations that allow to simplify expressions when considering single spherical harmonics components of δR.

An axisymmetric elongation or compression of the sphere is given by the $l = 2$ component of δR, i.e. $\delta R = \delta R_2 Y_{20}$. In this case, the eigenvalues are given by

$$\lambda'_{lm} = -l(l+1)\left[1 - \frac{\delta R_2}{R}\sqrt{\frac{5}{\pi}}\frac{l(l+1)-3m^2}{4l(l+1)-3}\right]. \tag{3.19}$$

We observe that λ'_{lm} depends on m, in contrast to the eigenvalues λ_{lm} on the undeformed sphere (Eq. 3.14). This reflects the spatial symmetry that is broken by the perturbation δR. For a given l, all spherical harmonics Y_{lm} can be expressed in terms of spatial rotations of the $m = 0$ mode Y_{l0} and linear combinations thereof [175]. Thus, they all share the same eigenvalue due to the isotropy of the sphere and the covariance of the Laplace-Beltrami operator. A deformation breaks this symmetry and thus the degeneracy of the λ_{lm}, analogous to the splitting of energy levels in an atom in response to an external electric or magnetic field [176, 177]. For an axisymmetric deformation as we consider here, only a degeneracy of the eigenvalues λ'_{lm} with respect to the sign of m remains, i.e. $\lambda'_{lm} = \lambda'_{l,-m}$.

An elongation of the spherical surface corresponds to $\delta R_2 > 0$. With this, Eq. 3.19 yields that modes with larger $|m|$ decay faster and that axisymmetric modes ($m = 0$) decay slower than on the undeformed sphere (Fig. 3.2A). This implies that on long times the components of c that are axisymmetric with respect to the geometric long axis (i.e. $\mathbf{z}$) dominate, when we consider diffusional dynamics starting from some initial pattern. Thus, for a pola pattern, corresponding to $l = 1$, diffusion favors alignment of the axis of polarity with the long axis, corresponding to $m = 0$ (Fig. 3.2C).

This phenomenon can simply be understood in terms of length scales: When the axis of polarity is aligned with the long axis the chemical pattern spreads over a larger length than when the axis of polarity is perpendicular to the long axis. Notably, we can find coordinates for any surface such that the Laplace-Beltrami operator reads

$$\Delta_{LB} = \frac{1}{l^2}\Delta_0, \tag{3.20}$$

where Δ_0 is the Laplace operator in flat two-dimensional space, and $l(s^1, s^2)$ is a coordinate-dependent length scale (see section 1.3.2). A deformation corresponds to a change in this length scale δl, i.e. it can be understood in terms of isotropic contractions ($\delta l < 0$) and expansions ($\delta l > 0$) of the surface. Thus, the geometry dependence of diffusional dynamics on a surface can in principle always be understood in terms of a change in length scales. For simple patterns and shapes the geometry dependence may be understood as the maximization of a length scale associated with the chemical gradient.

Diffusion on its own does not yield the spontaneous formation of a pattern. However, diffusion is crucial to many models of chemical pattern formation such as the classical Turing model [2, 178, 179, 180, 181]. Thus, we expect the geometry-dependence of two-dimensional diffusion

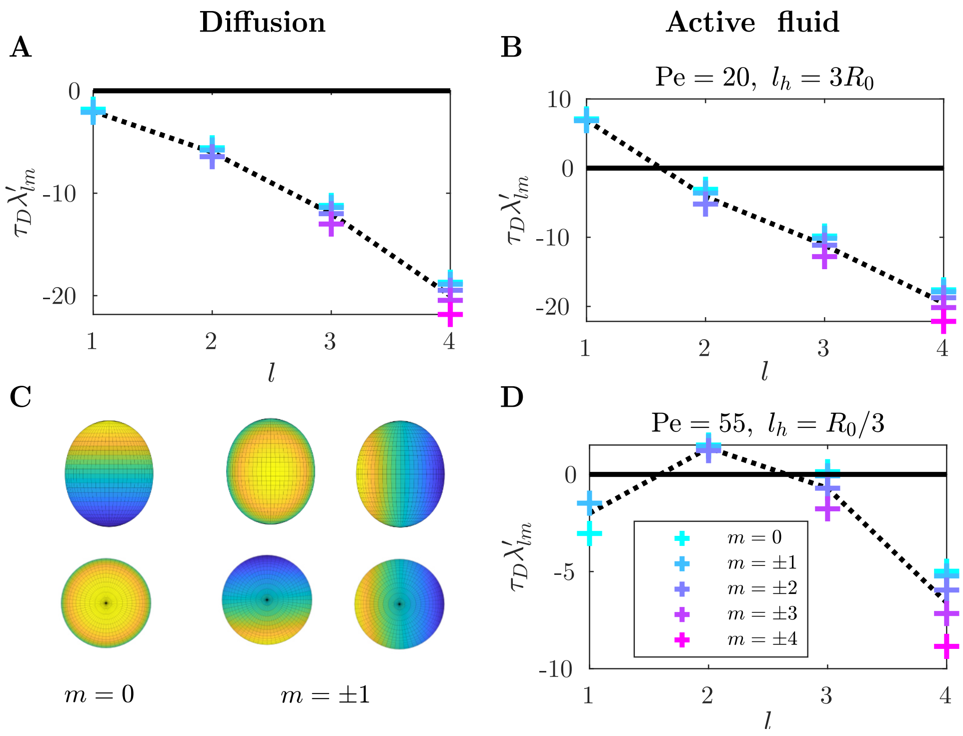

Figure 3.2: Linear concentration dynamics on a deformed sphere. **A**,**B**,**D**: Eigenvalues λ_{lm} of linear concentration dynamics on a sphere (black dashed lines) and on an elongated sphere (colored crosses with color denoting $|m|$, plotted for $\delta R_{20} = 0.2$) relative to the diffusion time scale $\tau_D = D/R_0^2$. **A**: Diffusion of a single chemical species. Eigenvalues correspond to eigenvalues of the Laplace-Beltrami operator (Eq 3.19) **B**,**D**: Diffusion and advection of a stress regulator in an active isotropic fluid (Eq. 3.24,3.26). **C**: Polar eigenmodes Y'_{1m} of the Laplace Beltrami operator for $\delta R_{20} = 0.2$ (Eq. 3.18). Note that there is no qualitative difference to the spherical harmonics Y_{1m} or to the eigenmodes of the active fluid model on such a geometry.

that we discussed here to have an impact on patterns in various biological surfaces. It is distinct from effects of boundary geometries that have been discussed for bulk diffusion in the context of pattern formation [95, 182, 183, 184].

3.3 Pattern formation in an active fluid model of the cell cortex

In the following we will study pattern formation in a minimal model of the cell cortex, which we introduced in sections 1.2.5 and 1.2.6. Briefly, we consider an active fluid surface with a static shape, where flows are driven by a pattern of active isotropic tension given by

$$t^{ij}_{\mathrm{act}} = \chi_0 f(c) g^{ij}, \tag{3.21}$$

where c is the concentration of a stress regulator and $f(c)$ is a monotonously increasing function with $f'(c_0) = 1/c_0$ that saturates for large c. The flow field v^i is dampened by the viscosities $\eta_s = \eta$ and $\eta_b = \alpha\eta$ of the cortex and friction with a rigid substrate, which defines a hydrodynamic length scale $l_h = \sqrt{\eta/\gamma}$. Self organized pattern formation results from advection of the stress regulator balanced by diffusion within the cortex and exchange with a homogeneous reservoir, corresponding to the cytoplasm (see dynamical equation Eq. 1.53 and Fig 1.11). An almost identical model has been studied on the sphere, where the formation of polar patterns and a stable contractile ring have been observed [135]. In this section we investigate how patterns and flows change, when considering a deformed sphere.

3.3.1 Linear stability of an active fluid film with anisotropic surface geometry

The trivial steady state of our model is $c = c_0 = \text{const.}$ with c_0 being a reference concentration resulting from the exchange with the bulk reservoir. In the following, we study our model by considering slight perturbations

$$\delta c(\theta, \varphi) = \sum_{l,m} c_{lm} Y_{lm}(\theta, \varphi) \tag{3.22}$$

of the homogeneous steady state. With this, the dynamics of the concentration field can be written in linear order of $\delta c / c_0$ as

$$\frac{\mathrm{d}}{\mathrm{d}t} \delta c_{lm} = \sum_{l'm'} T^{lm}_{l'm'} \delta c_{l'm'}(t), \tag{3.23}$$

where $T^{lm}_{l'm'}$ is matrix that can be calculated from the governing equations. On a sphere, $T^{lm}_{l'm'}$ is diagonal due to symmetry, i.e. $T^{lm}_{l'm'} = \lambda_{lm} \delta_{l,l'} \delta_{m,m'}$ with the eigenvalues λ_{lm} given by

$$\lambda_{lm} = -\frac{l(l+1)}{\tau_D} \left(1 + \frac{\tau_D k}{l(l+1)} - \frac{\mathrm{Pe}}{R_0^2/l_h^2 + (1+\alpha) l(l+1) - 2} \right). \tag{3.24}$$

Here, $\tau_D = D/R_0^2$ is the time scale of diffusion, k is the rate of exchange with the bulk reservoir and we have defined the Péclet number (Eq. 1.54) as

$$\mathrm{Pe} = \frac{\chi_0 R_0^2}{D\eta}. \tag{3.25}$$

Similar results have been obtained in [135], where interaction with a bulk fluid instead of a rigid substrate has been considered. For $\lambda_{lm} > 0$, the homogeneous state is linearly unstable and patterns emerge spontaneously. This threshold can understood in terms of a critical Péclet Pe^*, such that at least one mode is unstable ($\lambda_{lm} > 0$) for $\mathrm{Pe} < \mathrm{Pe}^*$, whereas for $\mathrm{Pe} > \mathrm{Pe}^*$ the homogeneous state is stable ($\lambda_{lm} < 0$ for all $l > 0$) [156, 136]. Close to this threshold, the pattern that emerges is given by the first unstable mode. For large hydrodynamic length ($l_h/R_0 > 1/\sqrt{2} \approx 0.7$), λ_{lm} decreases monotonously with l such that the modes with $l = 1$ become unstable first (see dashed line in Fig. 3.2B). This explains why in such a regime the formation of a polar pattern is observed in numerical simulations of the non-linear model [135]. For a small hydrodynamic length ($l_h/R_0 \ll 1$ with $k\tau_D \geq 1$), in contrast, λ_{lm} is maximal for some $l_{\max} > 1$. Thus, a regime can be found such that only the $l = 2$ modes are unstable (Fig.

3.2D). In such a regime, the formation of a ring as well as bipolar patterns has been observed in numerical simulations [135].

Upon a deformation $T^{lm}_{l'm'}$ is no longer diagonal, but it remains the matrix representation of a self-adjoint operator. As such, it has a real spectrum that we can calculate perturbatively as in the previous section (Eq. 3.17, 3.18). With this, we calculate the change in the eigenvalues $\delta\lambda_{lm}$ for an axisymmetric deformation in appendix E.4. In particular we consider an axisymmetric elongation of the cell, i.e. $\delta R = \delta R_2 Y_{20}$ with $\delta R_2 > 0$ yielding a shape given by Eq. 3.13 (see also Fig. 3.2C for chemical patterns on such a surface geometry). With this, we find

$$\tau_D \delta\lambda_{lm} = \frac{l(l+1) - 3m^2}{4l(l+1) - 3} \frac{\delta R_2}{R_0} \sqrt{\frac{5}{\pi}} \left[l(l+1) + \mathrm{Pe} \frac{\left[6(l-1)(l+2) - (R_0/l_h)^2 l(l+1)\right]}{\left[(R_0/l_h)^2 + (\alpha+1)l(l+1) - 2\right]^2} \right], \quad (3.26)$$

where we observe that the m dependence, given by the first factor, is of the same form as for pure diffusion (Eq. 3.19), as it results from the same mathematical object, the Wigner $3j$ symbol

$$\begin{pmatrix} l & l_R & l \\ m & m_R & -m \end{pmatrix} \quad (3.27)$$

with $l_R = 2$, $m_R = 0$. However the sign of the last factor given by the square brackets in Eq. 3.26 can vary depending on the viscosities of the cell cortex.

In the previous section we considered diffusional dynamics ($\chi'(c_0) = 0$). There we found that $\delta\lambda_{l0} > 0$ and $\delta\lambda_{lm}$ is monotonously decreasing with $|m|$. We obtain equivalent results in the regime of large hydrodynamic length, i.e. $l_h/R_0 > 2$, for modes with $l > 1$ (Fig. 3.2B). This favors the formation of axisymmetric patterns corresponding to modes with $m = 0$. For small hydrodynamic lengths, i.e. $l_h/R_0 < 1/\sqrt{6} \approx 0.4$, in contrast, we find that $\delta\lambda_{lm}$ is monotonously increasing with $|m|$ for a sufficiently large Péclet number when l is small compared to R_0/l_h. Thus, in the regime where the formation of nematic patterns is observed, polar patterns ($l = 1$) tend to align perpendicularly to the geometric long axis, as $\lambda'_{1,\pm1} > \lambda'_{1,0}$ (Fig. 3.2D). For larger l, however, the axisymmetric component dominates, i.e. it has the maximal eigenvalue λ_{lm}, no matter whether we consider small or large hydrodynamic lengths or diffusion limited dynamics as in the previous section.

During the specification of the AP axis in the *C. elegans* zygote, pattern formation is initialized by the localized removal of myosin motors from the cortex due to interaction with the male pronucleus (see section 1.1.2). Similarly, the cytokinetic ring of the AB cell that is crucial to the establishment of the DV axis forms in response to interactions of the spindle apparatus. Thus, in both cases pattern formation is triggered by a sizable reorganization of the cortex due to interaction with a cell-scale structure. Furthermore, the homogeneous state of the cortex before the triggering event appears to be stable with respect to fluctuations. The significance of linear stability calculations to such a scenario is unclear. Therefore, we focus on non-linear phenomena in the remainder of this chapter.

3.3.2 Rotational flow aligns tension pattern with surface geometry

In the following, we study the alignment of a stress regulator pattern with the surface geometry using our hydrodynamic model of the cell cortex and experimental data obtained by Teije C. Middelkoop. Most of the results of this chapter can also be found in our recent preprint [167] that has been in press at *PNAS* at the moment of writing.

During the establishment of the DV axis of the *C elegans* embryo, a rapid rotation of the embryo surface is often observed [167, 186]. It is found that the rotation requires the activity of myosin, suggesting that it is driven by actomyosin tension. Strikingly, the cortical flows associated with the rotation are an order of magnitude faster than any other component of the cortical flow around this time point of the cell cycle (compare for example Fig. 3.3D,E). These experimental observations suggests that the embryo is essentially free to rotate in the confining egg shell. This corresponds to a parameter regime where friction between the embryo surface and the rigid egg shell is almost negligible compared to viscosity of the cortex as the resulting hydrodynamic length is much larger than the system size. Using our model of the cell cortex for a slightly deformed spherical cell, we find that for a large hydrodynamic length the flow field is dominated by a rotational flow that spans the entire surface of the cell (see appendix E.4.2).

On the undeformed sphere, this flow component corresponds to a rigid body rotation $\mathbf{\Omega}$ of the sphere. As such it is limited only by friction. However, on such an isotropic surface a pattern of active tension χ does not yield a rotational flow, i.e. a flow with non-zero vorticity. In an anisotropic surface geometry, in contrast, shear viscosity yields a coupling of rotational and irrotational flow components (see section 4.1.2). As a consequence, a pattern of active tension can drive a rotation $\delta\mathbf{\Omega}$ of the entire cortex that scales with the deformation δR. Identifying the axis of rotation as the z axis ($\delta\mathbf{\Omega} = \delta\Omega\mathbf{z}$), we find that the rotation results from a misalignment between pattern of active tension and the surface geometry. This can be seen by writing the spherical harmonic coefficients of the deformation δR and the active tension χ in terms of a magnitude and an azimuthal angle

$$\delta R_{lm} = |\delta R_{lm}| e^{-im\varphi_R}, \quad \chi_{lm} = |\chi_{lm}| e^{-im\varphi_\chi}. \tag{3.28}$$

With this, the angular velocity of the cell scale rotation is given by

$$\delta\Omega = \left(\frac{l_h}{R_0}\right)^2 \sum_{l\geq 2, m>0} \frac{3}{2\pi} \frac{m\,[l(l+1)-2]}{(\alpha+1)l(l+1)-2} \frac{|\chi_{l,m}|}{\eta} \frac{|\delta R_{l,m}|}{R_0} \sin[m(\varphi_{\chi,lm} - \varphi_{R,lm})]. \tag{3.29}$$

Misalignment of components of tension pattern and surface geometry corresponds to a configuration, where $\sin[m(\varphi_{\chi,lm} - \varphi_{R,lm})] \neq 0$. Due to advection, the rotational flow implies a rotation

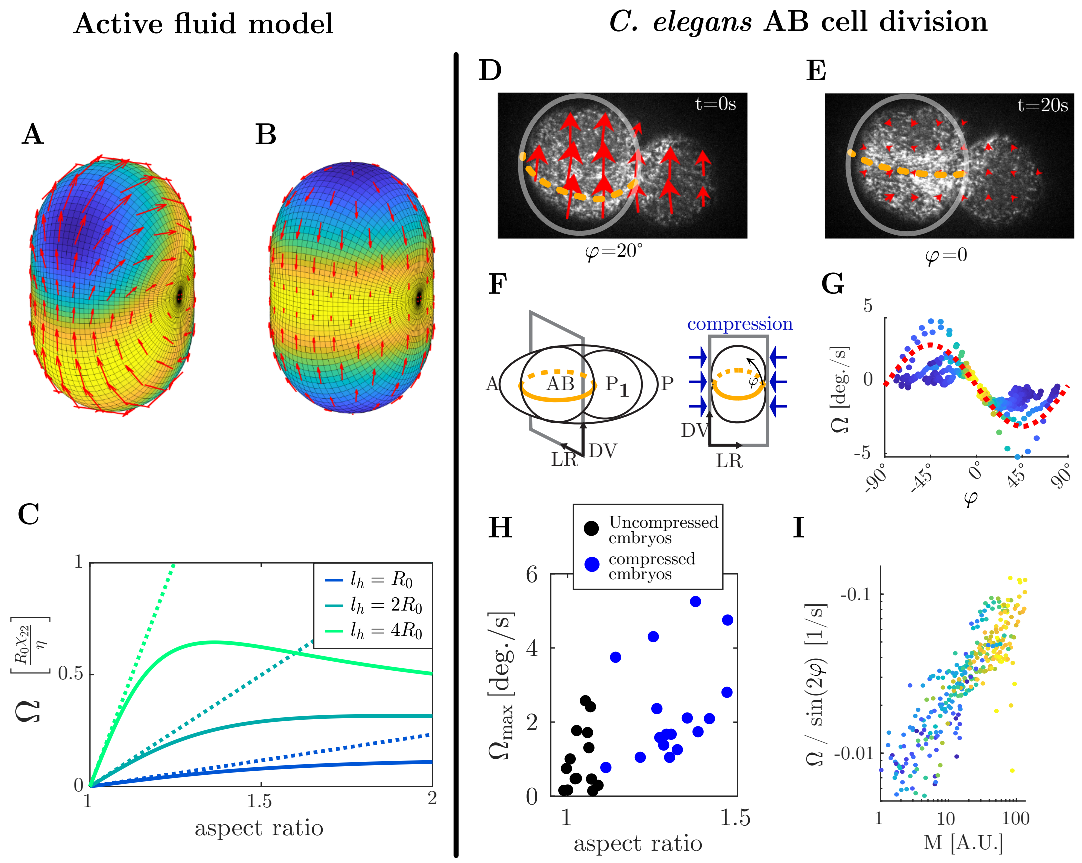

Figure 3.3: Rotation resulting from misalignment between the pattern of active tension and the surface geometry A,**B**: numerical solutions of the flow field (red arrows) for a ring of active tension χ denoted by the color (blue: $\chi = -1$, yellow: $\chi = 1$) for an elongated sphere with an aspect ratio of 1.5, with $l_h = 2R_0$, $\alpha = 1$. **C**: Plot of the deformation-triggered rotation, corresponding to the $l = 1, m = 0$ component of the rotational flow field (Eq. E.38), obtained from numerical solutions for shapes and tension patterns as in **A** for different hydrodynamic lengths and aspect ratios with $\alpha = 1$. **D-I**: analysis of experimental data obtained by Teije C. Middelkoop, as published in [167]. **D**, **E**: Cortical surface of a 2-cell *C. elegans* embryo expressing Lifeact [185] before (**D**) and after (**E**) the whole-embryo rotation. Red arrows denote flow field from PIV. φ denotes the angle of the cytokinetic ring, indicated by the orange dashed line, with respect to the short axis of the AB cell in the DV-LR plane. **F**: Schematic of the 2-cell embryo during AB cell division with blue arrows indicating compression of AB cell in the DV-LR plane due to mounting in the experimental setup. **G**: Angular velocity Ω of rotation as a function of the ring angle φ with respect to the short axis in the DV-LR plane. Colored points are single time points from single embryos. The color denotes the relative timing with respect to onset (blue) and end (yellow) of the whole embryo rotation. Red dashed line is $A \sin 2\varphi$ with $A = 2.5\,\mathrm{deg}/s$. Ω was obtained using PIV from embryos expressing flourescently labelled myosin. Final value of φ for each embryo was determined from the average DV intensity profile of the cortical layer of the AB cell, from this Ω was integrated to obtain φ for earlier time points. **H**: Maximal absolute rotation speed for embryos subject to varying degress of compression. Aspect ratio is the ratio of the long axis over the short axis of the AB cell in the DV-LR plane. **I**: Same data as in **G** but plotting $\Omega / \sin 2\varphi$ as a function of the intensity M of flourescent myosin in the ring.

of the stress regulator pattern c and hence the active tension pattern χ. Thereby $\delta\Omega$ yields a rotation of the tension pattern towards a configuration where $\cos[m(\varphi_{\chi,lm} - \varphi_{R,lm})] = -1$, which is a configuration where the cortical tension χ is maximal at inwardly deformed sections of the surface, i.e. where δR is minimal.

Let us consider for example a contractile ring on an elongated cell, which we construct in terms of the $l = 2$ and $m = 0, \pm 2$ spherical harmonics components of χ and δR such that the geometric long axis and the plane of the ring are both orthogonal to the z axis (Fig. 3.3A,B). Then, $\Delta\varphi = \varphi_{\chi,22} - \varphi_{R,22}$ defines the azimuthal angle between the ring and the long axis. Due to the rotation $\delta\Omega$, the tension pattern rotates towards $\cos 2\Delta\varphi = -1$, corresponding to a ring that is orthogonal to the long axis. Thereby, the circumference is minimized, such that we may understand the rotation as the result of an effective line tension of the contractile ring.

Recently such a rotation of the entire cortex was indeed observed during the alignment of the AP axis with long axis of the *C. elegans* zygote [99]. Importantly, Eq. 3.29 yields no aligning rotation for polar modes ($l = 1$). Thus, a purely polar pattern of active tension, corresponding to χ_{1m}, does not drive an aligning rotation with the long axis of the cell in first order of the shape anisotropy δR. This explains why, a contractile ring, the pseudo-cleavage furrow, is required for rapid alignment of the AP axis with the long axis of the *C. elegans* zygote, whereas polar asymmetry of actomyosin tension on its own is found to yield only slow alignment [99].

Also the rotation of the 2-cell embryo in Fig. 3.3D coincides with the formation of a contractile ring, the cytokinetic ring of the AB cell, visible as a white band of increased actin intensity in Fig. 3.3D,E. After the rotation, this band always lies in the imaging plane (Fig. 3.3E). Importantly, the embryos are compressed in the experimental setup such that the shape of the egg shell is non-axisymmetric around its longest axis corresponding to the AP axis of the embryo (Fig. 3.3F). Thus, the cross section of the AB cell in the orthogonal plane, the DV-LR plane, shows a well defined long axis that is often longer than the extension of the AB cell along the AP axis. In the experimental setup, the imaging plane is parallel to this long axis of the AB cell. Thus, the rapid rotation of the 2-cell embryo aligns the cytokinetic ring perpendicular to the long axis of the AB cell (corresponding to $\varphi = 0$ in Fig. 3.3G). Together with our model, this suggests that active tension in the cytokinetic ring drives this rotation due to misalignment between the pattern of actomyosin tension and the geometry of the egg shell.

In the following, we set out to test this hypothesis quantitatively. Eq. 3.29 yields that the rotation is proportional to the product of misalignment and active tension, i.e.

$$\delta\Omega = -\frac{1}{\tau_{\text{eff}}} |\chi_{2,2}| \sin(2\varphi), \tag{3.30}$$

with $\varphi = -(\varphi_{\chi,22} - \varphi_{R,22})$ being the axis of the ring with respect to the shorter axis of the cell in the DV-LR plane. $\chi_{2,2}$ corresponds to the level of tension in the cytokinetic ring. Importantly, this relation is more general than the model considered in Eq. 3.29. It generally corresponds to a rotation resulting from the coupling of a dynamic nematic (i.e. the ring pattern) to a static nematic (i.e. the elongated shape) order parameter, as given by the coefficient ζ_Q^2 in our coarse grained model (Eq. 3.3). Only the proportionality constant $1/\tau_{\text{eff}}$ depends on the viscosities and the specific geometry of the system. Thus, we expect the rotation speed of the 2-cell embryo to scale with the ring and the mechanical activity in the ring in the form of Eq. 3.30.

To test this, we analyzed the speed of rotation as a function of the orientation of the cytokinetic ring with respect to the geometric long axis in the DV-LR plane using microscopy images from *C. elegans* embryos with fluorescently labelled myosin molecules. We found that the speed of rotation is indeed maximal for an angle around ±45°, consistent with Eq. 3.30 (Fig. 3.3G). Often, the speed of rotation peaks slightly closer to 0°. This may be understood from an increased level of actomyosin tension at later times, as myosin is still accumulating in the cytokinetic ring. As a proxy for $\chi_{2,2}$ we quantify the intensity of flourescent myosin molecules in the cytokinetic ring M. We calculate M as the $m = 2$ component of the azimuthal profile of the intensity, averaged along the AP axis over the extent of the AB cell. We expect $\chi_{2,2}$ to be a non-linear but monotonously increasing function of M, corresponding to $f(c)$ in our model of the cortex. Indeed we find for the rotation speed Ω of the two-cell embryo that $\Omega/\sin 2\varphi$ increases monotonously with M, consistent with Eq. 3.30.

So far, we considered only linear calculations in terms of the shape anisotropy δR that are quantitatively valid for $\delta R/R_0 \ll 1$. However, the aspect ratio of the AB cell, defined as the ratio of the long axis with respect to the short axis, ranges between 1 and 1.5, corresponding to $\delta R/R_0 > 0.1$ (Fig. 3.3H). To test whether the qualitative insights of our analytical calculations are still valid in such a regime and beyond, we developed a pseudo-spectral method for calculating flow fields in general spherical geometries (see appendix F). With this we calculated the flow field for a ring pattern of active tension on an elongated cell, defined in terms of the spherical harmonic components χ_{2m}, δR_{2m} as before (Fig. 3.3A). From this we determined the speed of rotation as a spherical harmonics component of the flow field (Eq. E.38). We consider hydrodynamic lengths between R_0 and $4R_0$. With this, we find perfect agreement of the numerical results with the analytical calculation (Eq. 3.29) for aspect ratios smaller than 1.1. For larger aspect ratios the rotation speed saturates and even decays for $l_h > R_0$, as the rotation becomes viscosity-limited. Analyzing experimental data from 2-cell *C. elegans* embryos subject to varying degress of compression, we find that the rotation speed does indeed scale with the compression (Fig. 3.3H). Furthermore the rotation speed appears to saturate for aspect ratios greater than 1.1, consistent with a hydrodynamic length that is longer than the embryo.

Taken together, the rotation of the two-cell embryo is in quantitative agreement with a model where myosin-dependent tension in the cytokinetic ring drives a rotation due to misalignment of this active tension pattern with the geometry of the cell cortex. In our model, this aligning rotation results from the shear viscosity of the cortex. In chapter 4, we will further investigate how shear viscosity gives an active fluid film a sense of its geometry by transporting patches of mechanical activity towards certain points in the geometry.

3.3.3 Hertwig's rule as a consequence of torque balance

The DV axis of the *C. elegans* embryo is defined by the division axis of the AB cell. The rotation we studied in the previous section aligns this division axis with the long axis egg shell in the DV-LR plane. Thereby, the DV axis is aligned with the egg-shell geometry. So far, we have understood this process solely in terms of the cytokinetic ring. However, the cytokinetic ring is induced by the spindle apparatus due to spindle-cortex interactions [112]. As such, the spindle is the structure that defines the division axis. During the rotation of the 2-cell embryo, spindle and ring rotate together, which we attribute to cytoplasmic viscosity. Thereby the ring-driven rotation results in alignment of the spindle with the long axis (Fig. 3.4A). In other contexts it has been found that mechanical interactions between the spindle and the cortex align the spindle with respect to an externally controlled pattern of actomyosin tension [187]. In both scenarios the alignment of the cytokinetic ring with an external cue results in a corresponding alignment of the spindle.

Such a cytokinetic ring-based mechanism of alignment is in contrast to how the alignment of the cell division axis with the cell geometry has usually been understood (see section 1.1.7). Hertwig's rule states that a cell divides along their longest axis. This phenomenon has been attributed in particular to mechanical activity on the microtubules of the spindle. In the *C. elegans* AB cell, astral microtubules of the spindle pull at the cell cortex due to the activity of dynein motor proteins [188]. Strikingly, optogenetic over-activation of these pulling forces reveals that they result in short-axis alignment of the spindle, when myosin activity is reduced, thereby contradicting Hertwig's rule (Fig. 3.4C). In the following, we want to understand how such mechanical spindle-cortex interactions counteract the actomyosin driven alignment we have studied in the previous section.

To this end, we model spindle-cortex interactions in terms of an active force density $\mathbf{f}_{\text{spindle}}$ that acts on the cortex. We do not constrain $\mathbf{f}_{\text{spindle}}$ other than that it does not amount to a net force or torque acting on the cortex, since $\mathbf{f}_{\text{spindle}}$ describes cell-internal interactions, i.e.

$$\int_{\mathcal{S}} \mathrm{d}S\, \mathbf{f}_{\text{spindle}} = 0 = \int_{\mathcal{S}} \mathbf{X} \times \mathbf{f}_{\text{spindle}}, \tag{3.31}$$

where the surface $\mathcal{S}$ corresponds to the cell cortex that encloses the cell. These equations may also be derived from understanding $\mathbf{f}_{\text{spindle}}$ as a the contraction of a three-dimensional stress tensor $\sigma_{\alpha\beta}$ of the cytoplasmic material with the normal vector of the surface. In the absence of external forces or torques due to gravitiy or an external magnetic field, force and torque bal-

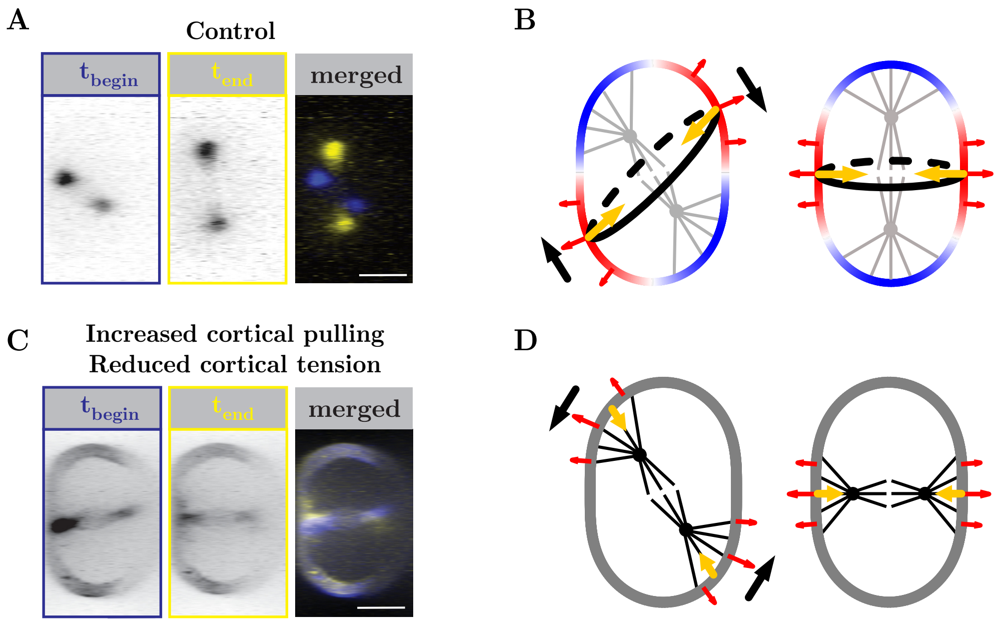

Figure 3.4: Orientation of the cell division axis as a consequence of torque balance. **A**: Spindle of the AB cell in the DV-LR plane imaged by Teije C. Middelkoop using fluorescently labelled tubulin. Long axis of the cell corresponds to vertical axis with which the spindle and thus the division axis aligns. t_{begin} and t_{end} denote time points at the beginning and the end of anaphase during which the whole embryo rotation is observed. **B**: Schematic of a cell rotation driven by tension in the cytokinetic ring (black line) understood in terms of torque balance. Rigid shell enforces shape of the cell by exerting forces (red arrows) normal to the surface that balance an inward force (yellow arrow) resulting from tension in the cell cortex (colored contour with red (blue) denoting elevated (reduced) cortical tension). When the division axis is not aligned with the long axis (left panel), the normal forces from the egg shell amount to a torque resulting in a rotation (black arrows) of the cell. Thereby, cortical tension ensures long-axis alignment of the division axis. **C**: Same as in **A** but for a genetically engineered embryo, where cortical pulling by astral microtubules of the spindles is increased and myosin activity is diminished. We observe short-axis alignment of the spindle. Due to a lack of myosin activity the cell does not divide properly. **D**: Schematic of a cell as in **B**, but for vanishing myosin activity such that forces due to cortical pulling (yellow arrows) by the spindle dominate. Due to torque balance this yields a rotation that aligns the spindle with the short axis.

ances yield $\sum_\alpha \partial_\alpha \sigma_{\alpha\beta}$ and $\sigma_{\alpha\beta} = \sigma_{\beta\alpha}$, from which Eq. 3.31 can be derived using Gauss's theorem.

Force balance (Eq. 1.24) on the cell cortex (which we understand as equivalent to the cell surface) reads

$$\nabla_i \mathbf{t}^{ij} = -\mathbf{f}_{\text{ext}} - \mathbf{f}_{\text{spindle}}, \tag{3.32}$$

where $\mathbf{f}_{\text{ext}} = -\gamma v^i \mathbf{e}_i + f^{\text{n}}_{\text{ext}} \mathbf{n}$ is the force from a rigid container such as the egg shell that enforces the shape of the cortex. Thus, $f^{\text{n}}_{\text{ext}}$ acts as a Lagrange multiplier given by the normal force balance equation (Eq. 1.26), which for our model yields

$$f^{\text{n}}_{\text{ext}} = C_{ij} t^{ij} - f^{\text{n}}_{\text{spindle}}. \tag{3.33}$$

With this, Eq. 3.31 implies

$$0 = \int_{\mathcal{S}} \mathrm{d}S\, \mathbf{X} \times \mathbf{f}_{\mathrm{ext}} = \int_{\mathcal{S}} \mathrm{d}S\, \left[\left(C_{ij} t^{ij} - f^{\mathrm{n}}_{\mathrm{spindle}} \right) (\mathbf{X} \times \mathbf{n}) - \gamma \mathbf{X} \times \mathbf{v} \right], \tag{3.34}$$

i.e. the net torque the rigid container exerts on the cell vanishes. This equation is valid for general surface shapes $\mathbf{X}$. It is particularly informative for an almost spherical surface. For a sphere with radius R_0, we have $\mathbf{X}/R_0 = \mathbf{n} = \mathbf{r}$ such that $\mathbf{X} \times \mathbf{n} = 0$. With this, Eq. 3.34 yields that the component of the cortical flow $\mathbf{v}$ that corresponds to a rigid body rotation vanishes, i.e.

$$\mathbf{\Omega} := \frac{1}{I} \int_{\mathcal{S}} \mathrm{d}S\, \mathbf{X} \times \mathbf{v} = 0, \tag{3.35}$$

where $I = \frac{8\pi}{3} R_0^4$ is the moment of inertia of the spherical surface. As we mentioned in the previous section, cortical tension cannot drive a rigid-body rotation of a spherical cortex, neither can cell-internal mechanical interactions ($\mathbf{f}_{\mathrm{spindle}}$).

In the following, we want to understand the deformation triggered rotation we have found in the previous section (Eq. 3.29) in terms of the balance of torques given by Eq. 3.34. To this end, we consider a slightly deformed sphere (Eq. 3.13) and decompose the flow field $\mathbf{v}$ driven by a given pattern of actomyosin tension χ and cortical pulling $\mathbf{f}_{\mathrm{spindle}}$ as

$$\mathbf{v} = \mathbf{v}_0 + \delta \mathbf{v}, \tag{3.36}$$

where $\mathbf{v}_0$ is the flow field these patterns of mechanical activity would drive on a sphere with radius R_0, whereas $\delta \mathbf{v}$ is a deviation linear in δR. Furthermore, we decompose $\delta \mathbf{v}$ into a deformation-triggered rotation $\delta \mathbf{\Omega}$ and an orthogonal residual $\delta \mathbf{v}_{\mathrm{res}}$ as

$$\delta \mathbf{v} = \delta \mathbf{\Omega} \times \mathbf{X}_0 + \delta \mathbf{v}_{\mathrm{res}}, \tag{3.37}$$

where $\mathbf{X}_0 = R_0 \mathbf{r}$. With this, the balance of torques (Eq. 3.34) yields

$$\delta \mathbf{\Omega} = \frac{1}{I} \left(\delta \mathbf{T}_{\mathrm{N}} + \delta \mathbf{T}_{\mathrm{res}} \right), \tag{3.38}$$

where $\delta \mathbf{T}_{\mathrm{N}}$ is a torque that results from the normal forces $f^{\mathrm{n}}_{\mathrm{ext}}$ due to the rotation $\delta \mathbf{n}$ of the surface normal relative to the undeformed sphere. $\delta \mathbf{T}_{\mathrm{res}}$ results from the friction forces against $\mathbf{v}_0$ due to the deformation. Using $\delta \mathbf{n} = -\mathbf{e}^i \partial_i \delta R$ [116], we obtain

$$\delta \mathbf{T}_{\mathrm{N}} = -\int_{\mathcal{S}} \mathrm{d}S\, \left(\frac{1}{R_0} t_i{}^i - f^{\mathrm{n}}_{\mathrm{spindle}} \right) \mathbf{X} \times \boldsymbol{\nabla} \delta R. \tag{3.39}$$

This means that normal forces can yield a torque, when the surface is anisotropic, i.e. $\boldsymbol{\nabla} \delta R = \mathbf{e}^i \partial_i \delta R \neq 0$. This torque results in a rotation. The torque due to normal forces $\delta \mathbf{T}_{\mathrm{N}}$ is proportional to the viscous and active stresses of the cortex, and to the curvature $1/R_0$. Hence,

$\delta\mathbf{T}_{\mathrm{N}}$ dominates over the torque from friction force $\delta\mathbf{T}_{\mathrm{res}}$ for large hydrodynamic lengths, i.e. $l_h/R_0 \gg 1$. In this regime we have $\delta\mathbf{\Omega} = \delta\mathbf{T}_N/I$. Identifying the axis of rotation as the z axis this yields

$$\delta\Omega = \left(\frac{l_h}{R_0}\right)^2 \sum_{l\geq 2,m>0} \frac{3m}{2\pi}\frac{|f^{\mathrm{n}}_{l,m}|}{\eta}|\delta R_{l,m}|\sin[m(\varphi_{f,lm}-\varphi_{R,lm})], \tag{3.40}$$

where $|f^{\mathrm{n}}_{l,m}|$ and $\varphi_{f,lm}$ are modulus and phase of the spherical harmonic components of the normal forces $f^{\mathrm{n}}_{\mathrm{ext}}$. We observe that a rotation results from a misalignment of the pattern of normal forces and the shape of the cell. It yields a rotation of the cortex towards $\cos[m(\varphi_{f,lm}-\varphi_{R,lm})] = -1$, corresponding to a configuration where the confining container is pulling at the cortex ($f^{\mathrm{n}}_{\mathrm{ext}} > 0$) where the surface of the cell is deformed inward ($\delta R < 0$) relative to the reference sphere. For $\mathbf{f}_{\mathrm{spindle}} = 0$, we recover the results of the previous section, i.e. Eq. 3.29. In particular, we find that a ring of active tension aligns perpendicularly with the long axis of an elongated cell. Here, we understand this is as a consequence of torque balance and the inward normal forces $C_{ij}t^{ij}$, that result from the product of curvature and tension of the cell cortex. For a dividing cell, this implies that the forces that drive the ingression of the cytokinetic ring also yield alignment of the cytokinetic ring perpendicular to the long axis, whenever the cell is free to rotate inside a confining container (Fig. 3.4B). Thus, in such a setting Hertwig's rule is a consequence of torque balance.

In the *C. elegans* AB cell as well as many other animal cells, the spindle pulls at the cortex at the poles of the cell in order to balance the forces required for elongation of the spindle [112, 188]. Again, such forces yield a rotation, when the division axis is not parallel or perpendicular to the long axis. Again, this yields an alignment where $\cos[2(\varphi_{f,l,2}-\varphi_{R,l,2})] = -1$ according to Eq. 3.40. However, the relation between the orientation of the force pattern $\varphi_{f,l,2}$ and the division axis is differs, when pulling forces from the spindle dominate over the forces resulting from cortical tension in the ring. Whereas tension in the cytokinetic ring yields inward forces at the ring (balanced by outward forces from the eggshell), the spindle pulls the poles inward. Hence spindle pulling forces favor a short-axis alignment of the poles of the cell (Fig. 3.4D). Thus, torque balance explains the orientation of the spindle in embryos where spindle pulling forces are over-activated and the myosin activity is inhibited (Fig. 3.4C). Taken together, we find that the orientation of the cell division axis with respect to a confining geometry is a direct consequence of torque balance, when the cell is free to rotate inside the confining container.

3.3.4 Cell elongation induces the formation of a contractile ring

We have found that a rotational flow aligns a ring of active tension orthogonal to the long axis of the fluid surface. This rotation dominates the flow field, when the hydrodynamic length is large. However, in such a regime, our dynamic model of the cortex does not yield the formation of a stable contractile ring, i.e. a ring with increased concentration c of the stress regulator. Instead, a polar pattern consisting of a single contractile patch is observed [135] (see also Fig. 3.2B and

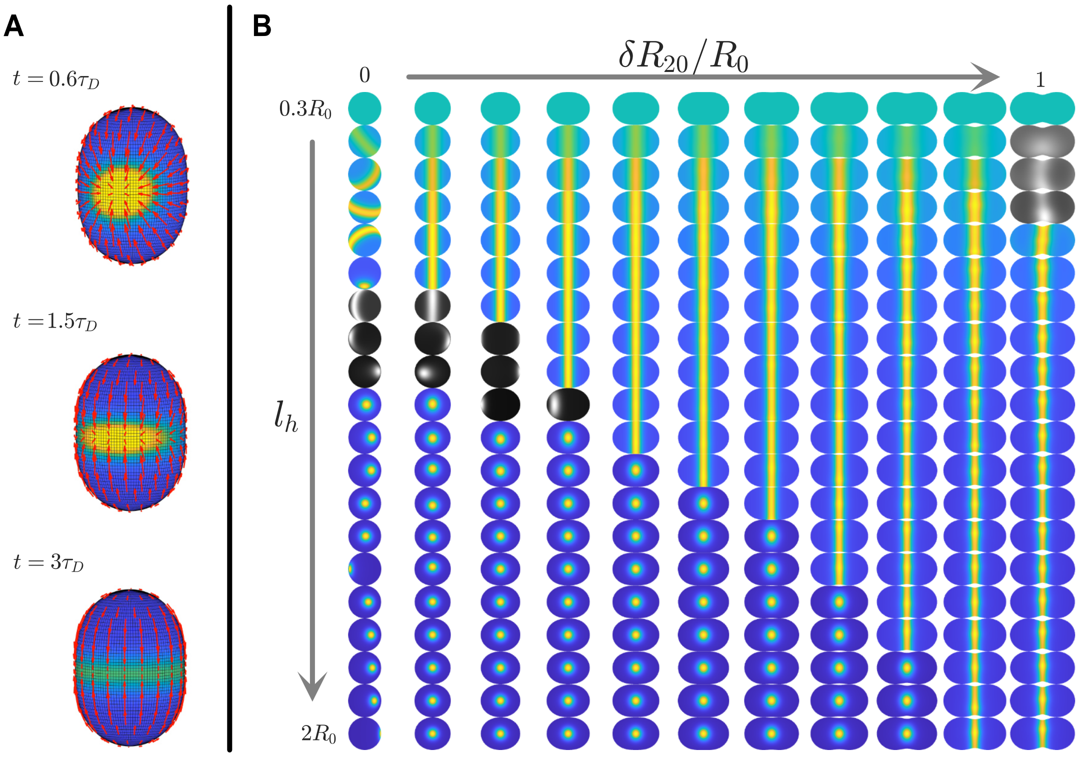

Figure 3.5: Surface geometry shapes non-linear steady states of active fluid film. We solve the non-linear dynamics of an active isotropic fluid film on a deformed sphere with a pseudo-spectral method (appendix F). Color code corresponds to concentration of stress regulator c, with yellow indicating high concentrations and thus high levels of active tension. Red arrows denote the flow field. **A**: Exemplary dynamics where initially a circular patch of high active tension forms and localizes to the saddle of the prolate sphere. There it drives a shear flow that deforms the circular patch into a ring. **B**: Steady state patterns as a function of the hydrodynamic length l_h and the magnitude of the static deformation δR_{20} (Eq. 3.13) corresponding to varying degrees of elongation. Each colored surface shows the steady state pattern on such an axisymmetric surface. Black-white colored surfaces show non-steady states (see Fig. J.5 for examples). Physical parameters are Pe $= 55$, $\alpha = 1$, $k\tau_D = 10$.

left row in Fig. 3.5B). We wondered, whether this pattern changes, when considering a deformed sphere. After all, all components of the flow field depend on the surface geometry. This may yield not only a rotation but also a deformation of the stress regulator pattern.

To this end, we developed a pseudospectral method (appendix F). Briefly, we decompose all flow and concentration field in terms of (spin-weighted) spherical harmonic components, which we use to calculate derivatives on a reference sphere. From this we calculate the derivative on the deformed sphere by making use of the Newman Penrose formalism and by calculating products of fields on a spherical grid. Using the spherical harmonic decomposition we represent the force balance equation as a matrix equation, which we invert to obtain the flow field for a given stress regulator pattern. With this we simulate the dynamics of the stress regulator concentration (Eq. 1.53) for a range of hydrodynamic lengths on surfaces with varying degrees of deformation (Fig. 3.5B).

As expected, we find that stable contractile rings always orient perpendicularly to the long axis of the cell. Thereby, the contractile ring is located at the saddle of the surface geometry, i.e. the minimum in Gaussian curvature. Notably, we find that also for polar patterns the patch of increased active tension localizes to this saddle. Thus, the axis of polarity is oriented perpendicular to the long axis, as predicted by the linear stability analysis in section 3.3.1. That this orientation persists in the non-linear regime can be understood from the principle we have found in section 3.3.2: in the regime of large hydrodynamic length, patches of heightened active tension align with regions of the surface that are deformed inward relative to a reference sphere (Eq. 3.29). In chapter 4, we will study the phenomenon of contractile patches localizing with saddle geometry for general surface geometries.

Strikingly, we observe the formation of stable contractile rings in a broad range of parameters. For larger hydrodynamic length, we often observe the formation of a polar patch in the linear regime as expected from linear stability analysis. For sufficiently strong deformations, we observe that the initially circular patch of active tension drives a shear flow that deforms the patch into a ring (Fig. 3.5A). As for the deformation triggered-rotation (Eq. 3.29), the flow field is a result of the pair of anisotropies of surface geometry and tension pattern. Specifically, we understand the shear flow driven by a circular patch as a consequence of the nematic anisotropy of the local surface geometry at the saddle, where the contractile patch is localized. We will further investigate this phenomenon in the next chapter. Taken together, an elongation of surface yields the formation of a stable contractile ring, as the surface geometry reshapes the pattern by reshaping the flow field.

Notably, we find also parameters where the dynamics do not converge to a steady state pattern. In particular, we observe rotations of a a single contractile patch on a sphere. This rotation does not correspond to a rotational flow but to a travelling wave of the concentration field (see Fig. J.5). We have predicted these rotations in our coarse-grained model (Fig. 3.1F). As such, they reflect the non-equilibrium nature of the model (see section 3.1). When considering a fluid film with identical material parameters on a deformed sphere, we observe complex dynamics, where the circular patch repeatedly deforms into a ring and viceversa (see Fig. J.5). The dynamics do not appear to be strictly oscillatory and might show some intermittency. This suggests, that coupling to shape anisotropy can give rise to chaotic dynamics in an active isotropic fluid. We plan to analyze this more carefully in the future.

3.4 Discussion

In this chapter, we have investigated how the shape of a cell impacts on patterns that form in the cell cortex. To this end, we developed analytical and numerical tools to solve and understand a hydrodynamic model of the cortex as well as experimental data from the *C. elegans* 2-cell embryo. We found that active tension in the cell cortex drives a whole cell rotation, when the pattern of active tension is not aligned with the geometry of the cell surface. As mechanical activity is controlled by chemical patterns, this rotation yields robust alignment of chemical patterns with the surface geometry. In particular, we found that a contractile ring aligns perpendicularly to the long axis of the cell. Thereby, the division axis of the *C. elegans* AB cell is aligned with the long axis of the cell. We note that such a ring-driven rotation has recently also been studied in the *C. elegans* zygote [99]. As we discussed in section 1.1.6, cortical tension in the pseudo-cleavage furrow, a structure akin to the cytokinetic ring, drives a rotation that aligns the AP axis with the long axis of the egg shell. This was understood using numerical simulations of an active nematic fluid and, phenomenologically, in terms of an effective line tension. Here, we have generalized this phenomenon to general anisotropies of shape and tension patterns in an active isotropic fluid.

Importantly, we found that a polar pattern of active tension does not yield parallel alignment of the axis of polarity with the long axis. In the linear regime, we found that the axis of polarity aligns perpendicularly to the long axis for strong mechanical activity, in particular for small hydrodynamic length. In the non-linear regime we also find perpendicular alignment, as the domain of high active tension localizes to the saddle of a prolate sphere. These results explain why the alignment of the AP and the DV axis of the *C. elegans* embryo with the long axes of the egg shell relies on rings of myosin-generated tension.

Furthermore, we also incorporated mechanical interactions of the cortex with the spindle. Using torque balance, we found that the cytokinetic ring and mechanical spindle-cortex interactions act antagonistically to define the orientation of the cell division axis with respect to the geometry of a cell, in agreement with experimental results. In particular, this implies that the forces that drive the ingression of the cytokinetic ring ultimately enforce an alignment of the division axis with the long axis of the cell, whenever the cell is free to rotate inside a confining shell. Taken together, we provided physical explanations for the alignment of body and cell division axes with a confining geometry. In particular we connected Hertwig's rule, i.e. the principle of cells dividing along their longest geometric axis, to the conservation of angular momentum.

Finally, we found that the surface geometry can not only yield alignment but reshapes the pattern. In particular, we numerically found that an elongated surface shape yields the formation of a stable contractile ring for a wide range of material parameters. This may serve as a feedback mechanism for the formation of the cytokinetic ring. Notably, the formation of a band of active tension has also been found in perturbed *C. elegans* zygotes [105]. In contrast to wild type embryos, the formation does not appear to be triggered by cortex-centrosome interactions. Also in contrast to wild type embryos, no aligning rotation is observed. This suggests that in the absence of other triggers the shape of the (P_0) cell defines the chemical patterns that form in the cortex. It remains to be tested, whether our model is sufficient to explain the experimentally observed geometry dependence.

Chapter 4

Geometry sensing by active flows

Biological cells are often said to sense their environment, as they respond to external stimuli in a complex yet predictable way that is beneficial for the survival of the cell or the organism the cell belongs to [189, 190]. A well studied example is chemotaxis: Bacterial or eukaryotic cells move towards a nutrient or away from a poison, as if they could smell it [190]. This phenomenon relies on receptor proteins and a complex network of signalling proteins that affect the cilia, flagella or cell cortex that give a cell its motility. Thereby the direction of movement is aligned with the gradient of a chemical concentration [190, 24].

Cells also respond to mechanical stimuli like squeezing the cell into a certain shape [189, 99, 191, 107]. In particular, cells tend to divide along their longest geometric axis (see section 1.1.7). We may thus say, cells sense their shape. Also in other contexts, biological cells have been found to sense their shape, specifically the curvature of their surface (see section 1.1.6). However, such curvature sensing is typically understood as curvature-dependent binding of specific proteins from the cytoplasm to the plasma membrane or other lipid membranes [101]. In the previous chapter, in contrast, we have shown that diffusive or advective movements of molecules within the cell surface naturally result in geometry-dependent patterns, giving a cell a sense of its longest axis. In particular, we have found that in an active fluid film such as the cell cortex, contractile patches localize to the saddle of a prolate spherical surface. In this chapter, we generalize this phenomenon to active particles in fluid films for general surface geometries and topologies. We demonstrate that such localized sources of mechanical activity sense the geometry by moving in response to the local flow field, and investigate what measure of the surface geometry they sense.

Throughout this chapter, we consider a static shape of the surface. We will start by studying contractile patches on a torus, where we observe that they move down the gradient of the geometric potential, a measure of the intrinsic surface geometry (section 4.1). Motivated by this, we investigate further how the surface geometry shapes the flow field of an active fluid. To this end, we use isothermal coordinates, which allows us to map the flow field of a curved fluid film to a flat fluid film (section 4.2.1). Furthermore, we investigate in analytical terms how the flow field changes upon static infinitesimal deformations of the surface (sections 4.2.2 and 4.2.3). Using these insights, we investigate how the geometry of a surface defines attractors towards which contractile points are advected (section 4.3.1). Furthermore, we investigate how general anisotropies of the surface geometry yield deformations of a contractile patch (section 4.3.2). In section 4.4, we test whether all these analytical calculations allow us to understand the patterns that emerge in an active isotropic fluid for complex surface geometries. Finally, we study active anisotropic particles embedded in a curved fluid film. These particles rotate and move by locally coupling to the flow they drive. In section section 4.5, we show how this flow coupling gives such particles a sense of the surrounding surface geometry.

4.1 Geometry sensing by an active isotropic fluid

4.1.1 Patches of active contractility are advected towards saddle geometries

In section 3.3.4, we investigated pattern formation in an isotropic active fluid film with anisotropic surface geometry. Using numerical solutions of the concentration dynamics, we found that steady state patterns emerge where a patch with a high concentration of the stress regulator colocalizes with the saddle of a prolate spherical surface. A high concentration $c > c_0$ corresponds here to a large active isotropic tension driving in-plane contractions. We have found that this colocalization of contractile patches with the saddle arises only in the non-linear regime, where contractile patches are advected towards the saddle (see sections 3.3.1,3.3.2). To illustrate this phenomenon, we initialize the system with a circular patch of elevated tension between the saddle and a pole (Fig. 4.1A), corresponding to a steady state of the model on an isotropic spherical surface [135]. On the prolate sphere, the flow driven by the circular patch is anisotropic as is the surface geometry. Advection by this flow yields a movement of the patch while keeping the circular shape of the patch largely unchanged. This movement can be understood as particular example of the rotation we discussed in section 3.3.2. Thereby, the contractile patch moves towards the saddle of the prolate sphere, where the Gaussian curvature κ is minimal. We wondered whether this advection of contractile patches towards minima in Gaussian curvature is also found for other surfaces.

To this end, we study the same minimal model as before but on a surface with toroidal topology. Again, we use a pseudo-spectral method to solve the dynamical equation numerically, using a Fourier instead of a spherical harmonics decomposition (appendix F). We consider identical physical parameters and a surface of similar size. With this, we find that a circular patch is advected towards the inner surface of the torus, i.e. the minimum in Gaussian curvature (Fig. 4.1B). Moreover, we find that a shear flow emerges that reshapes the circular patch into a ring spanning the inner surface of the torus, similarly to our observations on a prolate sphere (Fig. 3.5A). Thus, both on a prolate sphere and on a torus, the saddle geometry attracts contractile patches and facilitates the formation of a contractile band.

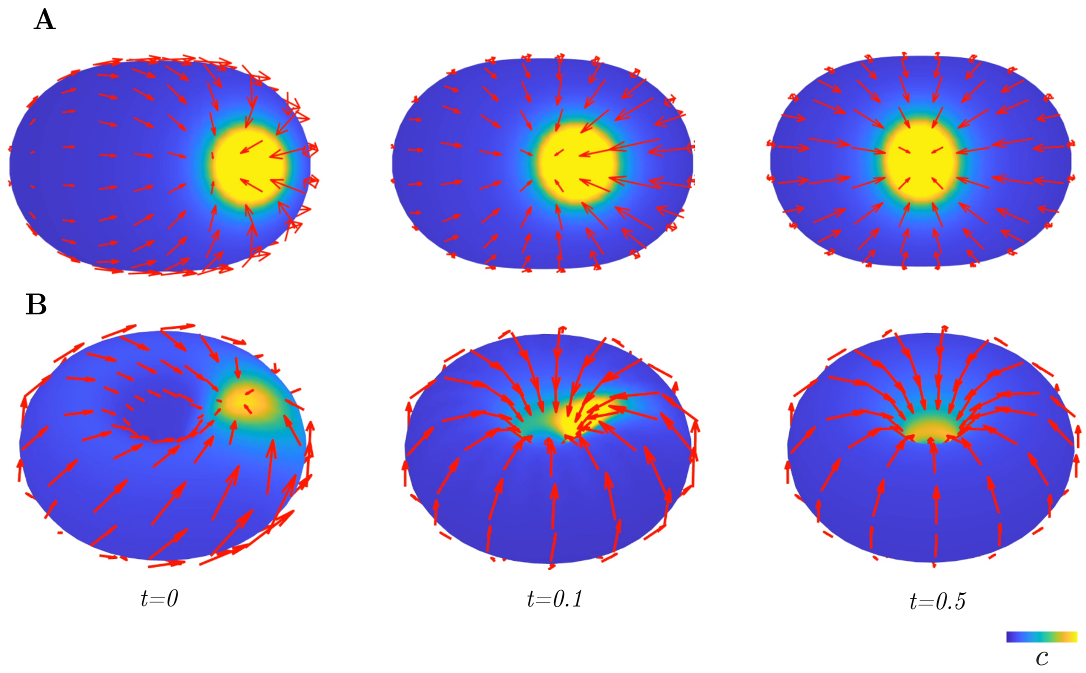

Figure 4.1: Contractile patches in a fluid film are advected towards saddle geometries. A,B: Snapshots of numerical solutions of Eq. 1.53 using a pseudo-spectral method (appendix F) for a prolate spherical geometry (**A**) and for a torus (**B**). Red arrows denote flow field and color denotes stress regulator concentration c. Physical parameters given in Table J.4. In both cases, we initialize with a circular patch which was obtained as the steady state on a sphere (**A**) or a cylinder with periodic boundary conditions (**B**). In both cases a steady state was reached, i.e. we did not observe considerable changes in c after $t = 0.5$ up to $t = 20$.

4.1.2 Contractile points sense the geometric potential of a torus

We set out to understand in more fundamental terms why a contractile patches move to the minimum of Gaussian curvature. To this end, we calculate the flow field of a tension monopole, i.e. stress regulator concentration $c = \delta(s^1 - s^1_0)\delta(s^2 - s^2_0)/\sqrt{g}$. As we are not aware of analytical solutions to this problem, we approximate the flow field numerically using a staggered grid (appendix G). From this, we calculate the velocity $\mathbf{v}_{\text{mono}}$ (green arrow in Fig. 4.2A) of the contractility monopole (see appendix I for a discussion of such velocity multipoles on a curved surface). $\mathbf{v}_{\text{mono}}$ corresponds to the average velocity in the immediate surrounding of the contractility monopole (Fig. J.1). It gives the direction in which a small contractile patch moves due to advection. Calculating $\mathbf{v}_{\text{mono}}$ for contractility monopoles at different positions on the surface yields a vector field that defines an attractor and a repeller (solid and dashed lines, respectively, in Fig. 4.2B). Small contractile patches are advected away from the repeller towards the attractor. For the given parameters, contractility monopoles are advected away from the outer side of the torus and accumulate at the inner side of the torus (i.e. div $\mathbf{v}_{\text{mono}} = \nabla_i v^i_{\text{mono}} < 0$, Fig. 4.2B). Importantly, $\mathbf{v}_{\text{mono}}$ depends only on the viscosities η, η_b and the friction coefficient γ defining the hydrodynamic length $l_h = \sqrt{\eta/\gamma}$. For all parameters we tried (with $0 \leq \alpha \leq 10$), we find that attractor and repeller coincide with the lines of minimal and maximal Gaussian curvature, respectively (Fig. 4.2C). This implies that shear viscosity is sufficient to yield the advection of a contractile point towards a saddle. Also in section 3.3.2, we have found that the sign of the rotation that aligns patterns of active tension with the surface geometry is independent of material parameters. Strikingly, this analytical result (Eq. 3.29), reveals that the aligning rotation vanishes for vanishing shear viscosity (corresponding to the limit $\alpha \to \infty$ with $\alpha l_h^2 = \text{const.}$) Together, this suggests that shear viscosity attracts contractile points to minima in Gaussian curvature.

To gain insight how such sense of Gaussian curvature results from shear viscosity, we write the flow field v_i as a Hodge decomposition, i.e. in terms of a harmonic field $\mathbf{v}_h$ and two (pseudo) scalar fields A, B that correspond to the irrotational and rotational flow components respectively (Eq. 1.67). With this decomposition, the tangential force balance equation of an isotropic active fluid with a pattern of active tension χ yields

$$\eta(\alpha+1)\Delta\Delta A + (2\eta\kappa - \gamma)\,\Delta A + 2\eta(\partial_i\kappa)(\partial^i A) + 2\eta(\epsilon^{ij}\partial_i B + v_h^j)(\partial_j\kappa) = -\,\Delta\chi \tag{4.1}$$

$$\eta\Delta\Delta B + (2\eta\kappa - \gamma)\,\Delta B + 2\eta(\partial_i\kappa)(\partial^i B) - 2\eta\epsilon_i{}^j(\partial^i A + v_h^i)(\partial_j\kappa) = 0 \tag{4.2}$$

$$P_h[2\eta\kappa(g^{ij}\partial_j A + \epsilon^{ji}\partial_j B + v_\mathrm{h}^i)] - \gamma v_\mathrm{h}^i = 0, \tag{4.3}$$

where P_h is the projection yielding the harmonic component of a vector field in the sense of a Hodge decomposition. On a closed surface with constant Gaussian curvature ($\partial_i\kappa = 0$), these three equations are uncoupled yielding $B = 0 = v_h^i$. Hence, on a sphere, the flow field driven by an arbitrary pattern of active tension χ is irrotational. This is not the case, however, on an anisotropic surface, such as the torus in Fig. 4.2. Notably, the coupling can be understood as the result of an effective friction coefficient $\gamma_\mathrm{eff} = \gamma - 2\eta\kappa$ (see also Eq. 1.69). Thereby, gradients of Gaussian curvature translate into a gradient of effective friction:

$$\partial_i\gamma_\mathrm{eff} = -2\eta\partial_i\kappa \tag{4.4}$$

In Fig. 4.2D-F, we plot a Hodge decomposition of the flow field of a contractility monopole obtained numerically (see appendix G.4). Strikingly, we find that rotational and harmonic flow component yield the monopole velocity $\mathbf{v}_\mathrm{mono}$ (green arrows), whereas the contribution to $\mathbf{v}_\mathrm{mono}$ from the irrotational component is on the order of the numerical error. Thus, the transport of contractile points towards the saddle is a consequence of the coupling of the flow components that results from the effective friction gradient $-2\eta\partial_i\kappa$. In intuitive terms, a contractile point is dragged towards the saddle due to an increased effective friction at the saddle that results from the product of shear viscosity and Gaussian curvature.

We use this insight to calculate the monopole velocity $\mathbf{v}_\mathrm{mono}$ analytically for a slightly anisotropic surface geometry, i.e. for $\kappa = \kappa_0 + \delta\kappa$ with $\kappa_0 = \text{const.}$ and $l_h^2\delta\kappa \ll 1$. We have found that $\mathbf{v}_\mathrm{mono}$ primarily results from a flow field that is constant around the position of the monopole and thus only friction limited (see Fig. 4.2E,F). Furthermore, we have found that this flow field results from the effective friction $\delta\gamma_\mathrm{eff} = -2\eta\delta\kappa$. Thus we can write the flow field $\delta\mathbf{v}$ that results from

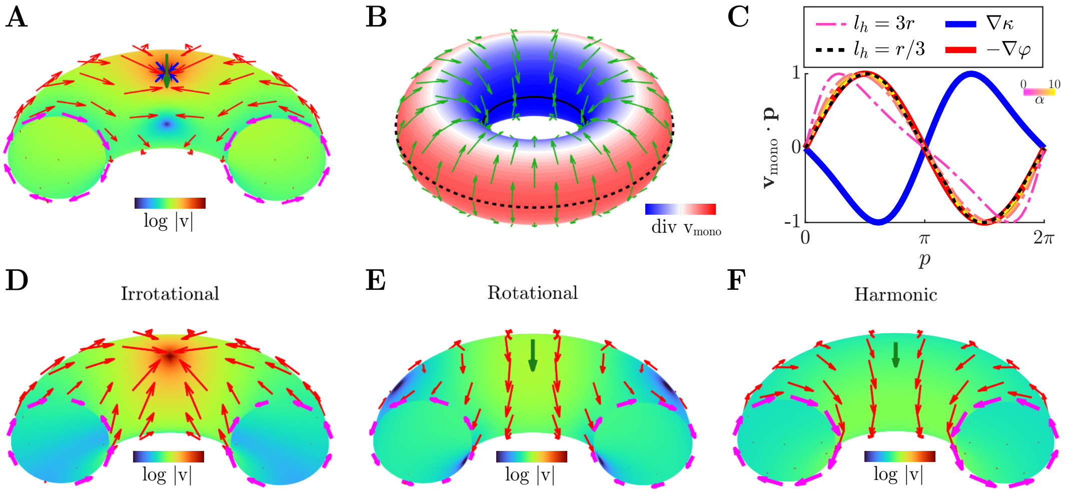

Figure 4.2: Tension monopoles on a toroidal surface drive transport along gradients of the geometric potential. **A**: Numerical solution (see appendix G) of the flow field around a tension monopole on a torus. For better illustration, only half the torus is shown. Red arrows indicate fluid velocity, blue arrows denote forces the monopole exerts onto the fluid film and green arrow denotes monopole velocity $\mathbf{v}_{\mathrm{mono}}$ corresponding to an average velocity around the monopole position (see appendix I and Fig. J.1). Color denotes modulus of fluid velocity on a logarithmic scale. Magenta arrows show poloidal velocity along a cross-section of the torus, where we observe a transport of the entire fluid film in a poloidal direction. **B**: Field of monopole velocities $\mathbf{v}_{\mathrm{mono}}$ (green arrows), obtained by calculating the flow field around monopoles as in **A** for different monopole positions. This yields a repeller (dashed line) and an attractor (solid line) of contractile points, i.e. tension monopoles. Color denotes the divergence of the field $\mathbf{v}_{\mathrm{mono}}$. **C**: Plot of $\mathbf{v}_{\mathrm{mono}}$ as in **B** as a function of the poloidal coordinate p for different hydrodynamic lengths, i.e. $l_h = 3R_1$ (colored dashed lines with color denoting $\alpha = \eta_b/\eta$) and $l_h = R_1/3$ (black dashed line, no considerable dependence on α is found for $\alpha < 10$, when normalizing the curves with respect to the maximum) . Blue line denotes gradient of Gaussian curvature κ. Red line shows the gradient $-\nabla\varphi$ with φ denoting the geometric potential (Eq. 4.8). We observe that numerical solutions for $\mathbf{v}_{\mathrm{mono}}$ collapse onto this line for small hydrodynamic lengths as predicted by Eq. 4.7. All curves denote projections onto the poloidal unit vector $\mathbf{p}$ and each curve is normalized with respect to the maximum modulus. **D**-**F**: Plots as in **A** of a Hodge decomposition of the flow field in **A** (see appendix G.4). We observe that the monopole velocity (green arrow) is due to the rotational and harmonic components and that the large-scale transport of the fluid film (as evident from the poloidal velocity (magenta) in the cross-sections) is due to the harmonic component.

the anisotropy $\delta\kappa$ close to the monopole as

$$\gamma\delta\mathbf{v} = 2\eta\delta\kappa\mathbf{v}_0, \tag{4.5}$$

where $\mathbf{v}_0 = \boldsymbol{\nabla} A_0$ is the flow field for $\delta\kappa = 0$. Close to the contractility monopole at $\mathbf{r}_{\mathrm{mono}}$, viscous forces dominate yielding

$$\eta(\alpha+1)\Delta_{LB}A_0 = -T\delta^{(2)}(\mathbf{r}-\mathbf{r}_{\mathrm{mono}})/\sqrt{g}. \tag{4.6}$$

where $T > 0$ is the magnitude of the tension monopole. With this we obtain

$$\mathbf{v}_{\mathrm{mono}} = \frac{1}{S_\epsilon}\int_{U_\epsilon(\mathbf{r}_{\mathrm{mono}})} \mathrm{d}S\,\delta\mathbf{v} = -2\frac{T}{\gamma(\alpha+1)}\boldsymbol{\nabla}\delta\varphi(\mathbf{r}_{\mathrm{mono}}), \tag{4.7}$$

where $U_\epsilon(\mathbf{r}_{\mathrm{mono}})$ denotes a neighborhood with surface area S_ϵ. We used here integration by parts, omitting boundary terms, which is valid for large enough U_ϵ such that A_0 vanishes on the boundary of U_ϵ. $\delta\varphi$ is the geometric potential associated with the anisotropy $\delta\kappa$ of the intrinsic surface geometry (Eq. 1.71). We introduced the geometric potential φ in section 1.3.2. It determines the metric of a surface in isothermal coordinates. As such, it defines the intrinsic geometry of a surface. Here, we find that a contractile point moves down the gradient of φ. For a torus, we find

$$\varphi = \varphi_0 - 2\log\left[\frac{R_1}{R_2} - \cos(p)\right], \tag{4.8}$$

with p being the poloidal coordinate and R_1, R_2 being the radii of the torus (see Eq. F.24 for the corresponding isothermal parametrization of a torus). This yields an analytical expression for the velocity of a contractility monopole on a torus for $l_h \ll R_1$. Strikingly, we find that the numerical results agree perfectly with this analytical calculation for small hydrodynamic length or large α (Fig. 4.2C). Taken together, we find that shear viscosity yields a transport of contractile points along gradients of the geometric potential on a torus. Thus, patches of active isotropic tension in a fluid film act as sensors of the geometric potential. In the following, we will generalize this insight to general surface geometries.

4.2 Deformation response of active flow in general surface geometries

In the previous section, we have found that the shear viscosity of a fluid film gives rise to the transport of a contractile point along gradients of the geometric potential for a slightly anisotropic surface geometry. This insight was based on linear calculation in terms of the anisotropy of the surface geometry. However, biological surfaces often have complex shapes far away from any isotropic idealization. In the following, we investigate in analytical terms how such surface geometries shape the flow field, going beyond small deformations of an isotropic surface. To this end, we adopt the formalism of spin-weighted fields (see section 1.3.1) and use an isothermal parametrisation of the surface (see section 1.3.2). With this, we present two approaches to understanding the geometry dependence of active flow: First, we show how the flow field of a curved fluid film can be mapped to a flat one by rescaling the viscosity and the friction coefficient. Thereby, gradients in measures of the surface geometry are mapped to gradients in material properties (section 4.2.1). Second, we study the change in the flow field upon an infinitesimal deformation of the surface in terms of Green's functions (sections 4.2.2 and 4.2.3).

4.2.1 Mapping anisotropies of the surface geometry to effective gradients in viscosity and friction

The geometry of a surface has a profound impact on the flows that emerge in an active fluid (see the previous section and chapter 3 for examples). In the previous section we have found that some of this impact can be understood in terms of an effective friction that results from the product of shear viscosity and Gaussian curvature. We found that a contractile point is effectively dragged towards the maximum of effective friction which is the saddle of a torus. Here we want to extend this approach to general surface geometries by using isothermal coordinates, which can be found for any surface (see section 1.3.2). In isothermal coordinates the metric and, thus, the intrinsic geometry of the surface is defined by a single real valued field $\varphi(s^1, s^2)$. We call φ the geometric potential, as it is related to the Gaussian curvature κ by a Poisson equation. In these coordinates, the Laplace-Beltrami operator Δ_{LB} is equivalent to the Laplace operator Δ_0 up to a rescaling by $e^{2\varphi}$ (Eq. 1.72). Furthermore, the covariant derivative operators $\eth$ and $\bar{\eth}$ from the Newman Penrose formalism can be expressed in terms of the Wirtinger derivatives $\partial_{\bar{z}}$ and ∂_z by rescaling the original field and its derivative by powers of the length scale $l = e^{\varphi}$ (Eq. 1.73). We use these relation to understand the impact of the surface geometry on the flow field in terms of a rescaled viscosity and a rescaled friction coefficient.

We consider a general force density ${}_{(1)}f$ that drives the flow field. In sections 4.3 and 4.5, we understand this force density as the divergence of some pattern of active stresses. As before we use a Hodge decomposition of the flow field (1.67). The derivative operators motivate a rescaling of flow field and force density given by

$$ {}_{(1)}f^r = e^{\varphi}\,{}_{(1)}f, \quad {}_{(1)}v^r = e^{\varphi}\,{}_{(1)}v = 2\partial_{\bar{z}} + {}_{(1)}v^r_h. \tag{4.9}$$

where the rescaled harmonic flow field ${}_{(1)}v^r_h = e^{\varphi}\,{}_{(1)}v_h$ obeys

$$\Delta_0\,{}_{(1)}v^r_h = 0. \tag{4.10}$$

With this, we evaluate the tangential force balance equation of a fluid film that governs the flow field (Eq. 1.69). We find it can be written as

$$2\partial_{\bar{z}}\eta_{\text{eff}}\Delta_0(F + \alpha\,\mathrm{Re}\,F) - \gamma_{\text{eff}}(2\partial_{\bar{z}}F + {}_{(1)}v^r_h) = -\,{}_{(1)}f^r, \tag{4.11}$$

where we introduced an effective viscosity η_{eff} and an effective friction coefficient γ_{eff}, given by

$$\eta_{\text{eff}} = e^{-2\varphi}\eta, \quad \gamma_{\text{eff}} = \gamma - 2\eta\kappa. \tag{4.12}$$

Eq. 4.11 and 4.10 are differential equations that determine the flow field in terms of F and ${}_{(1)}v^r_h$. Apart from η_{eff} and γ_{eff}, these equations are independent of the surface geometry. Thus, they allow us to calculate the flow field of a fluid film with arbitrary surface geometry by mapping it to a flat fluid film with effective heterogeneities in friction and viscosity.

As observed in the previous section the product of Gaussian curvature and shear viscosity gives rise to an effective friction γ_{eff}. Thereby, minima in Gaussian curvature correspond to maxima in effective friction. The geometric potential defines a rescaled viscosity η_{eff} that is maximal at minima in φ. We note that the effective viscosity η_{eff} does not correspond to a shear viscosity, when φ is non-constant. Instead, η_{eff} defines an effective bulk viscosity $(1 + \alpha)\eta_{\text{eff}}$ and an ef-

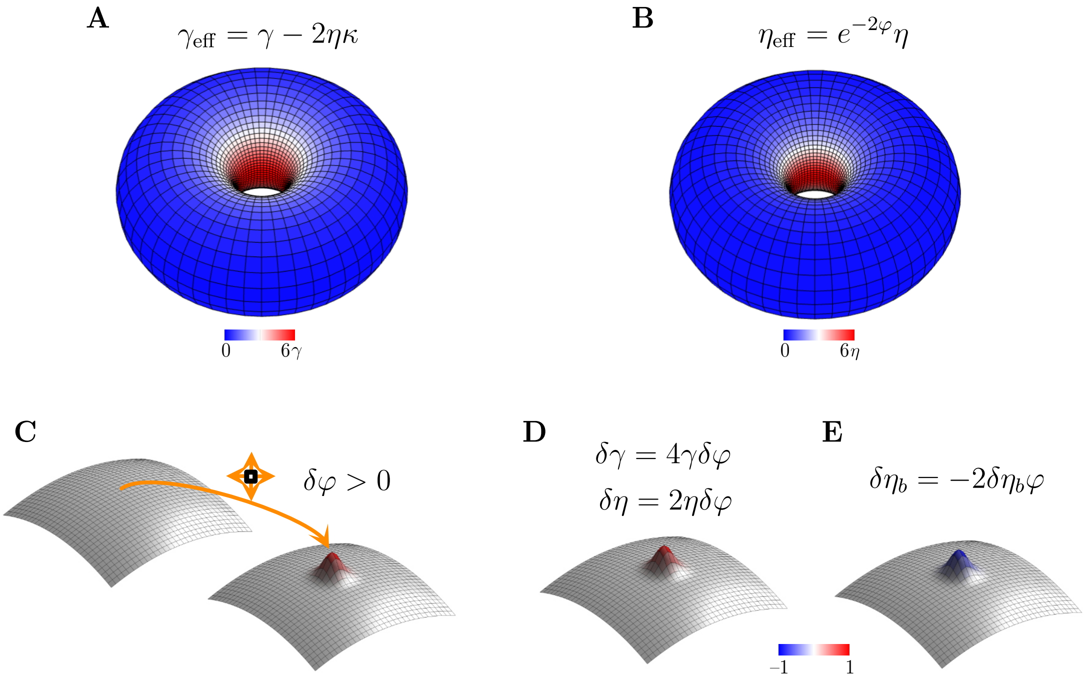
A
$\gamma_{\text{eff}} = \gamma - 2\eta\kappa$
0
6γ
B
$\eta_{\text{eff}} = e^{-2\varphi}\eta$
0
6η
C
$\delta\varphi > 0$
D
$\delta\gamma = 4\gamma\delta\varphi$
$\delta\eta = 2\eta\delta\varphi$
E
$\delta\eta_b = -2\delta\eta_b\varphi$
−1
1

Figure 4.3: Surface geometry defines effective viscosity and friction gradients As discussed in the main text, the impact of the intrinsic surface geometry on the flow field can be captured by effectively geometry-dependent material properties. **A**,**B**: Plots of effective friction coefficient γ_{eff} and effective viscosity η_{eff} (Eq. 4.12) for a torus with a smaller radius $R_2 = l_h$. See also Fig. 1.13 for a plot of φ and κ. We observe that γ_{eff} and η_{eff} are maximal at the saddle, i.e. the minimum in Gaussian curvature. **C**: Illustration of a surface deformation that corresponds to a localized isotropic expansion $\delta\varphi > 0$ of the surface. **D**: Effective change in shear viscosity η and friction coefficient γ for a localized expansion for vanishing bulk viscosity ($\alpha = 0$). We observe that an expansion of the surface effectively increases viscosity and friction coefficient **E**: Effective change in bulk viscosity for a localized expansion in the regime of vanishing shear viscosity ($\eta \to 0, \eta_b = \alpha\eta > 0$). We observe that an expansion effectively decreases bulk viscosity.

fective rotational viscosity η_{eff}. We understand here a rotational viscosity as an antisymmetric stress that is proportional to the vorticity (corresponding to a scenario where the intrinsic rate of rotation vanishes due to substrate interaction) [120]. In other words, it is torque density acting against the vorticity of the flow. For a non-vanishing hydrodynamic length, γ_{eff} and η_{eff} affect the flow field in a non-local manner. The flow field at position z_v that is driven by a force at position z_f depends on the geometry of all parts of the surface that are connected to z_v and z_f by a length on the order of the hydrodynamic length.

The rescaling of force density and flow field, in contrast, is purely local. Moreover, the rescaling factors for both fields are identical. Thus, the rescaling does not affect the flow field when evaluating the flow field at the same position where it was driven. In this chapter, we focus on localized sources of mechanical activity that are translated, rotated and deformed by the flow field in its immediate surrounding. For these scenarios, the rescaling of force and flow field can be omitted. Instead, we focus on the response to the surface geometry that arises on the hydrodynamic length scale due to the effective geometry-dependent material properties. In particular we will discuss how the effective gradients of viscosity and friction define attractors of contractile points in section 4.3.1.

In Eq. 4.11, φ and κ appear as independent features of the surface geometry that shape the flow field in distinct ways. However, it is the metric and, thus, the geometric potential φ that defines the intrinsic geometry of the surface, including the Gaussian curvature (see Eq. 1.71). For a deformation $\delta\mathbf{X}$ of a surface, it is the associated $\delta\varphi$ that defines the change in the intrinsic surface geometry. $\delta\varphi$ corresponds to locally isotropic area expansions ($\delta\varphi > 0$) and contractions ($\delta\varphi < 0$) of the surface. We would like to understand the impact of such expansions and contractions on the flow field.

When shear viscosity vanishes, Eq. 4.12 yields that a deformation $\delta\varphi$ effectively changes the bulk viscosity as

$$\delta\eta_b = -2\delta\varphi\eta_b \tag{4.13}$$

In words, an expansion of the surface ($\delta\varphi > 0$) relaxes the pressure from bulk viscosity. Thus, we expect that an expansion of the surface amplifies the flow driven by a force density, when the flow is limited only by bulk viscosity and friction.

When bulk viscosity vanishes, the force balance equation in isothermal coordinates reads

$$4e^{-3\varphi}\partial_z\left[\eta e^{2\varphi}\partial_{\bar{z}}\left(e^{-\varphi}\,{}_{(1)}v\right)\right] - \gamma\,{}_{(1)}v = -\,{}_{(1)}f. \tag{4.14}$$

We rescale the force as ${}_{(1)}f^r = e^{3\varphi}\,{}_{(1)}f$ and the velocity as ${}_{(1)}v^r e^{-\varphi}\,{}_{(1)}v$. With this we read off a rescaled shear viscosity $e^{2\varphi}\eta$ and a rescaled friction coefficient $e^{4\varphi}\gamma$. We note that in this case the rescaling factors of flow and force field differ, in contrast to Eq. 4.9. However, we can omit this local rescaling for a localised deformation at a distance, i.e. when $\delta\varphi$ vanishes where the flow is driven (${}_{(1)}f \neq 0$) and where it is evaluated. In this case, the change in the flow field is solely determined by the effective change in shear viscosity and friction coefficient given by

$$\delta\gamma = 4\gamma\delta\varphi, \quad \delta\eta = 2\eta\delta\varphi. \tag{4.15}$$

In words, an expansion of the surface effectively increases shear viscosity and friction.

φ defines also the Gaussian curvature κ (Eq. 1.71). κ is negative at minima in φ. Minima in φ are points where the surrounding area has been expanded with respect to this point, such that this point is surrounded by more surface area in a given distance to the point (see also Fig. 1.9). This explains why shear viscosity assigns regions of negative Gaussian curvature an increased effective friction. Thus, we sum up the geometry-dependence of flows limited by shear viscosity as: Adding more surface area around a point makes it harder to move the fluid film at that point. Saddle geometries as well as localised expansions of the surface, akin to protrusions (Fig. 4.3C,D), act as obstacles as they correspond to regions of effectively increased viscosity and friction.

In the previous section, we found that in particular the effective increase in friction fundamentally changes the flow field of an active isotropic fluid film and makes a contractile point move, as it yields a coupling of rotational and irrotational as well as harmonic flow components. This effective friction arises only from the shear viscosity η, but not from bulk viscosity $\eta_b = \alpha\eta$. This is a consequence of the tensorial nature of the shear rate. While bulk viscosity couples two scalar fields, the divergence of the flow field to the trace of the stress tensor, shear viscosity amounts to a coupling of two trace-less symmetric tensors. Such a tensor defines not only a magnitude but also a local angle or phase in the sense of a spin-weighted quantity. Parallel transport of such an object yields a rotation, whereas a scalar quantity remains unchanged. It is this rotation that gives rise to the non-vanishing commutator of the covariant derivative (Eq. 1.66), which in turn gives rise to the effective friction.

Taken together, we find that the flow field of a curved fluid film can be mapped to the flow field of a flat heterogeneous fluid film. Thereby, we map anisotropies of the surface geometry to effective gradients in the viscosities and the friction coefficient. This yields an intuition for understanding the geometry dependence of flow fields. In the following, we investigate this geometry dependence more explicitly, by calculating how the flow field changes, when one changes the geometry of a surface.

4.2.2 Complex Green's functions of force and deformation response

In an active fluid, the force generated by some mechanically active structure like a myosin foci depends on the geometry of this structure. This geometry dependence gives rise to variation of the force density $\delta\,{}_{(1)}f$ associated with a deformation $\delta\varphi$, when considering the deformation response of the flow field of an active fluid film. Such a geometry dependence has been considered for example for topological defects in an active nematic fluid film with vanishing hydrodynamic length [192]. Here in contrast, we focus on localised sources of mechanical activity, i.e. active stresses (or moments) that are non-vanishing only on a patch that is small compared to the hydrodynamic length and the length scales of the surface geometry. In this case, a geometry dependence of the flow arises only due to viscosity.

To get an understanding of how the surface geometry shapes the flow field due to viscosity, we study the geometry dependence of the Green's functions. For a tangential force density ${}_{(1)}f$, the resulting flow field ${}_{(1)}v$ can be calculated as

$$ {}_{(1)}v(z) = \int \mathrm{d}S' \left[{}_{(1,-1)}G(z,z')\,{}_{(1)}f(z') + {}_{(1,1)}G(z,z')\,{}_{(-1)}f(z') \right], \tag{4.16} $$

where here and in the following $z = s^1 + is^2$ denotes the coordinates and $\mathrm{dS}' = \sqrt{g}\mathrm{d}s^{1'}\mathrm{d}s^{2'}$. The Green's functions ${}_{(1,-1)}G$ and ${}_{(1,1)}G$ are fields with mixed spin weights (see appendix D).

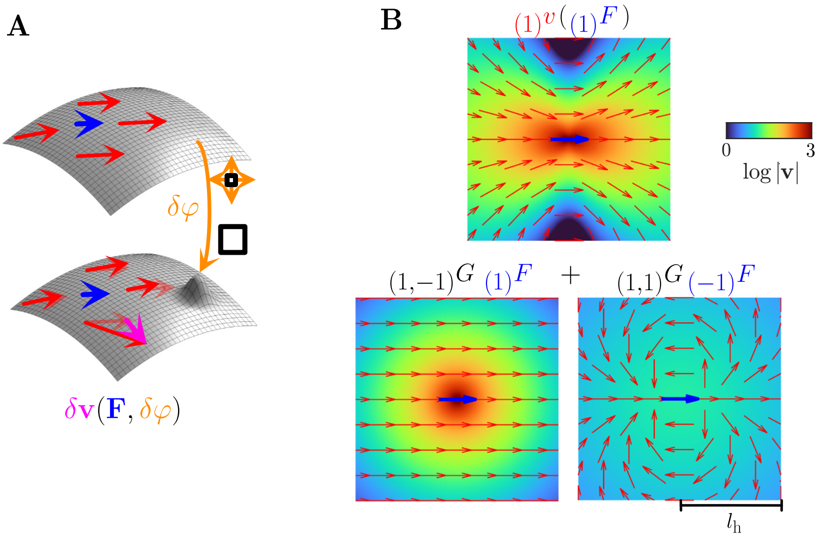
A
B
$\delta\varphi$
$\delta\mathbf{v}(\mathbf{F},\delta\varphi)$
${}_{(1)}v\,({}_{(1)}F\,)$
0
3
$\log|\mathbf{v}|$
${}_{(1,-1)}G\ {}_{(1)}F$
+
${}_{(1,1)}G\ {}_{(-1)}F$
l_h

Figure 4.4: Understanding the geometry dependence of active flow using complex Green's functions. **A**: Schematic for the change in the flow field $\delta\mathbf{v}$ upon a deformation corresponding to a localized surface expansion $\delta\varphi$ of the reference surface in the upper panel. Red arrows denote the flow field $\mathbf{v}$ and blue arrows denote the monopole force $\mathbf{F}$ that drives the flow. We investigate the deformation response of the flow field by evaluating the deformation response of the Green's functions. **B**: Upper panel: Flow field (red arrows) around a force monopole (blue arrow) in a flat incompressible fluid film ($\alpha \to \infty$). Lower panels: Decomposition of the flow field in the upper panel into the contributions from the complex Green's functions ${}_{(1,-1)}G = G_0$ and ${}_{(1,1)}G = G_2$, where we use the formalism of spin-weighted functions (see section 1.3.1 and appendix D). ${}_{(1,-1)}G$ (left panel) and ${}_{(1,1)}G$ correspond to the trace and trace-less symmetric components of the Oseen tensor, respectively. Formulas for flat fluid film are given in Eq. B.8, B.9.

The tangential force balance equation that governs the flow field (Eq. 1.69) yields the following differential equations for the Green's functions:

$$\bar{\eth}\eth\,{}_{(1,-1)}G(z,z') + \frac{\alpha}{2}\eth\left(\bar{\eth}\,{}_{(1,-1)}G(z,z') + \eth\overline{{}_{(1,1)}G(z,z')}\right) - \frac{1}{l_h^2}\,{}_{(1,-1)}G(z,z') = -\frac{1}{\eta}\delta_{z,z'} \tag{4.17}$$

$$\bar{\eth}\eth\,{}_{(1,1)}G(z,z') + \frac{\alpha}{2}\eth\left(\bar{\eth}\,{}_{(1,1)}G(z,z') + \eth\overline{{}_{(1,-1)}G(z,z')}\right) - \frac{1}{l_h^2}\,{}_{(1,1)}G(z,z') = 0. \tag{4.18}$$

Here all derivative operators, defined in Eq. 1.73, are understood with respect to $z, \bar{z}$. $\delta_{z,z'}$ denotes the Dirac distribution on a two-dimensional surface which we define in terms of the usual one-dimensional Dirac delta distributions as

$$\delta_{z,z'} = \delta(\mathrm{Re}[z-z'])\delta(\mathrm{Im}[z-z'])e^{-2\varphi(z')}. \tag{4.19}$$

For better readability, we will omit the spin-weights of the Green's functions in the following by defining

$$G_0(z,z') = {}_{(1,-1)}G(z,z'), \quad G_2(z,z') = {}_{(1,1)}G(z,z'). \tag{4.20}$$

For a flat incompressible fluid film (i.e. $\alpha \to \infty$, $\varphi = \text{const.}$, $G_0(|z-z'|)$) and $G_2(z-z')$ correspond to the trace and the trace-less symmetric component of the Oseen tensor, respectively (plotted in Fig. 4.4). For $\varphi \neq \text{const.}$, the Green's functions cannot be written as functions of $z-z'$. Still, they obey symmetry relations that follow from the self-adjointness of the differential operators in Eq. 4.17 and4.18:

$$G_0(z,z') = \overline{G}_0(z',z), \quad G_2(z,z') = G_2(z',z). \tag{4.21}$$

The Green's functions depend on the intrinsic surface geometry, which we understand in terms of a functional dependence on the geometric potential φ. Importantly, this relation between the Green's functions and φ is non-linear and non-local. However, we can calculate the differential $\delta G(z_v, z_f)/\delta\varphi(z)$ of a Green's function G with respect to a change in surface geometry $\delta\varphi(z)$ (see Fig. 4.4A for an illustration). $\delta\varphi(z)$ corresponds to a deformation that amounts to locally isotropic expansions and contractions of the surface. $\delta G(z_v, z_f)/\delta\varphi(z)$ is particularly informative, when we consider a surface $\mathcal{S}'$ that results from a continuous deformation of a reference surface $\mathcal{S}_0$ such as the sphere or a cylinder. Such a deformation can be understood in terms of a continuous map

$$\Phi: \ [0,1] \to C^2 \tag{4.22}$$

mapping a time-like variable x to a geometric potential $\Phi(x) = \varphi_x$ such that $\varphi_0 = \Phi(0)$ and $\varphi' = \Phi(1)$. φ_0 and φ' define the intrinsic geometry of $\mathcal{S}_0$ and $\mathcal{S}'$, respectively. The flow field ${}_{(1)}v'$ on the deformed surface with intrinsic geometry φ' can be written in terms of the flow field ${}_{(1)}v_0$ on the reference surface and an interaction Kernel ${}_{(1,0,\pm1)}K$ as

$$\begin{aligned} {}_{(1)}v'(z_v) = {}_{(1)}v_0(z_v) + \int_0^1 \mathrm{d}x \int \mathrm{d}S \int \mathrm{d}S_f \big[& {}_{(1,0,-1)}K(z_v,z,z_f)\, {}_{(1)}f(z_f) \\ & + {}_{(1,0,1)}K(z_v,z,z_f)\, {}_{(-1)}f(z_f) \big] \left.\frac{\mathrm{d}\varphi_x}{\mathrm{d}x}\right|_z, \end{aligned} \tag{4.23}$$

where ${}_{(1,0,\pm1)}K$ are defined as

$$ {}_{(1,0,-1)}K(z_v,z,z_f) = \frac{\delta\, {}_{(1)}v(z_v)}{\delta\varphi(z)\delta\, {}_{(1)}f(z_f)} = \frac{\delta G_0(z_v,z_f)}{\delta\varphi(z)} + 2G_0(z_v,z_f)\delta_{z,z_f} \tag{4.24}$$

$$ {}_{(1,0,1)}K(z_v,z,z_f) = \frac{\delta\, {}_{(1)}v(z_v)}{\delta\varphi(z)\delta\, {}_{(-1)}f(z_f)} = \frac{\delta G_2(z_v,z_f)}{\delta\varphi(z)} + 2G_2(z_v,z_f)\delta_{z,z_f}. \tag{4.25}$$

${}_{(1,0,\pm1)}K$ comprise the geometry-dependence of the flow generated by the force pattern ${}_{(1)}f$. Importantly, they can be written in terms of the Green's functions and their spatial derivatives for general surfaces, as we derive in appendix H.

4.2.3 Response of active flow to localized deformations

As an instructive example, we consider an intrinsically flat reference surface, i.e. a surface with vanishing Gaussian curvature. We calculate how the flow field ${}_{(1)}v$ of a force monopole changes upon a localised expansion $\delta\varphi = \delta_{z,z'}$ (Fig. 4.5). Such an expansion may be understood as a protrusion with a size much smaller than the hydrodynamic length. We consider different regimes

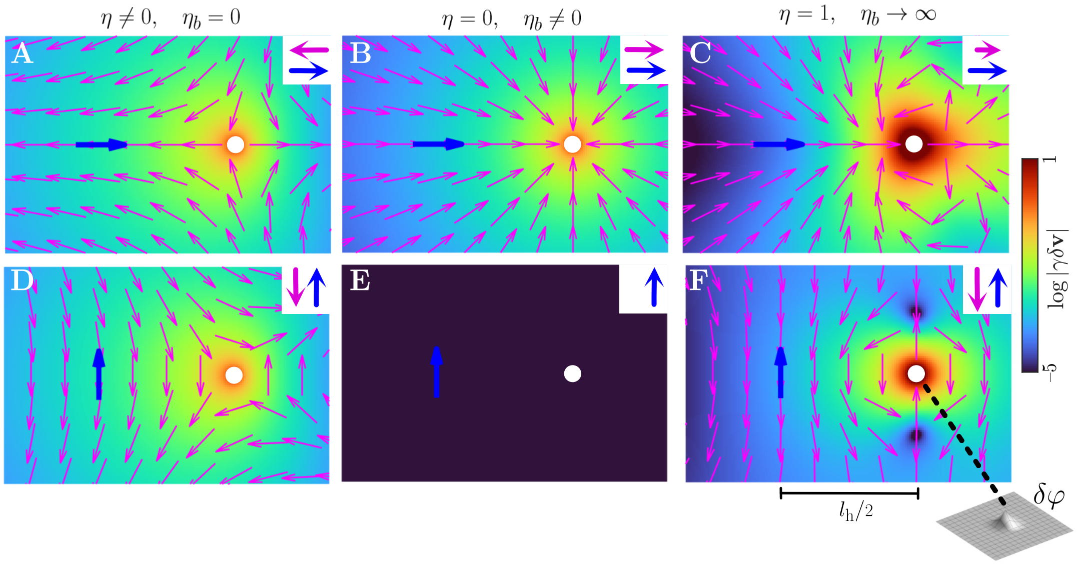

Figure 4.5: Differential of the flow field with respect to a deformation $\delta\varphi$ for a flat reference surface. Plots of ${}_{(1,0,-1)}K\,{}_{(1)}F + {}_{(1,0,1)}K\,{}_{(-1)}F$ (Eq. 4.24, 4.25) as function of z_v with $|z_f - z| = l_h/2$. This corresponds to the differential change in the flow field ${}_{(1)}\delta v$ (pink arrows) around a force ${}_{(1)}F$ (blue arrow) at z_f upon a differential expansion of the surface $\delta\varphi$ at z (indicated by white circles). $\delta\varphi$ corresponds to a localized deformation of the surface as illustrated in the lower right corner. **A**-**C**: ${}_{(1)}F = 1$ with $z - z_f = l_h/2$, i.e. the force is pointing towards the deformation. **D**-**F**: ${}_{(1)}F = 1i$, i.e. the force is rotated by 90° with respect to the force in **A**-**C**. Vectors in insets illustrate the orientation of $\delta\,{}_{(1)}v$ (pink arrow) evaluated at the position of the force z_f. We observe that $\delta\,{}_{(1)}v(z_f)$ is anti-parallel to ${}_{(1)}F$ for $\eta_b = 0$ (**A**,**D**), as given by Eq. 4.26. For $\eta \to 0, \eta_b > 0$, $\delta\,{}_{(1)}v(z_f)$ is parallel to ${}_{(1)}F$ (**B**) or vanishes (**E**) depending on the orientation of ${}_{(1)}F$, as given by Eq. 4.27. For an incompressible fluid film (**C**,**F**), $\delta\,{}_{(1)}v(z_f)$ may be parallel (**C**) or anti-parallel (**F**) to the force ${}_{(1)}F$, depending on the orientation of the force. For most angles, $\delta\,{}_{(1)}v(z_f)$ is anti-parallel to ${}_{(1)}F$, as the modulus $|\delta\,{}_{(1)}v(z_f)|$ is greater in panel **C** than in panel **F**, which yields the numerical result in Eq. 4.28. All flow fields were obtained by exact differentiation of the Green's functions for a flat fluid film (Eq. B.8,B.9) using MATLAB [193]. With this, $\delta\,{}_{(1)}v$ was obtained exactly analogous to appendix H.

of α and orientations of the force that drives the flow.

As we have found shear viscosity to be crucial to the geometry sensing of a contractile point in the previous section, we begin by considering the case of vanishing bulk viscosity ($\alpha \to 0$) (Fig. 4.5A,D). We observe that $\delta\,{}_{(1)}v$ contains a shear flow around z and that $\delta\,{}_{(1)}v$ overall points in the opposite direction of the force that is driving the flow. Both these components of $\delta\,{}_{(1)}v$ can be understood in terms of the effective increases in friction and viscosity in Eq. 4.15. We may say an expansion of the surface adds resistance against flow due to shear viscosity. Strikingly, we can formalize this notion of increased resistance in terms of a strict bound that is valid for any surface:

$$\left.\frac{\delta\,{}_{(1)}v(z_v)}{\delta\varphi(z)\delta\,{}_{(1)}f(z_f)}\right|_{z_v=z_f} = -4\gamma|G_0(z,z_f)|^2 - 2\eta|\eth G_0(z,z_f)|^2 \leq 0 \text{ for } z_f \neq z. \tag{4.26}$$

with equality restricted to a set of points (see appendix H.1 a derivation, note that ${}_{(1,0,1)}K$ vanishes for $\alpha = 0$). In words, the change in the flow field upon a surface expansion $\delta\varphi > 0$ points in the opposite direction to the force, when the flow field is evaluated where it is generated. We note that $\delta\,{}_{(1)}v$ scales with the modulus of the Green's function and, thus, the hydrodynamic length. As this inequality is valid for any closed surface geometry, it provides inside that go far beyond a linear calculation.

An analogous rationale applies to flows that are limited by bulk viscosity ($\eta_b = \alpha\eta$), i.e. in the limit $\eta \to 0, \alpha\eta = \text{const.}$. We found that an expansion of the surface ($\delta\varphi > 0$) relaxes the pressure from bulk viscosity (Eq. 4.15). Thus, an expansion of the surface amplifies the flow driven by a force monopole at a distance. Specifically, we find the following bound for the change in the velocity, evaluated at the position and in the direction of the force ${}_{(1)}F$ that drives the flow (see appendix H.2):

$$\mathrm{Re}\left[\frac{{}_{(1)}F}{|{}_{(1)}F|^2}\frac{\delta\,{}_{(1)}v(z_f)}{\delta\varphi(z)}\right] = \frac{4|G_P(z,z_f)|^2}{\eta_b}\left(1+\cos(2\Delta\psi)\right) \geq 0 \text{ for } z_f \neq z. \tag{4.27}$$

Here $G_P = {}_{(0,-1)}G_P$ is the propagator of the pressure (Eq. H.17). $\Delta\psi$ is the angle of the force vector ${}_{(1)}F$ with respect to an axis defined by G_P (see appendix H.2, note that both ${}_{(1,0,1)}K$ and ${}_{(1,0,-1)}K$ contribute to $\delta\,{}_{(1)}v$, but the bound is again due to ${}_{(1,0,-1)}K$). This inequality is valid for general closed surface geometries in the regime of vanishing shear viscosity, i.e $\eta \to 0, \eta_b \neq 0$. It is in direct contrast to Eq. 4.26 that applies to the regime of vanishing bulk viscosity, i.e. $\eta_b \to 0, \eta \neq 0$. Thus, the geometry dependence of the flow field results from a competition of the forces resulting from shear and bulk viscosity.

A particularly interesting regime is that of an incompressible fluid, i.e. $\alpha \to \infty$ with η and l_h non-vanishing and finite. Again, it is instructive to consider a deformation of an intrinsically flat surface (Fig. 4.5C,F). We find that $\delta\,{}_{(1)}v$ heavily depends on the orientation of the force with respect to the geodesic that connects the positions of force monopole and surface expansion. When the force is pointing towards the surface expansion, $\delta\,{}_{(1)}v$ is pointing in the same direction when evaluated at the position of the force (Fig. 4.5C). When the force is oriented perpendicularly, $\delta\,{}_{(1)}v$ is anti-parallel to the force (Fig. 4.5F). When we calculate the angular average over orientations of the force, we find that $\delta\,{}_{(1)}v$ is on average anti-parallel to the force, i.e.

$$\frac{1}{2\pi}\int_0^{2\pi} \mathrm{d}\psi_F\,\mathrm{Re}\left[\frac{\delta\,{}_{(1)}v(z_f)[{}_{(1)}f]}{\delta\varphi(z)}e^{-i\psi_F}\right]\Bigg|_{z_v=z_f} = {}_{(1,0,-1)}K(z_f,z,z_f) \leq 0 \tag{4.28}$$

with ${}_{(1)}f = Fe^{i\psi_F}\delta_{z',z_f}$ and $z \neq z_f$. Thus, the rationale we obtained from the regime of vanishing bulk viscosity generalizes to the regime of shear viscosity, when averaging over orientations of the force. We note that this inequality is only valid for a flat surface. For a general surface geometry, we find that this inequality remains valid, when gradients of pressure resulting from gradients of Gaussian curvature are small (appendix H.3). Thus, we find that the effect of shear viscosity on the geometry-dependence of the flow tends to dominates even when bulk viscosity is infinite. As we discussed in section 4.2.1, this is dominance is due to the effective friction that results from the tensorial nature of shear viscosity.

Taken together, we find that localized deformations modify the flow field at the position where it is driven in a predictable manner. In the remainder of this chapter, we will use this insight to investigate how localized sources of mechanical activity act as sensors of the surface geometry. Such geometry sensing at a distance results from the viscosities. As we have observed here, the viscosities yield that the flow field changes upon a deformation as $G\delta\varphi$ with G being a propagator that scales with the distance relative to the hydrodynamic length. As such, the viscosities give a localized source of mechanical activity a sense of the amount of surface area, quantified by φ, it is connected to within the hydrodynamic length.

4.3 Geometry sensing by a contractile point

In the following, we make use of the insights gained in section 4.2 to investigate how anisotropies in the surface geometry yield translation and deformations of a localized source of active tension. Thereby, we generalize the findings of chapter 4.1.2, where we considered a tension monopole on a torus. Again, we consider a monopole of active tension, i.e. a pattern of active tension given by

$$t^{ij}_{\mathrm{act}} = T\frac{\delta(s^1 - s^1_0)\delta(s^2 - s^2_0)}{\sqrt{g}}, \tag{4.29}$$

where s^1_0, s^2_0 are the coordinates of the monopole, and $T > 0$ has units of a force dipole. Such a contractile point may be interpreted as a model for a myosin focus. More generally, the flow field around a monopole yields a basis for understanding the flow field of a general pattern of active tension, similarly to the Green's functions we considered in the previous section.

4.3.1 Contractile points are attracted by saddles and protrusions

As in the previous section, we adopt the Newman Penrose formalism in isothermal coordinates (section 1.3.1,1.3.2). In such coordinates, the intrinsic surface geometry is defined by the geometric potential φ. In section 4.1.2, we found that contractile points move along gradients of φ on a torus. We understood this movement as the result of an effective friction gradient resulting from the product of shear viscosity and Gaussian curvature. In section 4.2.1, we found that the impact of the surface geometry on the flow field can generally be captured by geometry-dependent rescaling of flow and force fields, and of the viscosities and the friction coefficient. In the following, we want to use this insight to investigate, where contractile points move to in general surface geometries.

For simplicity, let us consider the regime of vanishing bulk viscosity (we discuss the effects of bulk viscosity in Fig. J.3). In this regime, we calculate how the flow field due to an active tension density χ changes upon an infinitesimal deformation in appendix H.1.1. We find that the change $\delta_{(1)}v$ can be understood in terms of two contributions (Eq. H.12): First an effective force density $-2\chi\eth\delta\varphi$. Second a hydrodynamic kernel K_{hyd} that captures the effective change in viscosity and friction we discussed in the previous section (Eq. H.13). Both terms result from shear viscosity. The effective force density drives a flow and thus a movement of a contractile point down the local gradient in $\delta\varphi$. Thus, this generalizes our findings for a torus in section 4.1.2 to general surface geometries. Importantly, however, one has to take also the hydrodynamic kernel K_{hyd} into account.

The hydrodynamic coupling to the geometry results from the effective change in friction and viscosity (Eq. 4.15) In section 4.2.3, we calculated the resulting change in the flow field $\delta\mathbf{v}$ for a force monopole. We found that $\delta\mathbf{v}$ is generally oriented oppositely to the force that drives it, when evaluated close to the position of this force. Furthermore, we found that $\delta\mathbf{v}$ scales with the moduli of the Green's functions and, thus, the distance between the site of the deformation and the position of the force (Eq. 4.26). A contractile point may be understood as an infinitesimal ring of forces $\mathbf{f}_i$ that all point towards its center, i.e. the position of the contractile point (Fig. 4.6A). Let us consider an obstacle in the fluid film, i.e. a small patch where friction and viscosity are locally increased. Introducing such an obstacle changes the flow field driven by the contractile point. Due to linearity of the governing equations, we can understand the change $\delta\mathbf{v}$ as the sum of the contributions from all the forces $\mathbf{f}_i$. For each force, the associated $\delta\mathbf{v}_i$ points oppositely to $\mathbf{f}_i$ and thus, away from the center of the contractile point. The sum of all $\delta\mathbf{v}_i$ evaluated at the center of the contractile point yields the velocity $\delta\mathbf{v}_{\mathrm{mono}}$ with which the monopole is advected. As $\mathbf{v}_i$ generally scales with the distance to the obstacle, we expect that $\delta\mathbf{v}_{\mathrm{mono}}$ is dominated by the contribution from the force that is closest to the obstacle. Thus, $\delta\mathbf{v}_{\mathrm{mono}}$ points towards the obstacle. The contractile point is advected towards the obstacle (Fig. 4.6B). Thus, we expect the hydrodynamic coupling to the geometry to result in a velocity of a tension monopole towards maxima in effective friction and viscosity.

For locally translation-invariant geometries, where $G_0(z, z_0) = G_0(|z - z_0|)$ we can make this statement explicit (see appendix H.1.1). We consider an infinitesimal deformation $\delta\varphi$ of the surface at a distance to a tension monopole at z_0. We find that $\delta\varphi$ yields a velocity at the tension monopole given by

$$\frac{\delta_{(1)}v_0(z_0)}{\delta\varphi(z_1)\delta\chi(z_0)} = \frac{1}{2}\eth_{z_0}|K_{\mathrm{hyd}}| = \eth_{z_0}\left(2\gamma|G_0(z,z_0)|^2 + \eta|\eth G_0|^2\right). \tag{4.30}$$

$|K_{\mathrm{hyd}}|$ quantifies how much two points in the surface are mechanically coupled due to viscosity. For an expansion ($\delta\varphi > 0$), the above equation says that a contractile point moves in the direction, where mechanical coupling to the position of the expansion is strongest. In other words, it is attracted by the expansion, which is expected given the associated increase in effective friction and viscosity (Eq. 4.15, see Fig. 4.6C for the deformation of a flat reference surface). For a general surface geometries, the situation can be more complicated than the argument in the previous paragraph suggests. Crucially, this argument does not incorporate the angles resulting from parallel transport of the $\mathbf{v}_i$ to the center. Still, we expect that the principle remains: Contractile points are attracted at a distance by regions where the viscosities and friction coefficient are (effectively) elevated. At the same shear viscosity pushes the contractile point down the local gradient of φ as we discussed above.

For vanishing bulk viscosity ($\alpha = 0$), this means that contractile points are attracted by maxima in φ at a distance, corresponding to localized protrusions. Close to the maximum, however they move down the gradient in φ. As a consequence, we expect contractile points to localize to the saddle of a protrusion.

For simple surfaces such as a torus or a prolate sphere, the mapping in Eq. 4.12 is useful. It yields an effective friction inversely proportional to the Gaussian curvature. We note that in this case, no local term proportional to the gradient in φ arises in this mapping, because the rescaled force $\partial_{\bar{z}}\chi$ is geometry-independent (Eq. 4.9). On such simple surfaces, the saddle that results from a global contraction is at the same time the minimum in φ and κ. Thus, the saddle is the maximum in the effective friction γ_{eff} and the effective viscosity η_{eff}, which drags contractile points towards the saddle. Notably, this statement is independent of α. Thus, we expect that contractile points generally move towards such saddle geometries, in agreement with the results of section 4.1.1.

Together, these two effects yield that a contractile point moves towards points z where φ in the neighborhood of z is large compared to $\varphi(z)$. This means that the movement of a contractile point maximizes the amount of surface area, quantified by φ, in the neighborhood of the contractile point (see also Fig. 1.9). In section 4.4, we will test whether these effects allow us to understand the patterns that form in an active fluid with complex surface geometry.

4.3.2 Flow field for a multipole of the surface geometry

A patch of active tension does not only move due to advection, but it may also rotate (section 3.3.2) or deform. For a small circular patch we have found that advection can yield a deformation of the circle into a band, when the patch is located at the saddle of a prolate sphere (Fig. 3.5A). This deformation is a consequence of a shear flow that results from the anisotropy of the surface geometry. In the following, we investigate the effect of such surface anisotropies on the flow field of a contractile point.

To this end, we consider a regime where the hydrodynamic length is small compared to the length scales of the surface geometry. In this regime, we can understand the surface geometry in terms of a slight deformation of an intrinsically flat surface. This deformation is captured by a field

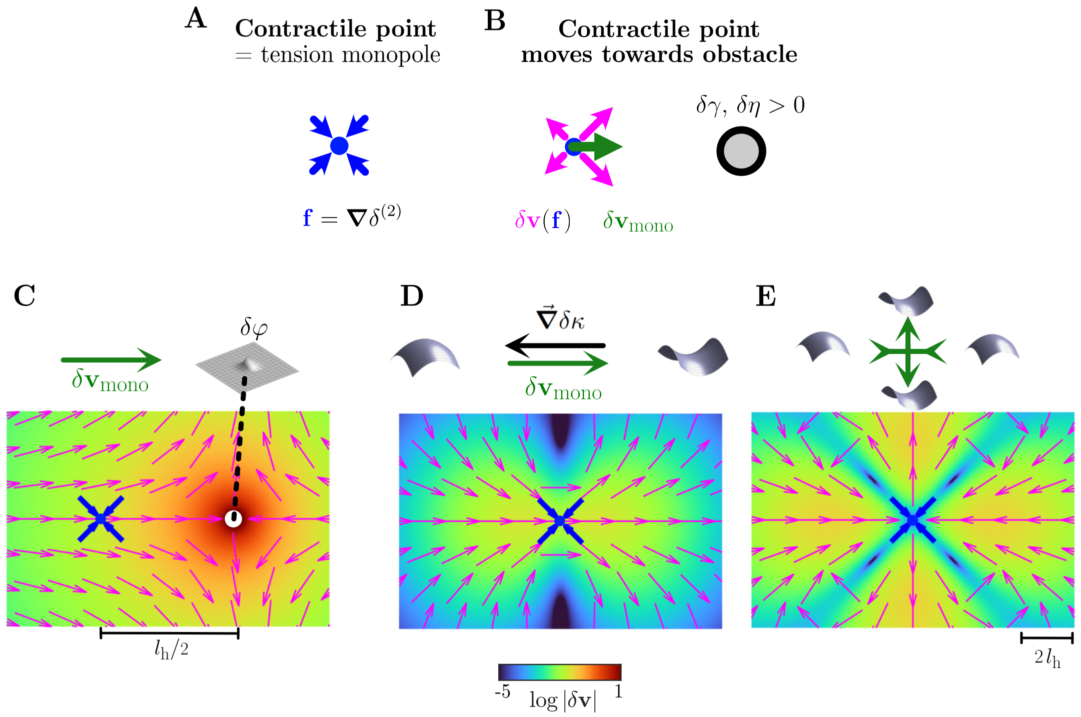

Figure 4.6: Shear viscosity attracts contractile points to protrusions and saddles. **A**: Illustration of the forces (blue arrows) from a tension monopole Eq. 4.29). Such a localised force density can be understood as an infinitesimal ring of forces that all point to the center of the ring. **B**: Inducing an obstacle, i.e. a local increase in friction and viscosity (grey area), yields an anisotropic change in the flow field and thereby the movement (green arrow) of a contractile point, i.e. a tension monopole (blue dot). The change in the flow field can be decomposed in the contributions $\delta\mathbf{v}(\mathbf{f})$ (pink arrows) from each force monopole (blue arrow). $\delta\mathbf{v}(\mathbf{f})$ is oriented oppositely to the force and scales with the distance to the obstacle. As a consequence, the contractile point moves towards the obstacle. This allows to understand the movement of contractile points in a curved surface using the effective gradients of viscosities and friction coefficient (see Fig. 4.3). For details see main text. **C-E**: Change in the flow field (pink arrows) around a tension monopole upon introducing a deformation of an otherwise flat fluid film with $\alpha = 0$. **C**: Localised surface expansion as in Fig. 4.5. We observe that a contractile point moves towards such an isotropic expansion, corresponding to a small protrusion. **D**: Contractile point moves down the Gaussian curvature gradient $\nabla\delta\kappa$, corresponding ${}_{(1)}\mathcal{K}$ in 4.33. **E**: Nematic anisotropy (${}_{(2)}\mathcal{K}$) of the surface geometry yields shear flow, where the fluid film extends along the axis of minimal Gaussian curvature. Flow field in **C** was obtained analytically as in appendix H.4. For the flow fields in **D**, **E**, the change in the viscous force was calculated analytically. From this the flow field was obtained by inverting the force balance equation in Fourier space using periodic boundary conditions and using a 256x256 square grid of size $10l_h$.

$\delta\varphi(z)$ around the contractile point at $z = 0$, where as $z = s^1 + is^2$ is the complex coordinate. $\delta\varphi$ is only defined up to reparametrizations of the surface. When $\delta\varphi$ is globally defined, it is defined up to a constant by virtue of Liouville's equation (Eq. 1.71, see also section 4.4). Due to the small hydrodynamic length, the contractile point sees only an open subset of the surface. On such an open subset, $\delta\varphi$ is defined up to holomorphic reparameterizations. Without loss of generality, we consider a parametrization of the surface such that

$$\delta\varphi\big|_{z=0} = 0 \quad \text{and } \partial_z^n \delta\varphi(z)\big|_{z=0} = 0 \text{ for } n \in \mathbb{N}, \tag{4.31}$$

corresponding to boundary conditions of $\delta\varphi$ at $z = 0$. With this, we write $\delta\varphi$ as a Taylor expansion:

$$\delta\varphi = |z|^2 \sum_{m=0}^{\infty} \sum_{n=m}^{\infty} (P_{mn} z^m \bar{z}^n + \bar{P}_{mn} \bar{z}^m z^n) = \sum_{m=0}^{\infty} \sum_{n=m}^{\infty} r^{m+n+2} \left(P_{mn} e^{i(m-n)\theta} + \bar{P}_{mn} e^{i(n-m)\theta} \right), \tag{4.32}$$

where we use polar coordinates r, θ. The complex coefficients P_{mn} with $m, n \neq 0$ correspond to anisotropies of the surface geometries. They have a rotational symmetry with respect to the position of the contractile point. This rotational symmetry can be denoted by $|n-m|$ in the sense of a spin-weight (Eq. 1.57). For example, the P_{mn} with $|n-m| = 1$ denote polar anisotropies of the surface geometry such as a gradient of Gaussian curvature, the $|n-m| = 2$ components corresponds to nematic anisotropies of the surface geometry such as a saddle, and so on. For simplicity, we consider only the lowest order in r for a given spin-weight $|n-m|$, i.e. we omit all P_{mn} with $m > 0$.

Using Liouville's equation, we calculate the Gaussian curvature field from $\delta\varphi$, yielding

$$\delta\kappa = \sum_{n=0}^{\infty} \left({}_{(n)}\mathcal{K} \bar{z}^n + {}_{(-n)}\mathcal{K} z^n \right). \tag{4.33}$$

The spin quantities ${}_{(n)}\mathcal{K}$ with positive n are given by

$${}_{(|n|)}\mathcal{K} = -4(n+1) P_{0,n}, \tag{4.34}$$

and negative spins denote the complex conjugate. Again, these quantities denote anisotropies of the surface geometry with the spin-weight denoting the rotational symmetry. In particular ${}_{(1)}\mathcal{K}$ denotes the gradient of Gaussian curvature. As such, Eq. 4.33 corresponds to a multipole expansion of the surface geometry in terms of the Gaussian curvature. In the following, we investigate how this multipole of the surface geometry shapes the flow field of a contractile point, i.e. a tension monopole. In section 4.5, we will consider also multipoles of (anisotropic) tension.

For simplicity, we consider the regime of vanishing bulk viscosity ($\alpha = 0$). Then, regions of positive $\delta\varphi$ correspond to regions effectively increased viscositiy and friction. As discussed above, we expect the contractile point to drive a flow towards regions of positive $\delta\varphi$ and thus negative Gaussian curvature $\delta\kappa$. In order to evaluate the flow field $\delta\ {}_{(1)}v$ that results from the anisotropy of the surface geometry, we make use of the results in section 4.2.3 and appendix H. As we derive in appendix H.4, we find that the local velocity of the contractile point is given by

$$ {}_{(1)}v_{\text{mono}} = -\frac{4T}{\pi\eta} l_h^2 \, {}_{(1)}\mathcal{K}. \tag{4.35}$$

Hence, the contractile point moves down the Gaussian curvature gradient. We note that the regime we consider here is distinct from the regime in section 4.1.2. There we also considered a small deformation, in the sense of $\delta\kappa l_h^2 \ll 1$. However, we considered a regime where the length scale of the Gaussian curvature gradient ($\delta\kappa/|\eth\delta\kappa|$), corresponding to the smaller radius of the torus, is on the order of the hydrodynamic length. With this, we found a velocity proportional to the gradient $\delta\varphi$, which reflects that contractile point sees the fluid on a scale where $\delta\varphi$ is well defined. Here, in contrast, we consider a much smaller hydrodynamic length, where only the gradient of Gaussian curvature is well defined. However the principle remains: A polar anisotropy of the surface geometry yields a velocity that transports the contractile point towards minimal Gaussian curvature, where points are surrounded by a maximal amount of surface area. .

The nematic anisotropy ${}_{(2)}\mathcal{K}$, in contrast yields a shear flow (see also Fig. 4.6E for a numerical solution). We find that the shear rate at the position of the contractile point is given by

$$ {}_{(2)}v_{\text{mono}} = \eth\delta\,{}_{(1)}v\big|_{z=z_0} = -\frac{112}{15}\frac{T}{\pi\eta} l_h^2 \, {}_{(2)}\mathcal{K}. \tag{4.36}$$

This corresponds to a contraction along the axis of maximal Gaussian curvature and an extension along the axis of negative Gaussian curvature. We have observed such a shear flow for a circular patch on the saddle of a prolate sphere (Fig. 3.5A). Eq. 4.36 shows that such a flow generally results from a contractile patch in such a saddle geometry.

Strikingly, we can generalize this phenomenon to general multipoles of the flow field, yielding

$$ \delta(\eth^{m_v}\bar{\eth}^{n_v}\ {}_{(1)}v)\big|_{z=z_0} = -\frac{4T l_h^{n+1}}{\eta l_h^{m_v+n_v}} N \delta_{n,1+m_v-n_v}\ {}_{(n)}\mathcal{K}, \tag{4.37}$$

where the dimensionless number $N > 0$ depends on m_v, n_v and n (Eq. H.45). The minus sign implies that the flow field yields an extension along axes of minimal Gaussian curvature.

We evaluated $\delta\ {}_{(1)}v$ also numerically for polar and nematic anisotropies of the surface geometry. We find that the flow towards sections of minimal Gaussian curvature is not limited to the position of the contractile point (see Fig. 4.6D,E) Thus, the contractile point does not only drive a movement of itself, but also of the surrounding fluid film on the order of the hydrodynamic length. For a nematic anisotropy, $|\delta\mathbf{v}|$ even increases away from the monopole up to a distance of about $3l_h$. For an extended domain of elevated active tension such a flow yields a spreading of the domain along the axes of minimal Gaussian curvature. Hence, contractile patches do not only move towards saddles, they also tend to spread over a saddle, as we have already observed for the prolate sphere (see Fig. 3.5).

All the analytical results in this section are valid for vanishing bulk viscosity, i.e. $\alpha = 0$. For $\alpha \neq 0$, the kernels ${}_{(1,0,\pm1)}K$ can still be calculated analytically, but the integrals (Eq. H.38) need to be calculated numerically. We used such numerical solutions for $0 < \alpha < 10$ to investigate the velocity of a contractile point in Gaussian curvature gradient. We found that the movement towards minimal Gaussian curvature persists (Fig.J.3C).

4.4 Pattern formation guided by the geometric potential

In chapter 3, we have found that surface geometry guides the formation of chemical patterns in an active fluid model of the cell cortex. There, we have understood this geometry in terms of a normal deformation δR of a reference sphere. However, δR becomes ill-defined for large deformations of a sphere. Furthermore, δR an extrinsic, i.e. embedding-dependent, measure of the surface geometry, whereas the physical model of the cortex we have proposed only depends on the intrinsic surface geometry.

The intrinsic geometry of a surface can be understood in terms of the geometric potential φ. In the previous sections, we have found analytically that a contractile point senses the geometric potential φ: A contractile point moves down the local gradient of φ is attracted by maxima in φ at a distance. We wondered, whether we can also understand the guiding of pattern formation in the cell cortex in terms of the geometric potential. To investigate this, we need to calculate φ for a given geometry of a cell cortex.

So far, we have understood φ in terms of the metric associated with an isothermal parametrization of the surface. This suggests that we first need to find isothermal coordinates for a given surface geometry to understand where a contractile point will move to. Finding such isothermal coordinates amounts to solving the Beltrami equation that has been the subject of various mathematical studies. As we will show in the following, Liouville's equation offers an alternative approach. With this, we calculate numerically the geometric potential of deformed spheres relative to a reference sphere. We then solve the active fluid model from chapter 3 on these complex surfaces, to compare the resulting patterns to the intrinsic surface geometry in terms of φ and κ.

4.4.1 Calculating the geometric potential using a reaction-diffusion model

Liouville's equation (Eq. 1.71) links the geometric potential φ to the Gaussian curvature κ via the Laplace Beltrami operator Δ_{LB}. Any parametrization $\mathbf{X}(s^1, s^2)$ of a curved surface yields

κ and Δ_{LB} (see section 1.2.1). Given κ and Δ_{LB}, Liouville's equation is a differential equation for φ. We propose here a physical interpretation of this equation in the spirit of Ricci flow: We consider a time-evolution of the scalar field φ given by

$$\partial_t \varphi = \Delta_{LB} \varphi + \kappa, \tag{4.38}$$

corresponding to a reaction diffusion model with κ as a source term. Then, solving Liouville's equation corresponds to finding the steady state pattern φ with $\partial_t \varphi = 0$.

Such a steady state does only exist, when the total flux to the surface vanishes,

$$\int_{\mathcal{S}} \mathrm{d}S \, \kappa = 0, \tag{4.39}$$

which defines a toroidal topology of the surface. Only for toroidal surfaces, global isothermal coordinates exist. For a spherical surface, isothermal coordinates are defined up to a point, where φ diverges (Fig. 1.13A). In this case φ is only defined up to boundary conditions at some chosen pole of the coordinate system. As such, the gradient of φ is not a truly intrinsic property of the surface. However, we may consider the difference $\delta\varphi = \varphi - \varphi_0$ with respect to a reference sphere with φ_0 and $\kappa_0 = \text{const.}$. Thereby, we understand the given anisotropic surface geometry as the result of a deformation of an isotropic surface by means of locally isotropic contractions and expansions of the surface. $\delta\varphi$ corresponds to the amount the reference surface needs to be expanded or compressed. For a slightly deformed sphere ($\delta R \ll R_0$), we can calculate $\delta\varphi$ from the change in the metric:

$$\delta\varphi = \delta(\log \sqrt{g}) = -2\frac{\delta R}{R_0} + \mathcal{O}(\delta R^2). \tag{4.40}$$

Note that this equation is valid, because $\delta g_{ij} \sim \delta_{ij}$ for an isotropic reference surface with $C_{ij} \sim \delta_{ij}$. Thus, the phenomena we have studied in chapter 3 in linear order of δR can equivalently be understood in terms of $\delta\varphi$.

Beyond the linear regime, we need to calculate $\delta\varphi$ by solving Liouville's equation for $\varphi = \varphi_0 + \delta\varphi$. This amounts to finding the steady state of

$$\partial_t \delta\varphi = \Delta_{LB} \delta\varphi + \kappa - e^{-2\delta\varphi} \kappa_0, \tag{4.41}$$

where we used Eq. 1.72 yielding $\Delta_{LB}\varphi_0 = -e^{-2\delta\varphi}\kappa_0$. This corresponds to a reaction diffusion system with a non-linear source term. We solve this dynamical equation on deformed spheres numerically using a pseudo-spectral method (appendix F). To allow for a steady state, we adapt the reference curvature κ_0 dynamically such that that $\delta\varphi$ relaxes towards a reference value $\delta\varphi_0 = 0$, i.e. we determine κ_0 at each time-step from the following equation

$$\int_{\mathcal{S}} \mathrm{d}S \, (\kappa - e^{-2\delta\varphi(t)} \kappa_0) = \int_{\mathcal{S}} \mathrm{d}S \, \delta\varphi, \tag{4.42}$$

With this we find that the dynamics converge to a steady state for various geometries (see Fig. 4.7B,F for two examples). Thus, we have found a method that allows us to understand the anisotropy of a complex (spherical) geometry in terms of the scalar field $\delta\varphi$.

4.4.2 Elucidating stress regulator patterns in complex surface geometries using the geometric potential

We have found that $\delta\varphi$ defines attractors of contractile points (see sections 4.1.2 and 4.3). In the following, we investigate whether this rationale can explain the geometry-dependent patterns that form in an active fluid model of the cortex (see section 3.3). To test this, we solved this active fluid model in complex surface geometries with a spherical topology. These shapes were obtained by randomly perturbing a sphere, in terms of a smooth field δR (see Fig. 4.7 for two examples of such shapes). We considered Péclet numbers of 55 and 110 and hydrodynamic lengths between $R_0/3$ and $3R_0$. Otherwise, we used the same parameters as in section 3.3.4. In this parameter regime, we found that the system converges to a steady state most of the time, consistent with our observations for prolate spheres (see Fig. 3.5B). For a large hydrodynamic length ($l_h = 3R_0$), we observed the formation of a single spot of elevated active tension (Fig. 4.7C,G). For smaller hydrodynamic lengths, we observed the formation of extended band-like patterns (Fig. 4.7D,H). Again, these observations are consistent with our findings for prolate spheres. Notably, different initial conditions yielded the same final pattern most of the time, though we plan to check this more systematically in the future. Thus, the complex geometry, does not fundamentally change the patterns that form, but the position and orientation of these patterns are clearly defined by the surface geometry.

For the same surface geometries, we also calculated the Gaussian curvature κ and from this the geometric potential $\delta\varphi$ as described above. We wanted to test whether variations of $\delta\varphi$ can explain the position of patches with elevated active tension. In other words: Does the active fluid film sense the geometric potential? To this end, we investigated to what extend the geometric chemical pattern c of the stress regulator at steady state is correlated with $\delta\varphi$ and κ. Specifically, we calculated for each realization of the model the correlation coefficient

$$C_{c,\varphi} = \frac{\langle (c - \langle c \rangle)\delta\varphi \rangle}{\sqrt{\langle (c - \langle c \rangle)^2 \rangle, \langle \delta\varphi^2 \rangle}}, \tag{4.43}$$

and equivalently for κ. Here $\langle \dots \rangle$ denotes the surface average

$$\langle x \rangle = \frac{1}{A} \int_{\mathcal{S}} \mathrm{d}S x. \tag{4.44}$$

These surface integrals were evaluated numerically using the spherical harmonic decomposition of the fields.

We have found in the previous section that a localised source of active tension tends to move

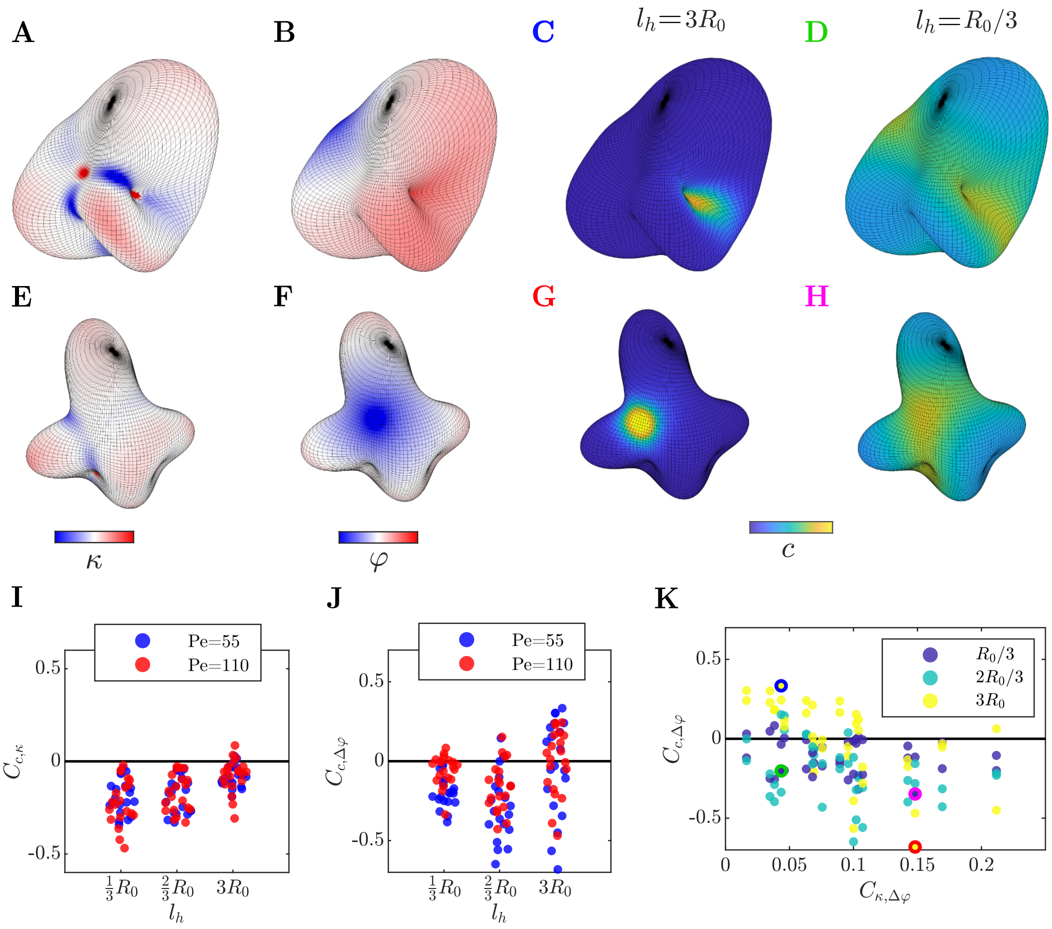

Figure 4.7: Geometric potential guides the formation of patterns in an active fluid model. **A-H**: Two examples of randomly deformed surfaces for which we determined the geometric potential and simulated the formation of patterns in an active fluid model (section 3.3) using a pseudo-spectral method. **A**,**E** Gaussian curvature with blue (red) color denoting negative (positive) values. **B,F** Geometric potential $\delta\varphi$ as determined from the reaction diffusion equation 4.41. **C**,**G**: Steady state patterns of the stress regulator for a large hydrodynamic length $l_h = 3R_0$ and $\mathrm{Pe} = 55$. Otherwise, we used the same parameters as in Fig. 4.1. **D**, **H**: Steady state patterns for a small hydrodynamic length $l_h = R_0/3$. **I**: Correlation coefficient between Gaussian curvature κ and the stress regulator pattern c revealing a negative correlation. Data points correspond to steady state patterns for 20 different spherical geometries as in **A**-**H**. **J**: Correlation coefficient between geometric potential $\delta\varphi$ and c. **K**: Correlation between $\delta\varphi$ and c as in **J**, but as a function of the correlation between $\delta\varphi$ and κ. Colors denote hydrodynamic lengths. We observe that for large hydrodynamic length (yellow circles), a small correlation between $\delta\varphi$ and κ yields a positive correlation between $\delta\varphi$ and c. Colored circular outlines indicate the examples shown in in **C**,**D**,**GH**.

towards minimal Gaussian curvature and drives a flow that yields an extension along axes of minimal Gaussian curvature. Indeed, we find that c and κ are negatively correlated in most of the surface geometries we studied. In particular for small hydrodynamic lengths $l_h < R_0$, we find that $C_{c,\kappa} < 0$ for all the geometries (n=20) and physical parameters we have tried. In this regime extended bands of elevate tension form, which extend as expected along the saddles of the surface, i.e. along minima and Gaussian curvature (compare Fig. 4.7A,E to Fig. 4.7D,H).

However, the intrinsic geometry and thus the attractors of contractile patches are defined by the geometric potential. In the previous sections, we have found that a localised source of active tension moves down the local gradient of φ, but that is also attracted by maxima in φ at a distance. Whether these effects lead to a colocalization of contractile points with minima or maxima in φ depends on the hydrodynamic length as well as the surface geometry. When the size of the contractile patch is small compared to the hydrodynamic length, we expect maxima in φ to attract contractile patches, However, when the surface geometry is such that κ increases monotonously with φ, we have found that contractile points move down the gradient in φ, irrespective of the hydrodynamic length (see sections 4.1.2 and 4.3). Taken together, we expect a positive correlation between φ and the active tension for large hydrodynamic lengths, but only when κ and φ are not strongly correlated. To test this, we calculated the correlation coefficient $C_{\kappa,\varphi}$ between κ and $\delta\varphi$. For a large hydrodynamic length ($l_h = 3R_0$), we indeed find that $C_{c,\delta\varphi} > 0$, when $C_{\kappa,\varphi}$ is small (Fig. 4.7K). In these cases, a single contractile spot forms and moves towards the global maximum in φ (Fig. 4.7C). On surfaces where κ and $\delta\varphi$ are more strongly correlated, we find the spot to localize to a saddle (Fig. 4.7G). This saddle may be far away from the maximum φ, such that $C_{c,\varphi} \leq 0$. Notably, we find that the magnitude correlation between φ and c is often stronger than between κ and c, when the hydrodynamic length is large such that the stress regulator localizes to a single spot. This provides further evidence, that localized sources of active tension act as sensors of the geometric potential.

4.5 Geometry sensing by active p-atic particles

So far we focused on contractile points, i.e. isotropic localized sources of mechanical activity, However, sources of mechanical activity in a living system are often, if not always, anisotropic. This anisotropy fundamentally changes the way such active particles couple to the surrounding flow. In the following, we investigate how this flow coupling gives such active particles a sense of the surface geometry of the fluid film they are embedded in.

4.5.1 Stress multipole in a curved surface

We consider a force multipole which we understand as a force density of the form

$$ {}_{(1)}f(z) = (-1)^{n_f+m_f} \eth^{n_f} \bar{\eth}^{m_f} \, {}_{(s)}P \delta_{z,z_0}, \quad s = 1 - n_f + m_f, \tag{4.45} $$

where ${}_{(s)}P$ denotes a spin quantity at z_0 that captures the orientation and magnitude of the stress multipole with $|s|$-fold rotational symmetry. The flow field of such a force multipole can be expressed in terms of gradients of the Green's functions as

$$ {}_{(1)}v = {}_{(s)}P\bar{\eth}_{z'}^{m_f}\eth_{z'}^{n_f}G_0(z,z') + {}_{(-s)}P\eth_{z'}^{m_f}\bar{\eth}_{z'}^{n_f}G_2(z,z'). \tag{4.46}$$

For simplicity, we focus on the lowest order multipole for a given orientational symmetry $|s|$ of the particle. Furthermore, we focus on anisotropic non-polar particles which do not move in the absence of an anisotropy of the surface geometry. Thus, we have $m_f = s-1 > 0$, $n_f = 0$. Then, Eq. 4.45 corresponds to a monopole of the nematic stress ${}_{(2)}t$ for $s = 2$. For $s > 2$, we obtain multipoles of nematic stress.

4.5.2 Anisotropic particles align with gradients of the Gaussian curvature

We consider a slight anisotropy of the surface geometry as in section 4.3.2. In appendix H.4, we calculate the resulting flow field $\delta\,{}_{(1)}v$ analytically. We evaluate the flow field in terms of multipoles ${}_{(s)}V(a)$ of $\delta\,{}_{(1)}v$ at a distance a from the stress multipole (see appendix I for details). These multipoles correspond to the Fourier components of the angular dependence of the flow field. They define spin-weighted quantities at the position of the stress multipole. In contrast to the spin-weighted quantities in the previous sections and chapters, quantities with positive and negative spin-weights are distinct, i.e. ${}_{(s)}V \neq {}_{(-s)}V$. This reflects that the underlying flow field $\delta\,{}_{(1)}v$ already is a complex field.

Due to symmetry we have

$$ {}_{(t)}V = N_{ts}^{(1)}\,{}_{(s)}P\,{}_{(t-s)}\mathcal{K} + N_{ts}^{(2)}\,{}_{(-s)}P\,{}_{(t+s)}\mathcal{K} \tag{4.47}$$

where we omitted the a dependence for simplicity. The constants $N_{ts}^{(1)}$, $N_{ts}^{(2)}$ depend on the viscosities and friction coefficient of the fluid film. Due to chiral symmetry, they are real numbers. For vanishing bulk viscosity ($\alpha = 0$), we find $N_{ts}^{(2)} = 0$, as a consequence of $G_2 = 0$. Strikingly, we find in this case $N_{ts}^{(1)} > 0$ (see appendix H.4). This reflects that an expansion $\delta\varphi > 0$ yields a flow field $\delta\,{}_{(1)}v$ that is opposed to the forces that drives it (see 4.2.3).

The imaginary component of ${}_{(0)}V$ defines a rotation Ω which can be written as

$$ \Omega = \Omega_0^s \operatorname{Im}[{}_{(s)}P\,{}_{(-s)}\mathcal{K}] = \Omega_0^s|{}_{(s)}P||{}_{(s)}\mathcal{K}|\sin(s(\theta_P - \theta_K)), \tag{4.48}$$

where the angles θ_P and θ_K denote the phases of ${}_{(s)}P$ and ${}_{(s)}\mathcal{K}$, respectively. When couplings of the active particles to the substrate are negligible, the active particle will rotate with the local flow field, i.e. $\partial_t\theta_P \sim \Omega$. As a consequence, the active particle rotationally aligns with the local anisotropy. This is the local analog to the global rotation we studied in section 3.3.2. The angular velocity Ω_0 is given by $\Omega_0 = N_{0,s}^{(1)} - N_{0,s}^{(2)}$. For $\alpha = 0$, we have $\Omega_0 > 0$ due to $N_{ts}^1 > 0$.

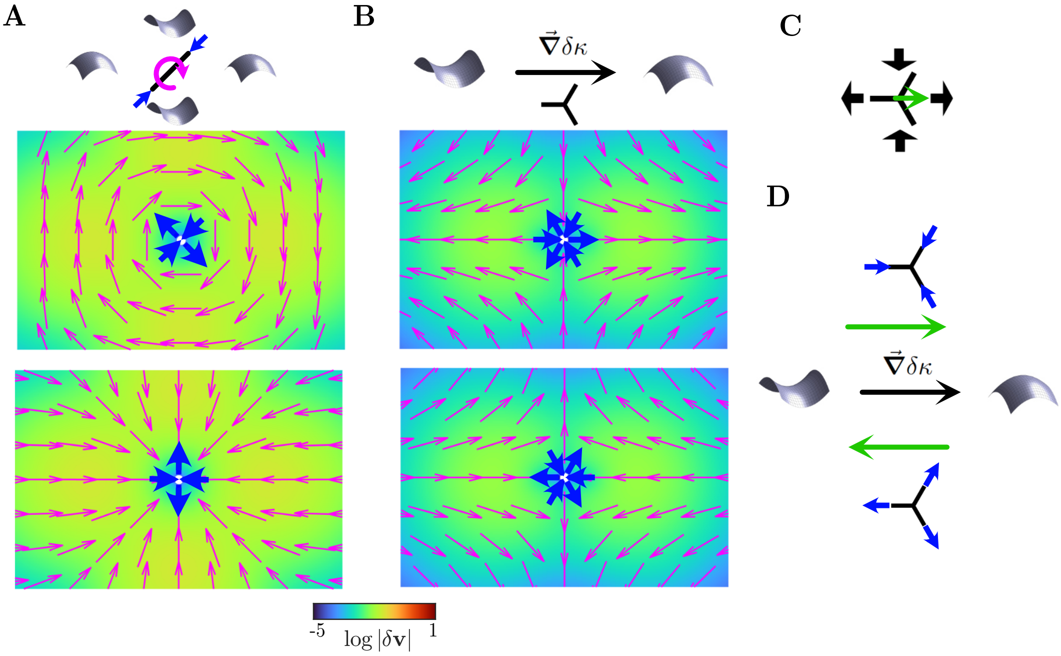

Figure 4.8: Rotation and translation of anisotropic active particles in multipoles of the surface geometry. **A**: Active particle with nematic symmetry ($s = 2$), corresponding to a monopole of active nematic stress, in a nematic anisotropy of the surface geometry (${}_{(2)}\mathcal{K}$). When the axes of stress and surface geometry are not parallely or perpendicularly aligned, a rotational flow arises (middle panel, Eq. 4.48). When the active particle rotates with this flow, it aligns with the surface geometry such that it contracts along the axis of maximal Gaussian curvature. In this configuration (lower panel), the active particle drives a contraction of the fluid film. Pink arrows correspond to flow field $\delta\, {}_{(1)}v$ that results from an anisotropic deformation $\delta\varphi$ of an otherwise flat flow field. Color denotes $\log|\delta\mathbf{v}|$. Blue arrows illustrate the forces the active particle exerts on the fluid film. Flow fields were obtained numerically for $\alpha = 0$ as in Fig. 4.6D,E. **B**: Analogous to **A**, but for a multipole of nematic stress with 3-fold rotational symmetry ($s = 3$) in a gradient of Gaussian curvature (${}_{(1)}\mathcal{K}$). Middle and lower panel correspond to different orientations of the active particle, as indicated by the blue arrows that illustrate the forces exerted by the active particle. In both cases, we observe that the flow field is dominated by a shear flow. **C**: Such a shear flow yields a translation (red arrow) for such an anisotropic particle. **D**: Depending on the orientation of the active forces with respect to the shape of the particle, the particle moves up or down the gradient of Gaussian curvature. For details see main text.

As a consequence ${}_{(s)}P$ aligns perpendicularly with ${}_{(s)}\mathcal{K}$. Hence, the axes along which the active particle contracts align with the axes of positive Gaussian curvature (see Fig. 4.8A for the example of a nematic monopole, i.e. $s = 2$). We note also that that the projection $\mathrm{Re}[{}_{(s)}P\, {}_{(-s)}\mathcal{K}]$ yields scalar, i.e. an isotropic contraction or expansion depending on the angle between surface anisotropy and stress multipole. For $\alpha = 0$, we obtain a contraction when the active particle is orientationally aligned with the surface anisotropy, i.e. for $\cos[s(\theta_P - \theta_K)] = -1$.

4.5.3 Flow coupling controls movement along gradient of Gaussian curvature

We consider a particle that moves by coupling to the local flow field. The velocity ${}_{(1)}V_p$ of the particle is a vector. For an isotropic particle such as a contractile point, only a polar component of the local flow field, i.e. ${}_{(\pm 1)}V$, can define such a vector. For an anisotropic particle, also a non-polar flow can yield a translation of the particle. For example, a bacterium drives a shear flow that yields a translation of the bacterium due to its polar shape [170]. Here, we consider a non-polar particle that has s-fold orientational symmetry, both in terms of the forces it exerts on the fluid film and in terms of its shape by which it couples to the flow. This scenario is motivated in particular by active nematic fluid films and the topological defects in these systems. With this, the velocity of the active particle in linear order of the local flow field can be written as

$$ {}_{(1)}V_p = \beta_0\, {}_{(1)}V^{(0)}_{\text{eff}} + \beta_1\, {}_{(s)}P\, {}_{(-s+1)}V^{(1)}_{\text{eff}} + \beta_2\, {}_{(-s)}P\, {}_{(s+1)}V^{(2)}_{\text{eff}}, \tag{4.49} $$

where

$$ {}_{(t)}V^{(i)}_{\text{eff}} = {}_{(t)}V + \epsilon_i \overline{{}_{(-t)}V}. \tag{4.50} $$

β_i, ϵ_i are constants that determine how the active particle moves in response to the local field. For a non-chiral particle, they are real.

In an isotropic surface geometry only the flow multipoles ${}_{(\pm s)}V$ are non-vanishing, such that a non-polar particle does not move, i.e. ${}_{(1)}V_p = 0$ for $s \neq 1$. However, the anisotropy of the surface geometry can yield such a translation. We consider here a gradient of Gaussian curvature. We have found in section 4.3.2 that a contractile point moves down a gradient of Gaussian curvature. Here we consider the movement of an anisotropic particle in first order of the gradient of Gaussian curvature ${}_{(1)}\mathcal{K}$. Due to symmetry, the resulting velocity of a non-polar particle can be written as

$$ {}_{(1)}V_p = \zeta_0 \delta_{s,0}\, {}_{(0)}P\, {}_{(1)}\mathcal{K} + \zeta_2 \delta_{s,2}\, {}_{(2)}P\, {}_{(-1)}\mathcal{K} + \zeta \left| {}_{(s)}P \right|^2 {}_{(1)}K, \tag{4.51} $$

where for a non-chiral system ζ, ζ_0, ζ_2 are real coefficients. In our model, they correspond to products of the coefficients in Eq. 4.47, 4.49 and 4.50. In particular, ζ_0 and ζ_2 result from the coupling β_0, i.e. a polar flow ${}_{(\pm 1)}V$ that the stress multipole drives in an anisotropic geometry. ζ_0 corresponds to the velocity of the contractile point we considered in the previous sections, whereas ζ_2 yields an orientation-dependent velocity of a nematic stress monopole. The hydrodynamic coupling to the surface geometry we consider here only becomes particularly relevant for a hydrodynamic length that is large compared to the size of the particle. In this regime, where coupling to the substrate is weak, we expect the particle to move in the same direction of the fluid, i.e. $\beta_0 > 0$. Thus, the sign of ζ_0 and ζ_2 is determined by the viscosities of the fluid film through the coefficients $N^{(1,2)}_{ts}$ in Eq. 4.47. When bulk viscosity is negligible, we find that contractile points move down the Gaussian curvature gradient, whereas nematic monopoles that are aligned according to Eq. 4.48 move up the Gaussian curvature gradient. Again, this is a consequence of $N^{(1)}_{ts} > 0$.

For $s \neq 0, 2$, a particle velocity arises only from ζ which is proportional to the coefficients β_1 and β_2. Such couplings arise in particular from the anisotropic shape of the active particle. Hence, the sign of β_1 and β_2 reflects a relation between the forces given by 4.45 and the shape anisotropy of the particle. This is similar to active nematics, where the sign of the active stress relative to the flow coupling defines whether an active nematic is extensile or contractile. Extensile particles push the fluid along their long axis, whereas contractile particles pull. Strikingly, the velocity arising from this flow coupling is independent of the orientation of ${}_{(s)}P$, i.e. ${}_{(1)}V_p \sim |{}_{(s)}P|^2$. The sign of ζ and hence $\beta_{1/2}$ determines whether the active particle will move up or down the gradient of Gaussian curvature ${}_{(1)}\mathcal{K}$. Hence, the coupling to the flow determines, whether an anisotropic particle is attracted or repelled by a saddle of the surface.

As an illustrative example, we consider an active particle with 3-fold rotational symmetry, consisting of three rigidly connected rods. The particle may pull or push the surrounding fluid along these rods. As before, we represent these forces as a multipole of the active nematic stress (${}_{(2)}t_{\text{act}} \sim \bar{\eth}\delta_{z,z_0}$). Such a particle drives a shear flow in a gradient of Gaussian curvature, which yields a translation of the a particle along this gradient (Fig. 4.8B,C). When the particle is contracting along the rods, we find that shear viscosity makes it move towards positive Gaussian curvature. An extensile particle, in contrast, moves towards negative Gaussian curvature (Fig. 4.8D).

4.6 Discussion

In this chapter, we have investigated how the intrinsic geometry of a surface shapes the flow field around localised sources of mechanical activity. To this end, we used isothermal coordinates, where the intrinsic geometry of the surface is defined by a single scalar field, the scalar potential φ. Variations in φ correspond to expansions ($\varphi > 0$) and contractions ($\varphi < 0$) of the surface relative to an isotropic reference surface. We found that such anisotropies in the surface geometry can be mapped to effective gradients in the viscosities and the friction coefficient. In particular, we found that expansions effectively increase the resistance to flow due to shear viscosity, i.e. they yield an effective increase in shear viscosity and friction. In other words, adding more surface area in a given distance to a point makes it harder to move the fluid film at that point. Importantly, these analytical results are valid for any closed surface geometry.

With this insight, we studied the movement of contractile patches in an active isotropic fluid film. We focused on monopoles of active tension. In an anisotropic surface geometry, such a contractile point moves towards certain points in the geometry. These attractors of contractile points are defined by the intrinsic surface geometry, i.e. φ. We found that a contractile point moves down the local gradient in φ, and is at the same time attracted by maxima in φ at a distance. In effect, contractile points tend to move towards points that are surrounded by a maximal amount of surface area. In particular, contractile points move towards the saddles of a torus or a prolate sphere, and towards the saddle of a protrusion.

We also tested whether these analytical calculations allow us to understand the patterns that form in an active fluid model of the cortex We obtained numerical solutions of this model in complex surface geometries. These geometries define friction and viscosity gradients through the geometric potential φ and the Gaussian curvature κ. Mapping Liouville's equation to a reaction diffusion system, we calculated φ. With this we found that the geometric potential and the Gaussian curvature guide the formation of patterns in an active fluid model of the cell cortex as expected from the analytical calculations.

The mapping of intrinsic geometry to material properties we found is a mathematical result. However, it may also be interpreted physically: Material properties and geometry together determine how forces are transmitted within a surface. In this sense, it is not surprising that the impact of the geometry on the flow field can be understood analogously to the impact of the material properties, i.e. the viscosities and the friction coefficient. The striking result of this chapter is that we can understand the combined effects in mathematically simple and physically intuitive terms. In particular, we found that the product of Gaussian curvature and shear viscosity yields an effective friction. Importantly, this result allowed us to understand the movement of contractile patches in an active fluid film. Notably, it has recently been found that contractile patches localize to maxima in friction in reconstituted actomyosin networks [194], as expected from the argument we gave in section 4.3.1. Here, we propose that the impact of the geometry on flows and patterns in the actomyosin cortex can be understood analogously.

In this chapter, we have focused solely on the effects of the intrinsic geometry of a surface. In a model of an active surface, a coupling to the extrinsic geometry, e.g. a curvature dependent binding rate, requires that a small segment of the surface is capable of sensing the geometry on its own. Such a local sense of geometry is distinct from the viscosity-mediated sense of geometry we studied here. Viscosity yields a sense of length scales and angles on the order of the hydrodynamic length. Hence, we expect the phenomena of this chapter to be particularly relevant in systems where the hydrodynamic length is large compared to the length scales of the constituent entities, i.e. cells or filaments.

A typical example is the cell cortex of the *C. elegans* zygote. In this system, a ring of cortical tension drives a rotation that aligns the AP axis with the long axis of the egg shell, as we have discussed in the previous chapter. Thereby, the contractile ring rotates towards the saddle, as expected also from the results of this chapter. Notably, such an alignment, albeit slower, is also found, when the contractile ring is removed by genetic perturbations [99]. Under these conditions, cortical flows result only from the relaxation of cortical tension at the posterior side (see section 1.1.2). Based on the results of this chapter, we propose that the viscosity of the cortex is sufficient to explain why this point of minimum cortical tension moves towards the maximum in Gaussian curvature.

Also epithelia often exhibit a large hydrodynamic length. For example, in the embryo of the fruit fly a localised source of mechanical activity has recently been found to move along a gradient of curvature [195]. Using a one-dimensional model, it has been suggested that this movement results from active moments. These active moments result from apical myosin activity that yields also a contraction within the plane. We wonder, whether this contraction could be sufficient to explain the curvature-dependent movement. Notably, the large-scale movements of the epithelial tissue reveal a hydrodynamic length on the order of the system size. Importantly, our mechanism relies on the global geometry of the surface and is, thus, not limited by the curvature gradient at the position of the source of mechanical activity. Thus, future experiments could test, whether a local coupling to the geometry, as proposed in [195], is sufficient to explain the robust alignment with the geometry they found.

We have studied here also anisotropic sources of mechanical activity. We have found that such anisotropic active particles align with the anisotropy of the surface geometry. Notably, such an alignment has indeed been found for actin filaments in migrating cells [196]. Again this has so far only been understood in a one-dimensional model. Furthermore, we have found that anisotropic particles move along gradients of Gaussian curvature. Importantly, we have found that the direction is controlled by the sign of the flow coupling. We have found that extensile particles move towards minimal Gaussian curvature, whereas contractile particles moves towards positive Gaussian curvature. Recently, an extensile nematic fluid film on a torus has been studied using *in vitro* experiments and numerical simulations [144]. Strikingly, it has been found that topological defects accumulate at the saddle of the torus, thus at minimal Gaussian curvature, as expected from our particle model. So far, no fundamental explanation of this non-equilibrium phenomenon has been suggested. Based on the results of this chapter, we wonder whether topological defects in a contractile nematic move towards positive Gaussian curvature. We plan to use the tools of this chapter to investigate the movements of topological defects in the future.

We have shown here and in the previous chapter that the intrinsic geometry of an active surface has a profound impact on patterns and flow fields. In most biological studies, in contrast, geometry is understood in a one-dimensional picture, where all information about the intrinsic geometry is lost. Here, we have also shown, that the impact of the intrinsic geometry is not only profound, but also but also understandable by considering the Gaussian curvature and the geometric potential. Thereby, we hope to motivate future studies to take the effects of the intrinsic geometry into account.

In this thesis, we focus on the impact of a static geometry on flows and patterns. However, these insights are also valuable to understand the interplay between patterns and shape, when the surface is dynamically deforming. We will elaborate on this further in chapter 6.

Chapter 5

Chiral flows controlled by embryo geometry

Proteins like filamentous actin are chiral molecules, i.e. their structure is distinct from its mirror image. The actomyosin cortex is an active gel that consists of these chiral molecules (see section 1.1.3). In general, we expect the molecular chirality to manifest in a chirality of the mechanical properties and dynamics of the actomyosin cortex (see section 1.2.4). Such a chirality has indeed been observed in cells across the animal kingdom. For example, in the nematode *C. elegans*, chiral counter-rotating flows in the actomyosin cortex arise during various cell divisions. These chiral cortical flows facilitate also the definition of the left-right body axis (see section 1.1.4). Thereby, the molecular chirality is translated into a chirality (=handedness) of the body plan. Similar phenomena have also been observed in snails.

Also cells from mouse embryos and human cell cultures have been found to have an actomyosin-based sense of handedness. Such cells assemble into chiral structures *in vitro*. Repeating these experiments with cells from a certain cell type produces structures with a consistent handedness, as long as the actomyosin cortex is not perturbed [127, 40]. Intriguingly, this actomyosin-based cellular chirality does not appear to contribute to defining the left-right asymmetry of the visceral organs in the mouse [59, 197]. Instead, the handedness of the body plan of mouse and potentially also human embryos is established by a cilia-based mechanism, as in fish and frog embryos (see section 1.1.4 for details).

Only in birds an actomyosin-dependent mechanism of left-right symmetry breaking is evident [67]. There, a leftward movement around the Hensen's node establishes the left-right asymmetry of the body plan by shifting domains of gene expression. Also in chameleon embryos, left-right symmetry breaking has been found to be cilia-independent [69]. Instead, left-right asymmetric tissue deformations are found that are likely due to mechanical activity of the actomyosin cortex. Notably, chameleon embryos also contain a structure akin to the avian primitive streak unlike frog or fish embryos [86]. This suggests that the evolution of an actomyosin-based mechanism of left-right symmetry breaking is linked to the innovation of the primitive streak.

In this chapter, we analyze data from quail embryos to understand how the tissue architecture of the primitive streak facilitates the leftward movement of cells in these embryos (section 5.1). To this end, we use the mechanical model of the primitive streak we developed in chapter 2. We generalize this model of an active viscous crack to a chiral active crack (section 5.1.2). Based on this model, we hypothesize that the primitive streak facilitates left-right symmetry breaking by providing a mechanical link between tissue layers. In section 5.1.3, we test this hypothesis using data from mechanically perturbed embryos.

In section 5.2, we ask whether also tissue curvature may facilitate chiral flows at the avian Hensen's node and beyond. To this end, we consider a generic mechanical model of a chiral active fluid film to understand the impact of curvature on the flow field (section 5.2.1). With this, we investigate also the impact of cell geometry on the chiral cortical flows that have been observed in *C. elegans* embryos (sections 5.2.3 and 5.2.4).

Based on all these physical insights, we ask whether embryo geometry may explain why some embryos make use of the actomyosin cortex to define the handedness of the body plan, whereas many others do not (section 5.3).

5.1 Mechanical model of avian left-right symmetry breaking

In the following, we analyze data from quail embryos as in chapter 2. As before the data was obtained by Julia Pfanzelter and Adrian Lahola-Chomiak from the lab of Stephan Grill at the MPI-CBG Dresden. The raw data was then analyzed by me as described in appendix C. In contrast to chapter 2, we focus here on the left-right asymmetric component of the measured flow field to infer a mechanical model of avian left-right symmetry breaking.

5.1.1 Deciphering the forces and torques driving avian left-right symmetry breaking

Left-right symmetry breaking has been found to rely on a leftward movement of cells around the Hensen's node in chick embryos [67]. Here we want to obtain a physical and, hence, quantitative understanding of this process. To this end, we consider the median flow field of 15 embryos in a local reference frame, as described in appendix C.2. At the time of maximum primitive streak extension ($t_{PS} = 0h$), we observe a rotational flow around the Hensen's node such that cells on the anterior side of the node move to the left (see Fig. 5.1A and appendix Fig. C.2). This suggests that as in chick embryos, left-right symmetry is broken by chiral flow of the epiblast tissue around the node.

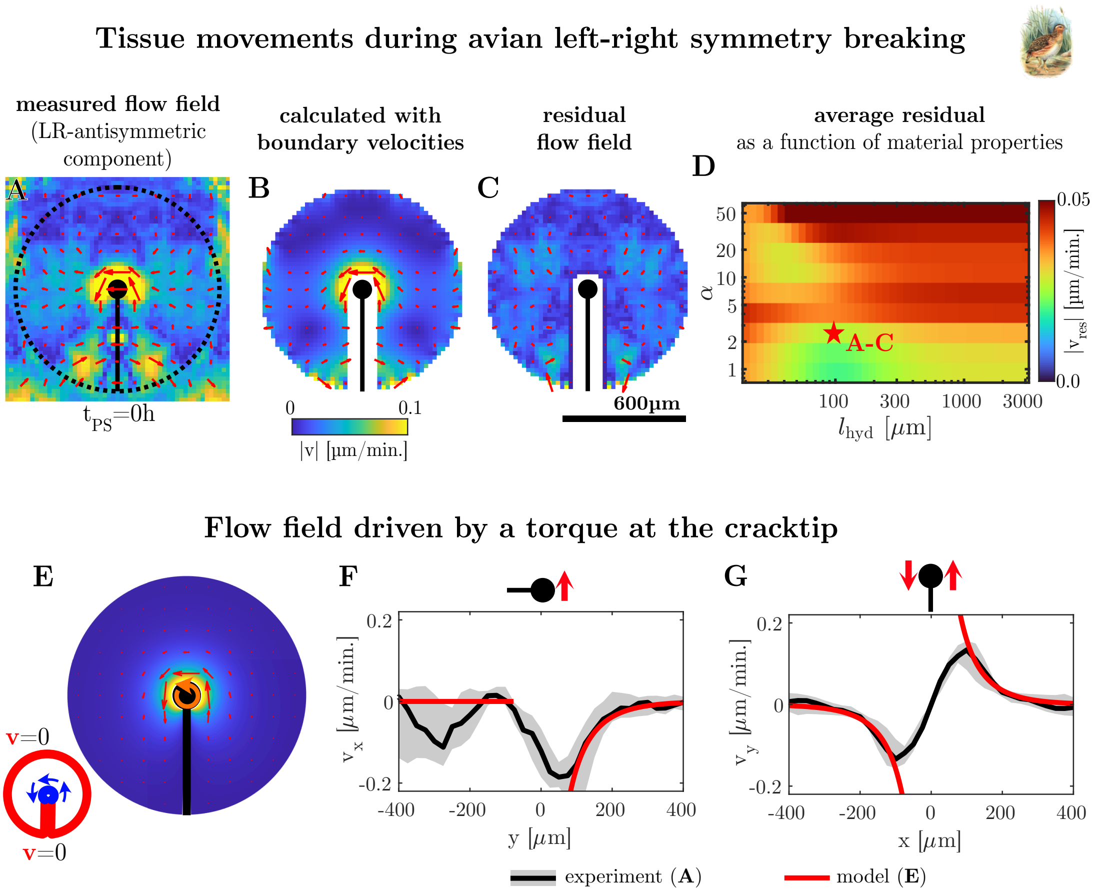

Figure 5.1: A torque at the Hensen's node drives the chiral flow of the avian epiblast. **A**: Left-right antisymmetric component of the average flow field (red arrows) of the epiblast of 15 quail embryos at the time point of maximum streak extension. (see appendix C for details). Color code denotes the modulus of the velocity. Note that we consider here a local reference frame, i.e. we subtract any global translations or rotations of the epiblast (see appendix C.2). **B**: Flow field of homogeneous fluid film with $l_h = 100\mu$m and $\alpha = 3$ calculated with measured boundary velocities as in Fig. 2.2B. **C**: Residual of measured flow field (**A**) after subtracting the flow field in **B**. **E**: Flow field (red arrows) of a homogeneous fluid film around a crack (black line). Boundary conditions are such that the flow field vanishes along the crack and that the crack tip (black circle) exerts a torque (pink arrow, $T_T/\eta = 4.4\mu\text{m}^2/h$) onto the fluid film. Color code denotes the modulus of the fluid velocity. Physical parameters are $\alpha = 3$, $l_h = 100\mu$ and we consider a crack tip size $a = 75\mu$m. **F**,**G**: Comparison of the measured flow field (**A**, black lines) to the flow field of the crack model in **E** (red lines). Gray area corresponds to $[5\%, 95\%]$ confidence interval from bootstrapping (see appendix C.3). **F**: leftward velocity v_x along the midline ($x = 0$) as a function of the anterior coordinate y relative to the node/cracktip. **G**: anterior velocity v_y along the left-right axis at the anterior position of the node ($y = 0$). $x > 0$ corresponds to right half of the embryo or fluid film.

Such a flow that involves the shearing of tissue needs to be driven by mechanical forces. Based on the results of chapter 2, we hypothesise that the forces driving the chiral flow of the tissue are generated within the primitive streak and the Hensen's node. To test this hypothesis, we use the same method as in section 2.1.3. Briefly, we model the epiblast as a homogeneous flow field and calculate the flow field from measured boundary velocities. We then compare this calculated flow field (Fig. 5.1B) to the measured flow field (Fig. 5.1A) . We find that the calculated flow field is in quantitative agreement with the measured flow field, when considering a compressible

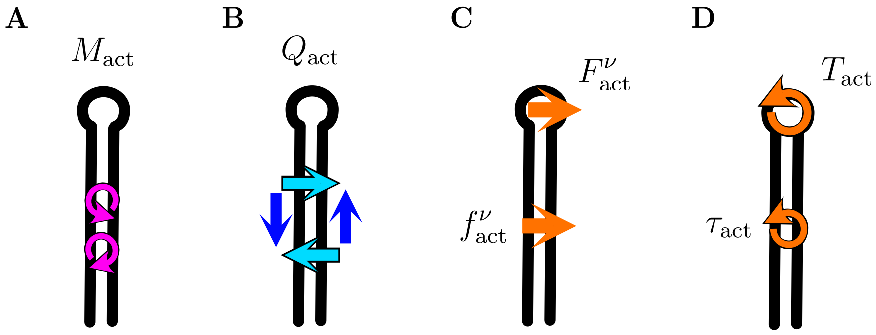

Figure 5.2: Mechanical model of an active chiral crack. Illustration of the terms that correspond to active chiral mechanical activity in Eq. 5.1-5.4. Black outline corresponds to crack with cracktip on top. **A**, **B** illustrate torque dipoles (M_{act}) and chiral force dipoles (Q_{act}) in the plane of the fluid film. **C,D** illustrate forces ($\mathbf{f}_{\text{act}}$, $\mathbf{F}_{\text{act}}$) and torques (τ_{act}, T_{act}) the substrate exerts on the crack and the cracktip. We hypothesize that the chiral flow in the avian embryo is driven by an active torque T_{act} generated within the Hensen's node. For further details see main text.

fluid film with a hydrodynamic length of 100μm (Fig. 5.1C,D). This small hydrodynamic length is in stark contrast to our findings for the symmetric flow field (see Fig. 2.2D). It suggests that the chiral flow around the node involves the movement of the epiblast relative to a substrate that the epiblast adheres to. We will elaborate further on this observation in section 5.1.4.

Taken together, our quantitative analysis of tissue movements suggests that left-right symmetry breaking in birds is driven by chiral forces and torques localised to the streak and the node.

5.1.2 Constitutive equations of an active chiral crack

In the following, we want to obtain a mechanical understanding of how these forces are generated. To this end, we consider a coarse-grained model of the streak as a one-dimensional line of active material embedded in a fluid film that is the epiblast. In section 2.2, we developed a mechanical model of such an active viscous crack. Here we want to generalize this theory to a chiral crack.

As before, we consider a crack that is constrained to the flat plane of the fluid film it is embedded in. Chirality or left-right asymmetry of the crack implies that we have to take into account the crack moment, specifically its normal component m_C (Eq. 2.15). We consider the following constitutive equation

$$m_C = -K\kappa_g + M_C^{\text{act}}, \tag{5.1}$$

where K is a bending stiffness and κ_g is the geodesic curvature (Eq. A.1). The active moment M_C^{act} is a tangential pseudo-vector. It corresponds to dipoles of normal torques (see Fig. 5.2A). Starting from configuration with $\kappa_g = 0$, a Gradient of M_C^{act} yields a torque (Eq. 2.15). This torque may be exerted on the fluid film (corresponding to τ_C) resulting relative sliding of the fluid film on the two sides of the crack (see Eq. 2.16). However, the torque may also act on the crack in terms of a normal stress t^{ν}_C, which may drive a bending of the crack. Importantly, we have to specify the balance between these torques. For this we consider the following constitutive equation

$$\tau_C + t_C^\nu = Q_{\mathrm{act}} + \eta_{C,\nu} \left[\partial_\lambda (v_L^\nu + v_R^\nu) - \frac{1}{d}(v_L^\lambda - v_R^\lambda) \right]. \tag{5.2}$$

Here Q_{act} is an active force dipole line density. Q_{act} may be understood as an active nematic stress that drives a contraction or extension along an axis that forms an angle of 45 degree with the crack axis (See Fig. 5.2B). The one-dimensional viscosity $\eta_{C,\nu}$ quantifies the dissipation associated with the corresponding shear flow.

As the chiral flow appears to be limited by mechanical interaction with a substrate, we take also substrate interactions of the crack, i.e. the streak, into account. To this end, we consider the following constitutitve equations for the force density $\mathbf{f}_{\mathrm{sub}}$ and the torque density τ_{sub} the substrate is exerting onto the crack material:

$$\mathbf{f}_{\mathrm{sub}} = \mathbf{f}_{\mathrm{act}} - \frac{\gamma_1}{2}(\mathbf{v}_L + \mathbf{v}_R), \quad \tau_{\mathrm{sub}} = \tau_{\mathrm{act}} - \frac{d\gamma_2}{2}(v_L^\lambda - v_R^\lambda), \tag{5.3}$$

where as before $\mathbf{v}_{L/R}$ are the velocities on the left and right side of the crack (Eq. 2.5), d is the thickness of the crack, and the superscript λ denotes the projection onto the tangent vector of the crack. γ_1 and γ_2 are friction coefficients that quantify the dissipation associated with the movement of the two sides of the crack relative to the substrate. In contrast, $\mathbf{f}_{\mathrm{act}}$ and τ_{act} result from mechanical activity of the crack material that propels the fluid film relative to the substrate (see Fig. 5.2C,D). We elaborate on the nature of this substrate in the next section.

Also at the crack tip corresponding to the Hensen's node, we consider a force $\mathbf{F}_{\mathrm{sub}}$ and a torque T_{sub} the substrate exerts onto the crack tip. Again we consider two friction coefficients (γ_1^T, γ_2^T) as well as active contributions such that force and torque read

$$\mathbf{F}_{\mathrm{sub}} = \mathbf{F}_{\mathrm{act}} - \gamma_1^T \mathbf{V}_T, \quad T_T = T_{\mathrm{act}} - \gamma_2^T d\Omega_T. \tag{5.4}$$

In a non-chiral left-right symmetric crack, the forces $\mathbf{f}_{\mathrm{act}}$ and $\mathbf{F}_{\mathrm{act}}$ point along the tangent vector of the crack and the torques $\tau_{\mathrm{act}}, T_{\mathrm{act}}, M_C^{\mathrm{act}}, Q_{\mathrm{act}}$ have to vanish. Here we consider a chiral flow that results from the chirality of a mechanically active material, i.e. the actomyosin cortex that drives cell rearrangements. Thus, all those torques and chiral forces may in general be non-vanishing.

However, we observe that the chiral flow in the quail embryo is localised to the crack tip, i.e. the Hensen's node. Therefore, we hypothesize that the chiral flow is driven by a leftward force $\mathbf{F}_C \sim -\boldsymbol{\nu}$ and a torque T_C the node exerts on the epiblast. These are related to the substrate forces and torques that the substrate and the streak exert on the node by force and torque balance (Eq. 2.13, 2.17). Away from the node, no consistent left-right antisymmetric flow at the streak is observed. Thus, we consider the substrate force and torque densities to vanish along the streak, i.e. $\mathbf{f}_{\mathrm{act}} = 0 = \tau_{\mathrm{act}} = Q_{\mathrm{act}}$. At the same time, we consider strong coupling of the streak to the substrate such that $\gamma_1^T, \gamma_2^T \to \infty$, and a large streak viscosity $\eta_{C,\nu}$. This regime corresponds to no-slip boundary conditions along the crack that is the streak. With this, we fit a force $\boldsymbol{\nu} \cdot \mathbf{F}_C$ and a torque T_C to the flow field using numerical solutions of the crack boundary conditions (appendix G). Strikingly, we find that a torque T_C is sufficient to quantitatively capture the experimental flow field (Fig. 5.1E-G). This suggests that avian left-right symmetry is broken by a torque the Hensen's node exerts on the epiblast.

Using the constitutive equations above and torque balance at the crack tip (Eq. 2.17), this torque is given by

$$T_C = T_{\mathrm{act}} + M_C^{\mathrm{act}} - \gamma_2^T d\Omega_T - K\kappa_g. \tag{5.5}$$

We observe that the torque the node exerts on the epiblast could rely on active mechanical interactions within the streak (M_C^{act}) or at the interface of the node to the substrate (T_{act}). In the experiment, it is sometimes oberved that the streak ruptures without affecting the chiral flow (data not shown). This suggests that the chiral flow relies on a torque T_{act} the substrate exerts on the node.

5.1.3 Mechanical coupling of tissue layers facilitates chiral tissue flows

Importantly, the Hensen's node is the point where all tissue layers of the embryo are connected through cell-cell connections (see section 1.1.5 and Fig. 1.5). We hypothesize that this allows for the generation of a torque dipole between the dorsal and ventral layers of the node (Fig. 5.3A). Thus, we interpret the rigid substrate in our model as the mesodermal and endodermal tissue that underlies the epiblast. To test, whether this substrate is indeed crucial to driving the chiral flow, we analyze data from experimentally perturbed embryos. As before this data was obtained by Julia Pfanzelter and Adrian Lahola-Chomiak and analyzed by me.

Using a human eye-brow the ventral tissue was scraped away 2-5h before the time point of maximum streak extension. This yields an embryo that consists of only one mostly unicellular epithelium (Fig. 5.3B). Importantly, we find that this profound perturbation of the embryonic tissue leaves the epiblast intact. As before, we obtained flow fields using particle image velocimetry (appendix C). However, we find that the flow field varies more strongly between time points and embryos than in the control condition. This complicates the analysis of the chiral flow. Therefore, we focus only on the movement of the node relative to the surrounding epiblast, which we obtain by averaging the flow field in a 100μm circle around the center of the node. As under control conditions, we observe that the node moves first anteriorly as the streak extends, and then posteriorly as the streak regresses (Fig. 5.3G). We find that the associated velocities are on the same order as under control conditions. However, we observe that the transition between the phases of streak extension and streak regression is considerably faster in the perturbed

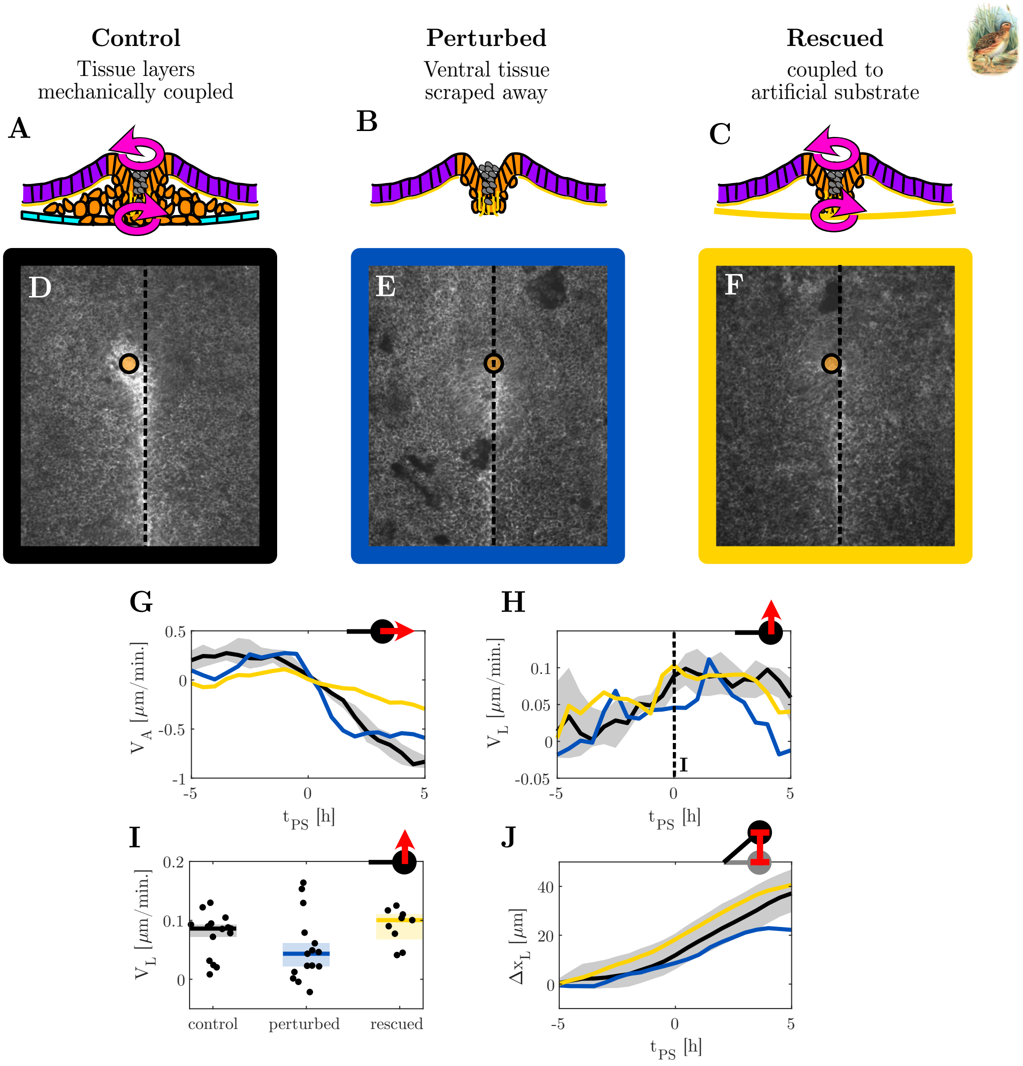

Figure 5.3: Leftward movement of the node relies on the mechanical coupling of tissue layers. **A**-**C**: Schematic cross-section of the primitive streak of the quail embryo as in Fig. 1.5F for different experimental conditions. Pink arrows denote dipole of torques that drive the chiral flow of the epiblast (violet) relative to the more rigid underlying material. (Prospective) meso- and endoderm tissue is drawn in orange, whereas the extra-embryonic hypoblast is colored in cyan. **A**: Unperturbed embryo, where mechanical coupling of tissue layers at the streak and the node facilitates the chiral flow of the epiblast. **B**: Embryo after mechanical removal of most of the hypoblast, endoderm and mesoderm tissue. **C**: Embryo that has been placed onto a protein membrane, specifically the vitelline membrane of another embryo, after removing the ventral tissue as in **B**. Cells adhere to this elastic membrane, facilitating the generation of a torque dipole between the epiblast and the vitelline membrane. **D-F** Microscopy images of quail embryos under the conditions described in **A-C** about 4h after the onset of the chiral flow. Cell debris in the middle of the streak is visible as a bright region. Black dashed lines denote morphological midline of the embryo as determined from the streak. The center of the Hensen's node is drawn as an orange filled circle. We observe that the node is displaced to the left of the midline in **D** and **F**. **G-J**: Quantification of node velocity. Solid lines correspond to medians of 15 control embryos (black), 15 perturbed embryos (blue) and 9 rescued embryos (yellow). Gray area denotes confidence interval of control data from bootstrapping (appendix C.3). **G**: Anterior node velocity as a function of time. Note that we consider the reference frame of the surrounding epiblast as in Fig. 5.1A. **H**: Leftward node velocity as a function of time. **I**: Leftward node velocity at the time point of maximum streak extension ($t_{PS} = 0$). Black points denote single embryos. **J**: Leftward displacement of node obtained by integrating the leftward velocity (**H**) over time, starting at $t_{PS} = -5h$. As before, microscopy images (in particular **D-F**) were obtained by Julia Pfanzelter and Adrian Lahola-Chomiak from the lab of Stephan Grill. This experimental data was then analyzed by me as shown in **G-J**.

embryos. This indicates that the initialization of streak regression does not rely on interactions of the epiblast with the underlying tissue.

Around the time-point of maximum streak extension, the chiral flow of the epiblast emerges. Under control conditions, the chiral flow of the epiblast involves a leftward movement of the node (Fig. 5.1A,F). As a consequence, the most anterior part of the streak is kinked to the left such that the node is positioned leftward compared to the axis of the posterior streak (Fig. 5.3D). Due to the bending stiffness K of the streak, such a kink ($\kappa_g \neq 0$) yields a torque (and also a force) that the node needs to balance (Eq. 5.5). In the perturbed embryos, where the ventral tissue has been removed, we expect that the node cannot exert such a torque or force on streak and epiblast. Strikingly, the leftward kink of the streak is indeed absent in some perturbed embryos (Fig. 5.3E). Furthermore, the quantification of the node velocity shows that the leftward movement of the node is inhibited after removing the ventral tissue: The average flow field of the perturbed embryos contains still a considerable leftward movement of the node, but the leftward velocity is reduced compared to the control condition (Fig. 5.3H,I). This reduction is evident in particular from the integrated leftward movement of the node (Fig. 5.3J). These observations are in agreement with our hypothesis that the leftward movement of the node is facilitated by a mechanical coupling of the tissue layers.

However, the removal of the ventral tissue perturbs also chemical interactions between tissue layers. Such chemical interaction may also affect the chiral flow of the epiblast. To test, whether the chiral flow relies primarily on mechanical interactions between the epiblast and some rigid substrate, perturbed embryos were placed onto an elastic protein membrane (Fig. 5.3C). In these embryos, we observe that overall tissue movements are reduced compared to the control condition (Fig. 5.3G). This indicates that the tissue is mechanically coupled to the surrogate substrate. Strikingly, this mechanical coupling appears to facilitate a leftward movement of the node: After placing the perturbed embryos on the surrogate substrate, timing and magnitude of the leftward movement are identical to the control condition (Fig. 5.3H-J). Thus, introducing a mechanical substrate rescues the control phenotype in terms of the leftward movement of the node.

Taken together, we conclude that the leftward movement of the node is facilitated by mechanical coupling of the epiblast to the underlying tissue layers. The underlying tissue acts like a rigid substrate that allows for the generation of an active torque at the node.

5.1.4 Two-layer model of the avian embryo

Together with the results from chapter 2, these observations motivate the following mechanical model of the avian embryo around the time point of maximum streak extension: We consider two flat fluid films with viscosities η_d and η_v corresponding to the dorsal epiblast and the underlying ventral tissue, respectively. We consider a bulk to shear viscosity ratio $\alpha = 3$ for both fluid films.

The tissue layers grow with growth rates G_d and G_v respectively. In the following we consider the growth rates to be spatially homogeneous. We model the mechanical coupling between the tissue layers away from the streak by a force density $\mathbf{f}_{d\to v}$ that the dorsal tissue exerts on the ventral tissue. It is balanced by a force density $\mathbf{f}_{v\to d}$ that the ventral tissue exerts on the dorsal tissue. We consider a linear constitutive equation,

$$\mathbf{f}_{d\to v} = -\mathbf{f}_{d\to v} = \gamma_{dv}(\mathbf{v}_d - \mathbf{v}_v), \tag{5.6}$$

that yields a coupling of the flow fields of dorsal ($\mathbf{v}_d$) and ventral ($\mathbf{v}_v$) tissue. With this, tangential force balance yields the following governing equations of the flow fields:

$$\Delta(\mathbf{v}_d + \mathbf{v}_v) + \alpha\partial_i\left[\operatorname{div}(\mathbf{v}_d + \mathbf{v}_v)\right] = -\frac{\gamma_{dv}}{\eta_d}\frac{\eta_v - \eta_d}{\eta_v}(\mathbf{v}_d - \mathbf{v}_v) \tag{5.7}$$

$$\Delta(\mathbf{v}_d - \mathbf{v}_v) + \alpha\partial_i\left[\operatorname{div}(\mathbf{v}_d - \mathbf{v}_v)\right] = -\frac{\gamma_{dv}}{\eta_d}\frac{\eta_v + \eta_d}{\eta_v}(\mathbf{v}_d - \mathbf{v}_v), \tag{5.8}$$

where Δ denotes the Laplace operator. Eq. 5.8 yields that the difference of the flow fields $\mathbf{v}_d - \mathbf{v}_v$ decays on the hydrodynamic length scale

$$l_h = \sqrt{\frac{\eta_d\eta_v}{\gamma_{dv}(\eta_v + \eta_d)}}. \tag{5.9}$$

Beyond this length scale, ventral and dorsal tissue move together as one fluid film with infinite hydrodynamic length.

This allows to reconcile the models for the left-right symmetric and antisymmetric components of the flow field. The torque dipole between the dorsal and the ventral half of the tissue drives a movement of the dorsal tissue (the epiblast) relative to the ventral tissue. Thus, it results in a velocity $\mathbf{v}_d - \mathbf{v}_v$ that decays on the hydrodynamic length scale l_h away from the node. This relative velocity implies also a net velocity $\mathbf{v}_d + \mathbf{v}_v$, when the viscosities of ventral and dorsal tissue differ. When shearing the ventral tissue requires much larger forces than shearing the dorsal epiblast ($\eta_v \gg \eta_d$), only the dorsal tissue moves while the ventral tissue acts as a rigid substrate.

Beyond the hydrodynamic length scale, however, dorsal and ventral tissue behave as a single fluid film. This fluid film is set into motion by the sum of the forces and force dipoles that the streak exerts on the dorsal and ventral tissue. In the model we consider here, chiral activity results only in a torque dipole. This torque dipole yields no effect when considering the sum of the dorsal and ventral torque. Thus, the active torque dipole that drives the rotation of the dorsal epiblast does not drive any velocities beyond the hydrodynamic length scale. This contrasts with the active force dipole p_C^{act} that drives the left-right symmetric flow towards the streak (see section 2.2.2). We do not expect this force-dipole to act equally on the dorsal and the ventral tissue. In fact, the actomyosin cables that are responsible for these forces are found only at the most dorsal (apical) surface of the tissue. Beyond the hydrodynamic length scale, however, such dorso-ventral asymmetries do not contribute to the flow field. Thus, the model of the left-right symmetric flow of the epiblast (see chapter 2) is in fact a model for the flow field of dorsal and ventral tissue layers $\mathbf{v}_d + \mathbf{v}_v$.

Taken together our two-layer model of the avian embryo provides two predictions: First, the two layers move together on the scale of the embryo. Second, the chiral flow involves a counter-rotation of the two layers. Strikingly, it has recently been found that the two layers move indeed together on a large scale (Aurelien Villedieu, personal communication). Preliminary data suggests also that the ventral tissue of the node does not rotate. Hence, the rotation of the dorsal tissue implies a counter-rotation of the layers. It remains to be seen, whether it is possible to isolate a viable node where the ventral tissue is unconstrained. In such a setting, we would expect the ventral tissue to rotate against the dorsal tissue.

5.2 Chiral flows facilitated by curvature gradients

In the previous section, we have found that the chiral flow of the avian epiblast is driven by a torque dipole generated at the Hensen's node. Notably, the tissue geometry at the Hensen's node is quite peculiar. In particular the surface of the tissue is curved in contrast to the bulk of the surrounding epithelium [68]. We wondered, whether this curvature may contribute to the generation of the torque dipole. Intriguingly, also left-right symmetry breaking in the nematode *C. elegans* relies on the generation of chiral flows by a curved structure, namely the cytokinetic furrow. This motivated us to consider a generic mechanical model of a chiral curved active fluid film (section 5.2.1). With this we investigate the impact of curvature on chiral flows (section 5.2.2), in particular in the context of chiral cortical flows observed in the *C. elegans* embryo (sections 5.2.3 and 5.2.4).

5.2.1 Constitutive equations

As in chapter 4, we adopt the formalism of spin-weighted quantities (see section 1.3.1). Briefly, real tensor and vector fields are understood as complex fields, with a prescript, the spin-weight, denoting the local rotational symmetry of the field. In particular, the symmetric tension tensor $\tilde{t}_{ij}$ (Eq. 1.33) is decomposed into its symmetric traceless-symmetric components ${}_{(2)}\tilde{t} \in \mathbb{C}$ and its trace ${}_{(0)}\tilde{t} \in \mathbb{R}$ (Eq. 1.58). Analogously, we have the trace-less symmetric bending moment ${}_{(2)}\tilde{m}$, whereas ${}_{(0)}\tilde{m} \in \mathbb{C}$ denotes the trace and the antisymmetric component of $\tilde{m}_{ij}$ (Eq. 1.34). The normal moment ${}_{(1)}m_n$, a (pseudo-)vector field, defines the spin-1 quantity ${}_{(1)}m_n$. We have found this formalism to be particularly elegant for chiral systems. It allows us to generalize the governing equations of an achiral system (see e.g. section 3.1) to a chiral system by simply replacing real coefficients by complex coefficients. This can be understood as a consequence of mapping the Levi-Cevita tensor ϵ_{ij} to the imaginary unit i (Eq. D.2).

With this, we consider a chiral active fluid film that is in contact with a rigid substrate that imposes the static shape of the fluid film. We consider the following constitutive equations for mechanical interactions within the fluid

$$
\begin{aligned}
{}_{(2)}\tilde{t} &= 2\eta e^{i\beta}\,{}_{(2)}v + \chi_Q e^{i\varepsilon_1}\,{}_{(2)}Q && (5.10)\\
{}_{(0)}\tilde{t} &= 2\eta\alpha\,\mathrm{Re}[{}_{(0)}v] + 2\chi_{\mathrm{iso}}c && (5.11)\\
{}_{(2)}\tilde{m} &= \zeta_Q e^{i\varepsilon_2}\,{}_{(2)}Q, \quad {}_{(0)}\tilde{m} = 2(\zeta^R_{\mathrm{iso}} + i\zeta^I_{\mathrm{iso}})c && (5.12)\\
{}_{(1)}m_n &= i\zeta_p e^{i\varepsilon_3}\,{}_{(1)}p && (5.13)
\end{aligned}
$$

Here, $\eta > 0$ is the viscosity of the fluid film that yields a shear viscosity $\eta\cos\beta$ and a bulk viscosity $\alpha\eta$. In a non-chiral fluid film, the phase $\beta \in [-\pi/2, \pi/2]$ vanishes such that $\cos\beta = 1$ and $\sin\beta = 0$. When chiral symmetry is broken, however, $\sin\beta$ is in general non-vanishing, which yields an odd viscosity $\eta\sin\beta$ [198]. The odd viscosity yields boundary forces that are perpendicular to the forces from shear viscosity. Combining the stresses from odd and shear viscosity, we obtain a shear stress along an axis that is rotated by 2β with respect to the axis of the shear rate tensor ${}_{(2)}v = \eth\,{}_{(1)}v$.

The flow field is driven by active stresses and moments. In chapters 3 and 4, we focused on an isotropic active stress controlled by a scalar field c and a real coupling constant χ_{iso}. In particular, we considered a contractile active fluid where $\chi_{\mathrm{iso}} > 0$. Here we consider also an isotropic active moment ${}_{(0)}\tilde{m}$ controlled by the real constants ζ^R_{iso} and ζ^I_{iso}. Importantly, the antisymmetric bending moment, $\mathrm{Im}\,\tilde{m}$, controlled by $i\zeta^I_{\mathrm{iso}}$ breaks chiral symmetry, as it couples the scalar c to a pseudoscalar (see section 1.2.4).

Furthermore, we consider also a vector field ${}_{(1)}p$ and a nematic field ${}_{(2)}Q$, corresponding to local order parameters. These fields allow to define anisotropic active stresses and moments controlled by χ_Q, ζ_Q and ζ_p. The phases $\varepsilon_i \in [-\pi, \pi]$ yield an angle between an active moment or stress and the corresponding order parameter, similarly to the viscous phase β. Such an angle breaks chiral symmetry, whenever $\sin\varepsilon_i \neq 0$. Note that $i\zeta_p$ does not break chiral symmetry for $\varepsilon_3 = 0$, as it couples a vector, ${}_{(1)}p$, to a pseudo-vector field, ${}_{(1)}m_n$ (see also section 1.2.4).

Finally, we consider also friction with the substrate controlled by a friction coefficient γ. For completeness, we consider also an active force density ${}_{(1)}f_{\mathrm{act}}$ and an active torque

$$\Gamma_{\mathrm{n}} = \tau_{\mathrm{act}}c \qquad (5.14)$$

that the substrate exerts on the fluid film. The real constant τ_{act} breaks chiral symmetry as it couples the scalar c to the pseudoscalar Γ_n. It corresponds to the active torque density that was used to explain chiral cortical flows in [39]. Here, however, we focus on chiral mechanical interactions within the fluid film, as given by Eq. 5.10-5.13.

5.2.2 Chiral active moments yield curvature-dependent chiral flows

With these constitutive equations, we derive the governing equations of the flow field using force and torque balance equation (see appendix D.4 for details). We obtain

$$\begin{aligned}\eta\left[\eth\bar{\eth}\eth(e^{i\beta}F+\alpha\,\mathrm{Re}\,F)+\left(2\kappa e^{i\beta}-\frac{\gamma}{\eta}\right)(\eth F+{}_{(1)}v_h)\right]&\\ =-{}_{(1)}f_{\mathrm{act}}+\zeta^R_{\mathrm{iso}}c\,\eth\,{}_{(0)}C+\frac{\zeta_Q}{4}\left({}_{(2)}Qe^{i\varepsilon_2}\eth\,{}_{(-2)}C+{}_{(-2)}Qe^{-i\varepsilon_2}\eth\,{}_{(2)}C\right)&\\ +i\eth\left(\tau_{\mathrm{act}}c+\frac{\zeta_Q}{2}\,\mathrm{Im}[{}_{(2)}Qe^{i\varepsilon_2}\,{}_{(-2)}C]\right)&\\ -\frac{1}{2}\bar{\eth}\left(\chi_Q e^{i\varepsilon_1}\,{}_{(2)}Q-2i\zeta^I_{\mathrm{iso}}c\,{}_{(2)}C+\zeta_p e^{i\varepsilon_3}\eth\,{}_{(1)}p\right)&\\ -\eth\left(\chi_{\mathrm{iso}}c-\frac{1}{2}\zeta_p\,\mathrm{Re}[\bar{\eth}e^{i\varepsilon_3}\,{}_{(1)}p]\right).&\end{aligned} \tag{5.15}$$

The left-hand side yields the force density that results from friction and the divergence of the viscous stresses. Note that we use here as before a Hodge decomposition of the flow field (Eq. 1.67). The right hand side yields an active force density resulting from active substrate interactions (${}_{(1)}f_{\mathrm{act}}$, τ_{act}) as well as the active stresses and moments of the fluid film. The first row of the right hand side contains terms that cannot generally be written as the divergence of an active stress. The second row corresponds to the divergence ($\eth$) of an effective active antisymmetric stress and thus an effective active torque density. The third row, in contrast, corresponds to the divergence ($\bar{\eth}$) of an effective trace-less symmetric active stress. Finally, the fourth row contains terms that can be written as the gradient of a scalar field corresponding to an effective isotropic active stress. We observe that the active normal moment ${}_{(1)}m_n \sim {}_{(1)}p$ can be mapped to an equivalent active symmetric stress. Therefore, we will neglect ${}_{(1)}m_n$ in the following. Also the active antisymmetric bending moment ($\sim \zeta^I_{\mathrm{iso}}$) can be mapped to an active symmetric stress. The axis of this active nematic stress is given by the axis of the anisotropic curvature ${}_{(2)}C$. Thus, the active antisymmetric bending moment yields a curvature-dependent effective active stress. Also for the other components of the active bending moment, we observe that they yield a curvature-dependent effective (tangential) force density. This reflects that the curvature of an active surface couples the normal and tangential components of a vector valued flux such as the stress tensor $\mathbf{t}^i$ and the moment tensor $\mathbf{m}^i$ (see in particular Eq. 1.25 and 1.29). As a consequence, active moments drive in-plane flows in a curved fluid film.

We observe that the symmetric components of the active bending moment (i.e. ${}_{(2)}\tilde{m}$ and $\mathrm{Re}[{}_{(0)}\tilde{m}]$) yield an effective force and torque density:

$$\tau_{\mathrm{eff}}=\frac{1}{2}\,\mathrm{Im}\left[{}_{(2)}\tilde{m}\,{}_{(-2)}C\right],\quad {}_{(1)}f_{\mathrm{eff}}=\frac{1}{4}\left({}_{(2)}\tilde{m}\eth\,{}_{(-2)}C+{}_{(-2)}\tilde{m}\eth\,{}_{(2)}C\right) \tag{5.16}$$

These terms cannot be mapped to a symmetric stress. As such they can yield a net force and torque, when integrating the effective tangential force density over the entire surface. When the flow field is only friction limited, this yields a net force and torque the fluid film is exerting on the substrate, seemingly violating (angular) momentum conservation. Importantly, however, the active bending moments contribute also to the normal force density the substrate exerts on the fluid film (Eq. D.17). These normal forces yields a net force and torque that balances the force and torque from the tangential force density, similarly to what we discussed in section 3.3.3. There, we found that this results in a rotation of the entire surface that aligns the pattern for normal forces with the geometry of the surface. Eq. 5.15 yields a local analog: By considering an effective free energy, we find that the effective forces and torques from the active bending moments drive translational and rotational alignment of the pattern of active moments with the local curvature of the surface (see appendix D.5). Hence, localised sources of active moments can act as sensors of the (extrinsic) curvature. In particular, isotropic active bending moments drive flows along the local gradient of mean curvature, a scenario that may apply to tissue movements during fruit fly development [195] (see also section 4.6).

Importantly, the rationale of minimizing an effective free energy also applies to a chiral active bending moment ${}_{(2)}\tilde{m}$, i.e. with $\varepsilon_2 \neq 0$. Hence, the chiral flow may be understood as aligning the pattern ${}_{(2)}Q$ with the curvature ${}_{(2)}C$ rotated by the angle $2\varepsilon_2$. We wonder whether this may explain the chiral morphology of the avian node [67]. Notably, this equilibrium rationale does not apply to the effective active nematic stress resulting from the isotropic chiral bending moment ($\sim \zeta^I_{\text{iso}}$).

5.2.3 Chiral counter-rotating flows facilitated by cell elongation

In the *C. elegans* embryo, chiral counter-rotating flows have been observed in the actomyosin cortex during symmetric cell divisions [22] (Fig. 5.4A). These chiral flows result from the mechanical activity of myosin motor molecules acting on the meshwork of helical actin filaments [39, 22, 44] (see section 1.1.3). On a hydrodynamic scale, this mechanical activity has been modeled in terms of an active torque density τ_{act} [39, 22]. Such a torque density requires the mechanical interaction of the cell cortex with a rigid substrate, presumably the egg shell. Intriguingly, the whole-embryo rotation we studied in section 3.3.2 suggests that the forces between the actomyosin cortex and the egg shell are negligible compared to the mechanical interactions within the cortex. Thus, we wondered whether the chiral counter-rotating flows may also be explained in terms of chiral interactions within the cortex.

To test this hypothesis, we consider a mechanical model of an active chiral fluid film as given by Eq. 5.10-5.12. For simplicity, we consider the active moments and stresses to be controlled by a single scalar field c, which may be understood as the concentration of a master stress regulator such as RhoA. We define the polar and nematic order parameters in terms of gradients of c:

$$ {}_{(1)}p = \eth c, \quad {}_{(2)}Q = \eth\eth c. \tag{5.17} $$

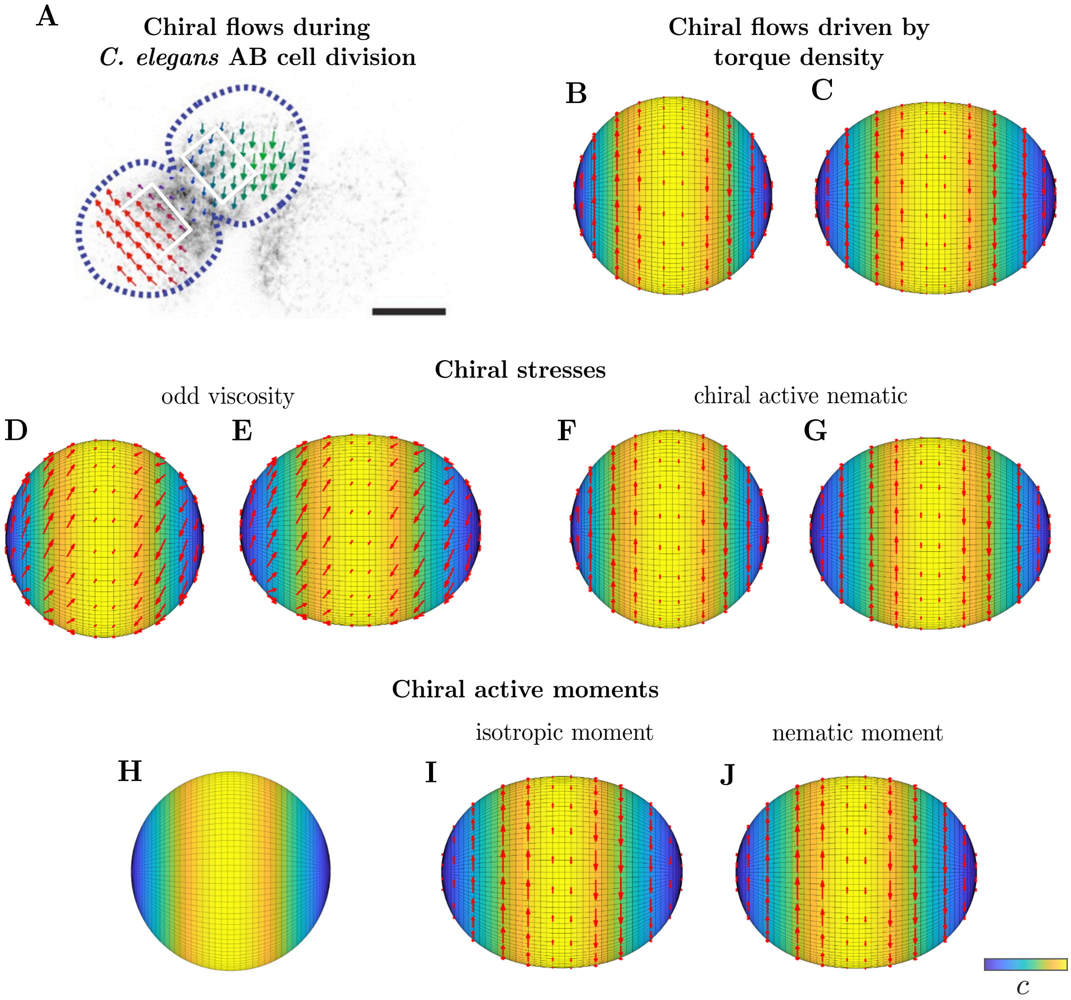
A
Chiral flows during
C. elegans AB cell division
Chiral flows driven by
torque density
B
C
Chiral stresses
odd viscosity
chiral active nematic
D
E
F
G
Chiral active moments
isotropic moment
nematic moment
H
I
J
c

Figure 5.4: Chiral counter-rotating flows driven mechanical activity in the actomyosin cortex. **A**: Cortical flows (red and green arrows) during cytokinesis of the *C. elegans* AB cell. Blue dashed line denotes the outline of the cell, where an ingression of the cytokinetic furrow is evident. Shading is intensity of fluourescently labelled myosin. Image taken from [22] with permission, Scale bar 10μm. **B**-**J** Numerical solutions of the flow field (red arrows) for a ring pattern of mechanical activity in chiral fluid films. Color denotes the concentration c that controls the active stresses and moments according to Eq. 5.10-5.12 and 5.17. The (static) pattern c is given by the spherical harmonic Y_{20}. In **B**, **D**, **F** and **H**, we consider a spherical geometry, whereas in **C**, **E**, **G**, **I** and **J**, we consider an axisymmetric deformation of the sphere given by Eq. 3.13 with $\delta R_{20} = R_0/2$. We consider here different scenarios, where in each scenario only one type of mechanical activity and only one chiral coupling constant is non-vanishing. **B**,**C**: Active torque density ($\tau_{\rm act} < 0$). **D**,**E**: Active isotropic stress ($\chi_{\rm iso} > 0$) in a chiral fluid film with odd viscosity ($\beta = -\pi/3$). **F**,**G** Chiral active nematic stress ($\chi_Q < 0, \varepsilon_1 = \pi/2$). **H**,**I**: Chiral active isotropic moment ($\zeta^I_{\rm iso} > 0$). **J**: Chiral active nematic moment ($\zeta_Q < 0$, $\varepsilon_2 = \pi/2$).

For simplicity, let us consider a cell with a perfectly spherical shape. In such a spherical geometry, the flow field can be understood in terms of spherical harmonic components A_{lm} and B_{lm} of the irrotational and the rotational flow field, respectively (see appendix E.3). Due to viscosity, the flow field is dominated by the modes with small l. A counter-rotating flow corresponds to the $l = 2, m = 0$ component of the rotational flow field, i.e. B_{20}. When the flow is driven by an active torque density, this flow component results from the component c_{20} of the torque density

c corresponding to an enrichment of c relative to the poles (Fig. 5.4B). Importantly such a pattern of actomyosin activity is indeed observed. It corresponds to the enrichment of RhoA and thus myosin and actin at the cytokinetic ring (see gray shading in Fig. 5.4A). Thus, considering an active torque density explains the experimentally found relationship between the pattern of myosin activity and flow field [39, 22]. However, this relationship is a consequence of symmetry and as such results from any linear model. Consider for example a chiral nematic active stress. Also in such a scenario, c_{20} yields a counter-rotation (Fig. 5.4F). Alternatively, we may consider a fluid film that is driven by an isotropic active stress. In a non-chiral fluid film, this drives a flow towards the contractile ring, corresponding to the A_{20} component of the irrotational flow field [135]. In a chiral fluid film with non-vanishing odd viscosity, however, the contractile ring drives also a counter-rotation (Fig. 5.4D). Thus, the chiral counter-rotating flows may indeed be explained in terms of chiral interactions within the cortex, even if cortex is isotropic, i.e. ${}_{(2)}Q = 0$.

When considering a spherical cell, the active bending moments do not contribute (Fig. 5.4H), since they do not drive active flows in an isotropic surface geometry, where ${}_{(2)}C = 0 = \eth\,{}_{(0)}C$ (see Eq. 5.15). However, the counter-rotating flows appear to arise only when the shape of the cell is markedly non-spherical, i.e. when the cytokinetic furrow has already started to ingress [22]. Thus, we need to evaluate our model for a non-isotropic surface geometry. As before, we use a pseudo-spectral method to calculate the flow field numerically for a given pattern of active stresses and moments (appendix F). As in the previous paragraph we consider a pattern c given by the $l = 2$, $m = 0$ spherical harmonics component. This time, however, we evaluate the spherical harmonics not on a sphere but on a spherical grid of a prolate axisymmetric surface. In such an anisotropic geometry, active moments drive tangential flows. In particular, we find that active chiral moments resulting from the component c_{20} of the stress regulator pattern drive counter-rotating flows (Fig. 5.4I,J). These flows are qualitatively indistinguishable from the counter-rotating flows that result from chiral stresses and torques. This is a consequence of our choice of the surface geometry, that is given by $l = 2$, $m = 0$ deformation of a sphere in the sense of Eq. 3.13. However, such a choice is not unrealistic since we expect that the deformation of the cell results from the same pattern of stresses that drive the in-plane flows [135, 23]. Importantly, the magnitude of the counter-rotating flows is highly sensitive to the surface geometry, when they are driven by active moments, as they are proportional to the anisotropy of the surface geometry. When such flows result from active stresses and torques, in contrast, the flow field depends only weakly on the geometry (see Fig. 5.4C,E,G). Thus, active chiral moments may explain, why the magnitude of chiral counter-rotating flows is correlated in time with the level of cytokinetic furrow ingression as observed in [22].

5.2.4 Chiral net rotation triggered by cell deformation

So far, we have focused on symmetrically dividing cells during *C. elegans* development. There, the nematic symmetry of the global pattern of actomyosin activity yields a chiral flow with pseudo-nematic symmetry, i.e. a counter-rotation. Importantly, also during asymmetric cell divisions chiral flows in the cortex have been observed. There the pattern of actomyosin activity is dominated by a polar asymmetry, corresponding to the c_{10} spherical harmonics component. As expected from symmetry, such cells exhibit a chiral flow with pseudo-polar symmetry, i.e. a net rotation (corresponding to the B_{10} component of the rotational flow) [22]. Intriguingly, such a net rotation cannot be driven by cell-internal mechanical activity, when the surface of the cell is axisymmetric around the axis of rotation [167] (see section 3.3.3 for a derivation for the special case of a spherical surface). Thus, a net rotation of the cortex of an axisymmetric cell would provide clear evidence for an active torque density that spins the embryo inside the egg shell.

However, it is unclear whether such a rotation has been observed [169, 49]. To the contrary, it has been shown, that a chiral rotation of the P_0 cell requires a non-axisymmetric egg-shell geometry [49]. During this chiral rotation, a band of actomyosin activity moves into the imaging plane, much like during the rotation of the 2-cell embryo we studied in section 3.3.2. This suggests that the net rotation of the P_0 cells is primarily driven by (non-chiral) actomyosin contractility. Such a tension-driven rotation aligns the pattern of active tension with the surface geometry (see Eq. 3.29). Prior to the rotation, it is found that myosin is enriched at the bulges of the compressed embryo [49]. Such a configuration corresponds to an unstable fixed point, where we expect any sort of chiral material property to be sufficient make the system rotate in one direction most of the time. In particular, a counter-rotating flow results in a rotational flux of the stress regulator concentration c, when c is asymmetrically distributed along the axis of rotation. In such a scenario, the chirality of the cortex contributes to triggering the rotation of the cortex and defines its handedness, but the net rotation of the cortex is driven by isotropic non-chiral mechanical activity.

Notably, we find that active moments can also drive a chiral net rotation on their own (see Fig. 5.2.4). This rotation can be understood from a torque that results from normal forces as in section 3.3.3. In contrast to chiral nematic stresses or odd viscous stresses, active moments contribute to the normal force even in an isotropic geometry (see Eq. D.18). Thereby, active chiral moments shift the pattern of normal forces relative to the pattern of the stress regulator c. Thus, in a configuration where the pattern of normal forces is aligned with the surface geometry in the sense of Eq. 3.40, active chiral moments yield a chiral shift of the pattern c with respect to the surface geometry.

Taken together, we suggest that the chiral cortical flows observed in the *C. elegans* embryo are consistent with a model where these flows result from chiral mechanical interactions within the cell cortex. We find that in such a scenario, chiral flows are highly sensitive to the geometry of the cell surface. This is a prediction that should be tested by future experiments, where the relationship between cell shape and chiral flows is quantitatively analyzed.

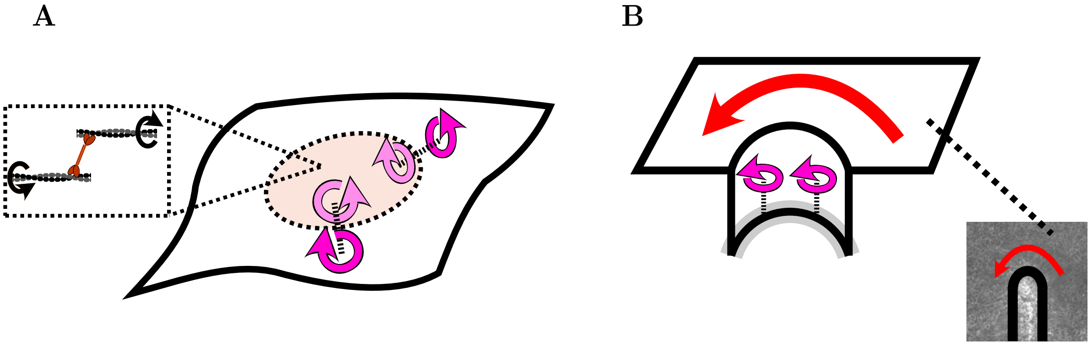

Figure 5.5: Capturing chiral flows in cell cortex and epithelium with active chiral moments. **A** Schematic of a patch of chiral mechanical activity in a fluid film such as the cell cortex. Pink arrows denote the torques the patch exerts on the surrounding fluid film and vice versa due to chiral active isotropic moments. Such moments result from molecular torque dipoles that are aligned with the tangential plane of the surface. Tangential torque dipoles result in particular from the action of myosin (red) interacting with actin filaments. **B**: Schematic of the surface geometry of the avian Hensen's node. Image in the lower right is a microscopy picture of the node of the quail embryo in Fig. 5.3D at the onset of chiral flow (red arrow). Away from the node and the streak, the surface of the embryo is mostly flat. At the streak and the node, cells are mechanically connected to the lower layers, whereas cells on the right and the left side of the streak are separated [78]. In section 5.1, we have shown that a torque dipole between tissue layers at the node drives the chiral flow. When considering the surface of cell connections, such torque dipoles are captured by an active chiral moment. At the node, the plane of inter-layer cell connections is curved, thereby connecting the left and the right halves of the streak. This curvature allows flows (red arrow) to be driven by torques (pink arrows) that are tangential to the plane of cell connections. Gray shading denotes the rotationally constrained lower layers.

5.3 Discussion

In this chapter, we have investigated actomyosin-driven chiral flows that facilitate left-right symmetry breaking in birds and nematodes. Analysing experimental data from quail embryos, we have found that the leftward movement of cells around the avian Hensen's node results from a torque that is generated within the node, presumably by actomyosin activity. Such a torque requires a substrate to act on. We have suggested that this substrate is the underlying ventral tissue. Importantly, this hypothesis is supported by perturbation experiments we analyzed here. These experiments have revealed that the presence of the ventral tissue is crucial to the leftward movement of the node. Strikingly, we found that replacing the ventral tissue by an elastic protein does not inhibit this leftward movement. Thus, the leftward movement requires a mechanical connection between the dorsal and the ventral tissue, but no chemical interactions between the tissue layers. Taken together, we find that the mechanical coupling of tissue layers provided by the primitive streak and the node is crucial to the chiral flow around the node and, thus, avian left-right symmetry breaking.

In the nematode *C. elegans*, chiral flows emerge in the actomyosin cortex at several time points in development [39, 22, 169]. While these flows have been understood as a result of actomyosin-driven torque generation [39], it has remained unclear what substrate they act on. Here, we find that these chiral flows may in fact not require such an external substrate. Instead, we propose that chiral flows result from chiral mechanical interactions within the cortex. In particular, we find that the chiral flows may result from an active isotropic chiral moment, corresponding to a density of torque dipoles. We understand such an isotropic moment (corresponding to $\mathrm{Im}\,_{(0)}m'$ in our notation) as the result of molecular torque dipoles that are aligned with the plane of the cortex. Most actin filaments are aligned with the plane of the cortex [23]. Hence, we expect tangential torque dipoles to result from myosin acting on these chiral filaments (see Fig. 1.3). Thus, a patch of increased actomyosin activity exerts torques on patches of the surrounding cortex where the torques are oriented along the line that connects the patches (see Fig. 5.5A). Importantly, such in-plane torques in a surface drive in-plane flows, only when the surface is curved. We propose that this explains why chiral flows arise primarily after the cytokinetic furrow has ingressed. More generally, we find that flows that result from different kinds of chiral mechanical interactions respond to changes in the surface geometry in a markedly distinct way. Thus, we suggest that understanding the mechanical nature of actomyosin chirality requires experimental investigations of the geometry-dependence of chiral flows.

Also in the avian embryo, we propose that it is not just the mechanical coupling of tissue layers but also the geometry of the Hensen's node that facilitates avian left-right symmetry breaking (see Fig. 5.5B). This physical picture suggests that the chiral flow may not require the localization of chiral activity to the node. Instead, the chiral flow may reflect the geometry of the node and the overall actomyosin-based chirality of the entire embryonic tissue.

The findings of this chapter have intriguing implications for the evolution of actomyosin-based left-right symmetry breaking. All animal cells have an actomyosin cortex [24]. Thus, Curie's principle implies that all cells are chiral in terms of their mechanical properties due to the chirality of the actin helix. Our study demonstrates that the extent to which chirality in an active fluid film manifests as chiral flows is highly dependent on the surface geometry. Based on these results, we suggest that whether an embryo makes use of the actomyosin cortex for left-right symmetry breaking crucially depends on the geometry of the embryo. For example, the actomyosin-based mechanism of left-right symmetry breaking found in birds may have co-evolved with a certain structure called the primitive streak, as we have discussed in the introduction of this chapter. Here we propose that this evolutionary link may be a consequence of the mechanical link between tissue layers provided by the primitive streak. Furthermore, the geometry of the Hensen's node, the tip of the streak, may have facilitated the evolution of the avian mode of left-right symmetry breaking. This hypothesis asks for further investigations of left-right symmetry breaking in chameleon embryos, where a blastopore is found instead of a Hensen's node at the tip of the streak [69, 86].

The evolutionary history of left-right symmetry breaking in nematodes is entirely unclear to the best of our knowledge. Here we find that the chiral flows that facilitate left-right (and dorsoventral) symmetry breaking in the nematode *C. elegans* may relie on an anisotropic shape of the cell. The shape of the cell is determined in particular by the egg shell that tightly confines the *C. elegans* embryo. Intriguingly the degree to which embryos are confined by the egg shell differs considerably among nematodes (see [199] and references therein). We wonder whether this might impact on chiral flows and thus left-right symmetry breaking in nematodes.

Chapter 6

Conclusion and Outlook

In this thesis, we have studied flows in the surfaces of cells and embryos. In particular, we have investigated how the geometry of a cell or an embryo guides such surface flows, when they are driven by mechanical activity within the surface. Directed movements of cells and molecules need to be driven by mechanical forces. The geometry of a cell or embryo, i.e. the angles and distance between constituents, determines how forces and torques can be transmitted. Consequently, the geometry of a living system profoundly influences where cells and molecules move to in response to forces and torques that are generated within such a system. Here, we elucidated this geometric control of active flows using the hydrodynamic theory of active surfaces.

We analyzed experimental data from quail and nematode embryos to decipher the forces that drive flows of cells and molecules during gastrulation and body axis specification. We then used analytical and numerical calculations to understand how embryo geometry impacts on the relation between mechanical forces and the resulting flows. To this end, we utilized concepts and tools from cosmology, quantum physics and fracture mechanics, as well as differential geometry and complex analysis. Thereby, we uncovered general principles that may allow us to understand various other living and artificial active systems. In the following, we briefly explain these principles once again.

In chapter 2, we developed a hydrodynamic theory of active viscous cracks, i.e. lines of mechanically active material embedded in a fluid film. With this, we inferred a mechanical model of the primitive streak from experimental flow fields. Within this model, we found that an elongation of the streak does not require extensile forces along the streak. Instead the flux into the streak yields a viscous force that drives its elongation against a line tension of the streak. Thus, it is the propagation of forces in the surrounding material that translates the forces generated within the streak into an elongation of the streak due to the polar geometry of the streak. Importantly, we could generalize these findings to the following principle governing the growth of active viscous cracks such as epithelial folds or the cytokinetic ring: Forces that drive a flux towards a crack drive also an extension of the crack due to the viscosity of the surrounding fluid.

In chapter 3, we investigated how the shape of a cell guides flows and pattern formation within the cell surface. To this end, we considered a minimal model of the actomyosin cortex as an active isotropic fluid film with static shape. We obtained exact results for slight anistropies of the cell shape and analyzed data from the *C. elegans* embryo during dorso-ventral axis specification. We found active cortical tension drives a whole-cell rotation, when the pattern of the cortical stress regulator is not aligned with the geometry of the cell. Notably, this rotation results from shear viscosity in an active fluid model of the cortex. Thus, it is the mechanics of the cortex that yield an alignment of chemical pattern and surface geometry. In particular, we found that a contractile ring aligns with the plane that is perpendicular to the long axis of the cell.

In chapter 4, we generalized these findings to more complex surface geometries to uncover general principles that govern the movement of localized sources of mechanical activity in a curved fluid film. We found that the impact of the surface geometry on the flow field can be understood in terms of effective gradients of friction and viscosity. This mathematical analogy between geometric and physical properties of fluid film reflects that they both together determine how forces are transmitted within the surface. In particular, we found that shear viscosity yields the following principle: When the surface area within the hydrodynamic distance to a point expands, moving the fluid at this point requires larger forces. Using this insight, we found that shear viscosity yields an advection of contractile points towards protrusions and saddle geometries. Furthermore, we found that the way an active anisotropic particle couples to the flow, e.g. whether it is extensile or contractile, controls whether the particle moves towards or away from a saddle geometry.

In chapter 5, we studied chiral flows in the avian embryo and in the cell cortex. This chiral flows are crucial to left-right symmetry breaking in avian and nematode embryos. Analyzing experimental flow fields from quail embryos with the active crack model, we revealed that the leftward movement of cells at the avian Hensen's node is driven by a torque dipole between tissue layers. Thus, left-right symmetry breaking in the avian embryo relies on the mechanical coupling of tissue layers provided by the structures of the primitive streak and the Hensen's node. Importantly, perturbation experiments have confirmed this theoretical prediction.
Using a generic mechanical model of an active chiral fluid film, we showed that chiral flows in the *C. elegans* cell cortex may be attributed to molecular torque dipoles within the cell surface. As a consequence of force and torque balance, such in-plane torques drive in-plane flows in a surface, but only for non-vanishing curvature. Hence, these chiral flows are highly sensitive to the curvature of the cell surface. Taken together, our findings reveal that the geometry of an embryo or a cell controls to what extent the chirality of mechanical interactions within such a living system gives rise to chiral flows of cells and molecules, as the geometry of an embryo or a cell determines how torques are transmitted.

While the principles uncovered in this thesis are inherently physical, they have clear implications for how embryo geometry impacts on developmental processes. Such an impact can arise on two distinct time scales: During the development of an embryo and on an evolutionary time scale. During the development of an embryo, anisotropies in the embryo geometry at a certain time point may guide subsequent processes, not unlike a morphogen gradient established early in development guides subsequent morphogenetic processes. Here, we found that the geometry of the egg shell of the *C. elegans* embryo guides the establishment of the body axes due to the mechanics of the cell cortex. Notably, these processes are examples of a more general phenomenon known as Hertwig's rule: Cells tend to divide along their longest axis. Here, we found that tension in the cytokinetic ring ensures that a cell divides along its longest axis, whenever the cell is free to rotate. Previous studies have shown that also microtubule-based force generation can ensure long-axis alignment of the division axis before the cytokinetic ring forms. However, here and in [167], we have shown that microtubule-based forces can also drive short-axis alignment. When the cell is free to rotate, however, we found that the cytokinetic ring ensures long-axis alignment independently of microtubule-based alignment. Importantly, we understand this as a general result of angular momentum conservation. This suggest that the generality of Hertwig's rule is a consequence of the cytokinetic ring.

Such general physical results provide also the ground for speculations on an evolutionary time scale. As the cytokinetic ring drives a rapid rotation of the cell in the case of misalignment, microtubule-based force generation may have evolved to avoid this rotation by ensuring long-axis alignment of the spindle prior to the formation of the cytokinetic ring. Also our investigation of chiral flows during left-right symmetry breaking has clear implications for the evolution of left-right symmetry breaking. We found that chiral flows resulting from molecular torque dipoles are highly sensitive to the geometry of a cell or an embryo. Thus, we speculate that differences in embryo geometry may explain why some embryos make use of the actomyosin cortex to break left-right symmetry and many others do not. Furthermore, these results may also help to explain why the chirality of the actomyosin cortex most of the time does not contribute to the left-right asymmetric morphogenesis of the visceral organs. Both on an developmental and on an evolutionary time scale, most developmental processes appear to be fairly robust with respect to changes in embryo geometry. Such a robustness seems incompatible with chiral flows that are highly sensitive to the geometry. Taken together, the mechanical principles found in this thesis help us to understand how embryo geometry impacts on developmental process on developmental and evolutionary time scales.

Importantly, the shape of an embryo does not only impact on developmental processes, but it is at the same time also the result of such processes. Many such morphogenetic processes are understood as being controlled by a pre-defined chemical pattern (see section 1.1.6). Here, we have turned this rationale on its head, by studying how the shape of an embryo controls the formation of patterns. Combining these two approaches yields a self-organized picture of morphogenesis, where pattern formation and shape deformations are coupled at all times. A few examples of such feedback loops in morphogenesis have already been studied, as we discussed in section 1.1.6 (see also [94] for a review). Notably, these examples of geometry sensing have so far been explained with one-dimensional models and pictures. This may explain, why the mechanisms proposed there rely on chemical fluxes between the surface and the underlying bulk material. Here, in contrast, we have shown how geometry sensing results from active flows within a surface. Strikingly, these flows are driven by the same sort of active stresses and moments that drive shape deformations of an active surfaces. Thus, we expert the result of this thesis to apply to various morphogenetic processes. Specifically, we expect geometry sensing by active flows to be relevant, whenever the morphogenesis of an epithelial sheet is accompanied by large-scale movements of cells within this surface.

Recently, theoretical studies have investigated the self-organized morphogenesis of active nematic and polar surfaces. In [200], the dynamics of deforming active liquid crystals has been studied numerically and in terms of linear stability analysis. In [150], in contrast, the concept of the geometric potential has been used to get some analytical insight into the self-organized morphogenesis of nematic surfaces beyond the linear regime. However, in this case the viscosity of the surface was neglected. Importantly, the impact of curvature on an active nematic surface, in particular the positioning of topological defects does not differ qualitatively from its passive analog [192]. As a consequence the results of [150] do not differ qualitatively from what one would expect from an equilibrium rationale. In viscous active nematic surfaces, in contrast, it has been found that the positioning of topological defects can be in stark contrast to the equilibrium configuration [144]. Intriguingly, no explanations for this phenomenon have been found. Here, we developed a framework to understand the impact of the surface geometry on active flows due to viscosity beyond the linear regime of the surface geometry. With this, we have shown that extensile active particles move towards saddle geometries, in agreement with the positioning of topological defects in an active extensile nematic fluid [144]. More generally, our framework allows to understand the impact of the surface geometry on flows and thus pattern formation in active fluid films. Thereby, we have laid the ground for understanding the self-organized morphogenesis of active surfaces.

Appendix A

A crack in a surface

This appendix supplements chapter 2. We provide conservation laws for a crack in a curved surface, generalizing the results of section 2.2.1.

A.1 Differential geometry

As in section 2.1.1, we consider a crack represented as a line $\mathcal{C}$ embedded in a curved surface $\mathcal{S}$. The line is parametrized as $\mathbf{Y}(\lambda)$, where λ is the coordinate of the crack. For simplicity an arc-length parametrisation such that $|\mathbf{e}_\lambda| = |\partial_\lambda \mathbf{Y}| = 1$. In general, the line $\mathcal{C}$ has a curvature, which we define as

$$\mathbf{C}_\lambda = \mathbf{e}^\lambda \times \partial_\lambda \mathbf{e}_\lambda = \kappa_g \mathbf{n} - \kappa_n \boldsymbol{\nu}_C, \tag{A.1}$$

corresponding to the axis of rotation of the tangent vector $\mathbf{e}_\lambda$, when walking along the crack. $\kappa_g, \kappa_\mathrm{n}$ are the geodesic and normal curvature of $\mathcal{C}$. $\mathbf{e}_\lambda$, $\boldsymbol{\nu}_C$ and $\mathbf{n}$ form the so called Darboux frame. The derivatives of these basis vectors along the crack read

$$\partial_\lambda \mathbf{e}_\lambda = \mathbf{C}_\lambda \times \mathbf{e}_\lambda = \kappa_n \mathbf{n} + \kappa_g \boldsymbol{\nu}_C \tag{A.2}$$

$$\partial_\lambda \mathbf{n} = -\kappa_n \mathbf{e}_\lambda - \kappa_{\nu n} \boldsymbol{\nu}_C \tag{A.3}$$

$$\partial_\lambda \boldsymbol{\nu}_C = -\kappa_g \mathbf{e}_\lambda + \kappa_{\nu n} \mathbf{n} \tag{A.4}$$

Here, $\kappa_{\nu n}$ denotes the torsion of the curve $\mathcal{C}$.

A.2 Conservation laws

In the following, we give conservation laws of mass density, momentum and angular momentum along the crack. This crack is in contact with the surface it is embedded in and with an underlying substrate.

Let us start by considering the conservation of mass. As mass is conserved, a change in the mass M of a line segment has to be balances by flux of mass to the crack. This gives rise to the following integral equation:

$$\partial_t M = \partial_t \int_a^b \mathrm{d}l \rho_C = \int_a^b (J_S + J_n) - j_C^\lambda\big|_b^a \tag{A.5}$$

where ρ_C is the mass density per unit length of the crack material. We consider here mass exchange between the crack and the ssubstrate (J_n) well as the surface (J_S). The mass flux line density J_S is given by

$$J_S = j_{L,\nu} - j_{R,\nu}, \tag{A.6}$$

where $j_{L,\nu}$ and $j_{R,\nu}$ denote the projections of the mass flux density $\mathbf{j}$ of the surface material onto $\boldsymbol{\nu}_C$ evaluated at the left and right crack boundary, respectively (see Eq. 2.5). Furthermore, we consider a transport of mass within the crack quantified by the mass flux density $\mathbf{j}_C$ which we write as

$$\mathbf{j}_C = \rho\left(\mathbf{v}_C - \tilde{\mathbf{v}}_C\right) \tag{A.7}$$

where we distinguish the center of mass velocity $\mathbf{v}_C = v_C^\lambda \mathbf{e}_\lambda + v_{C,\nu}\nu + v_{C,\mathrm{n}}\mathbf{n}$ of the crack material from the crack velocity $\tilde{\mathbf{v}}_\mathcal{C}$ defined as

$$\tilde{\mathbf{v}}_C := \partial_t \mathbf{Y} \tag{A.8}$$

We note that $\tilde{\mathbf{v}}_C$ and hence $\mathbf{j}_C$ is parametrization-dependent. With these definitions, mass conservation of a an infinitesimal line element yields the continuity equation

$$\partial_t \rho - \left(\tilde{v}_C^\lambda - v_C^\lambda\right)\partial_\lambda \rho = -\rho\left[\partial_\lambda v_C^\lambda + \mathbf{e}_\lambda \cdot \left(\mathbf{C}_\lambda \times \tilde{\mathbf{v}}_C\right)\right] \tag{A.9}$$

where $\mathbf{C}_\lambda$ denotes the curvature of the curve $\mathcal{C}$ as defined in Eq. A.1.
At the crack tip ($\lambda = 0$), mass conservation reads

$$\partial_t M_T = J_{T,S} + J_{T,\mathrm{n}} - j_C^\lambda\big|_{\lambda=0}, \tag{A.10}$$

where M_T is the mass of the crack tip and we consider mass exchange between crack tip and the surface ($J_{T,S}$), the crack tip and the substrate ($J_{T,\mathrm{n}}$) and between the tip and the crack.

Analogously, momentum conservation along the crack yields the force balance equation

$$\partial_\lambda \mathbf{t}_C = -\mathbf{f}_{C,\mathrm{sub}} + \mathbf{t}_{L,\nu} - \mathbf{t}_{R,\nu}, \tag{A.11}$$

where we neglect inertia terms. $\mathbf{f}_{C,\mathrm{sub}}$ denotes the force the substrate exerts on the crack and $\mathbf{t}_{L/R,\nu}$ denotes the stress tensor of the surface projected onto $\boldsymbol{\nu}$ and evaluate at the left and the right side of the crack. This equation can also be expressed in terms of the components using

Eq. A.2- A.4 as

$$\partial_\lambda t_C^\lambda - \kappa_n t_C^{\mathrm{n}} - \kappa_\nu t_C^\nu = -f_{\mathrm{ext}}^\lambda \tag{A.12}$$

$$\partial_\lambda t_C^n + \kappa_n t_C^\lambda + \kappa_{\nu n} t_C^\nu = -f_{\mathrm{ext}}^{\mathrm{n}} \tag{A.13}$$

$$\partial_\lambda t_C^\nu + \kappa_\nu t_C^\lambda - \kappa_{\nu n} t_C^n = -f_{\mathrm{ext}}^\nu, \tag{A.14}$$

where

$$\mathbf{f}_{\mathrm{ext}} = \mathbf{f}_{C,\mathrm{sub}} - \mathbf{t}_{L,\nu} + \mathbf{t}_{R,\nu} \tag{A.15}$$

Angular momentum conservation yields the torque balance equation along the crack:

$$\partial_\lambda \mathbf{m}_{\mathcal{C}} = -\boldsymbol{\tau}_{\mathrm{sub}} - \mathbf{e}_\lambda \times \mathbf{t}_{\mathcal{C}} + \mathbf{m}_{L,\nu} - \mathbf{m}_{R,\nu} - d\boldsymbol{\nu} \times (\mathbf{t}_{R,\nu} + \mathbf{t}_{L,\nu}), \tag{A.16}$$

where $\boldsymbol{\tau}_{\mathrm{sub}}$ is the torque density the substrate exerts on the crack and $\mathbf{m}_{L/R,\nu}$ denotes the projection of the moment tensor of the surface onto $\boldsymbol{\nu}$ at the left and the right side of the crack.

Appendix B

Analytical solutions of crack boundary conditions

This appendix supplements chapter 2, in particular section 2.3. We give here analytical solutions for flow fields around a crack in a flat fluid film.

For a flat geometry and in the absence of gradients of active stresses, the tangential force balance equation in the form of Eq. 1.69 simplifies to

$$4\partial_{\bar{z}}\partial_z\partial_{\bar{z}}(F + \alpha \operatorname{Re} F) - \frac{1}{l_h^2}\partial_{\bar{z}}F = 0, \tag{B.1}$$

with the flow field written as $\mathbf{Z} \cdot \mathbf{v} = {}_{(1)}v = \partial_{\bar{z}}F$ (see sections 1.3.1,1.3.2). In the following we will give solutions to this equation in a flat crack geometry, where the crack tip is centered at the origin of the cartesian coordinate system ($z = 0$) and the crack corresponds to the negative real axis in terms of z.

B.1 Integral form for finite hydrodynamic length

For a finite hydrodynamic length l_h, solutions to Eq. B.1 are given by solutions to

$$\Delta(F + \alpha \operatorname{Re} F) - \frac{1}{l_h^2}F = 0, \tag{B.2}$$

where Δ denotes the Laplace operator $4\partial_z\partial_{\bar{z}}$. In the following we use polar coordinates (r, θ). Using a Fourier decomposition of the angular dependence of F, the radial dependence of F is given by modified Bessel functions with the hydrodynamic length defining the length scale. Due to bulk viscosity, the real part A of $F = A + iB$ has characteristic length scale $l_h^A = l_h\sqrt{1+\alpha}$ that differs from the hydrodynamic length l_h of the rotational flow component B.

Let us consider an annulus centered around $z = 0$, i.e. the domain $\{z \in \mathbb{C} \big| a < |z| < R\}$. In this domain, solutions can be written as a multipole expansion:

$$A = \mathrm{Re}\left\{\sum_{m=0}^{\infty}\left[A_m^- K_{|m|}\left(\frac{r}{l_h^A}\right) + A_m^+ I_{|m|}\left(\frac{r}{l_h^A}\right)\right] e^{im\theta}\right\}, \tag{B.3}$$

$$B = \mathrm{Re}\left\{\sum_{m=0}^{\infty}\left[B_m^- K_{|m|}\left(\frac{r}{l_h}\right) + B_m^+ I_{|m|}\left(\frac{r}{l_h}\right)\right] e^{im\theta}\right\}, \tag{B.4}$$

where $A_m^{+/-}$ and $B_m^{+/-}$ are complex coefficients and the modified Bessel functions are defined as

$$I_m(r) = \lim_{\alpha\to m}\sum_{n=0}^{\infty}\frac{1}{n!\Gamma(\alpha+n+1)}\left(\frac{r}{2}\right)^{2n+\alpha}, \tag{B.5}$$

$$K_m(r) = \lim_{\alpha\to m}\frac{\pi}{2}\frac{I_{-\alpha}(r) - I_\alpha(r)}{\sin\alpha\pi}, \tag{B.6}$$

with Γ denoting the gamma function. $I_{|m|}(r)$ is monotonically increasing with r whereas $K_{|m|}(r)$ is monotonically decreasing. For $a \ll R$, A_m^-, B_M^- correspond to Fourier components of the boundary velocities or forces at the inner ring, i.e. $|z| = a$, whereas A_m^+, B_m^+ represent the boundary conditions at the outer ring, $|z| = R$.

We consider a crack along a line that connects the domain $|z| \leq a$, corresponding to the crack tip, with the outer circle $|z| = R$. The crack introduces boundary conditions along this line. Using force boundary conditions ($\mathbf{f}_{L/R} = \pm\mathbf{t}^i_{L/R}\nu_i$) on the left and right sides of the crack, we identify a force $\mathbf{f}_L + \mathbf{f}_R$ and a force dipole $d(\mathbf{f}_L - \mathbf{f}_R)$ at each point on the crack. The crack may thus be understood as a line of forces and force dipoles. The flow field ${}_{(1)}v$ resulting from a single force $\mathbf{F}\delta^{(2)}(x - x', y - y')$ at position $z' = x' + iy'$ in an infinite plane is given by the Green's function

$$G_{\mathrm{mono}}(z - z', \bar{z} - \bar{z}', \mathbf{F}) = G_0(z - z', \bar{z} - \bar{z}')\,{}_{(1)}F + G_2(z - z', \bar{z} - \bar{z}')\,{}_{(-1)}F, \tag{B.7}$$

where ${}_{(1)}F$ is the spin quantity correspond to the vector $\mathbf{F}$ (see section 1.3.1) and

$$G_0(z - z', \bar{z} - \bar{z}') = \frac{1}{4\pi\eta}\left[\frac{1}{\alpha+1}K_0(|z|/l_h^A) + K_0(|z|/l_h)\right] \tag{B.8}$$

$$G_2(z - z', \bar{z} - \bar{z}') = \frac{1}{4\pi\eta}\left[\frac{1}{\alpha+1}K_2(|z|/l_h^A) - K_2(|z|/l_h)\right]\frac{z^2}{|z|^2}, \tag{B.9}$$

see also section 4.2.2. A force dipole, given by a pair of forces $\pm\mathbf{F}$ separated by $d\boldsymbol{\nu}$ centered at z', yields a flow field

$$G_{\mathrm{dip}}(z - z', \bar{z} - \bar{z}', \mathbf{F}, \boldsymbol{\nu}) = d({}_{(1)}\nu\partial_z + {}_{(-1)}\nu\partial_{\bar{z}})G_{\mathrm{mono}}(z - z', \bar{z} - \bar{z}', \mathbf{F}), \tag{B.10}$$

where ${}_{(1)}\nu$ is the spin quantity corresponding to the vector $\boldsymbol{\nu}$. These derivatives can be calculated analytically using $|z| = \sqrt{z\bar{z}}$ and

$$\frac{\mathrm{d}}{\mathrm{d}x} I_\alpha(x) = \frac{1}{2}(I_{\alpha+1}(x) + I_{\alpha-1}(x)), \quad \frac{\mathrm{d}}{\mathrm{d}x} K_\alpha(x) = -\frac{1}{2}(K_{\alpha+1}(x) + K_{\alpha-1}(x)). \tag{B.11}$$

With this, we write the flow field around the crack in an integral form:

$$_{(1)}v(z) = {}_{(1)}v_0(z) + \int_0^L \mathrm{d}\lambda \left[G_{\mathrm{mono}}(z - z(\lambda), \mathbf{f}_{\mathrm{mono}}) + G_{\mathrm{dipo}}(z - z(\lambda), \mathbf{f}_{\mathrm{dipo}}, \boldsymbol{\nu})\right], \tag{B.12}$$

where $\mathbf{f}_{\mathrm{mono}}$ and $\mathbf{f}_{\mathrm{dipo}}$ are line densities of forces and force dipole, respectively. $_{(1)}v_0$ is a component of the flow field that is continous at the crack and can thus be written in terms of Eq. B.3,B.4. Since we defined the Green's functions for boundaries at infinity, $\mathbf{f}_{\mathrm{mono}}$ and $\mathbf{f}_{\mathrm{dipo}}$ do in general not correspond directly to the force and force dipoles given by $\mathbf{f}_L$ and $\mathbf{f}_R$. Eq. B.12 is particularly useful to calculate the flow field resulting from velocity boundary conditions at the crack numerically. To this end, the integral is discretized as a sum of force mono- and dipoles, as we describe in section C of the appendix.

B.2 Expansions in terms of holomorphic functions

B.2.1 Kolosov-Muskhelishvili formulas

In the regime of infinite hydrodynamic length, Eq. B.1 becomes

$$\partial_{\bar{z}}\partial_z\partial_{\bar{z}}(F + \alpha \operatorname{Re} F) = 0. \tag{B.13}$$

This equation is solved by

$$F = \frac{1}{2}\left[(2+\alpha)\bar{z}\hat{f} - \alpha z\bar{\hat{f}} + \bar{\hat{\hat{g}}}\right] \tag{B.14}$$

where $f = \partial_z \hat{f}$ and $g = \partial_z\partial_z\hat{\hat{g}}$ are holomorphic function obeying $\partial_{\bar{z}} f = 0 = \partial_{\bar{z}} g$, which we discussed in section 1.3.3. g corresponds to the harmonic component of the flow field with vanishing curl and divergence. Any functions f, g that are holomorphic on the domain of the fluid film solve Eq. B.13. Thus solving the flow field around a crack amounts to finding holomorphic functions that yield a flow and stress fields that obey the given boundary conditions [160, 157]. For given f, g, flow and stress fields are given by

$$_{(1)}v = 2\partial_{\bar{z}}F = (2+\alpha)\hat{f} - \alpha z\bar{f} + \bar{\hat{g}} \tag{B.15}$$

$$_{(2)}t = 8\partial_{\bar{z}}\partial_{\bar{z}}F = 4\eta\left[-\alpha z\overline{f'} + \bar{g}\right] \tag{B.16}$$

$$_{(0)}t = 8\alpha\partial_z\partial_{\bar{z}} \operatorname{Re}[F] = 8\alpha\eta \operatorname{Re}[f] \tag{B.17}$$

Eq. B.16,B.17 correspond to the Kolosov-Muskhelishvili formulas from the field of fracture mechanics [157, 163].

B.2.2 Non-integer power laws

On an annulus, they f, g can be written as Laurent expansions (Eq. 1.82), which corresponds to the limit of Eq. B.3,B.4 for $l_h \to \infty$. Thus, f, g are of the form z^m with $m \in \mathbb{Z}$. In order to capture the discontinuity at the crack one may augment this expansion with non-integer power laws ($m \notin \mathbb{Z}$), as is often done in the literature of fracture mechanics [158, 159]. Let us consider such a power law, i.e. $f, g \sim z^{m-1}$ yielding $\hat{f}, \hat{g} \sim z^m$ for $m \neq 0$. Specifically, we consider $\hat{g} = (a+ib)z^m$, $\hat{f} = (c+id)z^m$ with $a, b, c, d \in \mathbb{R}$. Then, the flow field reads

$$ {}_{(1)}v = (a-ib)\bar{z}^m + (2+\alpha)(c+id)z^m - m\alpha(c-id)z\bar{z}^{m-1}. \tag{B.18}$$

Using polar coordinates r, θ with $z = re^{i\theta}$, this yields

$$\begin{aligned} v_r = \mathrm{Re}\left[e^{-i\theta}\,{}_{(1)}v\right] =& r^m\big\{a\cos((m+1)\theta) - b\sin[(m+1)\theta] \\ & + [2-\alpha(m-1)]\,[c\cos((m-1)\theta) - d\sin((m-1)\theta)]\,\big\} && \text{(B.19)} \\ v_\theta = \mathrm{Im}\left[e^{-i\theta}\,{}_{(1)}v\right] =& r^m\big\{-a\sin((m+1)\theta) - b\cos[(m+1)\theta] && \text{(B.20)} \\ & - [2+\alpha(m+1)]\,[c\cos((m-1)\theta) + d\sin((m-1)\theta)]\,\big\}. && \text{(B.21)} \end{aligned}$$

Thus the complex power law translates into a power law radial dependence of the flow field. Furthermore, we observe that a, c and b, d correspond to the components that are symmetric and antisymmetric under a mirror transformation, i.e. $\theta \to -\theta$. Importantly, the flow field is discontinuous at $\theta = \pm\pi$, for $m \notin \mathbb{Z}$, which allows to consider crack boundary conditions. Let us consider a rigid crack with ${}_{(1)}v(\theta = \pm\pi) = 0$. Using the above expression as an ansatz, we have

$$0 = v_r(\theta = \pm\pi) = r^m\big\{-[a + (2-\alpha(m-1))c]\cos m\pi \pm [b + (2-\alpha(m-1))d]\sin m\pi\big\} \tag{B.22}$$

$$0 = v_\theta(\theta = \pm\pi) = r^m\big\{\pm[a - (2+\alpha(m+1))c]\sin m\pi + [b - (2+\alpha(m+1))d]\cos m\pi\big\}, \tag{B.23}$$

yielding the non-trivial solutions

$$a = -(2-\alpha(m-1))c \ \wedge\ b = (2+\alpha(m+1))d \ \wedge\ m \in \mathbb{Z} \tag{B.24}$$

$$b = -(2-\alpha(m-1))d \ \wedge\ a = (2+\alpha(m+1))c \ \wedge\ m \in \mathbb{Z} + \frac{1}{2}, \tag{B.25}$$

where $\mathbb{Z} + \frac{1}{2}$ denotes the set of half-integers. Thus, we can express the solution as a series of integer and half-integer power-laws with the coefficients defined by the above equations and the boundary conditions at the crack tip and the outer circle. For $\mathbf{v} \to 0$ at the crack tip and small size of the crack tip ($a/R \ll 1$), solutions are given by $m > 0$. Thus, the minimal m is $1/2$, which dominates the flow and stress fields close to the crack tip, implying that the stress field diverges as $1/\sqrt{r}$ at the crack tip, as we do indeed observe for the numerical example in 2.1G (see B.2C for a plot of the radial dependence of the stress field). This square root divergence is well known in the field of fracture mechanics [158, 162, 163]. There it is understood as a consequence of vanishing boundary forces at the crack. Solving force boundary conditions, requires the stress, which for our ansatz reads

$$
\begin{aligned}
{}_{(2)}t =& 4\eta m r^{m-1}\left[(a-ib)e^{-i(m-1)\theta} - \alpha(c-id)(m-1)e^{-i(m-3)\theta}\right] && \text{(B.26)}\\
{}_{(0)}t =& 8\alpha\eta m r^{m-1}\left[c\cos(m-1)\theta - d\sin(m-1)\theta\right] && \text{(B.27)}
\end{aligned}
$$

which yields

$$
\begin{aligned}
t_{\theta r}(\theta=\pm\pi) =& \frac{1}{2}\operatorname{Im}[{}_{(2)}t(\theta=\pm\pi)]\\
=& 2\eta m r^{m-1}\left\{\pm(a-\alpha(m-1)c)\sin m\pi + (b-\alpha(m-1)d)\cos m\pi\right\} && \text{(B.28)}\\
t_{\theta\theta}(\theta=\pm\pi) =& \frac{1}{2}\operatorname{Re}[{}_{(0)}t - {}_{(2)}t]\big|_{\theta=\pm\pi}\\
=& 2\eta m r^{m-1}\left\{[a-(2+(m-1)\alpha)c]\cos m\pi \mp [b-(2+(m-1)\alpha)d]\sin m\pi\right\}. && \text{(B.29)}
\end{aligned}
$$

Force-free boundary condition then yield again half-integer m since $\cos\pi/2 = 0$.

Linear coupling of different stress components yields other sets of non-integer power-laws [159]. For the viscous stress, a coupling between velocity and flow field arises from the viscosity η_{ing}. Let us consider a left-right symmetric passive crack (implying $b = 0 = d$) with vanishing 1D viscosity $\eta_C \to 0$, yielding $t_{\theta r}(\theta \pm \pi) = 0$, which is solved by

$$
m \in \mathbb{Z} \;\vee\; a = \alpha(m-1)c \tag{B.30}
$$

Furthermore, we consider a a thickness that approaches zero at the crack tip, implying $d_C \sim r$ close to the crack tip with an opening angle $\theta_C = \arctan[d'_C(r)]$. In such a scenario we can make use of the same ansatz to solve the mixed boundary condition given by Eq. 2.21, which with the ansatz reads

$$
4\eta m(\tan\theta_C)r^m\left[a-(2+(m-1)\alpha)c\right]\cos m\pi = -2\eta_{\text{ing}}r^m\left[a-(2+\alpha(m+1))c\right]\sin m\pi \tag{B.31}
$$

Using Eq. B.30, we obtain the following equation for m

$$
-2\eta m(\tan\theta_C)\cos m\pi = \eta_{\text{ing}}(1+\alpha)\sin m\pi, \tag{B.32}
$$

which yields a set of solutions $M \subset \mathbb{R}$, that is defined by the ratio of the rescaled ingression viscosity $\tilde{\eta}_{\text{ing}} = \eta_{\text{ing}}/\tan\theta_C$ over the rescaled viscosity $\tilde{\eta} = \eta/(1+\alpha)$ of the fluid film. For $m \in M$, the above equations is full-filled and hence our power-law ansatz yields a solution of the crack boundary conditions with. Thus, the material properties of crack and fluid film define a

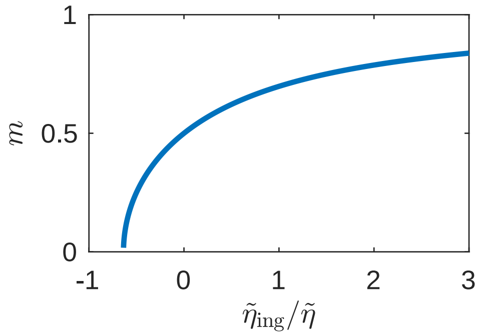

Figure B.1: Numerical solutions to Eq. B.32 for $0 < m < 1$ for different ingression viscosities $\tilde{\eta}_{\mathrm{ing}}$. For details, see main text.

set of power-laws. For $\tilde{\eta}_{\mathrm{ing}}/\tilde{\eta} \to 0$, corresponding to force free boundary conditions, $M = \mathbb{Z} + \frac{1}{2}$ and the minimal m with $m > 0$ is $m = 1/2$, i.e. stresses diverge as $1/\sqrt{r}$ close to the crack for non-diverging velocities at the crack tip. For $\tilde{\eta}_{\mathrm{ing}}/\tilde{\eta} \to \infty$, corresponding to the velocity boundary condition $v_\theta(\theta = \pm\pi) = 0$, $M = \mathbb{Z}$ and the minimal m with non-diverging velocity is $m = 1$ apart from a rigid body translation with $m = 0$. Thus, stresses do not diverge as the flow field corresponds to the flow field in the absence of a crack. Notably, this regime arises not only for large ingression viscosities $\eta_{\mathrm{ing}}/\eta \to \infty$, but also in the limit of incompressibility of the fluid film, i.e. $\alpha \to \infty$ with $\eta_{\mathrm{ing}} > 0$ (and $\eta_C \to 0$), and for a vanishing opening angle, i.e. $\tan\theta_C \to 0$. In between those limits, Eq. B.32 yields a set of non-integer m with non-integer differences between them. In Fig. B.1, we plot solutions to Eq. B.32 with $0 < m < 1$. We observe that for $\tilde{\eta}_{\mathrm{ing}} < 0$, i.e. an active crack that pulls at the fluid, when it flows towards it, there is a critical $\tilde{\eta}_{\mathrm{ing}} \sim 0.637\eta$ at which the solution m crosses the zero and the next solution is greater than 1.

Similarly, one can obtain a set of power laws for $\eta_C \neq 0$, when η_C scales linearly with r which may again be understood as the consequence of $d_C \sim r$. The power-law becomes observable as a divergence of the stress around the crack tip (see Fig. B.2C) for numerical solutions for different crack boundary conditions). However, this requires a separation of length scales, such that there is a regime between the length scale a of the crack tip and the length scale R at which the flow field is driven at the outer boundary or the active crack. For the epiblast however, we have $R/a \sim 10$, such that there is no r with $a \ll r \ll R$. Hence, it is not surprising that we do not find a divergence of stresses, corresponding to the shear rate and divergence, at the crack tip, i.e. the Hensen's node. This implies also, that we cannot infer material properties of the primitive streak in terms of characteristic power-laws of the flow field.

B.2.3 Expansion in terms of the complex logarithm

It appears that our system, a living crack with a finite sized crack tip, asks for an alternative approach to understand the experimental flow field analytically. When using non-integer power laws, one identifies the crack as the branch cut of the complex logarithm, as any power law z^m

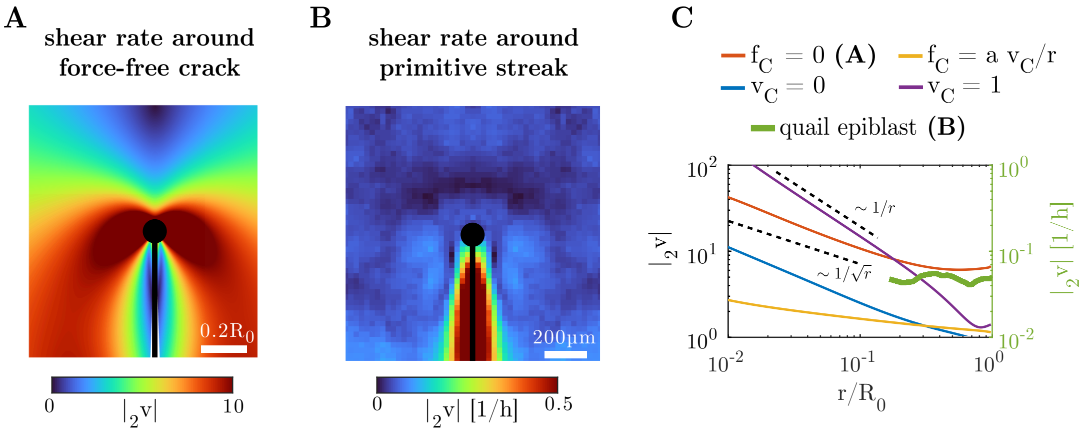

Figure B.2: **A**: modulus of shear rate for the numerical solution in Fig. 2.1F. Black line and circle indicate crack and crack tip, respectively. **B**: modulus of shear rate of symmetric flow field around the primitive streak (black line with circle corresponding to node). See also C.3. **C**: radial dependence of the angular average of the modulus of the shear rate for numerical solutions of different crack boundary conditions and the experimental data in **B** (green line). Red line corresponds to **A**. Blue line corresponds to Fig. 2.1G. Violet line corresponds to an active symmetric crack with crack boundary conditions $v_\theta = 1, t_{\theta r} = 0$ as in Fig. 2.6B, whereas yellow line corresponds to $\tilde{\eta}_{\text{ing}}/\tilde{\eta} \sim 3$

can be written as

$$z^m = \exp(m \log z) = z_0 \sum_{n=0}^{\infty} \frac{(\log z/z_0)^n}{n!} \tag{B.33}$$

with $z_0 \in \mathbb{C}$. Thus, any crack solution may be expanded in terms of $\log z$ around some reference point z_0. This statements becomes precise when considering a domain $D \subset \mathbb{C}$ defined by $|\log z/z_0| < \varepsilon$, which does not include the branch cut of $\log z$. $\log z$ maps D to a circle on which f, g are holomorphic and are thus given by Taylor expansions (see section 1.3.3). Using the original coordinates, f, g are then given by

$$f = \sum_{n=0}^{\infty} \tilde{f}_n (\log z)^n \quad g = \sum_{n=0}^{\infty} \tilde{g}_n (\log z)^n, \tag{B.34}$$

where $\tilde{f}_n, \tilde{g}_n$ are complex numbers with real and imaginary part corresponding to left-right symmetric and antisymmetric components of the flow field. For simplicity, we omitted z_0 corresponding to $z_0 = 1$. Symbolic integration with z then yields

$$\hat{f} = f_0 + \sum_{n=0}^{\infty} f_n z (\log z)^n \quad \hat{g} = g_0 + \sum_{n=0}^{\infty} g_n z (\log z)^n, \tag{B.35}$$

where we redefined the coefficients. We note, that f_n depends on all the $\tilde{f}_m$ with $m \geq n$. This flow field is given by

$${}_{(1)}v = {}_{(1)}V_0 + \sum_{n=0}^{\infty} \left[\bar{g}_n \bar{z} (\log \bar{z})^n + (2+\alpha) f_n z (\log z)^n - \alpha \bar{f}_n z \left((\log \bar{z})^n + n (\log \bar{z})^{n-1} \right) \right] \tag{B.36}$$

with ${}_{(1)}V_0$ is an integration constant corresponding to the rigid body translation. We note, that the branch cut of $\log z$ that corresponds to the crack is not defined at this point. Thus, this expansion works also for a curved crack by identifying this curved line with the branch cut of the complex logarithm.

B.3 Minimal model of the primitive streak

In the following, we consider a minimal model of the primitive streak as a left-right symmetric crack that drives fluid flow towards it. We consider the crack to be mechanically homogeneous in r, i.e.

$$t_C^r = t_C = \text{const.}, \tag{B.37}$$

corresponding to a parameter regime with $\eta_C \to 0$ and $t_C^{\text{act}} = \text{const.}$ Force balance (Eq. 2.20) then implies

$$t_R^{\theta r} - t_L^{\theta r} = 0. \tag{B.38}$$

Furthermore, we consider the parameter regime $(\eta_{\text{ing}} R)/(\eta d) \to \infty$ with $p_C^{\text{act}}/\eta_{\text{ing}} = j_{\text{act}} > 0$ with j_{act} being a constant. We understand this as a scenario where overdamped mechanical activity within the crack drives a constant flux j_{act} into the crack. At the crack tip, force balance (Eq. 2.13) implies

$$\mathbf{F}_T = -t_C \mathbf{r}(\theta = 0). \tag{B.39}$$

Furthermore, we consider plasticity of the crack tip to limit stresses at the crack tip, such that the stress at the crack tip may not diverge with an exponent $m < -1$. We note that this is in general not equivalent to the scenario of a rigid crack tip as given by Eq. 2.23, which we consider in the numerical solution for simplicity. As we consider the flow field close to the crack tip, i.e. at $r \ll R$, we do not need to consider boundary conditions at $r = R$ except the net velocity of the outer boundary (understood as the angular average of the flow field at $r = R$), which we put to zero.

These boundary conditions are solved by the field

$$\begin{aligned} {}_{(1)}v = & V_0 - \frac{1}{2\pi(\alpha+1)} \left(j_{\text{act}} - \frac{2+\alpha}{2\eta} t_C \right) \log \frac{r}{R} - j_{\text{act}} \frac{i\theta}{2\pi} \\ & + \frac{\alpha}{2(\alpha+1)} \left(\frac{j_{\text{act}}}{2\pi} - \frac{t_C}{4\eta\pi} \right) e^{2i\theta} + \mathcal{O}(r), \end{aligned} \tag{B.40}$$

where V_0 is a constant real velocity that depends on the boundary conditions at $r = R$. For finite α, the second term scaling with $\log r/R$ will dominate close to the crack tip. It yields a

${}_{(1)}v(\theta, r) = V_{\mathrm{act}} \log R/r$ with V_{act} being a real constant given by

$$V_{\mathrm{act}} = \frac{1}{2\pi(\alpha+1)} \left(j_{\mathrm{act}} - \frac{2+\alpha}{2\eta} t_C \right). \tag{B.41}$$

An active flux $j_{\mathrm{act}} > 0$ into the crack yields $V_{\mathrm{act}} > 0$ for vanishing line tension t_C, corresponding to a movement of the crack tip away from the crack. Thus, the active flux j_{act} into the crack drives a growth of the crack for vanishing line tension t_C. A line tension $t_C > 0$ drives a contraction of the crack, i.e. $V_{\mathrm{act}} < 0$ for $j_{\mathrm{act}} = 0$. Notably the logarithmic term proportional to j_{act} vanishes for $\alpha \to \infty$, i.e. when the fluid film is incompressible. For such parameters, the crack will always contract for $t_C > 0$ and $a \ll R$. Importantly, these results that follow from a logarithmic divergence of the velocity field are independent from boundary conditions at $r = R$ and also crack boundary conditions away from the crack tip, since such boundary conditions yield flow fields that scale as r^m with $m \geq 0$. We note also that the terms in Eq. B.40 all yields stresses that scale as $1/r$. Thus, they dominate the flow field at the crack tip for force boundary conditions at $r = R$.

Appendix C

Analysis of experimental data from quail embryos

In chapters 5 and 5, we use experimental data from quail embryos to infer a mechanical model of the quail embryo during the processes of gastrulation and left-right symmetry breaking. This data was obtained by Julia Pfanzelter and Adrian Lahola-Chomiak from the lab of Stephan Grill at the MPI-CBG Dresden. Embryos including the vitteline membrane from transgenic quails expressing a GFP membrane marker were transferred from the egg to a agarose based nutritive medium. There, they were imaged using a confocal microscope with a 20X objective using a time resolution of $3 - 10$min. The objective was located dorsally with respect to the embryo to image the epiblast. From this, a maximum intensity projection was obtained, i.e. at each xy-pixel, data from the z-layer with the maximal intensity was used. These 2D images were then analyzed by me as described in the following.

C.1 Particle image velocimetry and embryo alignment in space and time

We used PIVlab [154] to infer velocities of 64x64 pixel windows corresponding to grid of 40μmx40μm overlapping squares with the centers of neighboring squares seperated by 20μm. Four passes were used with window widths of 512, 256, 128 and 64 pixels.

In order to spatially align the data from different embryos, the position of the Hensen's node and the orientation of the primitive streak with respect to the node were manually annotated (with the help of J. Pfanzelter and A. Lahola-Chomiak). With this, we interpolate the flow field at grid points of a square grid with a width of 2000μm centered at the node identifying the axis of the streak (i.e. the AP axis) as the y axis. We use a grid spacing of 25μm and use a Gaussian kernel with a width $\sigma = 25\mu$m for interpolation. Using this grid, we average the flow field of each embryo in 1h time windows around the original time points of the experiment. From this, we

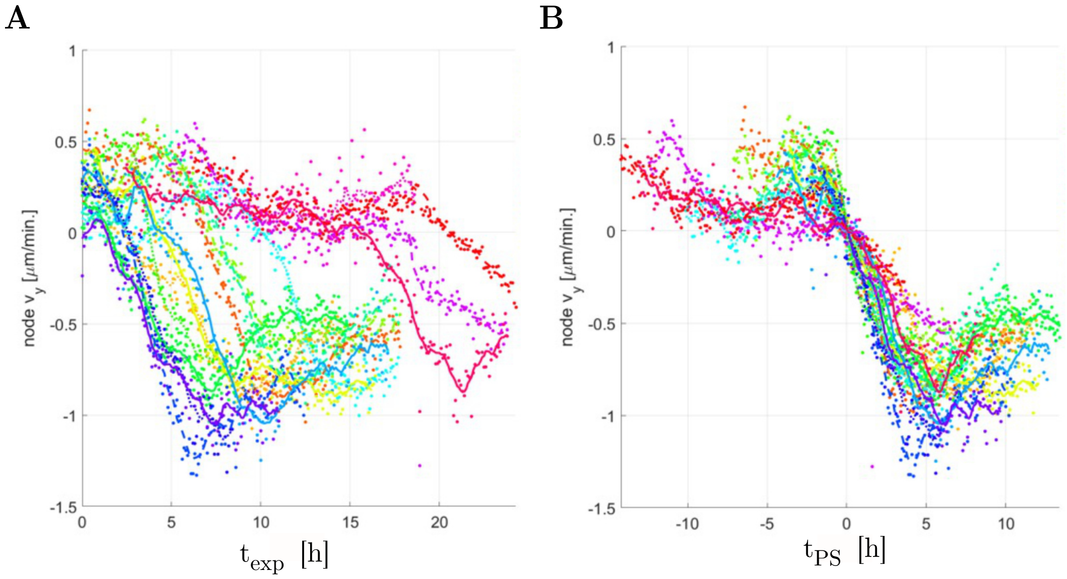

Figure C.1: AP velocity of Hensen's node with respect to neighboring epiblast, see main text for definition. Different colors correspond to different embryos. Points are data from single time points, whereas solid lines correspond to 1h moving averages, **A**: time with respect to start of experiment. **B**: time with respect to onset of streak regression.

determine the anterior-posterior velocity v_y of the node with respect to the surrounding epiblast, by calculating the average flow field within a radius of 100μm around the node and subtracting the average flow field in rectangles with coordinates $|x| \in [200\mu\text{m}, 400\mu\text{m}]$ and $y \in [-300\mu\text{m}, 300\mu\text{m}]$ with respect to the node. In Fig. C.1A, this velocity is plotted for 15 embryos. The velocity is positive for early time points, as the streak elongates and the node moves anteriorly. At late times, the velocity is negative as the streak regresses and the node moves posteriorly. We use the last time point where $v_y > 0$ as the reference time point t_{ref} corresponding to the onset of streak regression. We call the time with respect to this reference time point the primitive streak time $t_{PS} = t_{\text{exp}} - t_{\text{ref}}$. In Fig. C.1, v_y is plotted as a function of t_{PS}. We observe that the data from all experiments collapse onto a common curve, which validates our method for spatial and temporal alignment.

C.2 Flow field decomposition

Having aligned the embryos in space and time, we calculate an average flow field across the set of 15 embryos, by calculating the median or mean at each point in space and time. We decompose this flow field into a left-right symmetric and into a left-right antisymmetric component according to

$$\mathbf{v}_{\mathrm{sym}}(x,y) = \frac{1}{2}\left(v_x(x) - v_x(-x), v_y(x) + v_y(-x))^T\right) \tag{C.1}$$

$$\mathbf{v}_{\mathrm{asym}}(x,y) = \frac{1}{2}\left(v_x(x) + v_x(-x), v_y(x) - v_y(-x))^T\right). \tag{C.2}$$

In Fig. C.2 such a decomposition is shown for different time points using the median at each point in space and time. While for the left-right symmetric component, using the mean yields very similar results, for the left-right antisymmetric component, using the median gives more robust results as the mean is more susceptible to outliers. We observe that the LR-antisymmetric component is often dominated by large-scale translations that are only observed in a subset of embryos. Thus, they reflect embryo to embryo variability and not embryonic left-right symmetry breaking. To circumvent this, we fit a rigid body translation and rotation to the left-right antisymmetric flow field in a distance between 350μm and 600μm with respect to the node. Then we subtract this translation and rotation to obtain a velocity field in the thus defined reference frame. In the right column of Fig. C.2, the result is shown, where for $-2h \leq t_{PS} \leq 2h$ we observe a consistent counter-clockwise rotation and left-ward movement of the node. This is the chiral flow, we analyze in section 5.1.

C.3 Bootstrapping

In order to compare the measured flow field with theoretical calculations in chapter 2, we consider also derivatives of the flow field, specifically the divergence and the shear rate along the y or x axis. Calculating derivative in terms of finite differences of the median flow field yields noisy results. Instead, we calculate divergence and shear rate for each embryo separately using finite differences using a grid that is shifted by half the grid spacing in y and x with respect to the velocity grid. Then, we calculate the median of the resulting divergence and shear rate across embryos at each point in space and time. Finally, we calculate the left-right symmetric component. The results are plotted in Fig. C.3 ("measured" columns) in comparison to results from the calculated flow field in Fig. 2.2

C.4 Derivatives of experimental data

In order to obtain a measure of the experimental uncertainty, we made use of bootstrapping. Using random sampling with replacement, we generated 400 sets of $n = 15$ embryos from the original data set. For each set of embryos, we calculated the median flow field as described above. From these 400 median velocities, the 5^{th} and 95^{th} percentiles at each point in space and time were determined. This defines the range of uncertainty, which we indicate as shaded areas in Fig.2.5,5.1. For measures that depend on various data points, we calculated the measure for each of the 400 sets separately and subsequently calculated the 5th and 95th percentiles.

C.5 Calculating flow field from measured boundary velocities

In order to calculate the flow field from measured boundary velocities (see Fig. C.4,C.5), we make use of Eq. B.12, B.3,B.4. Discretizing the line integral in Eq. B.12, the flow field is given by

$$\begin{aligned}
{}_{(1)}v(z) = &\sum_{m=0}^{N_+} \left[a_m^+ V_m^{A,+,r}(z) + i b_m^+ V_m^{A,+,i}(z) + c_m^+ V_m^{B,+,r}(z) + i d_m^+ V_m^{B,+,i}(z)\right] \\
&+ \sum_{m=0}^{N_-} \left[a_m^- V_m^{A,-,r}(z) + i b_m^- V_m^{A,-,i}(z) + c_m^- V_m^{B,-,r}(z) + i d_m^- V_m^{B,-,i}(z)\right] \\
&+ \sum_{j=1}^{N_C} \big[A_j G_{\text{mono}}(z - z_j, \mathbf{x}) + B_j G_{\text{mono}}(z - z_j, \mathbf{y}) \\
&\qquad + C_j G_{\text{dipo}}(z - z_j, \mathbf{x}) + D_j G_{\text{dipo}}(z - z_j, \mathbf{y})\big],
\end{aligned} \tag{C.3}$$

where

$$V_m^{A/B,-,r}(z) = K_{m+1}(r/l_h^{A/B}) e^{i(m+1)\theta} + K_{m-1}(r/l_h^{A/B}) e^{-i(m-1)\theta} \tag{C.4}$$

$$V_m^{A/B,-,i}(z) = K_{m+1}(r/l_h^{A/B}) e^{i(m+1)\theta} - K_{m-1}(r/l_h^{A/B}) e^{-i(m-1)\theta} \tag{C.5}$$

$$V_m^{A/B,+,r}(z) = I_{m+1}(r/l_h^{A/B}) e^{i(m+1)\theta} + I_{m-1}(r/l_h^{A/B}) e^{-i(m-1)\theta} \tag{C.6}$$

$$V_m^{A/B,+,i}(z) = I_{m+1}(r/l_h^{A/B}) e^{i(m+1)\theta} - I_{m-1}(r/l_h^{A/B}) e^{-i(m-1)\theta} \tag{C.7}$$

and $\mathbf{x}, \mathbf{y}$ denote the unit basis vectors of the cartesian coordinate system. Here they correspond to the direction of the forces with $G_{\text{mono/dipo}}$ defined by Eq. B.7,B.10. $a_m^{+/-}, b_m^{+/-}, c_m^{+/-}, d_m^{+/-}, A_j, B_j, D_j, C_j$ are real coefficient which we determine from the measured boundary velocities using linear regression. As measured boundary velocities around the streak we use data points for which the minimal distance r_{min} to the negative y axis obeys $100\mu\text{m} \leq r_{\text{min}} < 125\mu\text{m}$ and for which $r < 600\mu\text{m}$. this yields $2N_C$ data points with $y < 0$ and $2(N_- + 1)$ data points with $y \geq 0$. As outer boundary velocities, we linearly interpolate the measured flow field at $2(N_+ + 1)$ equally distant points with on the outline of a circle with radius $600\mu m$, where we use $N_+ = 128$.

C.6 Inferring an effective model of the primitive streak using the complex logarithm

As discussed in section B.2, the flow field around a crack can be expanded in terms of the complex logarithm away from the crack, the crack tip and the outer boundary. We use this expansion, given by Eq. B.36, to obtain an effective model of the primitive streak in terms of the forces it is exerting on the epiblast. To this end, we truncate this series after $n = 1$ and use $z_0 = R/2$.

Truncating this series in such a way yields a flow field that is well behaved at the crack and the crack tip. For simplicity, we omit the $n = 0$ terms, which would dominate at the outer boundary away from the crack. Thus, the flow field is of the form

$$ {}_{(1)}v = V_0 + A\bar{z}(\log \bar{z}) + Bz\left[(2+\alpha)(\log z) - \alpha\left(\log \bar{z} + n\right)\right], \tag{C.8} $$

where $z = (y - ix)/z_0$, since the crack corresponds to the y axis in the experimental data. As we consider the left-right symmetric component of the flow field V_0, A, B are real numbers. For each time point we fit these numbers to the average flow field using $\alpha = 3$. We exclude data points with a distance $r > 600\mu$m with respect to the Hensen's node or a distance $r \leq 100\mu$m with respect to any point on the streak i.e. the negative y axis. This yields an analytical representation of the flow field. Eq. B.16,B.17 yield analytical expressions for the stress of the epiblast. We note that the pressure is only defined up to a constant, corresponding to the growth rate G. We choose G such that the viscous pressure ${}_{(0)}t$ vanishes, when averaging over the epiblast, i.e. the annulus between $r = 100\mu$m and $r = 600\mu$m. With this, we evaluate this stress at $\theta = \pm\pi$ for $r > 100$ to obtain the forces a one-dimensional crack, corresponding to the streak, exerts on the fluid film, corresponding to the epiblast. To obtain velocity V_y of the node and the force F_y the node is exerting on the epiblast, we use Eq. 2.24, 2.14 with $a = 100\mu$m by numerically calculating the boundary integrals. In order to calculate the flux J into the crack, we evaluate

$$ J = \int_a^R \mathrm{d}r(v_L^\theta(r) - v_R^\theta(r)) - a^2 \int_{-\pi}^{\pi} \mathrm{d}\theta\, v^r(r = a, \theta) \tag{C.9} $$

numerically.

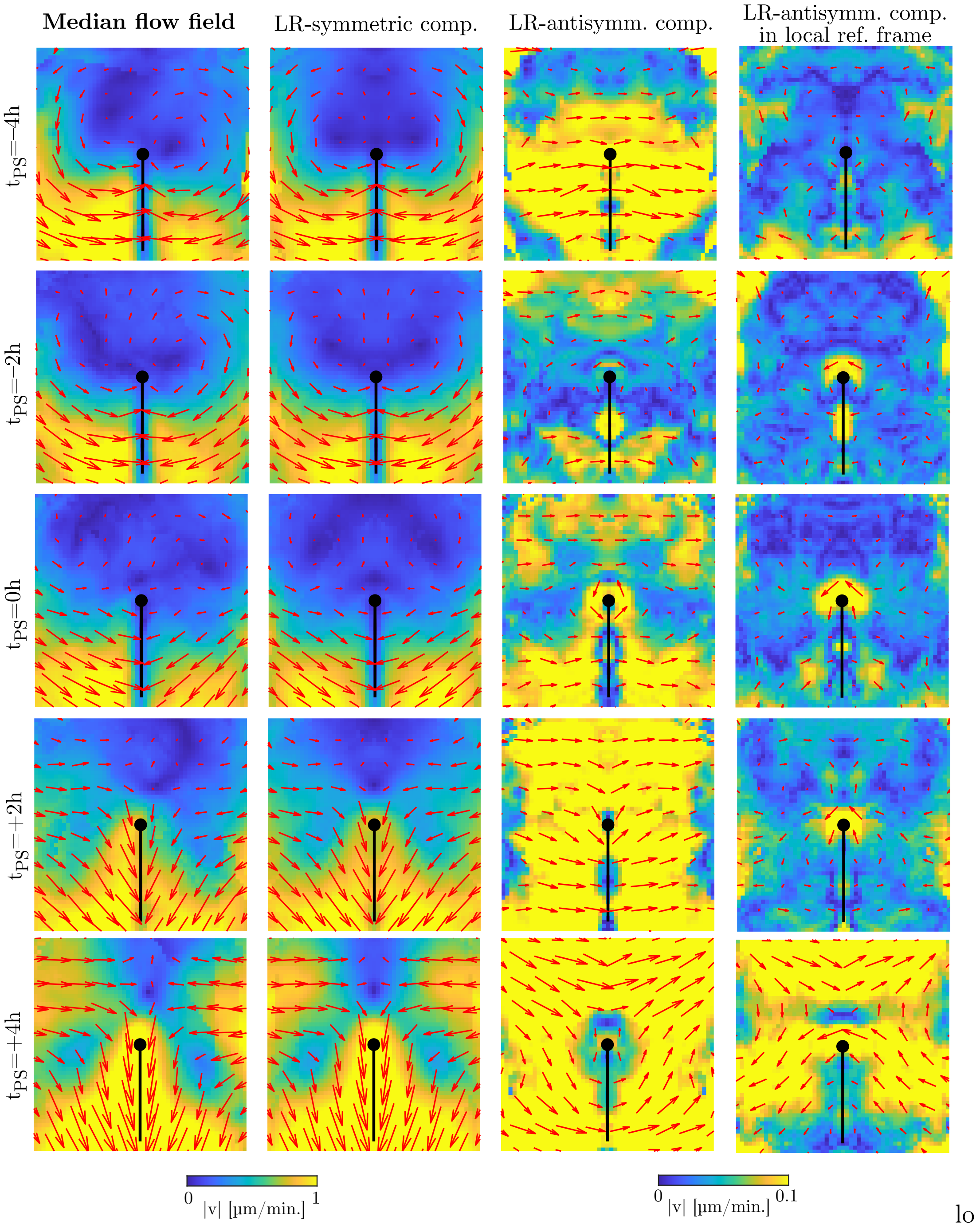

Figure C.2: Median flow field across 15 embryos. For definitions of left-right symmetric and antisymmetric component as well as the local reference frame in the rightmost column, see the main text of this appendix chapter.

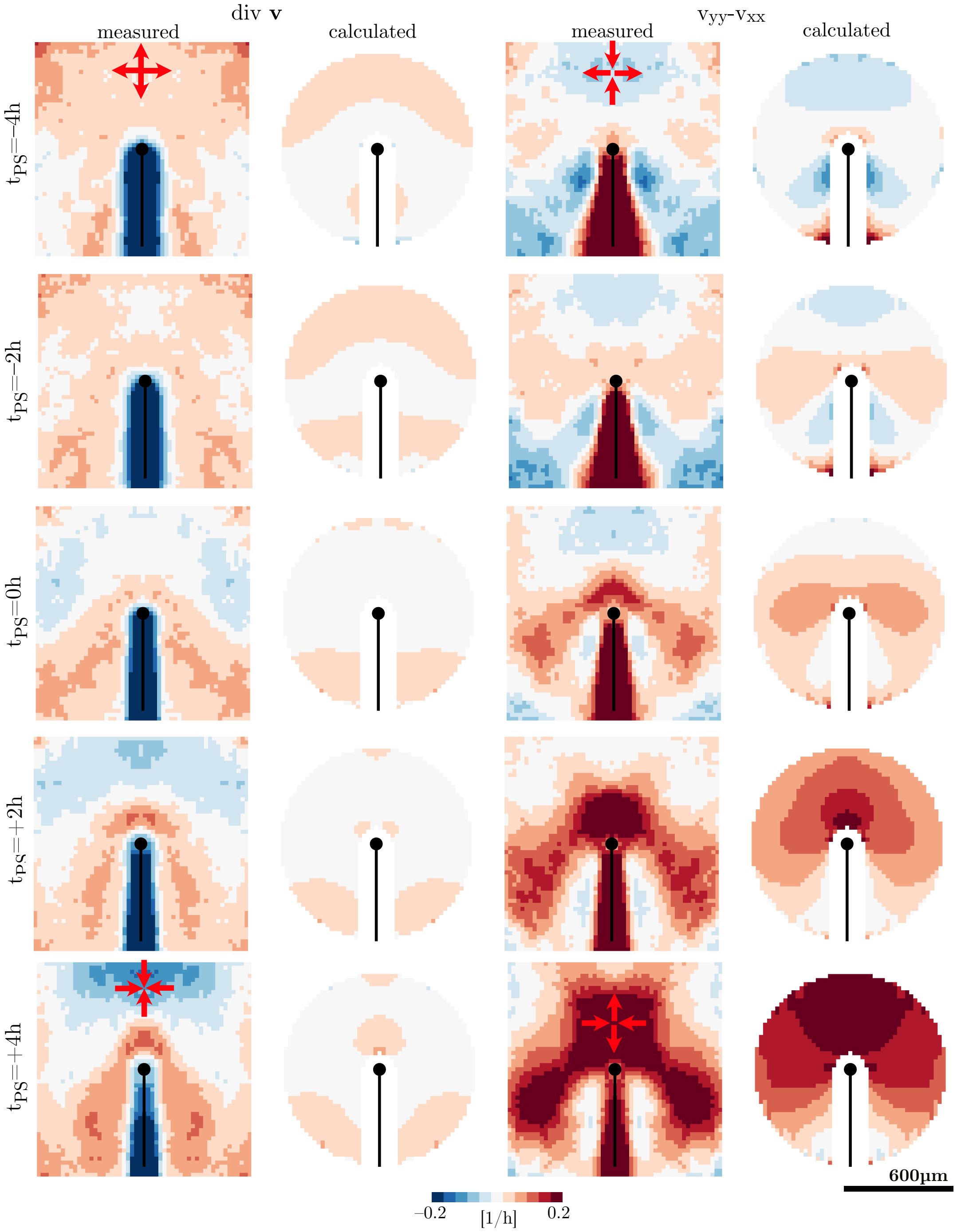

Figure C.3: Comparison of numerical derivatives of experimental data to results of theoretical calculation in Fig. C.4.

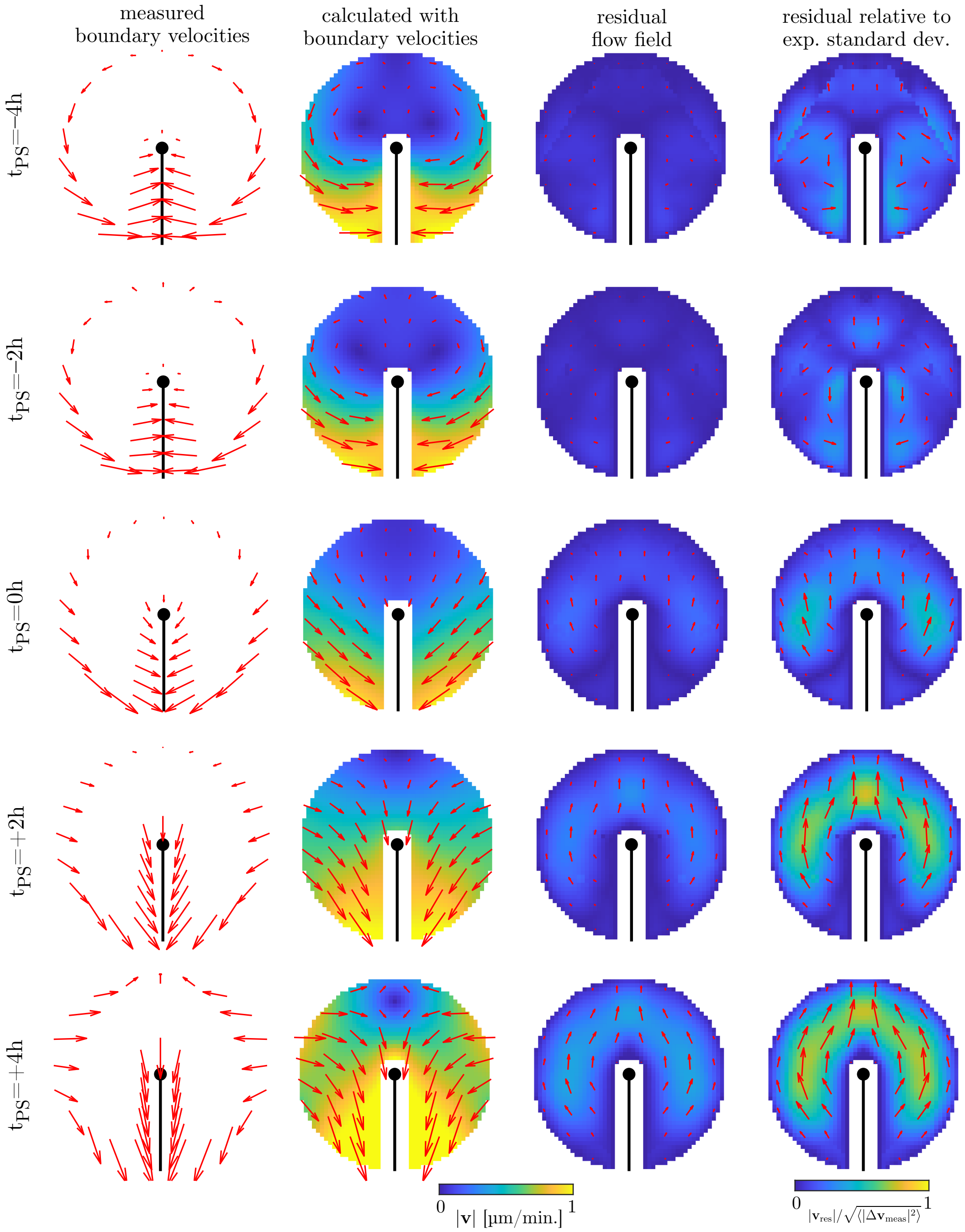

Figure C.4: Leftmost column: Mean left-right symmetric flow field across 15 embryos at the boundaries of the primitive streak and a circle with radius 600μm. Arrows are a representative selection of data points. Left middle column: Flow field calculated from velocity boundary conditions as described in the main text of this appendix chapter. Right middle column: Residual of the measured flow field after subtracting the calculated flow field. Rightmost column: Residual flow field divided by the experimental standard deviation, i.e. the square root of the variance across embryos.

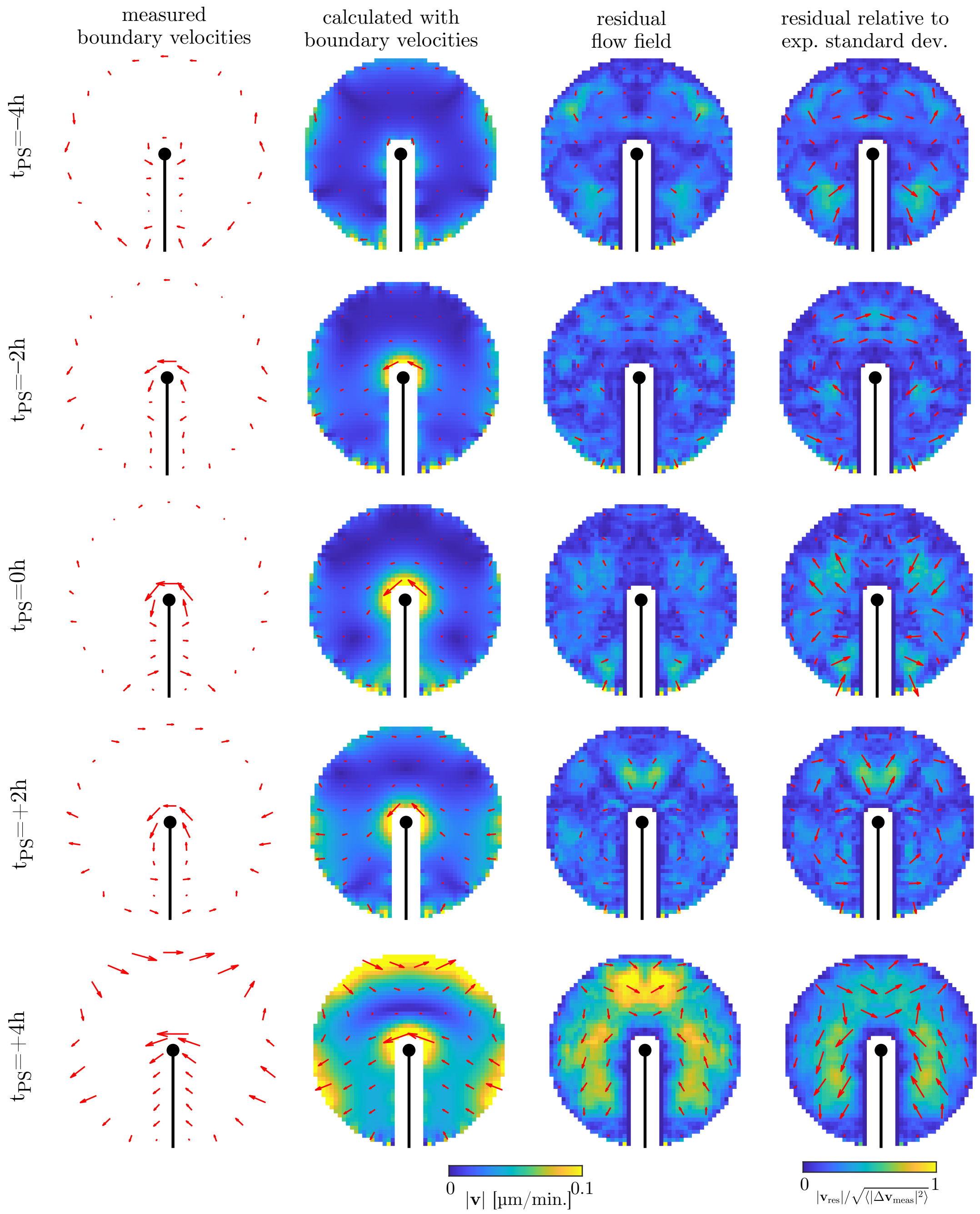

Figure C.5: Same as in Fig. 2.2, but using the left-right antisymmetric component of the measured median flow field in the local reference frame as in the rightmost column of Fig. C.2.

Appendix D

The Newman Penrose formalism applied to an active surface

This appendix supplements the introduction of the Newman Penrose formalism in section 1.3.1. Furthermore, we give tangential force and torque balance equations of an active surface, which allows us to derive the governing equation of a chiral active fluid film (Eq. 5.2.1).

D.1 Fields with mixed spin-weight

In section 4.2, we discuss Green's function on the curved surface using the Newman Penrose formalism. To understand such propagators, we introduce fields with mixed spin-weight which we denote as $(s_1, ..., s_N)G(z_1, ..., z_n)$ with s_i being the spin weights with respect to the coordinate system at position z_i. As before they are complex-valued fields. The spin-weights are defined by their behaviour under a global gauge transformation $\psi(z)$ that rotates the complex basis $\mathbf{Z}$. Under such a rotation, the mixed-spin-weight field transforms analogous to Eq. 1.57 as

$$(s_1, ..., s_N)G'(z_1, ..., z_n) = (s_1, ..., s_N)G(z_1, ..., z_n) \exp\left(\sum_j^N -is_j\psi(z_j)\right). \tag{D.1}$$

D.2 Some properties of spin-weighted quantities on a surface

From the definition of the complex basis $\mathbf{Z}$, we have

$$\bar{Z}^i Z^j = g^{ij} + i\epsilon^{ij}, \quad Z^i Z_i = 0. \tag{D.2}$$

With this, tensor contractions can be given in terms of the corresponding spin-weighted quantities as

$$X_iY^i = \mathrm{Re}[{}_1X\,{}_{-1}Y] = \frac{1}{2}({}_1X\,{}_{-1}Y + {}_{-1}X\,{}_1Y), \quad X_i\epsilon^{ij}Y_j = \mathrm{Im}[{}_{(-1)}X\,{}_{(1)}Y] \tag{D.3}$$

$$X_{ij}Y^{ij} = \frac{1}{2}\mathrm{Re}[{}_2X\,{}_{-2}Y + {}_0X\,{}_0\bar{Y}], \quad X_{ij}\epsilon^{i}{}_{k}Y^{kj} = \frac{1}{2}\mathrm{Im}[{}_{(-2)}X\,{}_{(2)}Y + {}_{(0)}X_{(0)}\bar{Y}]. \tag{D.4}$$

Using the spin-raising and lowering operators (Eq. 1.60, 1.61), we can also write divergences of vectors and tensors as

$$\nabla_iX^i = \mathrm{Re}[\bar{\eth}\,{}_{(1)}X], \quad Z_j\nabla_iX^{ij} = \frac{1}{2}(\bar{\eth}\,{}_{(2)}X + \eth\,{}_{(0)}X). \tag{D.5}$$

Importantly, the spin-raising and lowering operators obey a divergence theorem [201]

$$\int_{\mathcal{S}} \mathrm{d}S\eth\,{}_{(-1)}f = \int_{\mathcal{C}} \mathrm{d}l_{(1)}\nu\,{}_{(-1)}f. \tag{D.6}$$

D.3 Differential geometry

The basis $\mathbf{Z}$ can be written as

$$\mathbf{Z} = \eth\mathbf{X}. \tag{D.7}$$

With this, the Gauss-Weingarten equations yield

$$\eth Z = -\,{}_{(2)}C\mathbf{n} - \Gamma\mathbf{Z}, \quad \bar{\eth}\mathbf{Z} = -\,{}_{(0)}C\mathbf{Z} + \bar{\Gamma}\mathbf{Z}, \quad \eth\mathbf{n} = \frac{1}{2}({}_{(0)}C\mathbf{Z} + {}_{(2)}C\bar{\mathbf{Z}}) \tag{D.8}$$

Furthermore, we find that the curvature tensor obeys

$$\eth\,{}_{(0)}C = \bar{\eth}\,{}_{(2)}C. \tag{D.9}$$

D.4 Force and torque balance equations

Using the above identities, we can write the force and torque balance equations (Eq. 1.24 and 1.27) in terms of spin-weighted quantities as

$$\frac{1}{2}(\bar{\eth}\,{}_{(2)}t + \eth\,{}_{(0)}t) + \frac{1}{2}({}_{(2)}C\,{}_{(-1)}t_n + {}_{(0)}C\,{}_{(1)}t_n) = -\,{}_{(1)}f \tag{D.10}$$

$$\frac{1}{2}(\bar{\eth}\,{}_{(1)}t_n + \eth\,{}_{(-1)}t_n) - \frac{1}{2}\mathrm{Re}[{}_{(-2)}C\,{}_{(2)}t + {}_{(0)}C\,{}_{(0)}t] = -\,f_n \tag{D.11}$$

$$\frac{1}{2}(\bar{\eth}\,{}_{(2)}m + \eth\,{}_{(0)}m) + \frac{1}{2}({}_{(0)}C\,{}_{(1)}m_n + {}_{(2)}C\,{}_{(-1)}m_n) = i\,{}_{(1)}t_n - {}_{(1)}\Gamma \tag{D.12}$$

$$\mathrm{Re}[\bar{\eth}\,{}_{(1)}m_n] - \frac{1}{2}\mathrm{Re}[{}_{(2)}C\,{}_{(-2)}m + {}_{(0)}C\,{}_{(0)}m] = -\,\mathrm{Im}\,{}_{(0)}t - \Gamma_n \tag{D.13}$$

Using torque balance and the definitions of $\tilde{m}^{ij}$ and $\tilde{t}^{ij}$ (Eq. 1.33, 1.34), we obtain

$$
\begin{aligned}
{}_{(2)}t &= {}_{(2)}\tilde{t} + \frac{i}{2}({}_{(0)}m\,{}_{(2)}C + {}_{(2)}m\,{}_{(0)}C) && \text{(D.14)}\\
{}_{(0)}t &= \mathrm{Re}[{}_{(0)}\tilde{t}] - i\Gamma_n - i\,\mathrm{Re}[\bar{\eth}\,{}_{(1)}m_n] + \frac{i}{2}({}_{(-2)}C\,{}_{(2)}m + {}_{(0)}C\,{}_{(0)}m) && \text{(D.15)}\\
{}_{(2)}m &= i\,{}_{(2)}\tilde{m}, \quad {}_{(0)}m = i\,{}_{(0)}\tilde{m} && \text{(D.16)}
\end{aligned}
$$

Plugging this into the above force balance equations yields

$$
\begin{aligned}
-{}_{(1)}f =& \frac{1}{2}\left[\bar{\eth}\left({}_{(2)}\tilde{t} - 2\,\mathrm{Im}[{}_{(0)}\tilde{m}]\,{}_{(2)}C - i\eth\,{}_{(1)}m_n\right) + \eth\left({}_{(0)}\tilde{t} - \mathrm{Im}[\bar{\eth}\,{}_{(1)}m_n]\right)\right]\\
&- \frac{1}{2}\,\mathrm{Re}[{}_{(0)}\tilde{m}]\eth\,{}_{(0)}C + \frac{1}{4}\left({}_{(2)}\tilde{m}\eth\,{}_{(-2)}C + {}_{(-2)}\tilde{m}\eth\,{}_{(2)}C\right)\\
&- i\eth\left(\Gamma_n + \frac{1}{2}\,\mathrm{Im}[{}_{(2)}\tilde{m}\,{}_{(-2)}C\right) - \frac{i}{2}\left({}_{(2)}C\,{}_{(-1)}\Gamma + {}_{(0)}C\,{}_{(1)}\Gamma\right)\\
f_n =& \frac{1}{2}\,\mathrm{Re}[{}_{(-2)}C\,{}_{(2)}\tilde{t} + {}_{(0)}C\,{}_{(0)}\tilde{t}] + \mathrm{Im}[\bar{\eth}\,{}_{(1)}\Gamma] - \frac{{}_{(0)}C}{2}\,\mathrm{Im}[\bar{\eth}\,{}_{(1)}m] + \frac{1}{2}\,\mathrm{Im}[{}_{(-2)}C\eth\,{}_{(1)}m]\\
&- \frac{1}{2}\Delta_{LB}\,\mathrm{Re}\,{}_{(0)}\tilde{m} - \frac{1}{4}({}_{(0)}C\,{}_{(0)}C + {}_{(-2)}C\,{}_{(2)}C)\,\mathrm{Re}[{}_{(0)}\tilde{m}]\\
&- \frac{1}{2}\,\mathrm{Re}[\bar{\eth}\bar{\eth}\,{}_{(2)}\tilde{m}] - \frac{{}_{(0)}C}{4}\,\mathrm{Re}[{}_{(2)}\tilde{m}\,{}_{(-2)}C] && \text{(D.17)}
\end{aligned}
$$

The tangential force balance equation (${}_{(1)}f$) yields the govering equation of the flow field of a chiral active fluid film (Eq. 5.15) using the constitutive equations in section 5.2.1. For an isotropic surface (${}_{(2)}C = 0 = \eth\,{}_{(0)}C$), the normal force reads

$$
\begin{aligned}
f_n =& \frac{1}{2}\,\mathrm{Re}[{}_{(0)}C\,{}_{(0)}\tilde{t}] + \mathrm{Im}[\bar{\eth}\,{}_{(1)}\Gamma] - \frac{{}_{(0)}C}{2}\,\mathrm{Im}[\bar{\eth}\,{}_{(1)}m]\\
&- \frac{1}{2}\Delta_{LB}\,\mathrm{Re}\,{}_{(0)}\tilde{m} - \frac{1}{4}\,{}_{(0)}C\,{}_{(0)}C\,\mathrm{Re}[{}_{(0)}\tilde{m}] - \frac{1}{2}\,\mathrm{Re}[\bar{\eth}\bar{\eth}\,{}_{(2)}\tilde{m}] && \text{(D.18)}
\end{aligned}
$$

D.5 Effective free energy description of active moments

We define an effective free energy density in terms of the active moments

$$
f_{\text{eff}} = \frac{1}{2}\,\mathrm{Re}[{}_{(0)}\tilde{m}_{\text{act}}\,{}_{(0)}C + {}_{(2)}\tilde{m}_{\text{act}}\,{}_{(-2)}C] = \tilde{m}^i{}_j C_i{}^j \qquad \text{(D.19)}
$$

We determine the equilibrium stress and moment, by considering a deformation of the surface and using $\delta\mathcal{F} = \delta W$ (see section 1.2.3). We understand the active moment as a density of molecular torque dipoles, which is diluted upon an expansion of the surface such that

$$
\delta(\sqrt{g}f_{\text{eff}}) = \frac{\partial f_{\text{eff}}}{\partial(C_i{}^j)}\delta C_i{}^j \qquad \text{(D.20)}
$$

Thereby, we recover the active moment as the effective equilibrium moment:

$$\tilde{m}^{ij}_{\mathrm{eq,eff}} = \tilde{m}^{ij}_{\mathrm{act}}, \quad \tilde{t}^{ij}_{\mathrm{eq,eff}} = 0. \tag{D.21}$$

Thus, we recover the same governing equation of the fluid film by using the equilibrium moment associated with f_{eff} instead of an active moment. This equivalence reflects that ${\tilde{m}_i}^j$ is conjugate to ${C_i}^j$ in terms of the virtual work δW.

Appendix E

Definitions and applications of spin-weighted spherical harmonics

In the following, we give definitions and properties of spin-weighted spherical hamonics [138, 202, 203], as derived in the Newman Penrose formalism (see section 1.3.1). They form a basis of spin-weighted fields on the sphere. With this, we obtain in the following analytical results for flow field and linear stability of an active fluid film with a slightly anisotropic spherical geometry. Furthermore, we use such a decomposition in terms of spherical harmonics in the pseudo-spectral method we use to simulate the non-linear dynamics of an active fluid film with spherical topology (appendix F).

E.1 Definitions

(Scalar) spherical harmonic functions Y_{lm} with integers $l > 0$ and $|m| \leq l$ $l \in \mathbb{N}_0$ are the eigenfunctions of the Laplace Beltrami operator Δ_{LB} on the unit sphere, obeying

$$\Delta_{LB} Y_{lm} = -l(l+1) Y_{lm}. \tag{E.1}$$

We use a complex convention for Y_{lm}, as given [175]. Using the usual spherical coordinates θ, φ, they read for $m \geq 0$

$$Y_{lm} := e^{im\varphi} \sqrt{\frac{2l+1}{4\pi} \frac{(l-m)!}{(l+m_!}} P_l^m(\cos\theta), \tag{E.2}$$

where the associated Legendre polynomials are given by

$$P_l^m(\cos\theta) := \frac{(-1)^m}{2^l l!} (\sin\theta)^m \frac{\mathrm{d}^{l+m}}{(\mathrm{d}\cos\theta)^{l+m}} (\cos^2\theta - 1)^l. \tag{E.3}$$

For $m < 0$, Y_{lm} is given by

$$Y_{lm} = (-1)^m \bar{Y}_{l,-m}, \tag{E.4}$$

where $\bar{...}$ denotes the complex conjugate.

In the following, we adopt the Newman Penrose formalism (section 1.3.1) on a spherical surface with the common convention

$$\mathbf{Z} = \boldsymbol{\theta} + i\boldsymbol{\varphi}. \tag{E.5}$$

Using the spin-raising and lowering operators (Eq. 1.60,1.61), we define the spin-weighted spherical harmonics ${}_{(s)}Y_{lm}$ using the sign convention from [201] as

$$ {}_{(|s|)}Y_{lm} := (-1)^s \sqrt{\frac{(l-|s|)!}{(l+|s|)!}} \eth^s Y_{lm}, \quad {}_{(-|s|)}Y_{lm} := \sqrt{\frac{(l-|s|)!}{(l+|s|)!}} \bar{\eth}^s Y_{lm}, \tag{E.6}$$

where our sign convention of the $\eth, \bar{\eth}$ differs from [201].

E.2 Properties

From the definitions, we have

$$ {}_{(s)}Y_{lm} = (-1)^{m+s} \, {}_{(s)}\bar{Y}_{lm}. \tag{E.7}$$

Furthermore also the spin-weighted spherical harmonics obey an eigenvalue equation:

$$\bar{\eth}\eth \, {}_{(s)}Y_{lm} = [s(s+1) - l(l+1)] \, {}_{(s)}Y_{lm} \tag{E.8}$$

$$\eth\bar{\eth} \, {}_{(s)}Y_{lm} = [s(s-1) - l(l+1)] \, {}_{(s)}Y_{lm}. \tag{E.9}$$

As such they are the eignfunctions of a self-adjoint operator and form an orthogonal basis of complex functions on the (unit) sphere S^2 [138], i.e.

$$\int_{S^2} \mathrm{d}S \, {}_{(s)}Y_{lm} \, {}_{(s)}\bar{Y}_{l'm'} = \delta_{ll'}\delta_{mm'} \tag{E.10}$$

$$\sum_{lm} {}_{(s)}Y_{lm}(\theta', \varphi') \, {}_{(s)}\bar{Y}_{lm}(\theta, \varphi) = \delta(\varphi - \varphi')\delta(\cos\theta - \cos\theta'), \tag{E.11}$$

where $\delta(x)$ denotes the Dirac delta. With this, we can expand any spin-weighted field on the sphere as

$$ {}_{(s)}f(\theta, \varphi) = \sum_{lm} f_{lm} \, {}_{(s)}Y_{lm}(\theta, \varphi), \quad f_{lm} = \int_{S^2} \mathrm{d}S \, {}_{(s)}\bar{Y}_{lm} \, {}_{(s)}f. \tag{E.12}$$

We note that such an expansion is valid for any complex function on the sphere. As such, we can also use it to expand spin-weighted fields on other surface geometries with spherical topology. In this case the projections onto spherical harmonics are calculated as an integral on the unit sphere S^2 as in the above equations.

Spin-weighted spherical harmonics are related to Wigner D matrices [138, 201, 175], which correspond to spatial rotations of the scalar spherical harmonics:

$$ {}_sY_{lm}(\theta,\varphi) = (-1)^m \sqrt{\frac{2l+1}{4\pi}} D^l_{-m,s}(\varphi,\theta,0) = (-1)^m \sqrt{\frac{2l+1}{4\pi}} \langle l,-m|\, \mathcal{R}(\varphi,\theta,0)\, |l,s\rangle \tag{E.13} $$

This allows to calculate products of spin-weighted spherical harmonics using Clebsch-Gordan coefficients

$$ \int \mathrm{d}\Omega\, {}_{s_1}Y_{l_1m_1}\, {}_{s_2}Y_{l_2m_2}\, {}_{s_3}Y_{l_3m_3} = \sqrt{\frac{(2l_1+1)(2l_2+1)(2l_3+1)}{4\pi}} \begin{pmatrix} l_1 & l_2 & l_3 \\ m_1 & m_2 & m_3 \end{pmatrix} \begin{pmatrix} l_1 & l_2 & l_3 \\ -s_1 & -s_2 & -s_3 \end{pmatrix} \tag{E.14} $$

Here, we use the Wigner 3j symbol which is a particularly symmetric convention for writing Clebsch-Gordan coefficients.

E.3 Flow field on a sphere

The force balance equation for an isotropic active fluid (Eq. 1.69) using a Hodge decomposition ${}_{(1)}v = ðF$ on the sphere reads

$$ ð\Delta_{LB}(F + \alpha \operatorname{Re} F) - \left(\frac{1}{l_h^2} - \frac{2}{R_0^2}\right) ðF = -\frac{1}{\eta} ð\, {}_{(0)}\chi \tag{E.15} $$

Using the eigenvalue equation of the scalar spherical harmonics, this is solved by $F = A = \operatorname{Re} F$ with

$$ A_{lm} = \frac{R_0^2}{(R_0/l_h)^2 + (\alpha+1)l(l+1) - 2} \frac{\chi_{lm}}{\eta}. \tag{E.16} $$

E.4 Linear order calculations on a deformed sphere

E.4.1 Differential geometry

We consider a deformed spherical geometry

$$ \mathbf{X}' = \mathbf{X} + \delta\mathbf{X} = (R_0 + \delta R(\theta,\varphi))\mathbf{r}, \tag{E.17} $$

where for simplicity we choose length units such that $R_0 = 1$ in the following. We expand the deformation δR in (scalar) spherical harmonics

$$ \delta R(\theta,\varphi) = \sum_{lm} \delta R_{lm} Y_{lm}(\theta,\varphi) \tag{E.18} $$

Upon the deformation the normal vector changes as

$$ \delta\mathbf{n} = -(\partial_i \delta R)\mathbf{e}^i = -\operatorname{Re}[\bar{\mathbf{Z}} ð\delta R]. \tag{E.19} $$

where $\eth$ denotes the spin-raising operator on the undeformed sphere $\delta\mathbf{Z}$ is defined up to rotation. We use a convention for $\delta\mathbf{Z}$ such that

$$\delta\mathbf{Z} = -(\mathbf{Z}\cdot\delta n)\mathbf{n} = (\eth\delta R)\mathbf{n} = (\eth\delta R)\mathbf{r}, \quad \delta\bar{\mathbf{Z}} = (\bar{\eth}\delta R)\mathbf{r}. \tag{E.20}$$

Using $\mathbf{Z}' = \eth'\mathbf{X}'$, we have

$$\eth'\,{}_{(0)}f = (1-\delta R)\eth\,{}_{(0)}f \tag{E.21}$$

for a spin 0 field ${}_{(0)}f$ where $\eth'$ denotes the spin-raising operator on the deformed sphere. With this, we obtain

$$\delta\Gamma = -\delta R\Gamma - \eth\delta R \tag{E.22}$$

and thus

$$\eth'\,{}_{(s)}f = (1-\delta R)\eth\,{}_{(s)}f - s(\eth\delta R)\,{}_{(s)}f. \tag{E.23}$$

$$\bar{\eth}'\,{}_{(s)}f = (1-\delta R)\bar{\eth}\,{}_{(s)}f + s(\bar{\eth}\delta R)\,{}_{(s)}f. \tag{E.24}$$

With this we obtain

$$\delta\Delta_{LB} = -2\delta R\Delta_{LB}. \tag{E.25}$$

Furthermore we have

$$\delta\,{}_{(0)}C = -2\delta R - \bar{\eth}\eth\delta R, \quad \delta\,{}_{(2)}C = -\eth\eth\delta R, \quad \delta\kappa = \delta\,{}_{(0)}C. \tag{E.26}$$

E.4.2 Flow field of active isotropic fluid

We write the flow field as a Hodge decomposition ${}_{(1)}v = \eth F$ and calculate the change in the complex function F upon deformation of the sphere such that the flow field on the deformed sphere is given by

$${}_{(1)}v' = {}_{(1)}v + \delta\,{}_{(1)}v, \quad \delta\,{}_{(1)}v = \eth\delta F - \delta R\,{}_{(1)}v, \tag{E.27}$$

where ${}_{(1)}v$ fulfills the force balance equation on the undeformed sphere. With this and using the expression for the spin raising and lowering operators on the deformed sphere, the force balance equation on the deformed sphere in terms of δR reads

$$\eta\eth\Delta_{LB}(F_0 + \alpha\,\mathrm{Re}\,F) - (\gamma - 2\eta)\eth F = 2\eta\eth\left[\delta R(F + \alpha\,\mathrm{Re}\,F)\right] + 2\eta(2\delta R + \bar{\eth}\eth\delta R)\eth F, \tag{E.28}$$

where the right hand side corresponds to viscous force resulting from the deformation. Using the eigenvalue relations for the spin-weighted spherical harmonics and Eq. E.14 and the recursion relation

$$\sqrt{l_1(l_1+1)}\begin{pmatrix} l_1 & l_2 & l \\ -1 & 0 & 1 \end{pmatrix} + \sqrt{l_2(l_2+1)}\begin{pmatrix} l_1 & l_2 & l \\ 0 & -1 & 1 \end{pmatrix} = -\sqrt{l(l+1)}\begin{pmatrix} l_1 & l_2 & l \\ 0 & 0 & 0 \end{pmatrix} \tag{E.29}$$

for Wigner 3j symbols, we obtain

$$\delta A_{lm} = \frac{1}{\gamma + \eta\left[(\alpha+1)l(l+1) - 2\right]} \frac{S_{lm} + (-1)^m \bar{S}_{lm}}{2\sqrt{l(l+1)}} \tag{E.30}$$

$$\delta B_{lm} = \frac{-i}{\gamma + \eta\left[l(l+1) - 2\right]} \frac{S_{lm} - (-1)^m \bar{S}_{lm}}{2\sqrt{l(l+1)}}, \tag{E.31}$$

$$\begin{aligned} \frac{S_{lm}}{2} = \sum_{l_1,l_2,m_1,m_2} & \frac{(-1)^{m+1}\chi_{l_1m_1}\delta R_{l_2m_2}}{1/l_h^2 + (\alpha+1)l_1(l_1+1) - 2} \sqrt{\frac{(2l_1+1)(2l_2+1)(2l+1)}{4\pi}} \begin{pmatrix} l_1 & l_2 & l \\ m_1 & m_2 & m \end{pmatrix} \\ & \left\{ \left[l_2(l_2+1) - 2\right] \sqrt{l_1(l_1+1)} \begin{pmatrix} l_1 & l_2 & l \\ -1 & 0 & 1 \end{pmatrix} \right. \\ & \left. - (\alpha+1) l_1(l_1+1)\sqrt{l(l+1)} \begin{pmatrix} l_1 & l_2 & l \\ 0 & 0 & 0 \end{pmatrix} \right\} \end{aligned} \tag{E.32}$$

Using the selection rules for the Wigner 3j symbols, we have

$$S_{lm} = 0 \text{ for } (m_1 + m_2 \neq m) \vee (l > l_1 + l_1) \vee (l < |l_1 - l_2|). \tag{E.33}$$

Furthermore, all the Wigner 3-j matrices are real and we can use

$$\begin{pmatrix} l_1 & l_2 & l_3 \\ m_1 & m_2 & m_3 \end{pmatrix} = (-1)^{l_1+l_2+l_3} \begin{pmatrix} l_1 & l_2 & l_3 \\ -m_1 & -m_2 & -m_3 \end{pmatrix} \tag{E.34}$$

and Eq. E.4 together with the real-valuedness of A, B, χ to obtain

$$\bar{S}_{l,-m} = (-1)^{m_1+m_2+l_1+l_2+l} S_{lm}. \tag{E.35}$$

With this we find

$$A_{lm} = \frac{1}{\gamma + \eta\left[(\alpha+1)l(l+1) - 2\right]} \begin{cases} \frac{S_{lm}}{\sqrt{l(l+1)}}, & l_1 + l_2 + l \text{ even} \\ 0, & l_1 + l_2 + l \text{ odd} \end{cases} \tag{E.36}$$

$$\delta B_{lm} = \frac{-i}{\gamma + \eta\left[l(l+1) - 2\right]} \begin{cases} 0, & l_1 + l_2 + l \text{ even} \\ \frac{S_{lm}}{\sqrt{l(l+1)}}, & l_1 + l_2 + l \text{ odd} \end{cases} \tag{E.37}$$

We observe that for $l = 1$ δB_{lm} is only limited by friction (γ). Hence, this mode can dominate the flow field for small deformations, if the hydrodynamic length is large, i.e. $\delta R/R_0 > R_0^2/l_h^2 \ll 1$. On a sphere B_{1m} corresponds to a rigid body rotation $\delta\mathbf{\Omega}$. Identifying the rotation axis as the z axis such that $\mathbf{\Omega} = \mathbf{z}\Omega$, one has

$$\Omega = -\sqrt{\frac{3}{4\pi}} B_{1,0} \tag{E.38}$$

With this we obtain the rotation speed of the deformed sphere as

$$\delta\Omega = -\sqrt{\frac{3}{4\pi}}\delta B_{1,0} = i\frac{3}{4\pi\gamma}\sum_{l,m}(-1)^m \chi_{l,m}\delta R_{l,-m}\frac{m[l(l+1)-2)]}{(\alpha+1)l(l+1)-2}. \tag{E.39}$$

Writing the spherical harmonics coefficients in terms of an azimuthal angle and a magnitude as

$$\delta R_{lm} = |\delta R_{lm}|e^{-im\phi_{R,lm}}, \quad \delta\chi_{lm} = |\delta\chi_{lm}|e^{-im\phi_{\chi,lm}}, \tag{E.40}$$

we obtain

$$\delta\Omega = \frac{1}{\gamma}\sum_{l\geq 2, m>0}\frac{3}{2\pi}\frac{m\,[l(l+1)-2]}{(1+\alpha)l(l+1)-2}|\chi_{l,m}||\delta R_{l,m}|\sin[m(\phi_{\chi,lm}-\phi_{R,lm})]. \tag{E.41}$$

E.4.3 Chemical dynamics

In the following we consider dynamics of a single concentration field c on a deformed sphere as discussed in the main text in sections 3.2, 3.3.1.

E.4.3.1 Diffusion

Using Eq. E.25E.14, we obtain the matrix elements of the change in the Laplace Beltrami operator $\delta\Delta LB$ as

$$\begin{aligned}\int \mathrm{d}\Omega Y^*_{l_1m_1}\delta\Delta_{LB}Y_{l_2m_2} &= 2l_2(l_2+1)\int \mathrm{d}\Omega Y *_{l_1m_1}\delta\frac{\delta R}{R}\Delta Y_{l_2m_2}\\ &= 2l_2(l_2+1)\sum_{lm}\frac{\delta R_{lm}}{R}(-1)^{m_1}\sqrt{\frac{(2l_1+1)(2l+1)(2l_2+1)}{4\pi}}\\ &\qquad \begin{pmatrix} l_1 & l & l_2\\ -m_1 & m & m_2\end{pmatrix}\begin{pmatrix} l_1 & l & l_2\\ 0 & 0 & 0\end{pmatrix}\end{aligned} \tag{E.42}$$

Only summands with $m_1 = m + m + 2$ are non-zero. Here, we restrict ourselves to axisymmetric deformations. Choosing $\mathbf{z}$ as the axis of symmetry implies $\delta R_{lm} = 0$ for $m \neq 0$ and hence,

$$\int \mathrm{d}\Omega Y^*_{l_1m_1}\delta\Delta_{LB}Y_{l_2m_2} = \delta_{m_1,m_2}\cdots \tag{E.43}$$

In other words, $\delta\Delta_{LB}$ is diagonal when restricted to an eigenspace of Δ_{LB} on the undeformed sphere. This allows us to calculate eigenstates and eigenvalues of Δ'_{LB} in first order of $\delta R/R$ as

$$\lambda'_{lm} = -\,l(l+1) + \langle l,m|\,\delta\Delta_{LB}\,|l,m\rangle \tag{E.44}$$

$$Y'_{lm} = Y_{lm} + \sum_{l'\neq l}\frac{\langle l',m|\,\delta\Delta_{LB}\,|l,m\rangle}{l'(l'+1)+l(l+1)}Y_{l'm}, \tag{E.45}$$

where

$$\begin{aligned}\langle l', m| \delta\Delta |l, m\rangle &:= \int \mathrm{d}\Omega Y^*_{l'm} \delta\Delta_{LB} Y_{lm} \\ &= 2l(l+1) \sum_{l_2} \frac{\delta R_{l_2}}{R} (-1)^m \sqrt{\frac{(2l_1+1)(2l+1)(2l'+1)}{4\pi}} \\ &\qquad \begin{pmatrix} l' & l_2 & l \\ -m & m_2 & m \end{pmatrix} \begin{pmatrix} l' & l_2 & l \\ 0 & 0 & 0 \end{pmatrix}\end{aligned} \tag{E.46}$$

The dynamics of the concentration field are then given by

$$c = \sum_{lm} c_{lm} Y'_{lm} e^{D\lambda'_{lm} t} \tag{E.47}$$

For small l_2, the expressions simplify. For example for

$$\delta R = \delta R_2 Y_{20}, \tag{E.48}$$

the eigenvalues becomes

$$\lambda'_{lm} = -l(l+1) \left[1 - \frac{\delta R_2}{R} \sqrt{\frac{5}{\pi}} \frac{l(l+1) - 3m^2}{4l(l+1) - 3} \right] \tag{E.49}$$

We observe that for stretching along $\mathbf{z}$ (i.e. $\delta R_2 > 0$), modes with larger $|m|$ decay faster.

E.4.3.2 Linear stability of an active isotropic fluid

Using a Hodge decomposition of the flow field, with A denoting the irrotational component, Eq. 1.53 for a small deviation δc from the homogeneous state reads

$$\partial_t \delta c = \Delta_{LB}(D\delta c - c_0 \delta A), \tag{E.50}$$

where

$$\delta A_{lm} = M_{lm} \delta c_{lm} + \sum_{l'm'} \delta M^{lm}_{l'm'} \delta c_{l'm'} \tag{E.51}$$

This is solved by

$$c = \sum_{lm} c_{lm} Y'_{lm} e^{\lambda'_{lm} t} \tag{E.52}$$

The eigenvalues change upon deformation of the sphere as

$$\delta\lambda_{lm} = -\frac{\lambda_{lm}}{l(l+1)} \langle lm| \delta\Delta |lm\rangle + l(l+1) c_0 \delta M^{lm}_{lm}, \tag{E.53}$$

where using Eq. E.32, we obtain

$$\delta M_{lm}^{lm} = \sum_{l_2,m_2} \frac{(-1)^{m+1}\left[1+(-1)^{2l+l_2}\right]\chi'(c_0)\eta\delta R_{l_2m_2}}{[1/l_h^2+(\alpha+1)l_1(l_1+1)-2]^2}\sqrt{\frac{(2l+1)^2(2l_2+1)}{4\pi}}\begin{pmatrix} l & l_2 & l \\ m & m_2 & -m \end{pmatrix}$$
$$\left\{[l_2(l_2+1)-2]\begin{pmatrix} l & l_2 & l \\ -1 & 0 & 1 \end{pmatrix} - (\alpha+1)l(l+1)\begin{pmatrix} l & l_2 & l \\ 0 & 0 & 0 \end{pmatrix}\right\} \tag{E.54}$$

For

$$\delta R = \delta R_2 Y_{20}, \tag{E.55}$$

the eigenvalues become

$$\delta\lambda_{lm} = \frac{l(l+1)-3m^2}{4l(l+1)-3}\delta R_2\sqrt{\frac{5}{\pi}}\left[Dl(l+1) + \frac{c_0\chi'(c_0)\left[6\eta(l-1)(l+2)-\gamma l(l+1)\right]}{\left[\gamma+\eta\left((\nu+1)l(l+1)-2\right)\right]^2}\right] \tag{E.56}$$

Appendix F

A pseudo-spectral method for the simulation of active fluid films

In the following, we describe a numerical method for calculating the flow field and simulate the dynamics of a fluid film with spherical or toroidal topology and otherwise arbitrary surface geometry. In this method, we adopt the Newman-Penrose formalism (see section 1.3.1). This means that all vector and tensor fields are represented by complex valued fields, so called spin-weighted fields. Furthermore, we use a spectral decomposition of the fields to calculate derivatives on a reference surface. To calculate products of fields, a grid in real space is used. We use this method in chapters 3 and 4 to simulate the dynamics of active isotropic fluid films. In chapter 5, we use it also to calculate the flow field of a chiral active fluid film.

F.1 General algorithm

For any surface we define a complex basis vector $\mathbf{Z}$. This allows us to understand all vector and tensor fields as complex-valued spin-weighted fields. The algorithm relies entirely on this spin-weighted representation. Only for calculating $\mathbf{Z}$ and the spin connection Γ for a given surface $\mathbf{X}$, we make use three-dimensional vector representation.

The algorithm for simulating an active fluid film can be summed up as follows:

$$\text{Calculate static quantities of surface geometry.} \tag{F.1}$$

$$\text{Calculate matrix representation } M_{ij} \text{ of viscous force.} \tag{F.2}$$

$$\text{Invert } M_{ij}. \tag{F.3}$$

$$\text{Integrate } \partial_t c \text{ using Runge-Kutta algorithm.} \tag{F.4}$$

For a definition of M_{ij} see the next section. For integration $\partial_t c$ we use the spectral representation of c. Calculating $\partial_t c$ for a given c amounts to the following steps:

$$\text{Calculate the active force } f_{\text{act}} \text{ from } c. \tag{F.5}$$

$$\text{Calculate flow field } {}_{(1)}v \text{ from } f_{\text{act}} \text{ using } M_{ij}^{-1}. \tag{F.6}$$

$$\text{Calculate } \partial_t c \text{ from } c \text{ and } {}_{(1)}v \text{ as given in Eq. 1.53.} \tag{F.7}$$

For surfaces with spherical topology, the code was implemented in C and the inverse of M_{ij} as well as the matrix vector product in Eq. F.13 were calculated on a GPU using the Nvidia Cuda library [204]. For surfaces with toroidal topology, the code was implemented in MATLAB.

F.2 Solving the flow field using spectral decomposition

We represent all spin-weighted fields in terms of a spectral decomposition and in terms of its values on a real space grid. Consider for example, a spin-weighted field ${}_{(s)}f$. We denote its value on grid point $i \in [0, N_{\text{grid}} - 1]$ with complex coordinate z_i as ${}_{(s)}f_i$. Furthermore, we denote the projection on the j^{th} eigenfunction ${}_{(s)}Y_j$ with $j \in [0, N_S - 1]$ as $({}_{(s)}f)_j^S$. Spectral and real space representation of ${}_{(s)}f$ are related by synthesis

$$ {}_{(s)}f_i = \sum_{j=0}^{N_S-1} ({}_{(s)}f)_j^S \, {}_{(s)}Y_j(z_i). \tag{F.8}$$

Calculating the spectral space representation $({}_{(s)}f)_j^S$ from the real space grid values ${}_{(s)}f_i$ amounts to a linear transformation, e.g. a Fourier transformation. In the next section, we give an explicit formula for spherical harmonics transformation. There we give also formulas for numerical approximations of the spin-raising and lowering operators ð, $\bar{ð}$.

With these, we can calculate the viscous and friction force for a given velocity:

$$ {}_{(1)}f_{\text{visc}} = \eta \bar{ð} ð \, {}_{(1)}v + \alpha \eta ð \, \text{Re}[\bar{ð} \, {}_{(1)}v] - \gamma \, {}_{(1)}v. \tag{F.9}$$

We calculate numerically the viscous force for all eigenfunctions ${}_{(1)}Y_j$:

$$ {}_{(1)}f_{\text{visc}}[{}_{(1)}Y_j] = \eta \bar{ð} ð \, {}_{(1)}Y_j + \alpha \eta ð \, \text{Re}[\bar{ð} \, {}_{(1)}v] - \gamma \, {}_{(1)}Y_j. \tag{F.10}$$

The spectral decomposition of the viscous force defines the following matrix

$$ M_{ij} := ({}_{(1)}f_{\text{visc}}[{}_{(1)}Y_j])_i^S. \tag{F.11}$$

Solving the force balance equation for a given active force ${}_{(1)}f_{\text{act}}$ (see right hand side of Eq. 1.69 and Eq. 5.15), amounts to solving

$$ {}_{(1)}f_{\text{visc}} = - \, {}_{(1)}f_{\text{act}} \tag{F.12}$$

To this end, we invert M_{ij} numerically. Then the spectral representation of the flow field is given by

$$({}_{(1)}v)^S_i = -\sum_{j=0}^{N_S-1} (M^{-1})_{ij} ({}_{(1)}f_{\text{act}})^S_j. \tag{F.13}$$

F.3 Surfaces with spherical topology

We parameterize a surface with spherical topology as $\mathbf{X}(\theta, \phi)$, where θ and ϕ are spherical coordinates. We use a rectangular grid of size $N_{\text{ring}}\text{x}N_\phi$, such that rings with constant θ correspond to rows of the grid. We use a grid such that at the first ring we have $\theta_{0,i} = \pi/(2N_{\text{ring}})$ and at the last ring $\theta_{N_{\text{ring}}-1,i} = \pi - \pi/(2N_{\text{ring}})$. So, there are no grid points at the poles. For all the simulations, we used $N_{\text{ring}} = 60$, $N_\phi = 120$ yielding $N_{\text{grid}} = 7200$.

We decompose fields into spin-weighted spherical harmonics (see appendix E). Calculating the spherical harmonics representation of a field ${}_{(s)}f$ amounts to a projection in the sense of an integral (Eq. E.12). We use `libsharp2`, a C library, to calculate these projections numerically [205]. There the integral is approximated by the sum

$$({}_{(s)}f)^S_{lm} = \sum_{i=0}^{N_{\text{ring}}-1} \sum_{j=0}^{N_\phi-1} w_i \, {}_{(s)}f_{i,j} \, {}_{(s)}\bar{Y}_{lm}(\theta_i, \phi_j), \tag{F.14}$$

where w_i are quadrature weights of the rings. We use here Fejér's first quadrature rule for these weights[205]. In contrast to a Fourier transform, the spherical harmonics transform requires a greater number of points in real space than in spectral space to yield accurate results. For all the simulations, we used a maximal l value l_{max} yielding $N_s = l_{\text{max}}^2 = 2601$.

Note that `libsharp` uses a different sign convention for the spin-weighted spherical harmonics. Furthermore, it represents spherical harmonics components for $s \neq 0$ in terms of a rotational and an irrotational component, from which calculate the resulting spherical harmonics components (see [205] for details).

From the spherical harmonics transform, derivatives on the (unit) sphere can be calculated using Eq. E.6. We denote these operators on reference surface that is the unit sphere as $\eth_r$. Applied to a scalar field c, they yield the partial derivatives as

$$\eth_r c = \partial_\theta c + \frac{i}{\sin\theta}\partial_\phi c. \tag{F.15}$$

With this we calculate the covariant vectors $\mathbf{e}_i = \partial_i \mathbf{X}$ of the deformed sphere. We use a convention such that the real component of $\mathbf{Z}$ points in the direction of the covariant basis vector $\mathbf{e}_\theta$, i.e.

$$\mathbf{Z} = \frac{\mathbf{e}_\theta}{|\mathbf{e}_\theta|} + \frac{i}{|\mathbf{e}_\theta|}\mathbf{n} \times \mathbf{e}_\theta \text{ with } \mathbf{n} = \frac{\mathbf{e}_\theta \times \mathbf{e}_\phi}{|\mathbf{e}_\theta \times \mathbf{e}_\phi|}, \tag{F.16}$$

where we calculate products and non-linear terms on the real-space grid.

The derivative (i.e. $\eth, \bar{\eth}$) of a scalar field can be written as a linear combination of ∂_θ and ∂_ϕ and thus $\eth_r$ and $\bar{\eth}_r$. To this end, we calculate numerically the following factors

$$D_0 = \mathbf{Z} \cdot \bar{\eth}_r \mathbf{X}, \quad D_2 = \mathbf{Z} \cdot \eth_r \mathbf{X}. \tag{F.17}$$

Using Eq. 1.63, we find that the derivative operators on the deformed sphere can be written as

$$\eth\, {}_{(0)}f = \frac{2}{|D_0|^2 - |D_2|^2} \left[D_0 \eth_r\, {}_{(0)}f - D_2 \bar{\eth}_r\, {}_{(0)}f \right] \tag{F.18}$$

$$\bar{\eth}\, {}_{(0)}f = \frac{2}{|D_0|^2 - |D_2|^2} \left[\bar{D}_0 \bar{\eth}_r\, {}_{(0)}f - \bar{D}_2 \eth_r\, {}_{(0)}f \right] \tag{F.19}$$

With this, we can calculate the spin connection Γ as defined in Eq. 1.62. However, $\mathbf{Z}$ is ill-behaved at the poles of the grid. Therefore, we calculate it instead as

$$\Gamma = \mathbf{Z} \cdot \left[\eth \left(\mathbf{Z} - \mathbf{Z}_r \right) + D_0 \left(\Gamma_r \bar{\mathbf{Z}}_r - 4 \mathbf{n}_r \right) - D_2 \bar{\Gamma}_r \bar{\mathbf{Z}}_r \right], \tag{F.20}$$

which we derived using Eq. D.8. r-subscripts denote quantities on the unit sphere. In particular $\mathbf{Z}_r = \boldsymbol{\theta} + i\boldsymbol{\phi}$ and $\Gamma_r = -1/\tan(\theta)$, With this we calculate

$$\Delta\Gamma = \Gamma - \frac{2}{|D_0|^2 - |D_2|^2} \left[D_0 \eth_r \Gamma - D_2 \bar{\eth}_r \bar{\Gamma} \right]. \tag{F.21}$$

With this we can calculate the derivatives of general spin fields as

$$\eth\, {}_{(0)}f = \frac{2}{|D_0|^2 - |D_2|^2} \left[D_0 \eth_r\, {}_{(s)}f - D_2 \bar{\eth}_r\, {}_{(s)}f \right] + s \Delta\Gamma\, {}_{(s)}f \tag{F.22}$$

$$\bar{\eth}\, {}_{(0)}f = \frac{2}{|D_0|^2 - |D_2|^2} \left[\bar{D}_0 \bar{\eth}_r\, {}_{(s)}f - \bar{D}_2 \eth_r\, {}_{(s)}f \right] - s \overline{\Delta\Gamma}\, {}_{(s)}f, \tag{F.23}$$

where we again calculate $\eth_r, \bar{\eth}_r$ using the spectral representation of a field ${}_{(s)}f$, whereas products are calculated on the real-space grid.

F.4 Surfaces with toroidal topology

We parametrize surfaces with toroidal topology as $\mathbf{X}(x, y)$. We use a We use an isothermal parametrization. In particular, we consider a torus parametrized as

$$\mathbf{X}(x, y) = \frac{R_2 \sinh(\rho)}{\cos[\sinh(\rho) x] - \cosh(\rho)} \left(\sinh(\rho) \cos(y), \sinh(\rho) \sin(y), \sin[\sinh(\rho) x] \right)^T, \tag{F.24}$$

where $\cosh(\rho) = R_1/R_2$ and R_1,R_2 are the radii of the torus. Note that x corresponds to the poloidal angle up to a rescaling by $\sinh(\rho)$. For $\sinh(\rho) = 1$, corresponding to $R_2 \sim 0.7 R_1$, we can cover the entire torus with a square grid of equal size in x and y. We consider such a geometry in the simulation in section 4.1.1 using a 42x42 grid.

As we consider an isothermal parametrization, we have a metric $g_{ij} = l^2\delta_{ij}$. The length scale l is given by

$$l = \frac{R_2 \sinh(\rho)^2}{\cos[\sinh(\rho)x] - \cosh(\rho)}. \tag{F.25}$$

Furthermore, we have

$$\kappa = \frac{\cosh(\rho)\cos[\sinh(\rho)x] - 1]}{(R_2 \sinh(\rho))^2}. \tag{F.26}$$

We use

$$\mathbf{Z} = \frac{1}{l}\left(\partial_x \mathbf{X} + i\partial_y \mathbf{X}\right). \tag{F.27}$$

With this we can calculate $\eth, \bar{\eth}$ using Eq. 1.73. To calculate the partial derivatives, we decompose all fields in terms of a Fourier series using the discrete two-dimensional Fourier transform, as implemented in MATLAB [206]. Then we have

$$(\partial_{\bar{z}}\, {}_{(s)}f)^S_j = \frac{k_j}{2}({}_{(s)}f)^S_j, \quad (\partial_z\, {}_{(s)}f)^S_j = \frac{\bar{k}_j}{2}({}_{(s)}f)^S_j, \tag{F.28}$$

where $k_j = k_{x,j} + ik_{y,j}$ is the complex wave vector of a Fourier mode that we can write as

$$Y_j(z, \bar{z}) = e^{i(k_j \bar{z} + \bar{k}_j z)/2}. \tag{F.29}$$

Analogous to the spherical case we calculate $\eth, \bar{\eth}$ by calculating the Wirtinger in spectral space and the products in Eq. 1.73 in real space.

Appendix G

A staggered-grid method for spin-weighted fields

In the following, we briefly describe a staggered-grid method to calculate the flow field of a curved fluid film. We find that this better suited than spectral methods for calculating the flow fields around cracks and stress multipoles, in particular when using an isothermal parametrization. We use the Newman-Penrose formalism (see section 1.3.1), i.e. all vector and tensor fields are represented as complex valued fields, so called spin-weighted fields.

G.1 Staggered-grid

When using a staggered grid, different fields are evaluated on distinct grids that are shifted with respect to each other. Here we evaluate different spin-weighted fields on grids according to their spin-weight. We use a basis grid in terms of the coordinates x, y such that rows of the grid correspond to lines with $y = \text{const.}$. Denoting rows and columns on the fine basis grid as i and j, we use the following convention for the staggered grids:

$$\mathrm{Re}[{}_{(s)}f],\ s \text{ even}: \quad i \text{ even},\ j \text{ even} \tag{G.1}$$

$$\mathrm{Im}[{}_{(s)}f],\ s \text{ even}: \quad i \text{ odd},\ j \text{ odd} \tag{G.2}$$

$$\mathrm{Re}[{}_{(s)}f],\ s \text{ odd}: \quad i \text{ even},\ j \text{ odd} \tag{G.3}$$

$$\mathrm{Im}[{}_{(s)}f],\ s \text{ odd}: \quad i \text{ odd},\ j \text{ even} \tag{G.4}$$

When calculating products of spin-weighted fields, we use linear interpolation. When the factors are on the same grid, we evaluate the product on this grid and use linear interpolation to evaluate the field on the grid of the product. Otherwise, we evaluate the factors on the grid of the product.

G.2 Numerical derivatives

We consider a surface parametrized as $\mathbf{X}(x,y)$ that is defined on the fine basis grid. In particular we consider in chapter 4.a torus as parametrized in F.24. In Fig. J.2, we use $\rho = \text{asinh}(1)$ and a grid of size 162x162. In Fig. 4.2, we use $\rho = \text{asinh}(2)$ and a grid of size 192x384. On the fine grid, we use finite differences to calculate derivatives of $\mathbf{X}$ and thus the covariant vectors $\mathbf{e}_i$. We define $\mathbf{Z}$ as

$$\mathbf{Z} = \frac{\mathbf{e}_x}{|\mathbf{e}_x|} + \frac{i}{|\mathbf{e}_x|}\mathbf{n} \times \mathbf{e}_x \text{ with } \mathbf{n} = \frac{\mathbf{e}_x \times \mathbf{e}_y}{|\mathbf{e}_x \times \mathbf{e}_y|}, \tag{G.5}$$

From this we calculate Γ using Eq. 1.62, again using finite differences on the fine grid. Furthermore, we calculate the metric g_{ij} and with this the covariant components Z^i.

To calculate numerical derivatives of the physical fields, we make use of the staggered grid. We calculate partial derivatives by evaluating finite differences on the intermediate grid points. Then we use Eq. 1.60, 1.61 to calculate $\eth, \bar{\eth}$. As described above, we use linear interpolation to calculate products.

G.3 Flow field around force multipole

To calculate flow fields on a closed surface for a density of active forces ${}_{(1)}f_{\text{act}}$, we calculate a matrix representation of the viscous and friction forces as in appendix Eq. F.11. In contrast to appendix F, however, we do not use a decomposition in terms of a spectrum of the Laplace-Beltrami operator. Instead, we decompose the flow field in terms of the real space grid, corresponding to

$$Y_j(z_i) = \delta_{ij}. \tag{G.6}$$

To approximate the flow field around a force force monopole at z_i, we consider

$${}_{(1)}f_{\text{act}}(z_j) = \frac{{}_{(1)}F\delta_{ij}}{\Delta x \Delta y \sqrt{g(z_i)}}, \tag{G.7}$$

where $\Delta x, \Delta y$ are x and y resolutions of the grid. ${}_{(1)}F \in \{1, i\}$ is the force of the force monopole, which we consider to be purely real or imaginary, as the grid points of real and imaginary parts of ${}_{(1)}f_{\text{act}}$ are distinct. Similarly, we define the active tension field χ_{mono} tension monopole, from which we calculate numerically ${}_{(1)}f_{\text{act}} = \eth\chi_{\text{mono}}$.

G.4 Numerical Hodge decomposition

We want to decompose the numerical flow field as a Hodge decomposition

$${}_{(1)}v = \eth(A + iB) + {}_{(1)}v_h, \tag{G.8}$$

where $A, B \in \mathbb{R}$. Applying the $\bar{\eth}$ operator yields

$$\bar{\eth}\,{}_{(1)}v = \Delta_{LB}(A + iB) + \bar{\eth}\,{}_{(1)}v_h, \tag{G.9}$$

where $\bar{\eth}\,{}_{(1)}v_h$ is constant. We use the staggered grid to calculate $\bar{\eth}\,{}_{(1)}v$ numerically. Using linear interpolation, we determine $\bar{\eth}\,{}_{(1)}v$ on the fine basis grid. To invert this equation we make use of Eq. 1.72. Furthermore, we use the Discrete Fourier transform (DFT) on the fine grid to invert the Laplace operator

$$A + iB = \mathrm{DFT}^{-1}\left[\frac{1}{|k|^2}\mathrm{DFT}[l^2\bar{\eth}\,{}_{(1)}v]\right], \tag{G.10}$$

where k is the complex wave vector (see section F.4) and l is the length scale associated with the isothermal parametrisation (Eq. F.25). On a torus the harmonic flow field can be written as

$${}_{(1)}v_h = {}_{(1)}V_h l, \tag{G.11}$$

where ${}_{(1)}V_h = \text{const.}$. This allows us to calculate the harmonic flow field numerically as

$${}_{(1)}v_h = \frac{1}{l}P_{k=0}[l\,{}_{(1)}v], \tag{G.12}$$

where $P_{k=0}$ denotes the projection onto the constant component, which we calculate using DFT.

G.5 Solving crack boundary conditions

To solve boundary conditions, we use a logarithmic grid, i.e. we consider

$$\mathbf{X}(x, y) = (-\exp(x)\sin(x), \exp(x)\cos(x), 0)^T, \tag{G.13}$$

where $x \in [\log a, \log R]$ and $y \in [-\pi, \pi]$. We use a square grid in terms of x and y of size 512x512. As before, we calculate the matrix M_{ij} that yields the viscous force at position i due to a velocity at j. We use this to solve velocity boundary conditions. To this end, we denote the set of indices that are enclosed by the boundary at I, whereas the set of boundary indices is denoted as B. We consider a homogeneous fluid inside the boundary such that the viscous force has to vanish. With this, we find we can calculate the enclosed flow field ${}_{(1)}v$ resulting from a boundary velocity ${}_{(1)}v_B$ as

$${}_{(1)}v_i = \sum_j -(M_{I,I}^{-1}M_{I,B})_{i,j}\,{}_{(1)}v_{B,j}. \tag{G.14}$$

From this, we calculate a matrix $M_{F,V}$ that gives the boundary force resulting from a boundary velocity. With this force and mixed boundary conditions can be written as a linear equation for the boundary velocities. Solving this equation allows to calculate the flow field from the velocity boundary equation as given above.

Appendix H

Deformation response of active flow

In the following, we calculate the functional derivative of the Green's functions with respect a variation $\delta\varphi$ of the geometric potential, corresponding to a deformation of the surface (see section 4.2.2). Thereby, we will gain some general insight into how the surface geometry of an active fluid film shapes the flow field that active stresses or forces generate.

H.1 For flows limited by shear viscosity

We start by considering the case of vanishing bulk viscosity. Thereby, the tangential force balance equation of a fluid film driven by a force pattern ${}_{(1)}f$ simplifies to

$$(\eta\bar{\eth}\eth - \gamma)\,{}_{(1)}v = -\,{}_{(1)}f. \tag{H.1}$$

We observe that the complex field ${}_{(1)}v$ is linear in ${}_{(1)}f$, i.e. the equation is invariant under a rotation $e^{i\psi}$ of force and velocity field. In this sense, ${}_{(1)}v$ is independent of ${}_{(-1)}f$, implying $G_2 = 0 = {}_{(1,0,1)}K$. Upon a deformation $\delta\varphi$ the differential operators change as

$$\delta\eth\,{}_{(s)}X = (s-1)\delta\varphi\eth\,{}_{(s)}X - s\eth(\delta\varphi\,{}_{(s)}X), \quad \delta\bar{\eth}\,{}_{(s)}X = -(1+s)\delta\varphi\bar{\eth}\,{}_{(s)}X + s\bar{\eth}(\delta\varphi\,{}_{(s)}X), \tag{H.2}$$

where ${}_{(s)}X$ is some spin field and we made use of Eq. 1.73. This gives rise to a change in the viscous force $\delta\,{}_{(1)}f_{\text{visc}}$ given by

$$\frac{1}{\eta}\delta\,{}_{(1)}f_{\text{visc}} = \delta(\bar{\eth}\eth)\,{}_{(1)}v = -3\delta\varphi\bar{\eth}\eth\,{}_{(1)}v - \bar{\eth}\eth(\delta\varphi\,{}_{(1)}v) + 2\bar{\eth}(\delta\varphi\eth\,{}_{(1)}v) \tag{H.3}$$

Using Eq. 4.16, we can calculate the change in the flow field that results from this force and express the velocity field in terms of the force field. We consider a closed surface and use partial integration to make use of Eq. 4.17. Thereby we obtain the kernel

$$
\begin{aligned}
{}_{(1,0,-1)}K = \frac{\delta\,{}_{(1)}v(z_v)}{\delta\varphi(z)\delta\,{}_{(1)}f(z_f)} =& -4\gamma G_0(z,z_f)\bar{G}_0(z,z_v) - 2\eta(\eth G_0(z,z_f))(\bar{\eth}\bar{G}_0(z,z_v)) \\
&+ 3\bar{G}_0(z,z_v)\delta_{z_f,z} + G_0(z,z_f)\delta_{z_v,z}. \qquad \text{(H.4)}
\end{aligned}
$$

The first two terms comprise a hydrodynamic coupling to the geometry, in the sense that they are non-vanishing for $z_v \neq z \neq z_f$, i.e. the flow field at z_v driven by a force at z_f changes upon a deformation $\delta\varphi$, even if $\delta\varphi$ vanishes in a neighborhood around z_v and z_f. They can be understood as an effective change in friction in shear viscosity given by

$$
\delta\gamma = 4\gamma\delta\varphi, \quad \delta\eta = 2\eta\delta\varphi \qquad \text{(H.5)}
$$

that results from the deformation $\delta\varphi$. We observe that an expansion of surface area ($\delta\varphi > 0$) gives rise to an effective increase in friction and shear viscosity. Thus, we may say that an expansion adds resistance against flow, due to shear viscosity. In particular, we find that

$$
\left.\frac{\delta\,{}_{(1)}v(z_v)}{\delta\varphi(z)\delta\,{}_{(1)}f(z_f)}\right|_{z_v=z_f} = -4\gamma|G_0(z,z_f)|^2 - 2\eta|\eth G_0(z,z_f)|^2 \leq 0. \qquad \text{(H.6)}
$$

with equality restricted to a set of points, when the surface and thereby G_0 is smooth. This means that a localized expansion of surface area away from a point force that is exerted on the fluid film yields a change in the flow field at this point with a direction opposite to the force. The strength of this coupling to the geometry scales with $|G_0(z,z_f)|^2$ and hence the distance between the points z and z_f relative to the hydrodynamic length. This inequality is of particular interest to active fluids, where the flow field driven by a pattern of active stresses feeds back on the pattern dynamics. When active stress regulators are localized to a small patch as observed for the isotropic active fluid model in the previous chapter, the pattern dynamics are dominated by the flow field within this patch. Importantly, the change in the flow field $\delta\,{}_{(1)}v$ is smooth at $z_f = z_v$, when $\delta\varphi(z_f) = 0$. Hence, the inequality in H.6 implies that for almost any points z and z_f in a smooth surface and $z \neq z_f$, there exists an open neighborhood $U_\varepsilon(z_f)$ such that

$$
\forall z_v \in U_{\varepsilon(z_f)}: \ \mathrm{Re}\left[\frac{\delta\,{}_{(1)}v(z_v)}{\delta\varphi(z)\delta\,{}_{(1)}f(z_f)}\right] < 0 \qquad \text{(H.7)}
$$

For a global deformation of the surface (i.e. $\varphi(z_v), \varphi(z_f) \neq 0$), also the local terms in Eq. H.4 have to be taken into account. However, we can always rescale the reference surface such that $\delta\varphi(z_f) = 0$, whereby Eq. H.6 still holds. In this sense, we may say that a deformation that corresponds to an expansion of the surface relative to a reference point, adds resistance against flow at this reference point. Since the inequality in Eq. H.6 holds for any surface geometry, it holds also for a finite deformation as defined in Eq. 4.22 as long as $\varphi'(z_f) - \varphi_0(z_f) = 0$. In other words, Eq. H.6 provides insight that goes far beyond a linear order calculation.

For a global deformation of the surface, it is informative to rewrite the differential in terms of the Gaussian curvature. Using Liouville's equation (Eq. 1.71, we find

$$\begin{aligned}\frac{\delta\,{}_{(1)}v(z_v)}{\delta\varphi(z)\delta\,{}_{(1)}f(z_f)} =& + 2\eta G_0(z,z_f)\bar{G}_0(z,z_v)\frac{\delta\kappa}{\delta\varphi} + 2\eta(\bar{\eth} G_0(z,z_f))(\eth\bar{G}_0(z,z_v)) \\ &+ \bar{G}_0(z,z_v)\delta^{(2)}(z_f,z) - G_0(z,z_f)\delta^{(2)}(z_v,z),\end{aligned} \tag{H.8}$$

Importantly, the local terms vanish for $z_f = z_v$. Expaning $\delta\varphi$ in eigenmodes Y_k of the Laplace Beltrami operator with eigenvalues $-\lambda_k$ (see section 3.2) as $\delta\varphi = \sum_k \delta\varphi_k Y_k$, we have

$$\delta\kappa = 2\delta\varphi\kappa + \sum_k \lambda_k \delta\varphi_k Y_k. \tag{H.9}$$

Thus, we have $\delta\varphi/\delta\kappa > 0$, when $\delta\varphi$ is given by single mode and $\kappa > 0$. This applies to deformations of the sphere we considered in chapter 3.

H.1.1 Deformation response for a density of active tension

We are particularly interested, how the geometry-dependence of the flow field shapes patterns in an active isotropic fluid film (see chapter 3 and sections 4.1 and 4.4). In this case the force density is given by

$${}_{(1)}f = \eth\chi = e^{-\varphi}\eth\chi, \tag{H.10}$$

where χ is the density of active tension. Let us consider a deformation, whereby the tension density changes as $\delta\chi = -2\delta\varphi$ due to dilution. Thus, the force changes as

$$\delta\,{}_{(1)}f = -3\delta\varphi\eth\chi - 2\varphi\chi\eth\delta\varphi. \tag{H.11}$$

The first summand corresponds to a simple rescaling of the force. The second summand however yields a force density proportional to the gradient of $\delta\varphi$. With this we calculate the change in the velocity field due to the deformation using Eq. H.4, which yields

$$\begin{aligned}\delta\,{}_{(1)}v = -\int \mathrm{d}S_0 \Big\{ \chi(z_0) \int \mathrm{d}S\, \delta\varphi(z)\eth_{z_0} K_{\mathrm{hyd}}(z_v,z,z_0) \\ + 2G(z,z_0)\eth_{z_0}\delta\varphi(z_0)\Big\} + \delta\varphi\,{}_{(1)}v,\end{aligned} \tag{H.12}$$

where the hydrodynamic kernel is given by

$$K_{\mathrm{hyd}}(z_v,z,z_0) = -4\gamma G_0(z,z_0)\bar{G}_0(z,z_v) - 2\eta(\eth G_0(z,z_0))(\bar{\eth}\bar{G}_0(z,z_v)) \tag{H.13}$$

as in Eq. H.4. This hydrodynamic interaction yields an attraction of contractile points to maxima in φ in the distance, resulting from the effective increase in friction and viscosity. The term proportional to $\eth\delta\varphi$, in contrast, is an effective force density pointing down the gradient of $\delta\varphi$.

In a flat surface we have $G_0(z, z_0) = G_0(|z - z_0|)$ and thus $\eth_{z_0} G_0(z, z_0) = -\eth G_0(z, z_0)$ and $G_0 = \bar{G}_0$. With this we evaluate the change in velocity $\delta\, {}_{(1)}v$ upon a deformation $\delta\varphi$ at a distance to a tension monopole at z_0. We find

$$\delta\, {}_{(1)}v(z_0) = \frac{T}{2} \int \mathrm{d}S_1\, \delta\varphi(z_1) \eth_z 0 | K_{\mathrm{hyd}}(z_0, z_1, z_0). \tag{H.14}$$

H.2 For flows limited by bulk viscosity

In analogy to the previous section, we consider the case of vanishing shear viscosity, corresponding to the limit $\alpha \to \infty$ with $l_h^2/\alpha = \alpha\eta/\gamma =$ const.. Then, the tangential force balance equation can be written as

$$\eth\, {}_{(0)}P + \gamma\, {}_{(1)}v = {}_{(1)}f, \tag{H.15}$$

where

$${}_{(0)}P = -\eta_b \,\mathrm{Re}[\bar{\eth}\, {}_{(1)}v] \tag{H.16}$$

is the pressure due to bulk viscosity η_b. Eq. H.15 can be solved in terms of the Green's function as defined in Eq. 4.16-4.18. Note that both Green's functions G_0 and G_2 are in this case non-vanishing in contrast to the previous section. Additionally, we define a propagator of the pressure, i.e.

$$G_P(z, z') = {}_{(0,-1)}G_P(z, z') = -\frac{\eta_b}{2} \left(\bar{\eth} G_0(z, z') + \eth \overline{G}_2(z, z') \right), \tag{H.17}$$

with all derivatives acting with respect to z. Thereby, $G_P(z, z_f)\, {}_{(1)}F + G_P(z, z_f)\, {}_{(-1)}F$ yields the pressure at coordinate z that results from the flow driven by a force ${}_{(1)}F$ at z_f. Notably, its complex conjugate $\overline{G}_P(z_0, z_v)$ corresponds to the velocity at z_v that results from a force density ${}_{(1)}f(z) = \eth\delta_{z,z_0}/2$, i.e. a contractility monopole at z_0.

Analogously to the previous section, we calculate the change in the flow field from the change in viscous forces that results from a deformation $\delta\varphi$. Due to G_2, we have to calculate two kernels: ${}_{(1,0,1)}K$ as well as ${}_{(1,0,-1)}K$, as the flow field depends on the orientation of the force with respect to the surface geometry. On a closed surface, we find that they can be written as

$${}_{(1,0,-1)}K = \frac{\delta\, {}_{(1)}v(z_v)}{\delta\varphi(z)\delta\, {}_{(1)}f(z_f)} = \frac{4}{\eta_b} G_P(z, z_f) \overline{G}_P(z, z_v) + \bar{G}_0(z, z_v)\delta_{z_f, z} - G_0(z, z_f)\delta_{z_v, z}, \tag{H.18}$$

$${}_{(1,0,1)}K = \frac{\delta\, {}_{(-1)}v(z_v)}{\delta\varphi(z)\delta\, {}_{(1)}f(z_f)} = \frac{4}{\eta_b} \overline{G}_P(z, z_f) \overline{G}_P(z, z_v) + G_2(z, z_v)\delta_{z_f, z} - G_2(z, z_f)\delta_{z_v, z}, \tag{H.19}$$

We observe that the hydrodynamic terms, i.e. the first summand in Eq. H.18 and H.19, respectively, yield a change in the flow field that results from a change in pressure

$$\delta P = -2P\delta\varphi, \tag{H.20}$$

or equivalently a change in bulk viscosity $\delta\eta_b = -2\eta_b\delta\varphi$. We may thus say, that a surface expansion ($\delta\varphi > 0$) locally relaxes the pressure from bulk viscosity. This implies that a deformation $\delta\varphi$ that is limited to points, where the pressure vanishes, does not change the flow field away from the site of the deformation.

In analogy to Eq. H.6, we want to derive how the flow field changes at the point where it is driven. To understand how the flow field driven by a force ${}_{(1)}f = {}_{(1)}F\delta_{z,z_f}$ changes upon a static deformation (with $\delta\varphi(z_f) = 0$) we have to take into account both kernels, i.e.

$$\frac{\delta\, {}_{(1)}v(z_f)}{\delta\varphi(z)} = {}_{(1,0,-1)}K(z_f, z, z_f)\, {}_{(1)}F + {}_{(1,0,1)}K\, {}_{(-1)}(z_f, z, z_f)F \tag{H.21}$$

Writing pressure propagator and force locally in terms of phase and magnitude, i.e. $G_P = {}_{(0,-1)}G_P = |G_P|e^{-i\theta_P}$, ${}_{(1)}F = Fe^{i\theta_F}$, we obtain from Eq. H.18, Eq. H.19

$$\frac{\delta\, {}_{(1)}v(z_f)}{\delta\varphi(z)} = \frac{4|G_P(z, z_f)|^2}{\eta_b}\left(1 + e^{2i(\theta_P(z,z_f)-\theta_F)}\right) {}_{(1)}F. \tag{H.22}$$

We observe that the square of the pressure propagator defines an axis and that the change in the flow field depends on the orientation of the force with respect to this axis. For perpendicular alignment, i.e. $\cos[2(\theta_P - \theta_F)] = -1$, the change in the flow field $\delta\, {}_{(1)}v$ vanishes, whereas for parallel alignment, i.e. $\cos[2(\theta_P - \theta_F)] = 1$, $\delta\, {}_{(1)}v(z_f)$ is orientated parallel to the force ${}_{(1)}F$. In general, we have that the scalar product of the force and and the change in the velocity field for a surface expansion ($\delta\varphi \geq 0$) is strictly positive

$$\mathrm{Re}\left[{}_{(-1)}F\frac{\delta\, {}_{(1)}v(z_f)}{\delta\varphi(z)}\right] \geq 0 \tag{H.23}$$

with equality restricted to curves with $\cos[2(\theta_P - \theta_F)] = -1$. This inequality, where $\eta_s = 0, \eta_b > 0$, is directly opposite to Eq. H.6,H.7, where $\eta_s > 0, \eta_b = 0$. In other words, adding surface area around a force yields additional dampening of the flow due to shear viscosity and reduces dampening due to bulk viscosity. When both shear and bulk viscosity are non-vanishing these two effects compete.

H.3 Interplay of bulk and shear viscosity in defining the deformation response

As before, we calculate the variation of the flow field for a deformation $\delta\varphi$, but this time for non-vanishing bulk and shear viscosity, i.e. for some $\alpha > 0$. As in the previous section we calculate the angular average of the change in the flow field at the position of the force z_f for a deformation away from the point force ($z_f \neq z$). We find that for a general closed surface it can be written as

$$\begin{aligned}\frac{\delta G_0(z_f,z_f)}{\delta\varphi(z)} =& -\frac{4\eta}{l_h^2(1+\alpha)}\left(|G_0(z,z_f)|^2+|G_2(z,z_f)|^2\right) - 2\eta\left(|\eth G_0(z,z_f)|^2+|\eth G_2(z,z_f)|^2\right)\\ &- \frac{2\eta\alpha}{l_h^2(1+\alpha)}|G_0(z,z_f)-G_2(z,z_f)|^2\\ &- 4\eta\,\mathrm{Re}[\bar{G}_0(z_f,z)\eth G_P(z,z_f)+G_2(z_f,z)\bar{\eth} G_P(z,z_f)] + \frac{4}{\alpha\eta}|G_P(z,z_f)|^2, \end{aligned} \tag{H.24}$$

Due to the two summands resulting from the pressure, $\delta G_0(z_f,z_f)/\delta\varphi$ is not strictly negative for arbitrary surfaces. For an incompressible fluid, i.e. in the limit $\alpha\to\infty$, $l_h=$ const., G_P remains finite and thus $|G_P(z,z_f)|^2/\alpha$ vanishes. The term proportional to the gradient of pressure, however, does not.

Importantly, we can make further progress for surfaces of constant Gaussian curvature for an incompressible fluid film. Then the force balance equation reads

$$\eta\bar{\eth}\eth\,{}_{(1)}v - \bar{\eth}P - \gamma\,{}_{(1)}v = -\,{}_{(1)}f. \tag{H.25}$$

Calculating the divergence of both sides of the equation, yields a Poisson equation for the pressure

$$\begin{aligned}\frac{1}{\eta}\Delta_{LB}P =& \frac{1}{2}\left(\bar{\eth}\bar{\eth}\eth\,{}_{(1)}v + \bar{\eth}\,{}_{(1)}f + \eth\eth\bar{\eth}\,{}_{(-1)}v + \eth\,{}_{(-1)}f\right)\\ =& \frac{1}{2}\left(\bar{\eth}\,{}_{(1)}f + \eth\,{}_{(-1)}f\right) + {}_{(1)}v\bar{\eth}\kappa + {}_{(-1)}v\eth\kappa,\end{aligned} \tag{H.26}$$

where we used Eq. 1.66 and the incompressibility condition $\bar{\eth}\,{}_{(1)}v + \eth\,{}_{(-1)}v = 0$. We observe that the pressure around a force monopole is a harmonic function on a surface with constant Gaussian curvature.

We write the flow field in terms of the pressure using the propagator for vanishing bulk viscosity $\alpha=0$ which we denote as G_0^0:

$${}_{(1)}v(z) = \int \mathrm{d}S' G_0^0(z,z')({}_{(1)}f(z') - \eth P(z')) \tag{H.27}$$

To make progress, we consider the case that harmonic contributions to the flow field are negligible. This is valid for a sphere, and in the regime of small hydrodynamic length on arbitrary surfaces. With this we can write the propagator of the velocity field as a propagator of F:

$$G_0^0(z,z') = \eth G_F^0(z,z') \tag{H.28}$$

This allows us to use partial integration to evaluate Eq. H.27 using the Poisson equation for the pressure (for $\eth\kappa = 0$). With this we obtain

$$
{}_{(1)}v(z) = \frac{1}{2}\int \mathrm{d}S' G_0^0(z, z')\,{}_{(1)}f(z'). \tag{H.29}
$$

Thus, on a surface with constant Gaussian curvature and negligible harmonic flow fields we have

$$
\lim_{\alpha\to\infty} G_0 = \frac{1}{2}\lim_{\alpha\to 0} G_0. \tag{H.30}
$$

This implies that the calculation of δG_0 for vanishing bulk viscosity $\alpha = 0$ applies also to the incompressible regime, when the hydrodynamic length scale is small compared to the length scale of the gradient of Gaussian curvature.

H.4 Force multipole in a multipole of the surface geometry

We consider a force multipole which we understand as a force density of the form

$$
{}_{(1)}f(z) = (-1)^{n_f+m_f}\eth^{n_f}\bar{\eth}^{m_f}\,{}_{(s)}X\delta_{z,z'}, \quad s = 1 - n_f + m_f, \tag{H.31}
$$

where ${}_{(s)}X$ denotes a spin quantity at z' that captures the orientation and magnitude of the stress multipole with $|s|$-fold rotational symmetry. A tension monopole corresponds to $n_f = 1$ $m_f = 0$ with ${}_{(0)}X < 0$. A force multipole with $n_f = 0$, $m_f > 0$ corresponds to a multipole of the active nematic tension ${}_{(2)}t_{\mathrm{act}}$.

The flow field of such a force multipole can be expressed in terms of gradients of the Green's functions as

$$
{}_{(1)}v = \bar{\eth}_{z'}^{m_f}\eth_{z'}^{n_f}G_0(z, z') + \eth_{z'}^{m_f}\bar{\eth}_{z'}^{n_f}G_2(z, z'). \tag{H.32}
$$

For simplicity, we consider the regime of vanishing bulk viscosity in the following, such that $G_2 = 0$. In a flat fluid film with $\varphi = 0$. The Green's function is given by

$$
G_0(z, z') = \frac{1}{2\pi\eta}K_0(|z - z'|/l_h), \tag{H.33}
$$

where $K_n(r)$ denotes the modified Bessel function. The Bessel functions obey the recurrence relations

$$
K_n(x) = -\frac{1}{2}(K_{n+1}(x) + K_{n-1}(x)), \quad K_n(x) = -\frac{x}{2n}(K_{n-1}(x) - K_{n+1}(x)). \tag{H.34}
$$

With this we find

$$
\eth^n\bar{\eth}^m K_n(|z|) = \frac{(-1)^{m+n}}{2\pi}\frac{z^n\bar{z}^m}{|z|^{n+m}}K_{|m-n|}(|z|) = \frac{(-1)^{n+m}}{2\pi}e^{i(n-m)\theta}K_{|m-n|}(r). \tag{H.35}
$$

and thus the flow field of a force multipole at $z = 0$ in a flat fluid film reads

$$ {}_{(1)}v = \frac{1}{l_h^{n_f+m_f}} \frac{{}_{(s)}X}{2\pi\eta} e^{i(n_f-m_f)\theta} K_{|m_f-n_f|}(r/l_h). \tag{H.36}$$

We consider a deformation away from the multipole, i.e. a field of isotropic expansions and contractions $\delta\varphi$ that obeys

$$\exists\epsilon > 0 : \delta\varphi(z) = \Theta(|z| - \epsilon)\delta\varphi(z). \tag{H.37}$$

We evaluate the flow field and its derivatives at the position of the multipole $z_0 = 0$ using H.4, which yields

$$\delta(\eth^{m_v}\bar{\eth}^{n_v}\ {}_{(1)}v)(z_0) = \int_{\mathcal{S}} {}_{(s)}X \mathrm{d}S_1 \delta\varphi(z_1)\, \eth_z^{m_v}\bar{\eth}_z^{n_v}\bar{\eth}_{z_0}^{m_f}\eth_{z_0}^{n_f}\ {}_{(1,0,-1)}K(z, z_1, z_0)\big|_{z=z_0}, \tag{H.38}$$

where

$$ {}_{(1,0,-1)}K(z, z_1, z_0) = -\,4\gamma G_0(z_1, z_0)\bar{G}_0(z_1, z) - 2\eta(\eth G_0(z_1, z_0))(\bar{\eth}\bar{G}_0(z_1, z)). \tag{H.39}$$

With this and Eq. we obtain for $z_0 = 0$

$$\frac{\delta(\eth^{m_v}\bar{\eth}^{n_v}\ {}_{(1)}v)(z_0)}{\delta\varphi(z)_1} = -\frac{1}{l_h^{m_v+n_v+m_f+n_f}} \frac{{}_{(s)}X}{(2\pi)^2\eta} e^{i(m_v-n_v-m_f+n_f)} h(r/l_h), \tag{H.40}$$

where

$$h(r/l_h) = \frac{2}{l_h^2}\left(2K_{|m_v-n_v|}(x)K_{|m_f-n_f|}(x) + K_{|1+m_v-n_v|}(x)K_{|1+m_f-n_f|}(x)\right) > 0. \tag{H.41}$$

For a deformation of the form

$$\delta\varphi = -\frac{4}{n+1}|z|^2\left({}_{(n)}\mathcal{K}\bar{z}^n + {}_{(-n)}\mathcal{K}z^n\right) \tag{H.42}$$

we obtain

$$\begin{aligned}
&\delta(\eth^{m_v}\bar{\eth}^{n_v}\ {}_{(1)}v)(z_0)\\
=&\frac{8}{n+1}\frac{2^{1+n}(1+n)!}{(3+n)!}\frac{l_h^{2+n}}{l_h^{m_v+n_v+m_f+n_f}}\frac{{}_{(s)}X}{2\pi\eta}\\
&\big[|4-m_v+n_v+2n|\,|1+m_v-n_v|!\,|n+n_v-m_v|!\ {}_{(n)}\mathcal{K}\delta_{n,m_v-n_v-m_v+n_f}\\
&\quad + |4-m_v+n_v+n|\,|1+m_v-n_v+n|!\,|m_v-n_v|!\ {}_{(-n)}\mathcal{K}\delta_{n,-m_v+n_v+m_v-n_f}\big],
\end{aligned} \tag{H.43}$$

where we evaluated the radial integral in Eq. H.38 with Eq. H.40 using Mathematica [207].

Importantly, all factors are positive, such that we may write

$$\delta(\eth^{m_v}\bar{\eth}^{n_v}\,{}_{(1)}v)(z_0) = N\delta_{s+n,1+m_v-n_v}\,{}_{(s)}X\,{}_{(n)}\mathcal{K}, \tag{H.44}$$

with $N > 0$. For a tension monopole, i.e. $m_f = 0$, $n_f = 1$, ${}_{(0)}X = -T < 0$, we have

$$\begin{aligned}\delta(\eth^{m_v}\bar{\eth}^{n_v}\,{}_{(1)}v)(z_0) = &-\frac{4Tl_h^{n+1}}{\pi\eta l_h^{m_v+n_v}}\frac{2^{1+n}n!}{(3+n)!}\\ &\Big[(5+n)\,n!\,{}_{(n)}\mathcal{K}\delta_{n,1+m_v-n_v} + (5+2n)\,(n+1)!\,{}_{(-n)}\mathcal{K}\delta_{-n,1+m_v-n_v}\Big].\end{aligned} \tag{H.45}$$

Since $\delta\varphi = 0$ for $|z| < \epsilon$, $\delta\,{}_{(1)}v$ is continuous at $z = 0$. Thus we can expand $\delta\,{}_{(1)}v$ as a Taylor expansion:

$$\delta\,{}_{(1)}v = \sum_{m=0}^{\infty}\sum_{k=0}^{\infty} V_{mk} z^m \bar{z}^k, \tag{H.46}$$

where

$$V_{mk} = \frac{1}{m!k!}\partial_z^m\partial_{\bar{z}}^k\delta\,{}_{(1)}v\big|_{z=0} = \frac{1}{m!k!}2^{-m-k}\bar{\eth}^m\eth^k\delta\,{}_{(1)}v\big|_{z=0}. \tag{H.47}$$

With this we can write the multipoles of $\delta\,{}_{(1)}v$ as defined in Eq. I.10 as

$${}_{(t)}V(a) = \sum_{m=0}^{\infty} a^{2m+t} V_{t-1+m,m} \tag{H.48}$$

$${}_{(-t)}V(a) = \sum_{m=0}^{\infty} a^{2m+t} V_{m,t+1+m} \tag{H.49}$$

for $t \geq 0$. Thus, we can write them as

$${}_{(t)}V = N_{ts}^{(1)}\,{}_{(s)}X\,{}_{(t-s)}\mathcal{K}, \tag{H.50}$$

where for $t \geq 0$ we have with Eq. H.43

$$N_{ts}^{(1)} = \sum_{m=0}^{\infty}\frac{a^{2m+t}}{(t-1+m)!m!2^{2m+t-1}}\frac{\delta(\eth^m\bar{\eth}^{t-1+m})\delta\,{}_{(1)}v}{\delta\,{}_{(s)}X\delta\,{}_{(t-s)}\mathcal{K}} > 0 \tag{H.51}$$

and analogously for $t < 0$.

Appendix I

On multipoles in a curved surface

In the following, we make use the Newman Penrose formalism in isothermal coordinates (section 1.3.1 and 1.3.2) to define multipoles of vector fields on a curved surface. To this end, we follow an approach from the field of general relativeity that is based on conformal Killing vector fields [208]. On a surface, conformal Killing vector fields are vector fields ${}_{(1)}x$ obeying

$$\eth\,{}_{(1)}x = 0. \tag{I.1}$$

Using

$$\eth\,{}_{(1)}x = \frac{1}{l^2}\partial_{\bar{z}} l\,{}_{(1)}x \tag{I.2}$$

we obtain

$${}_{(1)}x = l f(z), \quad \partial_{\bar{z}} f = 0, \tag{I.3}$$

i.e. any conformal Killing vector field corresponds to a holomorphic function f. As there are infinitely independent holomorphic functions, there are infinitely many conformal Killing vector fields. Furthermore, any holomorphic function and hence any conformal Killing vector field is uniquely defined by by its value and all its derivatives at some reference point z_0. We define the conformal Killing vector fields ${}_{(1)}x_n$ ($n \in \mathbb{N}$) with respect to $z = 0$ by

$$\bar{\eth}^{(m)}\,{}_{(1)}x_n|_{z=0} = \delta_{m,n}\,{}_{(1-n)}X. \tag{I.4}$$

Thus, they are vector fields that are uniquely and covariantly defined by a quantity ${}_{((1-n))}X$ corresponding to an object with $|n-1|$-fold rotational symmetry at $z = 0$. Without loss of generality, we may set ${}_{(s)}X = 1$ such that the convention of ${}_{(s)}X$ coincides with the convention of **Z**. Furthermore, we define the anti-conformal Killing vector fields ${}_{(1)}x_{-n}$ by

$$\bar{\eth}\,{}_{(1)}x_{-n} = 0, \quad \eth^{(m)}\,{}_{(1)}x_{-n}|_{z=0} = \delta_{m,n}\,{}_{(1+n)}X \quad (m, n \in \mathbb{N}) \tag{I.5}$$

The fields ${}_{(1)}x_{\pm n}$ are vector fields that have some s fold rotational symmetry with respect to a point of reference. In particular ${}_{(1)}x_1$ (with ${}_{(0)}X \in \mathbb{R}$) defines an isotropic vector field around

$z = 0$.. In the following we use this to quantify the flow field around the location of the stress multipole by defining

$$ {}_{(s)}V(a) = \frac{1}{L} \int_{\Gamma(a)} \mathrm{d}l \frac{\mathrm{Re}[{}_{(1)}\nu \, {}_{(-1)}x_1]}{|\, {}_{(1)}x_1|} \frac{{}_{(1)}x_{1-s} \, {}_{(-1)}v}{|\, {}_{(1)}x_{1-s}|}, \tag{I.6} $$

where $\Gamma(a)$ is some contour around $z = 0$ with a characteristic length scale a. In particular, we define the velocity of the stress multipole at $z = 0$ as

$$ {}_{(1)}V = \lim_{a \to 0} {}_{(1)}V(a). \tag{I.7} $$

We note, that such a limit may not always exist. In this case the contour $\Gamma(a)$ becomes relevant, which reflects the finite size of for example the active particle at $z = 0$.

The fields ${}_{(1)}x_n$ become particularly simple by locally reparametrising the surface such that

$$ \varphi\big|_{z=0} = 0, \quad \eth^{(m)}\varphi\big|_{z=0} = 0 \quad (m \in \mathbb{N}). \tag{I.8} $$

With this, we obtain

$$ {}_{(1)}x_n = \frac{l}{n!} \, {}_{(1-n)}X z^n, \quad {}_{(1)}x_{-n} = \frac{1}{n!} \frac{1}{l} \, {}_{(1+n)}X \bar{z}^n. \tag{I.9} $$

Furthermore we use the convention ${}_{(s)}X = 1$. Thereby the flow components ${}_{(s)}V(a)$ with $a/l \ll l^2\kappa$ become

$$ {}_{(s)}V(a) = \frac{1}{2\pi} \int_0^{2\pi} \mathrm{d}\theta e^{i(1-s)\theta} \, {}_{(-1)}v(|z| = a) \tag{I.10} $$

Thus, the multipoles ${}_{(s)}V$ of the flow field correspond to the Fourier components of the angular dependence of the flow field. In particular, the multipole velocity is simply the average velocity along the circle. This motivates the numerical calculation of the monopole velocity as described in Fig. J.1.

Appendix J

Supplemental figures and tables

	F	**G**	**H**	**I**
l_h/R	20	20	20	1/6
G	1	1	0	0
α	1000	1000	5	2
a/R	0.01	0.01	0.01	1/6
b.c. at $r = R$	$\mathbf{v} = 0$	$\mathbf{t}^r = 0$	$\mathbf{t}^r(\theta) = \mathbf{F},\ \langle\mathbf{v}\rangle_\theta{=}0$	$\mathbf{v} = 0$
b.c. at $\theta = \pi$	$\mathbf{t}^\theta{=}0$	$\mathbf{v} = 0$	$\mathbf{t}^\theta = \boldsymbol{\theta}$	$\mathbf{v} = 0$
b.c. at $\theta = -\pi$	$\mathbf{t}^\theta{=}0$	$\mathbf{v} = 0$	$\mathbf{t}^\theta = \boldsymbol{\theta}$	$\mathbf{v} = 0$
$\mathbf{v}(r = a, \theta)$	$\mathbf{V}_T{+}\Omega_T\boldsymbol{\theta}$	$\mathbf{V}_T{+}\Omega_T\boldsymbol{\theta}$	$\mathbf{V}_T{+}\Omega_T\boldsymbol{\theta}$	$\mathbf{V}_T{+}\Omega_T\boldsymbol{\theta}$
crack tip b.c.	$\mathbf{F}_T = 0 = \Gamma_T$	$\mathbf{V}_T = 0 = \Omega_T$	$\mathbf{F}_T = 0 = \Gamma_T$	$\mathbf{F}_T = 0,\ \Gamma_T = 1$

Table J.1: Material parameters and boundary conditions (b.c.) of the numerical solutions in 2.1F-I, using an arbitrary unit of time.

	A	**B**
l_h/R	20	20
G	0	0
α	3	3
a/R	0.01	0.01
b.c. at $r = R$	$\mathbf{t}^r(\theta) = \mathbf{F},\ \langle\mathbf{v}\rangle_\theta{=}0$	$\mathbf{t}^r(\theta) = \mathbf{F},\ \langle\mathbf{v}\rangle_\theta{=}0$
b.c. at $\theta = \pi$	$\mathbf{t}^\theta = \boldsymbol{\theta}$	$t^{\theta r}{=}0,\ v^\theta = 1$
b.c. at $\theta = -\pi$	$\mathbf{t}^\theta = \boldsymbol{\theta}$	$t^{\theta r}{=}0,\ v^\theta = -1$
$\mathbf{v}(r = a, \theta)$	$\mathbf{V}_T{+}\Omega_T\boldsymbol{\theta}$	$\mathbf{V}_T{+}\Omega_T\boldsymbol{\theta}$
crack tip b.c.	$\mathbf{F}_T = 0 = \Gamma_T$	$\mathbf{F}_T = 0 = \Gamma_T$

Table J.2: Material parameters and boundary conditions (b.c.) of the numerical solutions in 2.6A,C, using an arbitrary unit of time.

Fig.	γ_1^p	γ_1^Q	γ_2^p	γ_2^Q	χ_1	χ_2	ζ^p	ζ_1^{pQ}	ζ_2^{pQ}	ζ_1^Q	ζ_2^Q	ζ_3^Q	ζ_3^{pQ}
C	1	-1	-1	-1	1	1	1	0	0	0	0	0	0
D	0.8	1	-1	-1	1	1	0	0	0	0	0	1	0
E	1	1	-1	-1	1	-1	0	0	0	0	0	0	0
F	1	1	-1	-1	1	-1	-0.076	0.008	-0.415	-0.238	0.301	-0.471	0.429

Table J.3: Physical parameters of the numerical solutions plotted in 3.1

Fig.	η	l_h	Pe	α	k	D	$f(c)$	R_0	δR_{20}	R_1	R_2
A	1	3	55	1	10	1	$2c^2/(c_0^2+c^2)$	1	0.4		
B	1	3	55	1	10	1	$2c^2/(c_0^2+c^2)$			1	0.7071

Table J.4: Physical parameters of the numerical solutions plotted in 4.1

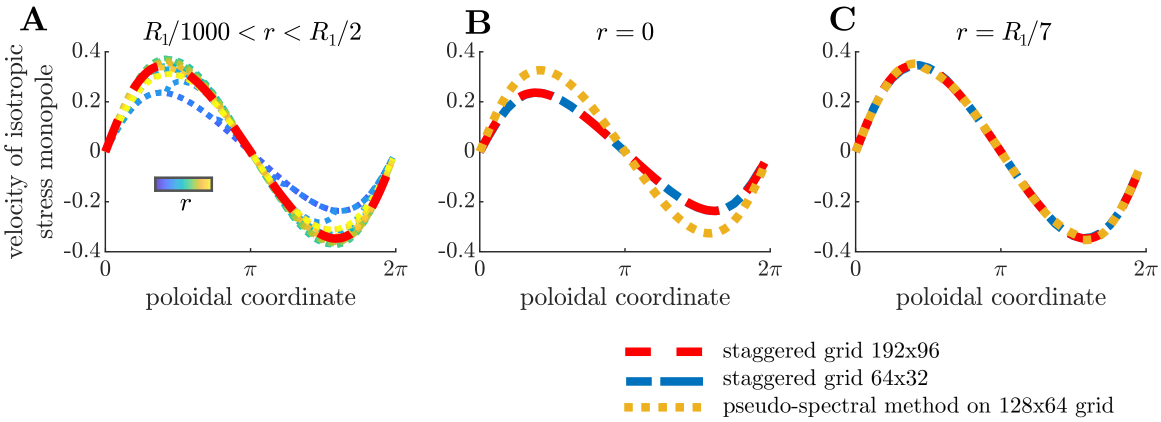

Figure J.1: Numerical calculation of tension monopole velocity on a torus. We calculate the velocity of a tension monopole from the numerical flow field (see appendix G). To this end, we average the three-dimensional vector **v** on the outline of a circle in coordinate space with radius r/l centered at the position of the tension monopole, motivated by appendix I. This average velocity is then projected into the tangent plane defined by **Z** at the position of the tension monopole. Due to the symmetry of the geometry (i.e. a torus with $\sinh(\rho)$ as defined in Eq. F.24), the velocity points always along the poloidal direction. We plot here the projection on the normalized poloidal tangent vector, using different grids and numerical methods. Physical parameters are $\alpha = 1$, $l_h = 3R_1$. **A**: Staggered grid of size 192x96 using different radii r for calculating the monopole velocity from the flow field. We observe that beyond the resolution of the grid, the monopole velocity is fairly independent of r. In Fig. 4.2, we use $r = R_1/7$ corresponding to the red curve. **B**: Monopole velocity for $r = 0$, i.e. the flow field is evaluated at the grid point of the tension monopole. We use staggered grids of size 192x96 (red curve) and 64x32, which yield similar results. When we use a usual square grid and solve the flow field using a pseudo-spectral method (yellow curve, see appendix F), however, the result differs, indicating that the monopole velocity we calculate using $r = 0$ depends on how we discretize the problem. **C**: Same as in **B**, but using $r = R_1/7$. We observe that the monopole velocity we find is independent of the numerical method we use to calculate the flow field.

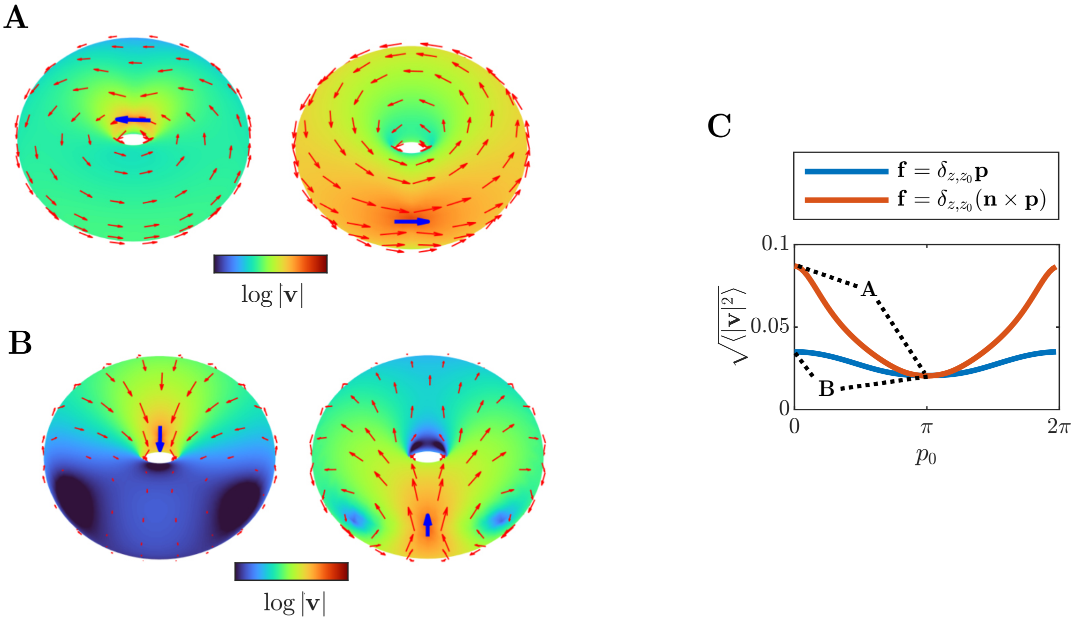

Figure J.2: Flow field of force monopoles in an incompressible toroidal fluid film. **A**: Flow field (red arrows) of a force monopole, i.e. a force density given by a dirac delta (Eq. 4.19), with the force pointing in the toroidal direction. Color denotes logarithm of the modulus of the velocity from $\log|\mathbf{v}| = -6$ to $\log|\mathbf{v}| = 0$. Lengths of arrows are also logarithmically scaled. Left panel: Force monopole (blue arrow) on the inner surface at poloidal coordinate $p_0 = 0.9\pi$. Right panel: Force monopole on the outer surface at $p_0 = \pi/15$. **B**: As in **A** but for force pointing in the poloidal direction. **C**: Surface average of the flow fields of force monopoles as in **A,B** as a function of the poloidal coordinate of the monopole position. We observe that the average velocity is minimal for $p_0 = \pi$, where γ_{eff} and η_{eff} are maximal (see Fig. 4.3A,B and main text. Physical parameters are $\eta = 1$, $\alpha = 1000$, $l_h = 2$. Radii of the torus are $R_1 = 1.4$, $R_2 = 1$. All flow fields were solved using a pseudospectral method (appendix F) on an 81x81 isothermal grid.)

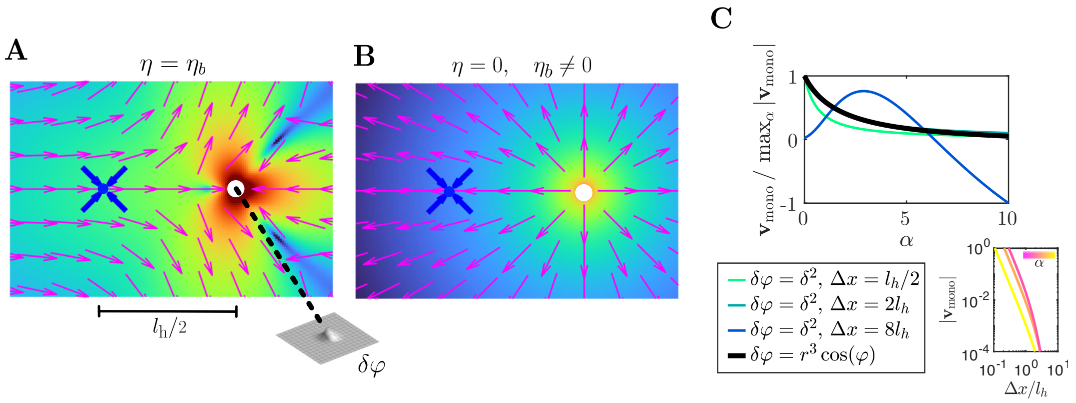

Figure J.3: Interplay of bulk and shear viscosity in the context of geometry sensing by a contractile point. **A,B** Change in the flow field around a tension monopole (blue dot) upon an infinitesimal expansion (white circle) of the surface, as in Fig. 4.6C, but for non-vansishing bulk viscosity. When shear viscosity vanishes (**B**), we observe that the contractile point moves away from the expansion, opposed to the case of vanishing bulk viscosity. For $\alpha = \eta_b/\eta = 1$ (**A**), we observe that the attraction resulting from shear viscosity dominates. **C**: Upper panel: Velocity of a tension monopole next to a surface expansion (colored curves, as in **A,B**) or in a gradient of Gaussian curvature (black curve, as in Fig. 4.6D). We observe that a contractile point always moves towards a surface expansion ($v_{\mathrm{mono}} > 0$), when shear viscosity is non-vanishing, i.e. the distance Δx between contractile point and surface expansion is on the order of the hydrodynamic length l_h. Also in a gradient of Gaussian curvature, we find that a contractile point always moves down the gradient. Note that we normalized all curves with respect to their maximum modulus. In the lower right panel, in contrast, we plot the actual non-normalized velocity of a tension monopole as a function of the distance Δx between the monopole and the surface expansion for various α.

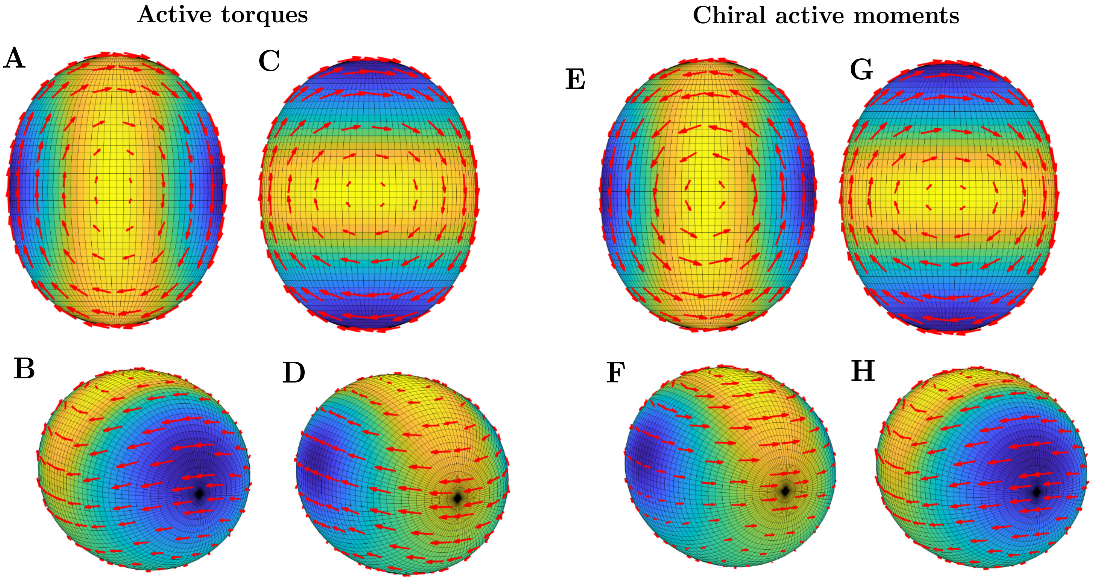

Figure J.4: Chiral deformation-triggered net rotation Flow fields for a polarized ring of chiral mechanical activity c (yellow coloring) in a fluid film with the geometry of a prolate sphere. Upper row corresponds to view as in Fig. 5.4, whereas in the lower row, also the poles are shown to illustrate the asymmetry of the pattern c and the resulting flow field. **A**-**D**: Active torque density as in Fig. 5.4B,C. We find that the polarized pattern c drives a rotation around the axis of this polarity, independent of the orientation of the ring with respect to the surface geometry. **A**-**H**: Isotropic chiral active moments as in Fig. 5.4I. We find that also active chiral moments drive a net rotation. However, we find that the direction of the rotation reverses between **E,F** and **G,H**. This reflects that the rotation is triggered by the deformation in contrast to **A**-**D**. Hence the rotation is reversed, when considering the inverse deformation of the surface with respect to the pattern.

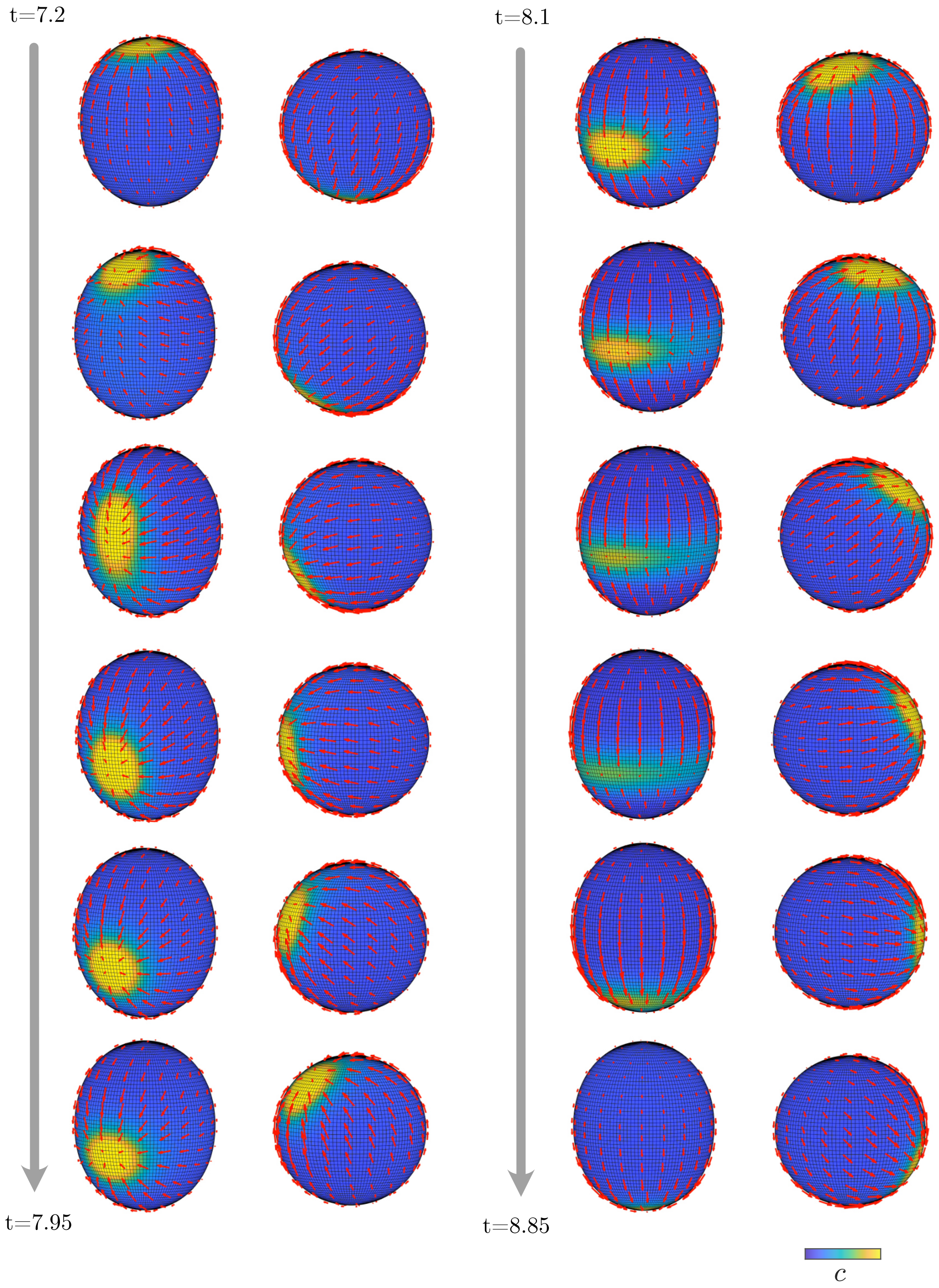

Figure J.5: Surface geometry shapes dynamical patterns in active fluid model Example of numerical solutions of the active fluid model in section 3.3 for parameters where no steady state emerges, corresponding to gray patterns in Fig. 3.5B. We simulate pattern formation starting from a random perturbation of the homogeneous state and compare the dynamics on a sphere (2nd and 4th column) to the dynamics on a deformed sphere (1st and 3rd column). On a sphere, we observe a circular patch traveling around the sphere, corresponding to a dynamic steady state. On the deformed sphere, in contrast, we observe repeated transitions between a circular patch and a ring, yielding potentially chaotic dynamics. In both cases the physical parameters are $\mathrm{Pe} = 55$, $l_h = 0.67R_0$, $\alpha = 1$, $f(c) = 2c^2/(c_0^2 + c^2)$, $k\tau_D = 10$, and time t is given in units of τ_D.

Bibliography

[1] Chonnettia Jones and Ping Chen. Planar cell polarity signaling in vertebrates. *Bioessays*, 29(2):120–132, 2007.

[2] Lewis Wolpert. Positional information and the spatial pattern of cellular differentiation. *Journal of theoretical biology*, 25(1):1–47, 1969.

[3] Lewis Wolpert, Cheryll Tickle, and Alfonso Martinez Arias. *Principles of development*. Oxford University Press, USA, 2015.

[4] Tetsuya Nakamura and Hiroshi Hamada. Left-right patterning: conserved and divergent mechanisms. *Development*, 139(18):3257–3262, 2012.

[5] Erich Roessler and Maximilian Muenke. Midline and laterality defects: left and right meet in the middle. *Bioessays*, 23(10):888–900, 2001.

[6] Hiroshi Hamada, Chikara Meno, Daisuke Watanabe, and Yukio Saijoh. Establishment of vertebrate left–right asymmetry. *Nature Reviews Genetics*, 3(2):103–113, 2002.

[7] Jeffrey D Lee and Kathryn V Anderson. Morphogenesis of the node and notochord: the cellular basis for the establishment and maintenance of left–right asymmetry in the mouse. *Developmental dynamics: an official publication of the American Association of Anatomists*, 237(12):3464–3476, 2008.

[8] Richard CV Tyser, Elmir Mahammadov, Shota Nakanoh, Ludovic Vallier, Antonio Scialdone, and Shankar Srinivas. Single-cell transcriptomic characterization of a gastrulating human embryo. *Nature*, 600(7888):285–289, 2021.

[9] Henry Gray. *Anatomy of the human body*, volume 8. Lea & Febiger, 1878.

[10] James R Priess. Notch signaling in the c. elegans embryo. *WormBook: The Online Review of C. elegans Biology [Internet]*, 2005.

[11] Christian P Petersen and Peter W Reddien. Wnt signaling and the polarity of the primary body axis. *Cell*, 139(6):1056–1068, 2009.

[12] Edwin Munro, Jeremy Nance, and James R Priess. Cortical flows powered by asymmetrical contraction transport par proteins to establish and maintain anterior-posterior polarity in the early c. elegans embryo. *Developmental cell*, 7(3):413–424, 2004.

[13] Peter Gross, K Vijay Kumar, Nathan W Goehring, Justin S Bois, Carsten Hoege, Frank Jülicher, and Stephan W Grill. Guiding self-organized pattern formation in cell polarity establishment. *Nature Physics*, 15(3):293–300, 2019.

[14] Carrie R Cowan and Anthony A Hyman. Centrosomes direct cell polarity independently of microtubule assembly in c. elegans embryos. *Nature*, 431(7004):92–96, 2004.

[15] Mirjam Mayer, Martin Depken, Justin S Bois, Frank Jülicher, and Stephan W Grill. Anisotropies in cortical tension reveal the physical basis of polarizing cortical flows. *Nature*, 467(7315):617–621, 2010.

[16] Lesilee Rose and Pierre Gönczy. Polarity establishment, asymmetric division and segregation of fate determinants in early c. elegans embryos. *WormBook*, 2014.

[17] Carsten Hoege and Anthony A Hyman. Principles of par polarity in caenorhabditis elegans embryos. *Nature reviews Molecular cell biology*, 14(5):315–322, 2013.

[18] Jeremy Nance. Par proteins and the establishment of cell polarity during c. elegans development. *Bioessays*, 27(2):126–135, 2005.

[19] Kenji Sugioka and Bruce Bowerman. Combinatorial contact cues specify cell division orientation by directing cortical myosin flows. *Developmental cell*, 46(3):257–270, 2018.

[20] Anthony A Hyman and John G White. Determination of cell division axes in the early embryogenesis of caenorhabditis elegans. *The Journal of cell biology*, 105(5):2123–2135, 1987.

[21] Pierre Gönczy and Lesilee S Rose. Asymmetric cell division and axis formation in the embryo. *WormBook*, page 1, 2005.

[22] Lokesh G Pimpale, Teije C Middelkoop, Alexander Mietke, and Stephan W Grill. Cell lineage-dependent chiral actomyosin flows drive cellular rearrangements in early caenorhabditis elegans development. *Elife*, 9:e54930, 2020.

[23] Anne-Cecile Reymann, Fabio Staniscia, Anna Erzberger, Guillaume Salbreux, and Stephan W Grill. Cortical flow aligns actin filaments to form a furrow. *Elife*, 5:e17807, 2016.

[24] Bruce Alberts, Dennis Bray, Karen Hopkin, Alexander D Johnson, Julian Lewis, Martin Raff, Keith Roberts, and Peter Walter. *Essential cell biology*. Garland Science, 2015.

[25] Michael Murrell, Patrick W Oakes, Martin Lenz, and Margaret L Gardel. Forcing cells into shape: the mechanics of actomyosin contractility. *Nature reviews Molecular cell biology*, 16 (8):486–498, 2015.

[26] Bruce L Goode and Michael J Eck. Mechanism and function of formins in the control of actin assembly. *Annu. Rev. Biochem.*, 76:593–627, 2007.

[27] Guillaume Salbreux, Guillaume Charras, and Ewa Paluch. Actin cortex mechanics and cellular morphogenesis. *Trends in cell biology*, 22(10):536–545, 2012.

[28] Miguel Vicente-Manzanares, Xuefei Ma, Robert S Adelstein, and Alan Rick Horwitz. Non-muscle myosin ii takes centre stage in cell adhesion and migration. *Nature reviews Molecular cell biology*, 10(11):778–790, 2009.

[29] Michael Lorenz and Kenneth C Holmes. The actin-myosin interface. *Proceedings of the National Academy of Sciences*, 107(28):12529–12534, 2010.

[30] Jacques Prost, Frank Jülicher, and Jean-François Joanny. Active gel physics. *Nature physics*, 11(2):111–117, 2015.

[31] Karsten Kruse and F Jülicher. Actively contracting bundles of polar filaments. *Physical review letters*, 85(8):1778, 2000.

[32] Martin Lenz, Todd Thoresen, Margaret L Gardel, and Aaron R Dinner. Contractile units in disordered actomyosin bundles arise from f-actin buckling. *Physical review letters*, 108 (23):238107, 2012.

[33] Pierre Ronceray, Chase P Broedersz, and Martin Lenz. Fiber plucking by molecular motors yields large emergent contractility in stiff biopolymer networks. *Soft matter*, 15(7):1481–1487, 2019.

[34] Viktoria Wollrab, Julio M Belmonte, Lucia Baldauf, Maria Leptin, François Nédeléc, and Gijsje H Koenderink. Polarity sorting drives remodeling of actin-myosin networks. *Journal of cell science*, 132(4):jcs219717, 2019.

[35] Jean Hanson and J Lowy. The structure of f-actin and of actin filaments isolated from muscle. *Journal of molecular biology*, 6(1):46–IN5, 1963.

[36] Robert H Depue and Robert V Rice. F-actin is a right-handed helix. *Journal of molecular biology*, 12(1):302–IN28, 1965.

[37] Ichiro Sase, Hidetake Miyata, Shin'ichi Ishiwata, and Kazuhiko Kinosita Jr. Axial rotation of sliding actin filaments revealed by single-fluorophore imaging. *Proceedings of the National Academy of Sciences*, 94(11):5646–5650, 1997.

[38] Hiroaki Mizuno, Chiharu Higashida, Yunfeng Yuan, Toshimasa Ishizaki, Shuh Narumiya, and Naoki Watanabe. Rotational movement of the formin mdia1 along the double helical strand of an actin filament. *Science*, 331(6013):80–83, 2011.

[39] Sundar Ram Naganathan, Sebastian Fürthauer, Masatoshi Nishikawa, Frank Jülicher, and Stephan W Grill. Active torque generation by the actomyosin cell cortex drives left–right symmetry breaking. *elife*, 3:e04165, 2014.

[40] Yee Han Tee, Tom Shemesh, Visalatchi Thiagarajan, Rizal Fajar Hariadi, Karen L Anderson, Christopher Page, Niels Volkmann, Dorit Hanein, Sivaraj Sivaramakrishnan, Michael M Kozlov, et al. Cellular chirality arising from the self-organization of the actin cytoskeleton. *Nature cell biology*, 17(4):445–457, 2015.

[41] Angus Davison, Gary S McDowell, Jennifer M Holden, Harriet F Johnson, Georgios D Koutsovoulos, M Maureen Liu, Paco Hulpiau, Frans Van Roy, Christopher M Wade, Ruby Banerjee, et al. Formin is associated with left-right asymmetry in the pond snail and the frog. *Current Biology*, 26(5):654–660, 2016.

[42] Reiko Kuroda, Kohei Fujikura, Masanori Abe, Yuji Hosoiri, Shuichi Asakawa, Miho Shimizu, Shin Umeda, Futaba Ichikawa, and Hiromi Takahashi. Diaphanous gene mutation affects spiral cleavage and chirality in snails. *Scientific Reports*, 6(1):34809, 2016.

[43] Masanori Abe and Reiko Kuroda. The development of crispr for a mollusc establishes the formin lsdia1 as the long-sought gene for snail dextral/sinistral coiling. *Development*, 146 (9):dev175976, 2019.

[44] Teije C Middelkoop, Júlia Garcia-Baucells, Porfirio Quintero-Cadena, Lokesh G Pimpale, Shahrzad Yazdi, Paul W Sternberg, Peter Gross, and Stephan W Grill. Cyk-1/formin activation in cortical rhoa signaling centers promotes organismal left–right symmetry breaking. *Proceedings of the National Academy of Sciences*, 118(20):e2021814118, 2021.

[45] Stephanie Schonegg and Anthony A Hyman. Cdc-42 and rho-1 coordinate acto-myosin contractility and par protein localization during polarity establishment in c. elegans embryos. *Development*, 2006.

[46] Yu Chung Tse, Michael Werner, Katrina M Longhini, Jean-Claude Labbe, Bob Goldstein, and Michael Glotzer. Rhoa activation during polarization and cytokinesis of the early caenorhabditis elegans embryo is differentially dependent on nop-1 and cyk-4. *Molecular biology of the cell*, 23(20):4020–4031, 2012.

[47] Masatoshi Nishikawa, Sundar Ram Naganathan, Frank Jülicher, and Stephan W Grill. Controlling contractile instabilities in the actomyosin cortex. *Elife*, 6:e19595, 2017.

[48] Sonja Kühn and Matthias Geyer. Formins as effector proteins of rho gtpases. *Small GTPases*, 5(3):e983876, 2014.

[49] Deepika Singh, Devang Odedra, Priyanka Dutta, and Christian Pohl. Mechanical stress induces a scalable switch in cortical flow polarization during cytokinesis. *Journal of Cell Science*, 132(19):jcs231357, 2019.

[50] Carl-Philipp Heisenberg and Yohanns Bellaïche. Forces in tissue morphogenesis and patterning. *Cell*, 153(5):948–962, 2013.

[51] Adam C Martin, Matthias Kaschube, and Eric F Wieschaus. Pulsed contractions of an actin–myosin network drive apical constriction. *Nature*, 457(7228):495–499, 2009.

[52] Adam C Martin and Bob Goldstein. Apical constriction: themes and variations on a cellular mechanism driving morphogenesis. *Development*, 141(10):1987–1998, 2014.

[53] Liyuan Sui, Silvanus Alt, Martin Weigert, Natalie Dye, Suzanne Eaton, Florian Jug, Eugene W Myers, Frank Jülicher, Guillaume Salbreux, and Christian Dahmann. Differential lateral and basal tension drive folding of drosophila wing discs through two distinct mechanisms. *Nature communications*, 9(1):4620, 2018.

[54] Mattia Serra, Guillermo Serrano Nájera, Manli Chuai, Alex M Plum, Sreejith Santhosh, Vamsi Spandan, Cornelis J Weijer, and L Mahadevan. A mechanochemical model recapitulates distinct vertebrate gastrulation modes. *Science Advances*, 9(49):eadh8152, 2023.

[55] Manli Chuai, Guillermo Serrano Nájera, Mattia Serra, Lakshminarayanan Mahadevan, and Cornelis J Weijer. Reconstruction of distinct vertebrate gastrulation modes via modulation of key cell behaviors in the chick embryo. *Science Advances*, 9(1):eabn5429, 2023.

[56] Nobutaka Hirokawa, Yosuke Tanaka, Yasushi Okada, and Sen Takeda. Nodal flow and the generation of left-right asymmetry. *Cell*, 125(1):33–45, 2006.

[57] Katalin Eitler, András Bibok, and Gábor Telkes. Situs inversus totalis: a clinical review. *International journal of general medicine*, pages 2437–2449, 2022.

[58] Nigel A Brown and LEWIS Wolpert. The development of handedness in left/right asymmetry. *Development*, 109(1):1–9, 1990.

[59] Hiroshi Hamada. Molecular and cellular basis of left–right asymmetry in vertebrates. *Proceedings of the Japan Academy, Series B*, 96(7):273–296, 2020.

[60] Michael Levin, Randy L Johnson, Claudio D Sterna, Michael Kuehn, and Cliff Tabin. A molecular pathway determining left-right asymmetry in chick embryogenesis. *Cell*, 82(5): 803–814, 1995.

[61] Chikara Meno, Yukio Saijoh, Hideta Fujii, Masako Ikeda, Takahiko Yokoyama, Minesuke Yokoyama, Yutaka Toyoda, and Hiroshi Hamada. Left–right asymmetric expression of the tgfβ-family member lefty in mouse embryos. *Nature*, 381(6578):151–155, 1996.

[62] Oscar H Ocaña, Hakan Coskun, Carolina Minguillón, Prayag Murawala, Elly M Tanaka, Joan Galcerán, Ramón Muñoz-Chápuli, and M Angela Nieto. A right-handed signalling pathway drives heart looping in vertebrates. *Nature*, 549(7670):86–90, 2017.

[63] WB Wood. Evidence from reversal of handedness in c. elegans embryos for early cell interactions determining cell fates. *Nature*, 349(6309):536–538, 1991.

[64] Christian Pohl and Zhirong Bao. Chiral forces organize left-right patterning in c. elegans by uncoupling midline and anteroposterior axis. *Developmental cell*, 19(3):402–412, 2010.

[65] Harald Hutter and Ralf Schnabel. Establishment of left-right asymmetry in the caenorhabditis elegans embryo: a multistep process involving a series of inductive events. *Development*, 121(10):3417–3424, 1995.

[66] Sabitri Ghimire, Veronika Mantziou, Naomi Moris, and Alfonso Martinez Arias. Human gastrulation: The embryo and its models. *Developmental biology*, 474:100–108, 2021.

[67] Jerome Gros, Kerstin Feistel, Christoph Viebahn, Martin Blum, and Clifford J Tabin. Cell movements at hensen's node establish left/right asymmetric gene expression in the chick. *Science*, 324(5929):941–944, 2009.

[68] Verena Dathe, Anton Gamel, Jörg Männer, Beate Brand-Saberi, and Bodo Christ. Morphological left-right asymmetry of hensen's node precedes the asymmetric expression of shh and fgf8 in the chick embryo. *Anatomy and embryology*, 205(5):343–354, 2002.

[69] Natalia A Shylo, Sarah E Smith, Andrew J Price, Fengli Guo, Melainia McClain, and Paul A Trainor. Morphological changes and two nodal paralogs drive left-right asymmetry in the squamate veiled chameleon (c. calyptratus). *Frontiers in Cell and Developmental Biology*, 11:1132166, 2023.

[70] Jérôme Collignon, Isabella Varlet, and Elizabeth J Robertson. Relationship between asymmetric nodal expression and the direction of embryonic turning. *Nature*, 381(6578):155–158, 1996.

[71] Shigenori Nonaka, Hidetaka Shiratori, Yukio Saijoh, and Hiroshi Hamada. Determination of left–right patterning of the mouse embryo by artificial nodal flow. *Nature*, 418(6893): 96–99, 2002.

[72] William Gilpin, Matthew Storm Bull, and Manu Prakash. The multiscale physics of cilia and flagella. *Nature Reviews Physics*, 2(2):74–88, 2020.

[73] A Hilfinger and F Jülicher. The chirality of ciliary beats. *Physical biology*, 5(1):016003, 2008.

[74] Lydia Djenoune, Mohammed Mahamdeh, Thai V Truong, Christopher T Nguyen, Scott E Fraser, Martina Brueckner, Jonathon Howard, and Shiaulou Yuan. Cilia function as calcium-mediated mechanosensors that instruct left-right asymmetry. *Science*, 379(6627): 71–78, 2023.

[75] Takanobu A Katoh, Toshihiro Omori, Katsutoshi Mizuno, Xiaorei Sai, Katsura Minegishi, Yayoi Ikawa, Hiromi Nishimura, Takeshi Itabashi, Eriko Kajikawa, Sylvain Hiver, et al. Immotile cilia mechanically sense the direction of fluid flow for left-right determination. *Science*, 379(6627):66–71, 2023.

[76] Marko T Boskovski, Shiaulou Yuan, Nis Borbye Pedersen, Christoffer Knak Goth, Svetlana Makova, Henrik Clausen, Martina Brueckner, and Mustafa K Khokha. The heterotaxy gene galnt11 glycosylates notch to orchestrate cilia type and laterality. *Nature*, 504(7480): 456–459, 2013.

[77] Silke S Schröder, Nikoloz Tsikolia, Annette Weizbauer, Isabelle Hue, and Christoph Viebahn. Paraxial nodal expression reveals a novel conserved structure of the left-right organizer in four mammalian species. *Cells Tissues Organs*, 201(2):77–87, 2016.

[78] Lisandro Maya-Ramos and Takashi Mikawa. Programmed cell death along the midline axis patterns ipsilaterality in gastrulation. *Science*, 367(6474):197–200, 2020.

[79] Guillermo Serrano Nájera and Cornelis J Weijer. Cellular processes driving gastrulation in the avian embryo. *Mechanisms of development*, 163:103624, 2020.

[80] Michael Levin, Thorleif Thorlin, Kenneth R Robinson, Taisaku Nogi, and Mark Mercola. Asymmetries in h+/k+-atpase and cell membrane potentials comprise a very early step in left-right patterning. *Cell*, 111(1):77–89, 2002.

[81] Martin Blum, Axel Schweickert, Philipp Vick, Christopher VE Wright, and Michael V Danilchik. Symmetry breakage in the vertebrate embryo: when does it happen and how does it work? *Developmental biology*, 393(1):109–123, 2014.

[82] Emily Sempou, Valentyna Kostiuk, Jie Zhu, M Cecilia Guerra, Leonid Tyan, Woong Hwang, Elena Camacho-Aguilar, Michael J Caplan, David Zenisek, Aryeh Warmflash, et al. Membrane potential drives the exit from pluripotency and cell fate commitment via calcium and mtor. *Nature Communications*, 13(1):6681, 2022.

[83] Viktor Hamburger and Howard L Hamilton. A series of normal stages in the development of the chick embryo. *Journal of morphology*, 88(1):49–92, 1951.

[84] Sophie J Ainsworth, Rachael L Stanley, and Darrell JR Evans. Developmental stages of the japanese quail. *Journal of Anatomy*, 216(1):3–15, 2010.

[85] Guillermo Serrano Nájera and Cornelis J Weijer. The evolution of gastrulation morphologies. *Development*, 150(7), 2023.

[86] Matthew J Stower, Raul E Diaz, Lucia Carrera Fernandez, Mary White Crother, Brian Crother, Adolfo Marco, Paul A Trainor, Shankar Srinivas, and Federica Bertocchini. Bimodal strategy of gastrulation in reptiles. *Developmental Dynamics*, 244(9):1144–1157, 2015.

[87] Arthur Michaut, Alexander Chamolly, Aurelien Villedieu, Francis Corson, and Jerome Gros. A tension-induced morphological transition shapes the avian extra-embryonic territory. *bioRxiv*, pages 2024–02, 2024.

[88] Mehdi Saadaoui, Didier Rocancourt, Julian Roussel, Francis Corson, and Jerome Gros. A tensile ring drives tissue flows to shape the gastrulating amniote embryo. *Science*, 367 (6476):453–458, 2020.

[89] Emil Rozbicki, Manli Chuai, Antti I Karjalainen, Feifei Song, Helen M Sang, René Martin, Hans-Joachim Knölker, Michael P MacDonald, and Cornelis J Weijer. Myosin-ii-mediated cell shape changes and cell intercalation contribute to primitive streak formation. *Nature cell biology*, 17(4):397–408, 2015.

[90] Rodrigo Fernandez-Gonzalez, Sérgio de Matos Simoes, Jens-Christian Röper, Suzanne Eaton, and Jennifer A Zallen. Myosin ii dynamics are regulated by tension in intercalating cells. *Developmental cell*, 17(5):736–743, 2009.

[91] Helge Stalsberg. Mechanism of dextral looping of the embryonic heart. *The American Journal of Cardiology*, 25(3):265–271, 1970.

[92] Rushikesh Sheth, Luciano Marcon, M Félix Bastida, Marisa Junco, Laura Quintana, Randall Dahn, Marie Kmita, James Sharpe, and Maria A Ros. Hox genes regulate digit patterning by controlling the wavelength of a turing-type mechanism. *Science*, 338(6113): 1476–1480, 2012.

[93] Jelena Raspopovic, Luciano Marcon, Laura Russo, and James Sharpe. Digit patterning is controlled by a bmp-sox9-wnt turing network modulated by morphogen gradients. *Science*, 345(6196):566–570, 2014.

[94] Darren Gilmour, Martina Rembold, and Maria Leptin. From morphogen to morphogenesis and back. *Nature*, 541(7637):311–320, 2017.

[95] Amy E Shyer, Tyler R Huycke, ChangHee Lee, L Mahadevan, and Clifford J Tabin. Bending gradients: how the intestinal stem cell gets its home. *Cell*, 161(3):569–580, 2015.

[96] Mijo Simunovic, Emma Evergren, Andrew Callan-Jones, and Patricia Bassereau. Curving cells inside and out: roles of bar domain proteins in membrane shaping and its cellular implications. *Annual review of cell and developmental biology*, 35:111–129, 2019.

[97] Atsushi Shimada, Hideaki Niwa, Kazuya Tsujita, Shiro Suetsugu, Koji Nitta, Kyoko Hanawa-Suetsugu, Ryogo Akasaka, Yuri Nishino, Mitsutoshi Toyama, Lirong Chen, et al. Curved efc/f-bar-domain dimers are joined end to end into a filament for membrane invagination in endocytosis. *Cell*, 129(4):761–772, 2007.

[98] Klaus Fütterer and Laura M Machesky. "wunder" f-bar domains: going from pits to vesicles. *Cell*, 129(4):655–657, 2007.

[99] Archit Bhatnagar, Michael Nestler, Peter Gross, Mirna Kramar, Mark Leaver, Axel Voigt, and Stephan W Grill. Axis convergence in c. elegans embryos. *Current Biology*, 33(23): 5096–5108, 2023.

[100] Amy E Shyer, Tuomas Tallinen, Nandan L Nerurkar, Zhiyan Wei, Eun Seok Gil, David L Kaplan, Clifford J Tabin, and L Mahadevan. Villification: how the gut gets its villi. *Science*, 342(6155):212–218, 2013.

[101] Bruno Antonny. Mechanisms of membrane curvature sensing. *Annual review of biochemistry*, 80:101–123, 2011.

[102] Bianca Habermann. The bar-domain family of proteins: a case of bending and binding? the membrane bending and gtpase-binding functions of proteins from the bar-domain family. *EMBO reports*, 5(3):250–255, 2004.

[103] Ludger Johannes, Robert G Parton, Patricia Bassereau, and Satyajit Mayor. Building endocytic pits without clathrin. *Nature reviews Molecular cell biology*, 16(5):311–321, 2015.

[104] Bob Goldstein and Steven N Hird. Specification of the anteroposterior axis in caenorhabditis elegans. *Development*, 122(5):1467–1474, 1996.

[105] Kerstin Klinkert, Nicolas Levernier, Peter Gross, Christian Gentili, Lukas von Tobel, Marie Pierron, Coralie Busso, Sarah Herrman, Stephan W Grill, Karsten Kruse, et al. Aurora a depletion reveals centrosome-independent polarization mechanism in caenorhabditis elegans. *Elife*, 8:e44552, 2019.

[106] Oscar Hertwig. *Welchen Einfluß übt die Schwerkraft auf die Theilung der Zellen?* Number 2. G. Fischer, 1884.

[107] Nicolas Minc, David Burgess, and Fred Chang. Influence of cell geometry on division-plane positioning. *Cell*, 144(3):414–426, 2011.

[108] Pedro Campinho, Martin Behrndt, Jonas Ranft, Thomas Risler, Nicolas Minc, and Carl-Philipp Heisenberg. Tension-oriented cell divisions limit anisotropic tissue tension in epithelial spreading during zebrafish epiboly. *Nature cell biology*, 15(12):1405–1414, 2013.

[109] Jérémy Sallé and Nicolas Minc. Cell division geometries as central organizers of early embryo development. In *Seminars in Cell & Developmental Biology*, volume 130, pages 3–11. Elsevier, 2022.

[110] Tom PJ Wyatt, Andrew R Harris, Maxine Lam, Qian Cheng, Julien Bellis, Andrea Dimitracopoulos, Alexandre J Kabla, Guillaume T Charras, and Buzz Baum. Emergence of homeostatic epithelial packing and stress dissipation through divisions oriented along the long cell axis. *Proceedings of the National Academy of Sciences*, 112(18):5726–5731, 2015.

[111] Christopher B O'Connell and Yu-li Wang. Mammalian spindle orientation and position respond to changes in cell shape in a dynein-dependent fashion. *Molecular biology of the cell*, 11(5):1765–1774, 2000.

[112] Rebecca A Green, Ewa Paluch, and Karen Oegema. Cytokinesis in animal cells. *Annual review of cell and developmental biology*, 28:29–58, 2012.

[113] Akatsuki Kimura and Shuichi Onami. Computer simulations and image processing reveal length-dependent pulling force as the primary mechanism for c. elegans male pronuclear migration. *Developmental cell*, 8(5):765–775, 2005.

[114] Hirokazu Tanimoto, Jeremy Sallé, Louise Dodin, and Nicolas Minc. Physical forces determining the persistency and centring precision of microtubule asters. *Nature physics*, 14(8): 848–854, 2018.

[115] Kenji Kimura and Akatsuki Kimura. Intracellular organelles mediate cytoplasmic pulling force for centrosome centration in the caenorhabditis elegans early embryo. *Proceedings of the National Academy of Sciences*, 108(1):137–142, 2011.

[116] Guillaume Salbreux and Frank Jülicher. Mechanics of active surfaces. *Physical Review E*, 96(3):032404, 2017.

[117] Carl Friedrich Gauss. *Disquisitiones generales circa superficies curvas*. Dieterich, 1828.

[118] Riccardo Capovilla and Jemal Guven. Stresses in lipid membranes. *Journal of Physics A: Mathematical and General*, 35(30):6233, 2002.

[119] Sybren Ruurds De Groot and Peter Mazur. *Non-equilibrium thermodynamics*. Courier Corporation, 2013.

[120] Frank Jülicher, Stephan W Grill, and Guillaume Salbreux. Hydrodynamic theory of active matter. *Reports on Progress in Physics*, 81(7):076601, 2018.

[121] Anatol W Fritsch, Andrés F Diaz-Delgadillo, Omar Adame-Arana, Carsten Hoege, Matthäus Mittasch, Moritz Kreysing, Mark Leaver, Anthony A Hyman, Frank Jülicher, and Christoph A Weber. Local thermodynamics govern formation and dissolution of caenorhabditis elegans p granule condensates. *Proceedings of the National Academy of Sciences*, 118 (37):e2102772118, 2021.

[122] Donald G Miller. Thermodynamics of irreversible processes. the experimental verification of the onsager reciprocal relations. *Chemical Reviews*, 60(1):15–37, 1960.

[123] Pierre-Gilles De Gennes and Jacques Prost. *The physics of liquid crystals*. Number 83. Oxford university press, 1993.

[124] Lars Onsager. Reciprocal relations in irreversible processes. i. *Physical review*, 37(4):405, 1931.

[125] Lars Onsager. Reciprocal relations in irreversible processes. ii. *Physical review*, 38(12): 2265, 1931.

[126] Pierre Curie. Sur la symétrie dans les phénomènes physiques, symétrie d'un champ électrique et d'un champ magnétique. *J. Phys. Theor. Appl.*, 3(1):393–415, 1894.

[127] Leo Q Wan, Kacey Ronaldson, Miri Park, Grace Taylor, Yue Zhang, Jeffrey M Gimble, and Gordana Vunjak-Novakovic. Micropatterned mammalian cells exhibit phenotype-specific left-right asymmetry. *Proceedings of the National Academy of Sciences*, 108(30):12295–12300, 2011.

[128] Sundar R Naganathan, Marko Popović, and Andrew C Oates. Left–right symmetry of zebrafish embryos requires somite surface tension. *Nature*, 605(7910):516–521, 2022.

[129] Harold Jeffreys. On isotropic tensors. In *Mathematical Proceedings of the Cambridge philosophical society*, volume 73, pages 173–176. Cambridge University Press, 1973.

[130] Arnab Saha, Masatoshi Nishikawa, Martin Behrndt, Carl-Philipp Heisenberg, Frank Jülicher, and Stephan W Grill. Determining physical properties of the cell cortex. *Biophysical journal*, 110(6):1421–1429, 2016.

[131] Amin Doostmohammadi, Jordi Ignés-Mullol, Julia M Yeomans, and Francesc Sagués. Active nematics. *Nature communications*, 9(1):3246, 2018.

[132] Thuan Beng Saw, Amin Doostmohammadi, Vincent Nier, Leyla Kocgozlu, Sumesh Thampi, Yusuke Toyama, Philippe Marcq, Chwee Teck Lim, Julia M Yeomans, and Benoit Ladoux. Topological defects in epithelia govern cell death and extrusion. *Nature*, 544 (7649):212–216, 2017.

[133] Sebastian J Streichan, Matthew F Lefebvre, Nicholas Noll, Eric F Wieschaus, and Boris I Shraiman. Global morphogenetic flow is accurately predicted by the spatial distribution of myosin motors. *Elife*, 7:e27454, 2018.

[134] William J Bowen and Harold L Martin. The diffusion of adenosine triphosphate through aqueous solutions. *Archives of biochemistry and biophysics*, 107(1):30–36, 1964.

[135] Alexander Mietke, V Jemseena, K Vijay Kumar, Ivo F Sbalzarini, and Frank Jülicher. Minimal model of cellular symmetry breaking. *Physical review letters*, 123(18):188101, 2019.

[136] Justin S Bois, Frank Jülicher, and Stephan W Grill. Pattern formation in active fluids. *Biophysical Journal*, 100(3):445a, 2011.

[137] Ezra Newman and Roger Penrose. An approach to gravitational radiation by a method of spin coefficients. *Journal of Mathematical Physics*, 3(3):566–578, 1962.

[138] Joshua N Goldberg, Alan J MacFarlane, Ezra T Newman, Fritz Rohrlich, and EC George Sudarshan. Spin-s spherical harmonics and ð. *Journal of Mathematical Physics*, 8(11): 2155–2161, 1967.

[139] Farzan Vafa, Grace H Zhang, and David R Nelson. Defect absorption and emission for p-atic liquid crystals on cones. *Physical Review E*, 106(2):024704, 2022.

[140] Luca Giomi, John Toner, and Niladri Sarkar. Hydrodynamic theory of p-atic liquid crystals. *Physical Review E*, 106(2):024701, 2022.

[141] Mark Bowick and Alex Travesset. The geometrical structure of 2d bond-orientational order. *Journal of Physics A: Mathematical and General*, 34(8):1535, 2001.

[142] Ralph Abraham, Jerrold E Marsden, and Tudor Ratiu. *Manifolds, tensor analysis, and applications*, volume 75. Springer Science & Business Media, 2012.

[143] Ingo Nitschke, Sebastian Reuther, and Axel Voigt. Discrete exterior calculus (dec) for the surface navier-stokes equation. *Transport processes at fluidic interfaces*, pages 177–197, 2017.

[144] DJG Pearce, Perry W Ellis, Alberto Fernandez-Nieves, and L Giomi. Geometrical control of active turbulence in curved topographies. *Physical review letters*, 122(16):168002, 2019.

[145] Carl Friedrich Gauss. Allgemeine auflosung der aufgabe die theile einer gegebnen flache auf einer andern gegebnen flache so abzubilden dass die abbildung dem abgebildeten in den kleinsten theilen ahnlich wird. astronomische abhandlungen herausgegeben von hc schumacher, drittes heft. *Gauss Werke Band*, 4:189–216, 1825.

[146] Mark J Bowick and Luca Giomi. Two-dimensional matter: order, curvature and defects. *Advances in Physics*, 58(5):449–563, 2009.

[147] Peter Henrici. *Applied and computational complex analysis, Volume 3: Discrete Fourier analysis, Cauchy integrals, construction of conformal maps, univalent functions*, volume 41. John Wiley & Sons, 1993.

[148] Wilhelm Wirtinger. Zur formalen theorie der funktionen von mehr komplexen veränderlichen. *Mathematische Annalen*, 97(1):357–375, 1927.

[149] Michael Eastwood and Paul Tod. Edth-a differential operator on the sphere. In *Mathematical Proceedings of the Cambridge Philosophical Society*, volume 92, pages 317–330. Cambridge University Press, 1982.

[150] Farzan Vafa and L Mahadevan. Active nematic defects and epithelial morphogenesis. *Physical Review Letters*, 129(9):098102, 2022.

[151] Karen M Downs, Kimberly E Inman, Dexter X Jin, and Allen C Enders. The allantoic core domain: new insights into development of the murine allantois and its relation to the primitive streak. *Developmental dynamics: an official publication of the American Association of Anatomists*, 238(3):532–553, 2009.

[152] Jonas Ranft, Markus Basan, Jens Elgeti, Jean-François Joanny, Jacques Prost, and Frank Jülicher. Fluidization of tissues by cell division and apoptosis. *Proceedings of the National Academy of Sciences*, 107(49):20863–20868, 2010.

[153] Vincent Fleury. An elasto-plastic model of avian gastrulation. *Organogenesis*, 2(1):6–16, 2005.

[154] Eize Stamhuis and William Thielicke. Pivlab–towards user-friendly, affordable and accurate digital particle image velocimetry in matlab. *Journal of open research software*, 2(1):30, 2014.

[155] George Keith Batchelor. *An introduction to fluid dynamics*. Cambridge university press, 1967.

[156] Alexander Mietke. *Dynamics of active surfaces*. PhD thesis, Technische Universität Dresden Dresden, 2018.

[157] Nikolaĭ Ivanovich Muskhelishvili et al. *Some basic problems of the mathematical theory of elasticity*, volume 15. Noordhoff Groningen, 1953.

[158] Max L Williams. On the stress distribution at the base of a stationary crack. *J. Appl. Mech*, 24:109–114, 1957.

[159] Maria Comninou. Interface crack with friction in the contact zone. *J. Appl. Mech*, 44: 780–781, 1977.

[160] Harold M Westergaard. Bearing pressures and cracks: Bearing pressures through a slightly waved surface or through a nearly flat part of a cylinder, and related problems of cracks. *J. Appl. Mech*, 6:A49–A53, 1939.

[161] Alan Arnold Griffith. Vi. the phenomena of rupture and flow in solids. *Philosophical transactions of the royal society of london. Series A, containing papers of a mathematical or physical character*, 221(582-593):163–198, 1921.

[162] Emmanuel E Gdoutos. *Fracture mechanics: an introduction*, volume 263. Springer Nature, 2020.

[163] Daniel Maugis. *Contact, adhesion and rupture of elastic solids*, volume 130. Springer Science & Business Media, 2013.

[164] Dietmar Gross and Thomas Seelig. *Fracture mechanics: with an introduction to micromechanics*. Springer, 2017.

[165] Paolo Caldarelli, Alexander Chamolly, Olinda Alegria-Prévot, Jerome Gros, and Francis Corson. Self-organized tissue mechanics underlie embryonic regulation. *bioRxiv*, pages 2021–10, 2021.

[166] Raphaël Etournay, Marko Popović, Matthias Merkel, Amitabha Nandi, Corinna Blasse, Benoît Aigouy, Holger Brandl, Gene Myers, Guillaume Salbreux, Frank Jülicher, et al. Interplay of cell dynamics and epithelial tension during morphogenesis of the drosophila pupal wing. *Elife*, 4:e07090, 2015.

[167] Teije C Middelkoop, Jonas Neipel, Caitlin E Cornell, Ronald Naumann, Lokesh G Pimpale, Frank Jülicher, and Stephan W Grill. A cytokinetic ring-driven cell rotation achieves hertwig's rule in early development. *bioRxiv*, pages 2023–06, 2023.

[168] Amy Shaub Maddox, Lindsay Lewellyn, Arshad Desai, and Karen Oegema. Anillin and the septins promote asymmetric ingression of the cytokinetic furrow. *Developmental cell*, 12(5):827–835, 2007.

[169] Stephanie Schonegg, Anthony A Hyman, and William B Wood. Timing and mechanism of the initial cue establishing handed left–right asymmetry in caenorhabditis elegans embryos. *Genesis*, 52(6):572–580, 2014.

[170] Knut Drescher, Raymond E Goldstein, Nicolas Michel, Marco Polin, and Idan Tuval. Direct measurement of the flow field around swimming microorganisms. *Physical Review Letters*, 105(16):168101, 2010.

[171] André Scholich. *Biaxial Nematic Order in Liver Tissue.* PhD thesis, Technische Universität Dresden Dresden, 2018.

[172] André Scholich, Simon Syga, Hernán Morales-Navarrete, Fabián Segovia-Miranda, Hidenori Nonaka, Kirstin Meyer, Walter de Back, Lutz Brusch, Yannis Kalaidzidis, Marino Zerial, et al. Quantification of nematic cell polarity in three-dimensional tissues. *PLoS computational biology*, 16(12):e1008412, 2020.

[173] Mircea Craioveanu, Mircea Puta, Themistocles M Rassias, Mircea Craioveanu, Mircea Puta, and Themistocles M Rassias. Spectral properties of the laplace-beltrami operator and applications. *Old and New Aspects in Spectral Geometry*, pages 119–211, 2001.

[174] Mark Kac. Can one hear the shape of a drum? *The american mathematical monthly*, 73 (4P2):1–23, 1966.

[175] Dmitriĭ Aleksandrovich Varshalovich, Anatoliĭ Nikolaevitch Moskalev, and Valerij Kel'manovĭc Khersonskii. *Quantum theory of angular momentum.* World Scientific, 1988.

[176] Christopher J Foot. *Atomic physics*, volume 7. OUP Oxford, 2004.

[177] Gernot Münster. *Quantentheorie.* Walter de Gruyter, 2006.

[178] Alan Mathison Turing. The chemical basis of morphogenesis. *Bulletin of mathematical biology*, 52:153–197, 1990.

[179] Alfred Gierer and Hans Meinhardt. A theory of biological pattern formation. *Kybernetik*, 12:30–39, 1972.

[180] André-Joseph Koch and Hans Meinhardt. Biological pattern formation: from basic mechanisms to complex structures. *Reviews of modern physics*, 66(4):1481, 1994.

[181] Shigeru Kondo and Takashi Miura. Reaction-diffusion model as a framework for understanding biological pattern formation. *science*, 329(5999):1616–1620, 2010.

[182] Dominik Thalmeier, Jacob Halatek, and Erwin Frey. Geometry-induced protein pattern formation. *Proceedings of the National Academy of Sciences*, 113(3):548–553, 2016.

[183] Raphaela Geßele, Jacob Halatek, Laeschkir Würthner, and Erwin Frey. Geometric cues stabilise long-axis polarisation of par protein patterns in c. elegans. *Nature communications*, 11(1):539, 2020.

[184] Laeschkir Würthner, Andriy Goychuk, and Erwin Frey. Geometry-induced patterns through mechanochemical coupling. *Physical Review E*, 108(1):014404, 2023.

[185] Julia Riedl, Alvaro H Crevenna, Kai Kessenbrock, Jerry Haochen Yu, Dorothee Neukirchen, Michal Bista, Frank Bradke, Dieter Jenne, Tad A Holak, Zena Werb, et al. Lifeact: a versatile marker to visualize f-actin. *Nature methods*, 5(7):605–607, 2008.

[186] Deepika Singh and Christian Pohl. Coupling of rotational cortical flow, asymmetric midbody positioning, and spindle rotation mediates dorsoventral axis formation in c. elegans. *Developmental cell*, 28(3):253–267, 2014.

[187] Manasi Kelkar, Pierre Bohec, Matthew B Smith, Varun Sreenivasan, Ana Lisica, Léo Valon, Emma Ferber, Buzz Baum, Guillaume Salbreux, and Guillaume Charras. Spindle reorientation in response to mechanical stress is an emergent property of the spindle positioning mechanisms. *Proceedings of the National Academy of Sciences*, 119(26):e2121868119, 2022.

[188] Sachin Kotak and Pierre Gönczy. Mechanisms of spindle positioning: cortical force generators in the limelight. *Current opinion in cell biology*, 25(6):741–748, 2013.

[189] Pere Roca-Cusachs, Raimon Sunyer, and Xavier Trepat. Mechanical guidance of cell migration: lessons from chemotaxis. *Current opinion in cell biology*, 25(5):543–549, 2013.

[190] Julius Adler and Wung-Wai Tso. " decision"-making in bacteria: Chemotactic response of escherichia coli to conflicting stimuli. *Science*, 184(4143):1292–1294, 1974.

[191] Adam Shellard and Roberto Mayor. Collective durotaxis along a self-generated stiffness gradient in vivo. *Nature*, 600(7890):690–694, 2021.

[192] Farzan Vafa, David R Nelson, and Amin Doostmohammadi. Active topological defect absorption by a curvature singularity. *Journal of Physics: Condensed Matter*, 35(42): 425101, 2023.

[193] The MathWorks Inc. Symbolic math toolbox version: 9.2 (r2022b), 2022. URL `https://www.mathworks.com`.

[194] Alexandra Colin, Magali Orhant-Prioux, Christophe Guérin, Mariya Savinov, Wenxiang Cao, Benoit Vianay, Ilaria Scarfone, Aurélien Roux, Enrique M De La Cruz, Alex Mogilner, et al. Friction patterns guide actin network contraction. *Proceedings of the National Academy of Sciences*, 120(39):e2300416120, 2023.

[195] Emily W Gehrels, Bandan Chakrabortty, Marc-Eric Perrin, Matthias Merkel, and Thomas Lecuit. Curvature gradient drives polarized tissue flow in the drosophila embryo. *Proceedings of the National Academy of Sciences*, 120(6):e2214205120, 2023.

[196] Tianchi Chen, Andrew Callan-Jones, Eduard Fedorov, Andrea Ravasio, Agustí Brugués, Hui Ting Ong, Yusuke Toyama, Boon Chuan Low, Xavier Trepat, Tom Shemesh, et al. Large-scale curvature sensing by directional actin flow drives cellular migration mode switching. *Nature physics*, 15(4):393–402, 2019.

[197] Audrey Desgrange, Jean-François Le Garrec, and Sigolène M Meilhac. Left-right asymmetry in heart development and disease: forming the right loop. *Development*, 145(22): dev162776, 2018.

[198] JE Avron. Odd viscosity. *Journal of statistical physics*, 92:543–557, 1998.

[199] Sungrim Seirin-Lee, Kazunori Yamamoto, and Akatsuki Kimura. The extra-embryonic space and the local contour are crucial geometric constraints regulating cell arrangement. *Development*, 149(9):dev200401, 2022.

[200] Ludwig A Hoffmann, Livio Nicola Carenza, and Luca Giomi. Tuneable defect-curvature coupling and topological transitions in active shells. *Soft Matter*, 19(19):3423–3435, 2023.

[201] Antony Lewis, Anthony Challinor, and Neil Turok. Analysis of cmb polarization on an incomplete sky. *Physical Review D*, 65(2):023505, 2001.

[202] Izrail Moiseevich Gelfand, Robert Adolfovich Minlos, and Z Ya Shapiro. *Representations of the Rotation and Lorentz Groups and their Applications.* Courier Dover Publications, 2018.

[203] Ezra T Newman and Roger Penrose. Note on the bondi-metzner-sachs group. *Journal of Mathematical Physics*, 7(5):863–870, 1966.

[204] NVIDIA, Péter Vingelmann, and Frank H.P. Fitzek. Cuda, release: 10.2.89, 2020. URL `https://developer.nvidia.com/cuda-toolkit`.

[205] Martin Reinecke and Dag Sverre Seljebotn. Libsharp–spherical harmonic transforms revisited. *Astronomy & Astrophysics*, 554:A112, 2013.

[206] The MathWorks Inc. Matlab version: 9.13.0 (r2022b), 2022. URL `https://www.mathworks.com`.

[207] Wolfram Research, Inc. Mathematica, Version 13.1. URL `https://www.wolfram.com/mathematica`. Champaign, IL, 2022.

[208] Robert Geroch. Multipole moments. i. flat space. *Journal of Mathematical Physics*, 11(6): 1955–1961, 1970.

Versicherung

Hiermit versichere ich, dass ich die vorliegende Arbeit ohne unzulässige Hilfe Dritter und ohne Benutzung anderer als der angegebenen Hilfsmittel angefertigt habe; die aus fremden Quellen direkt oder indirekt übernommenen Gedanken sind als solche kenntlich gemacht. Die Arbeit wurde bisher weder im Inland noch im Ausland in gleicher oder ähnlicher Form einer anderen Prüfungsbehörde vorgelegt. Die Arbeit wurde in Dresden am Max-Planck-Institut für Physik komplexer Systeme unter der Betreuung von Prof. Dr. Frank Jülicher und am Max-Planck-Institut für molekulare Zellbiologie und Genetik under der Betreuung von Prof. Dr. Stephan Grill angefertigt.

Jonas Neipel
Dresden, Mai 2024